

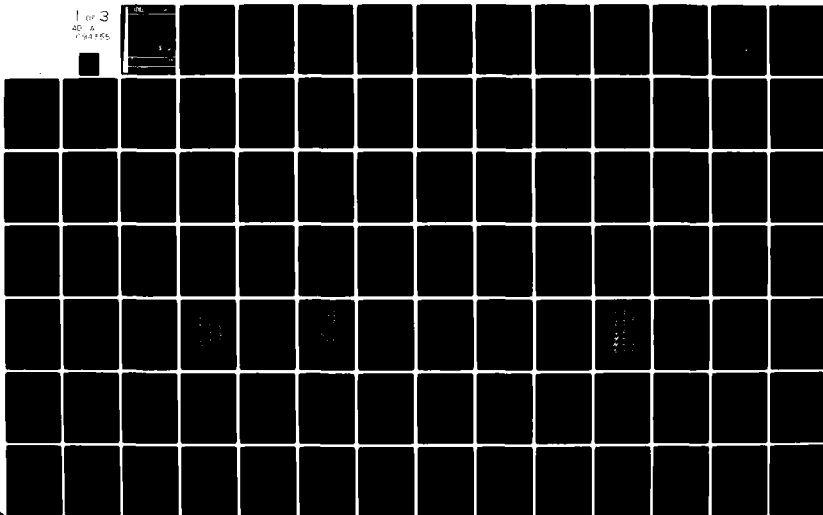
AD-A094 355

HAWAII INST OF GEOPHYSICS HONOLULU
LOPEZ ISLAND OCEAN BOTTOM SEISMOMETER INTERCOMPARISON EXPERIMENT--ETC(U)
OCT 80 G H SUTTON, B T LEWIS, J EWING
HIG-80-4

F/6 8/11
N00014-75-C-0209
NL

UNCLASSIFIED

1 of 3
AD A
198705



AD A094355

LOPEZ ISLAND OCEAN BOTTOM SEISMOMETER INTERCOMPARISON EXPERIMENT

Final Report

G. H. SUTTON, B. T. R. LEWIS, J. EWING,
F. K. DUENNEBIER, B. IWATAKE, J. D. TUTHILL,
and others

OCTOBER 1980

Prepared for
OFFICE OF NAVAL RESEARCH

DTIC
ELECTR
FEB 2 1981

F

FILE COPY

1473

LOPEZ ISLAND OCEAN BOTTOM SEISMOMETER
INTERCOMPARISON EXPERIMENT¹

Final Report

G. H. Sutton², B. T. R. Lewis³, J. Ewing⁴,
F. K. Duennebie², B. Iwatake², and J. D. Tuthi¹³

October 1980

¹ The authors listed above prepared this report. Other contributors are all the additional participants in the field experiment listed in Appendix A. The experiment was designed and organized principally by G. H. Sutton², J. Ewing⁴, B. T. R. Lewis³, P. Pomeroy⁵, and J. Orcutt⁶, with the cooperation of all other participants. Funding for this experiment and report was supplied by the Office of Naval Research.


² Hawaii Institute of Geophysics, Honolulu, Hawaii 96822.

³ University of Washington, Seattle, Washington 98195.

⁴ Woods Hole Oceanographic Institution, Woods Hole, Massachusetts 02543.

⁵ Lamont-Doherty Geological Observatory, Palisades, New York 10964 (now at Roundout Assoc., Stone Ridge, New York).

⁶ Scripps Institution of Oceanography, La Jolla, California 92093.


Charles E. Helsley
Director,
Hawaii Institute of Geophysics

ABSTRACT

The purpose of the Lopez Island Ocean Bottom Seismometer Intercomparison Experiment was to determine the effects of coupling and bottom currents on ocean bottom seismometers. Twelve operational OBS's, three specially designed three-component systems and a hydrophone were compared with each other. Unlike seismometers placed on hard rock at land stations, ocean bottom seismometers can be affected by soft sediments (which act as lossy mechanical springs) and by buoyancy. Coupling through soft sediments can modify the response to ground motion much as a low pass filter does, and high buoyancy tends to counteract this effect. These effects are observed in the Lopez data, which consist of signals from mechanical transient tests, cap shots, airgun pulses, and general background noise. The modification of response is pronounced for some instruments and barely noticeable in others. Instruments that stand high in the water relative to their base width tend to be susceptible to rocking motion that shows up as a mechanical cross coupling between horizontal and vertical motion. Correlation of Lopez results with coupling theory suggests that it is possible to design ocean bottom seismometers that will couple well to any sediment. Current levels at the Lopez site (<5 cm/sec) were too small to produce noticeable effect on any of the instruments; however, the same design criteria that will minimize coupling problems will also lessen problems caused by ocean currents.

CONTENTS

	<u>Page</u>
Abstract	iii
List of Tables	vi
List of Figures	vi
List of Appendixes	vii
I. INTRODUCTION	1
II. EXPERIMENT DESCRIPTION	3
Site Choice and Description	3
Recording System	8
Measurement of Response	8
Physical Oceanography Data	13
III. INSTRUMENTATION	13
IV. COUPLING	35
Response to Vertical Input on Vertical Geophones	35
Response to Vertical Input on Horizontal Geophones	42
Horizontal Input Recorded on Vertical Geophones	42
Response to Horizontal Input on Horizontal Geophones	48
V. NOISE MEASUREMENTS	48
Characteristics of Ambient Seismic Noise	50
Comparison of Noise with Shot-Generated Surface Waves	50
Comparison Between Hydrophone and Seismometer Data	57
Correlation of Background Noise with Currents	57
VI. CONCLUSIONS	67
VII. FUTURE DEVELOPMENTS	70
ACKNOWLEDGMENTS	71
REFERENCES	72
APPENDIXES A through J	various pp.

Accession For	
NTIS GRA&I	<input checked="" type="checkbox"/>
DTIC TAB	<input type="checkbox"/>
Unannounced	<input type="checkbox"/>
Justification	
By	
Distribution/	
Availability Codes	
Dist	Avail and/or Special
A	

LIST OF TABLES

<u>Table</u>	<u>Page</u>
II-1. Physical Properties of Shoal Bay Sediments	7
II-2. Instrument Locations	10
III-1. OBS Physical Characteristics	32
III-2. OBS Response Formulae	34
IV-1. OBS Coupling Parameters	40

LIST OF FIGURES

<u>Figure</u>	<u>Page</u>
I-1. Lopez Island Experiment standard seismometers	2
II-1. Location map of Lopez Island	4
II-2. Map of Shoal Bay	5
II-3. Reflection profiles	6
II-4. Instrument locations	9
II-5. Transient tests	11
II-6. Tidal records	12
III-1. (PL) Plate standard	15
III-2. (SP) Spike standards	16
III-3. (ND) Neutral density standard	17
III-4. Preamplifier	18
III-5. Standard hydrophone	19
III-6. (BIO) Bedford Institute of Oceanography OBS	20
III-7. (HIGB) Hawaii Institute of Geophysics Burp-Out OBS	21
III-8. (HIGS) Hawaii Institute of Geophysics Standard OBS	22
III-9. (LDGO) Lamont-Doherty Geological Observatory OBS	23
III-10. (MIT) Massachusetts Institute of Technology OBS	24
III-11. (OSU) Oregon State University OBS	25
III-12. (SIO) Scripps Institution of Oceanography OBS	26
III-13. (UCSB) University of California at Santa Barbara OBS	27
III-14. (USGS) U. S. Geological Survey OBS	28
III-15. (UTC) University of Texas at Galveston OBS	29
III-16. (UWF) University of Washington "Flower Pot" OBS	30
III-17. (UW) University of Washington OBS	31
III-18. OBS response curves	33
IV-1. Coupling schematic	36
IV-2. Theoretical amplitude response	37
IV-3. Theoretical versus actual response	39
IV-4. Bottom coupling frequencies	41
IV-5. Airgun shot 182	43
IV-6. Seismic and transient response comparison	44
IV-7. Recordings exhibiting good response	45
IV-8. Comparison of good and poor responses	46
IV-9. Airgun shot 182 time domain	47
IV-10. Horizontal transient tests on vertical sensors	49

LIST OF FIGURES (cont'd.)

Figure		Page
V-1.	Noise recorded on PL V	51
V-2.	Noise particle motion on PL V	52
V-3.	Noise preceding airgun shot 182	53
V-4.	Particle motion for Figure V-3	54
V-5.	Wavenumber spectrum at 2 Hz	55
V-6.	Record section for cap shot	56
V-7.	Spectrum for airgun shot 131 on PL V	58
V-8.	Particle motion of surface waves on PL V	59
V-9.	Dispersion curves	60
V-10.	Comparison of PL and hydrophone signals	61
V-11.	Comparison of pressure and geophone spectra	62
V-12.	Water currents versus rank	63
V-13.	Noise spectra - UCSB V versus SP	65
V-14.	5-Hz noise versus current, SP V	66
V-15.	3-Hz and 9-Hz noise versus current, UCSB V	68

LIST OF APPENDIXES

Appendix

A.	Contributors to the Lopez Island Ocean Bottom Seismometer Intercomparison Experiment
B.	Catalog of Lopez Island Experiment Digitized Events
C.	Selected Digitized Events Recorded During the Lopez Island Noise Studies
D.	Noise Studies
E.	Coupling of Ocean Bottom Seismometers to Soft Bottoms <i>G. H. Sutton, F. K. Duennebier, and B. Iwatake</i>
F.	The Vertical Response of an Ocean Bottom Seismometer: Analysis of the Lopez Island Vertical Transient Tests <i>S. J. Zelikovitz and W. A. Prothero, Jr.</i>
G.	Stoneley Waves, Lopez Island Noise, and Deep Sea Noise from 1 to 5 Hz <i>J. D. Tuthill, B. T. R. Lewis, and J. D. Garmany</i>
H.	Instrumental Waveform Distortion on Ocean Bottom Seismometers <i>B. T. R. Lewis and J. D. Tuthill</i>
I.	Bottom Seismometer Observation of Airgun Signals at Lopez Island <i>S. H. Johnson and R. E. McAlister</i>
J.	Current-Generated Noise Recorded on Ocean Bottom Seismometers <i>F. K. Duennebier, G. Blackinton, and G. H. Sutton</i>

I. INTRODUCTION

Between June 13 and 30, 1978 a field intercomparison of several ocean bottom seismograph (OBS) systems was conducted in Shoal Bay, Lopez Island (Puget Sound), Washington. Participants in the experiment are listed in Appendix A. The two main reasons for the field test were: (1) to compare the responses of the instruments, which have quite varied mechanical configurations, when coupled to the earth through soft sediments comparable to those of the ocean floor; and (2) to determine the susceptibility of the instruments to noise induced by near-bottom ocean currents. The results of this experiment should provide information important for the design of OBS systems that will minimize noise and optimize coupling characteristics.

Signals recorded on ocean bottom seismograph geophones are often monochromatic and complicated. Whether these features are natural in origin or caused by the presence of the OBS is a major question to be answered by this test. Some data indicated that the presence of the OBS on the soft sediments could severely distort the motion of the ground; however, the extent of this problem for OBS's of different configurations was unknown. The complications present on many geophone records are not observed on ocean bottom hydrophones, thus the question: do geophone data add any useful information that cannot be obtained from hydrophones?

Some data have indicated that near-bottom ocean currents can increase noise levels on OBS's enough to make them unusable during high-current periods; therefore, we wanted to test as many systems as possible for susceptibility to ocean current noise.

In addition to 12 operational OBS's supplied by 10 different research organizations, three sets of three-component ($T_0 = 1$ sec) seismometers and a hydrophone were included to provide standards for comparison: a "spike standard" was pushed firmly into the bottom; a "plate standard" with a smooth, hemispherical superstructure on a large, flat, circular plate was placed on the sediments; and a "neutral density standard" with a roughly spherical shape was floated within the uppermost sediment (Fig. I-1). The instruments were placed within a few meters of each other, and four current meters were installed around the array to monitor water circulation in the bay.

Data were obtained from each sensor by hard wiring analog signals to land where they were recorded by a 24-channel digital system. About 250 seismic records were obtained; these include signals from mechanical transient tests, seismic signals from 211 airgun shots and 8 blasting caps, and 12 samples of background noise (Appendix B). In addition to the digital recording, many of the instruments recorded internally, supplying valuable supplementary data.

Mechanical transient tests were conducted to provide some quantitative estimate of the coupling function between the ocean bottom and the OBS package, including possible cross coupling between horizontal

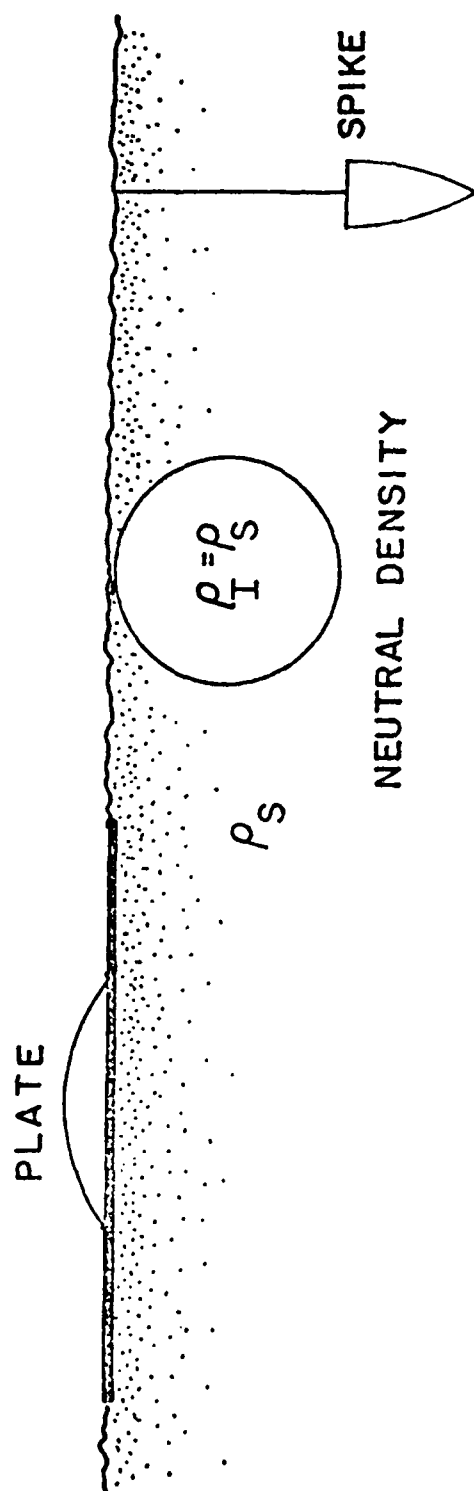


Fig. I-1. Lopez Island Experiment standard seismometers.

and vertical motions. The procedure is analogous to the classical weight lift test for earthquake seismographs, although because of buoyancy the response of the seismic system to the mechanical transient test is not necessarily the same as that to a seismic input.

In this report we summarize the results of the Lopez Island intercomparison test. Representative data are shown with the text, and selected records from each recorded sensor are shown in Appendix C. Additional justifications for the results are presented in the referenced papers, included as appendices to this report.

II. EXPERIMENT DESCRIPTION

Achievement of the test goals required: a logistically favorable site that was reasonably seismically quiet and had sediments with physical properties comparable to those of deep-sea sediments; a system for digitally recording multiple channels simultaneously; a method for measuring total instrument response, including the effects of the bottom; and the measurement of physical oceanographic data such as tidal height and current velocities. The implementation of each of these requirements is described below.

Site Choice and Description

The requirements that a site have sediments with physical properties similar to those of deep-sea sediments, reasonably low noise levels, and be logistically accessible with respect to scuba divers, power, and transportation, removed from consideration most sites in or adjacent to open ocean, because of surf noise, and sites that were too remote. A site that met all the requirements was situated at the northern end of Lopez Island, in the San Juan Islands in Washington State. Its general location is shown in Figure II-1 and the specific location, Shoal Bay, Figure II-2.

Shoal Bay lies between Humphrey Head and Upright Head, which consist mostly of consolidated siltstone-sandstone conglomerates of marine origin. The water depth in Shoal Bay is a fairly uniform 6 to 7 meters at low water and is underlain by a generally constant 3 m of acoustically transparent soft silty mud; this latter fact was determined from reflection profiles taken with a 3-KHz system (Fig. II-3). It is not known whether this mud is underlain by the hard conglomerates or by less competent glacial material that would in turn be underlain by the conglomerates.

Several short gravity cores were taken in the area of the instrument array and the physical properties of the top 7 cm were measured (Table II-1). These sediments were almost exclusively silt and were



Fig. II-1. Location map of Lopez Island area. Dash-dot line is the U.S.-Canada border.

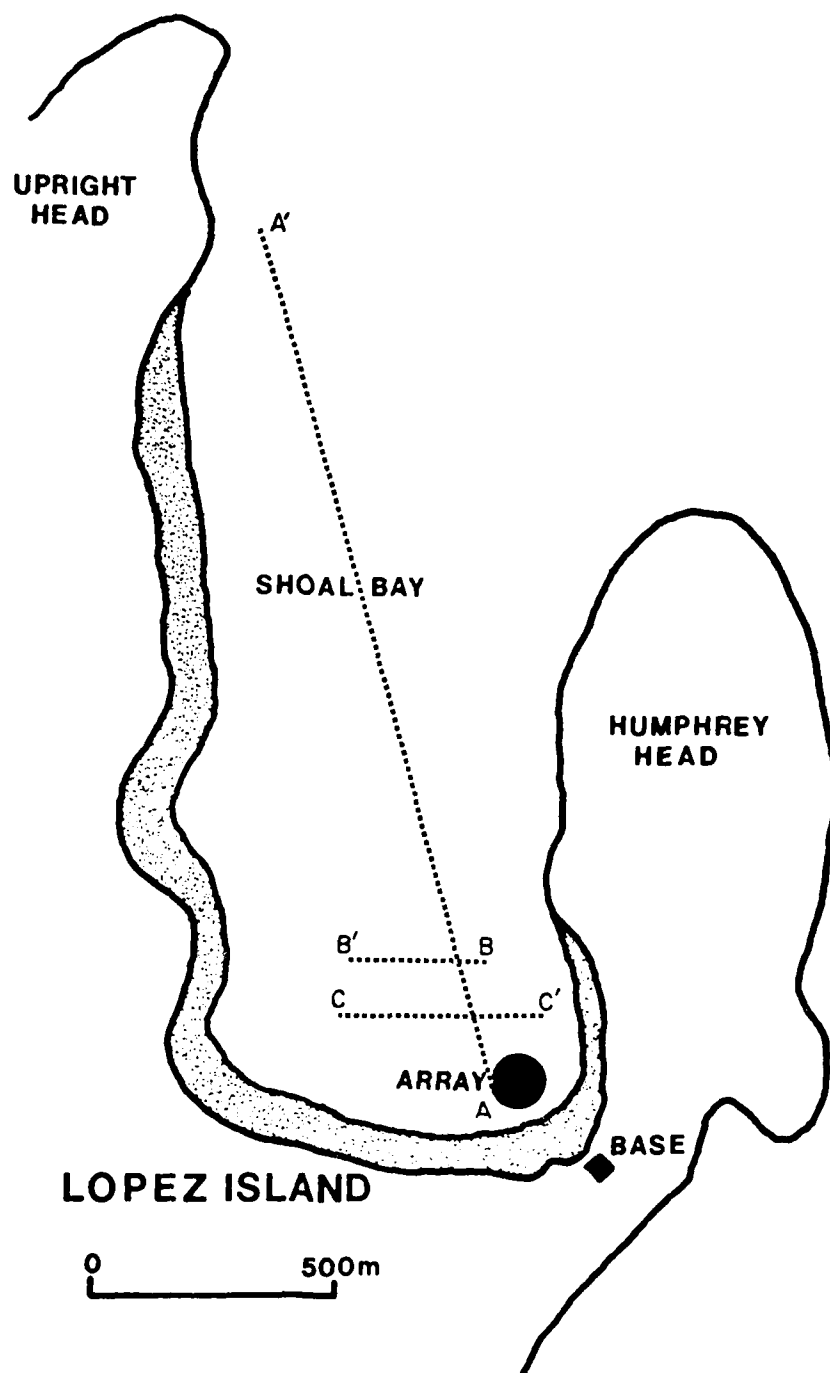


Fig. II-2. Map of Shoal Bay, Lopez Island showing the location of the test array and the base station, and locations of the reflection profiles shown in Figure II-3. Light shading denotes tidal flat.

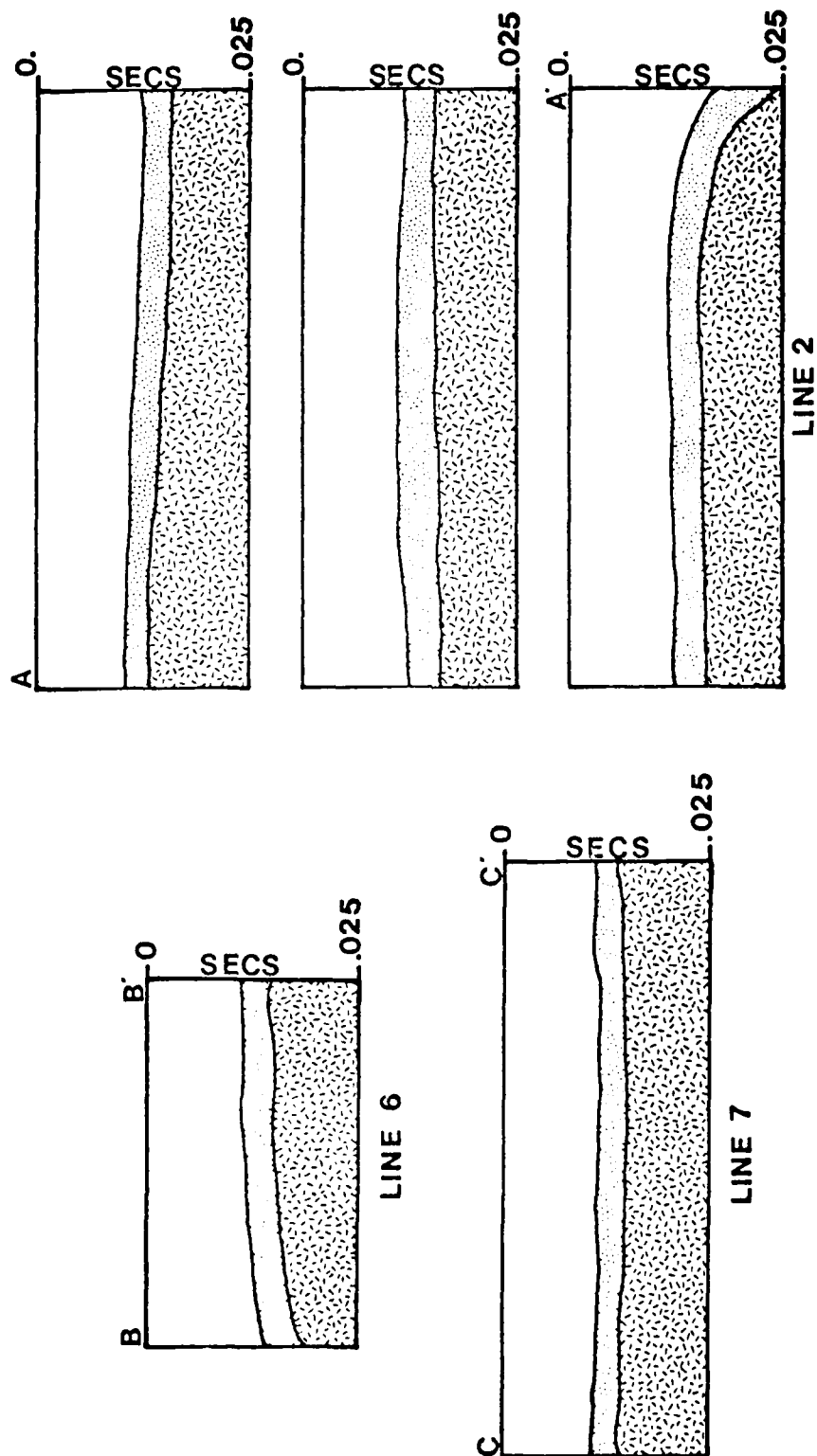


Fig. II-3. Reflection profiles from Shoal Bay. The profiles show a relatively uniform layer of unconsolidated sediment over a harder unknown material.

TABLE II-1. Physical Properties of Shoal Bay Sediments

	sample:	1	2	3	average
DENSITY, g/cc		1.60	1.56	1.54	1.57
PCROSITY, %		71.66	68.03	64.40	68.03

GRAIN SIZE

% sand 4.3

% silt 93.6

% clay 2.0

MINERALOGY

% Quartz 55

% Plagioclase 35

% Mica-Kaolinite-
heavy minerals 10

found to be slightly greater in density and lower in porosity than typical deep-sea muds.

Recording System

The general locations of the OBS array, current meters, and the house used as recording base and workshop are shown in Figure II-2. The relative locations of the instruments shown in Figure II-4 and Table II-2 were initially determined by sea surface triangulation with respect to the current meters and later refined with seismic wave triangulation (Tuthill, 1980). Instruments with only one horizontal geophone were oriented to make the horizontal sensitive to North-South motion. To transfer the data from the OBS's to the recording facility in the house, a 24-channel cable with underwater pluggable connectors was deployed. Each OBS was required to have matching connectors and cables that could be plugged into this cable. The shore-based recording facility consisted of analog recorders and a 24-channel digital recording unit.

Measurement of Response

In addition to the recording of numerous noise samples, two types of controlled source experiments were performed.

The first was from number 8 caps detonated on the bottom at distances less than 100 m from the array and 211 40-cu-in. airgun shots fired at a variety of distances and azimuths from the array. These sources were used primarily to evaluate the response of the different OBS designs to the same source. Accurate source-receiver distances were not determined; in hindsight this proved to be an unfortunate omission since some interesting surface wave modes were observed and dispersion measurements were degraded by the lack of accurate distance measurements. (Information on source times and locations is on file with groups at UW and HIG.)

The second consisted of mechanical transient tests applied directly to each instrument. The purpose of these transient tests was to provide a quantitative estimate of the transfer function between the ocean bottom and the OBS package, including possible cross coupling between horizontal and vertical motion. The transients were obtained by electromagnetically releasing a float from each system, thereby generating a step of force. Tests were performed in the vertical and two orthogonal horizontal directions as shown schematically in Figure II-5. Signal size was adjusted for each instrument by modifying the number of small wooden floats used or the amount of scuba air trapped within an inverted tomato can used as a float. The latter procedure was used for the larger instruments.

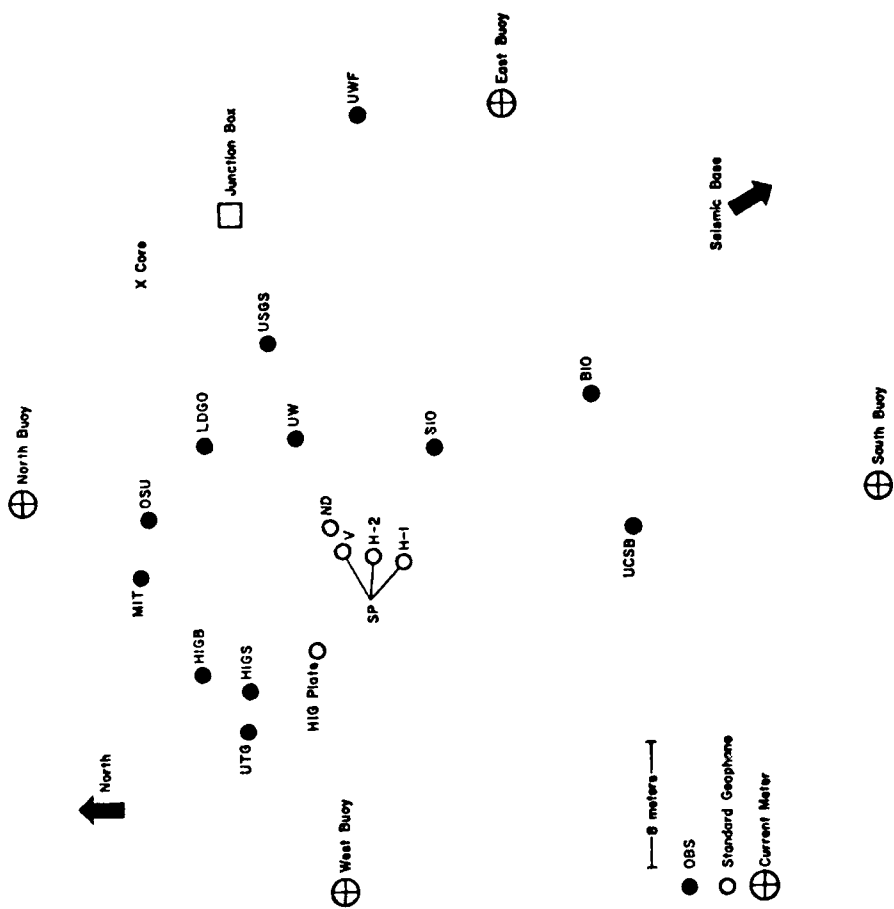


Fig. II-4. Location of OBS array. The array was located by least-squares methods from seismic arrival time data. The letters next to each instrument refer to the institute that built it (Appendix A).

TABLE 11-2. Coordinates for Each OBS Determined
by Least Squares

(east,north), meters from center	
<hr/>	
SPIKE V	(-3.53, 7.39)
SPIKE H1	(-4.31, 3.42)
SPIKE H2	(-3.90, 5.43)
PLATE	(-9.84, 9.15)
NEUTRAL DENSITY	(-2.03, 8.12)
UCSB	(-2.28, -11.29)
BIO	(6.24, -8.66)
SIO	(2.96, 1.39)
UW TRIPOD	(3.73, 10.21)
UW CONCRETE	(24.25, 6.02)
USGS	(9.82, 11.96)
OSU	(-1.27, 19.75)
MIT	(-4.92, 20.26)
HIG BOOBS	(-11.24, 16.44)
HIG STANDARD	(-12.35, 13.42)
UTG	(-14.95, 13.58)
LDGO	(3.39, 16.10)
 Coordinates for the Four Current Meters	
South	(0.00, -27.0)
North	(0.00, 27.77)
West	(-25.24, 7.57)
East	(24.85, -3.30)

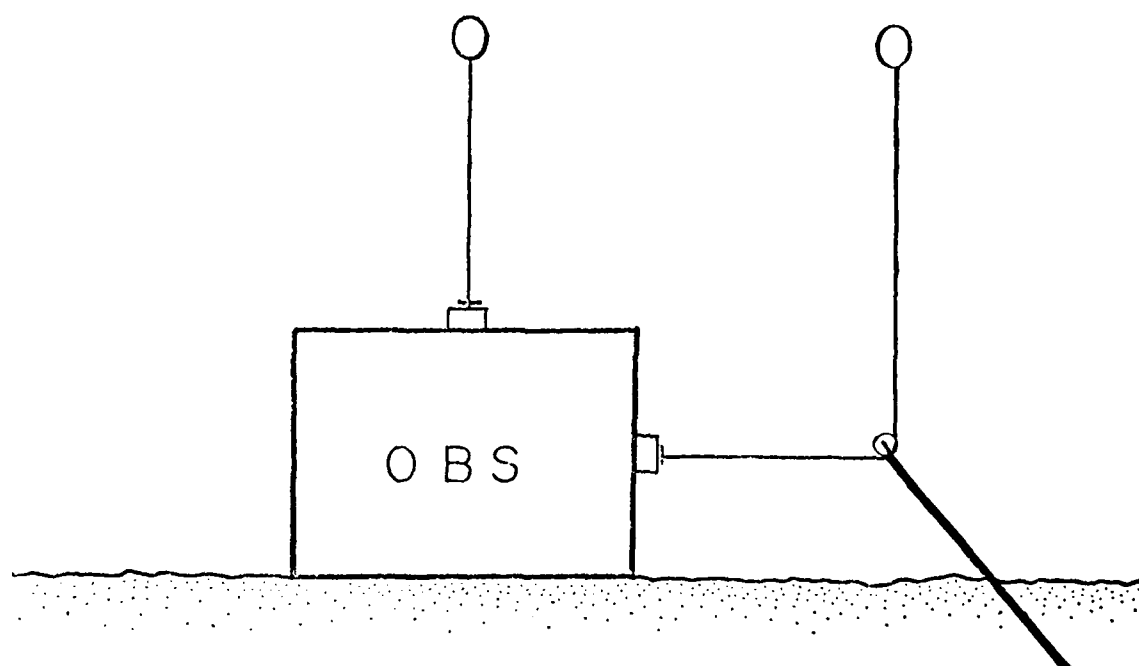


Fig. 11-5. Mechanical transient tests. Impulses are applied to each instrument to determine coupling parameters. A float is released by breaking the circuit in an electromagnet holding the float to the instrument. From Sutton et al., 1980 (Appendix E).

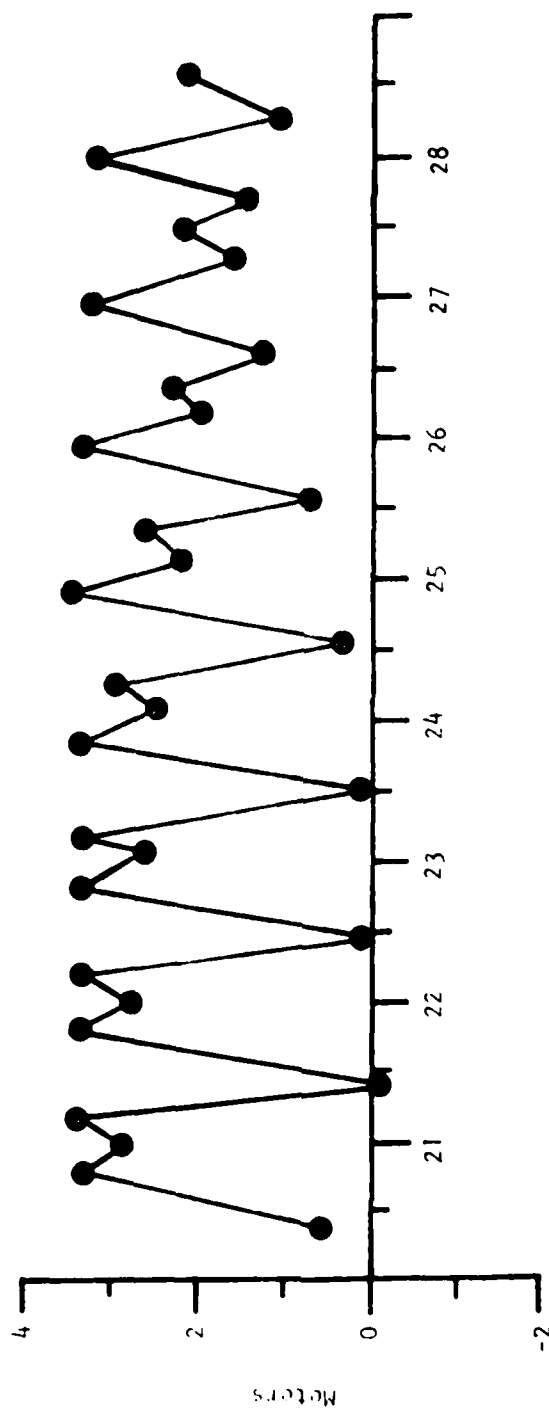


Fig. II-6. Tidal records for Shoal Bay, Lopez Island from June 20 to 28, 1978.

Physical Oceanography Data

Physical oceanography information gathered during the intercalibration study consisted of current records from four Andraa current meters surrounding the main instrument grouping. Currents were measured at a distance of 2 m above the sea floor and recorded at 15-min intervals. The current meter moorings were approximately 40 m from each other. Each mooring was individually anchored with a single railroad wheel and buoyed by a single ORE float of positive buoyancy (300 lb). The currents were extremely weak; peak currents were 6 cm/sec. Water temperatures ranged between 11 and 12°C and salinities ranged between 35.9 and 36.5 ppt.

The SDS (sediment dynamics system) was deployed near the center of the array. This device records tide elevations, temperature, and current speeds and directions, and photographs the bottom. Pressure, temperature, and currents were recorded at 15-min intervals. Photographs were taken at 1-hr intervals. A limited number of records are available of 1024 pressure measurements taken at 1-sec intervals. Data are available for the period June 20 to 28, 1978. Because of the weak currents, current direction measurements made with the SDS are not reliable. The speeds agree with those measured with the Andraa current meters.

Tidal records for the experiment duration are shown in Figure II-6.

III. INSTRUMENTATION

Twelve instrument systems were tested at Lopez Island and their data were compared with data from four "standard" instruments. The characteristics of the 12 instruments and the method used to record data are discussed in this section.

Each of the 12 instruments records data differently when in use on the ocean bottom; however, since the purpose of this test was not to judge recording systems, signals were taken from each system as analog voltages before the normal recording systems. Each institute supplied an external plug on its OBS for each sensor, and voltages were conditioned to be between 15 volts. Wires from each sensor were connected to a junction box on the bottom that was wired to shore. An attenuator panel on land allowed for gain adjustment before digitizing. Data were digitized with a 16-bit DFS-IV multi-channel system supplied by SIO and were also recorded on monitor paper records. For distribution, the data were translated into a standard format on 9-track digital tape. It was possible to record only 22 sensors out of 36 at any one time; thus the recording channels were rearranged occasionally so that representative signals could be obtained from each component.

The standard instruments (plate, spike, and neutral density) were devised by HIG and LDGO to provide the best fidelity of ground motion possible on the basis of three different assumptions. The plate (PL)

provides a large bearing surface and very low bearing pressure, thus causing coupling resonances to be above the seismic range. Its low profile and streamlined shape should also minimize current-induced noise. The spike (SP) instruments were driven into the sediments to provide coupling with material with higher shear strength than that of surface sediments. This should also move coupling resonances to high frequencies and eliminate current-induced noise. The neutral density standard (ND) was made with a density approximately that of the sediment in which it was buried. This instrument should respond without coupling effects because of the lack of density contrast, and should be insensitive to current-induced noise because of its burial. Drawings of these instruments are shown in Figures III-1 to III-3. Each of the standards contained three orthogonal HS10-1 geophones connected to a preamplifier (Fig. III-4). Electrical calibration transients were applied to all standard components to insure proper (matched) operation.

In addition to the geophone standards, a hydrophone standard was provided by LDO (Fig. III-5). It was supplied with an internal preamplifier.

The 12 systems tested were as different as any set of systems can be. Drawings of each system are shown in alphabetical order in Figures III 6 to 17, and important physical parameters of each system are given in Table III-1. Blanks in the table reflect information not available at the time of printing. If additional information concerning a particular instrument is required, the reader is directed to the list in Appendix A giving the names and addresses of each institute, persons involved in the experiment and abbreviation of the institution and its package.

Figure III-18 shows the amplitude response of each instrument used in the system including sensors, electronics, and amplifiers up to the point where the signal was taken off for the test. Although we attempted to reference all instruments to the same level, the reference level may be in error in some cases. Note also that the HIG response curves are for gain 7 of their automatic gain control system; the absolute level for any particular signal depends on the gain step in which the sensor amplifier was operating. Also, the University of Washington instruments employ square root compression. The signal passed to the recorder is the square root of the values shown in Figure III-18. In some cases where all sensors have the same response in a particular instrument, only one response curve is shown.

Table III-2 gives the velocity transfer function of each instrument together with the values of associated constants.

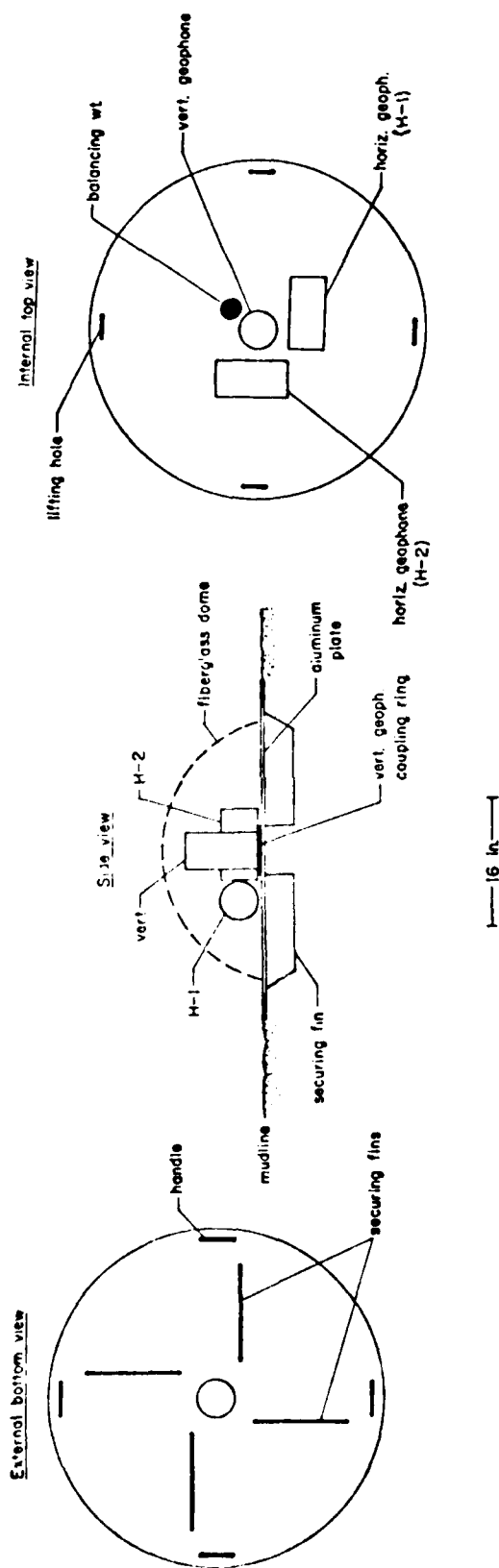


FIG. III-1. Plate Standard.

This instrument is an aluminum disc (4-in. diameter) with three HS-10 1-Hz geophones mounted on its upper surface. The geophones are mounted orthogonally, with one horizontal geophone end-up pointing to the north (H-1), the other (H-2) pointing to the east, and the vertical geophone in the center. A 4-kg balancing weight is mounted on the plate to insure that the center of mass remains at its midpoint. To limit any noise produced by current action, the geophones are covered with a fiberglass dome.

A set of four securing fins are attached to the bottom face of the plate, insuring good coupling with the sediment. Four elongated holes along the outer edge of the plate aid in handling and emplacement of the instrument. A level bubble is emplaced at the top of the dome. Numerous holes were drilled in the plate and the dome to allow any trapped water or air to escape. When in position at the bottom, the mudlevel is just below the upper face of the plate.

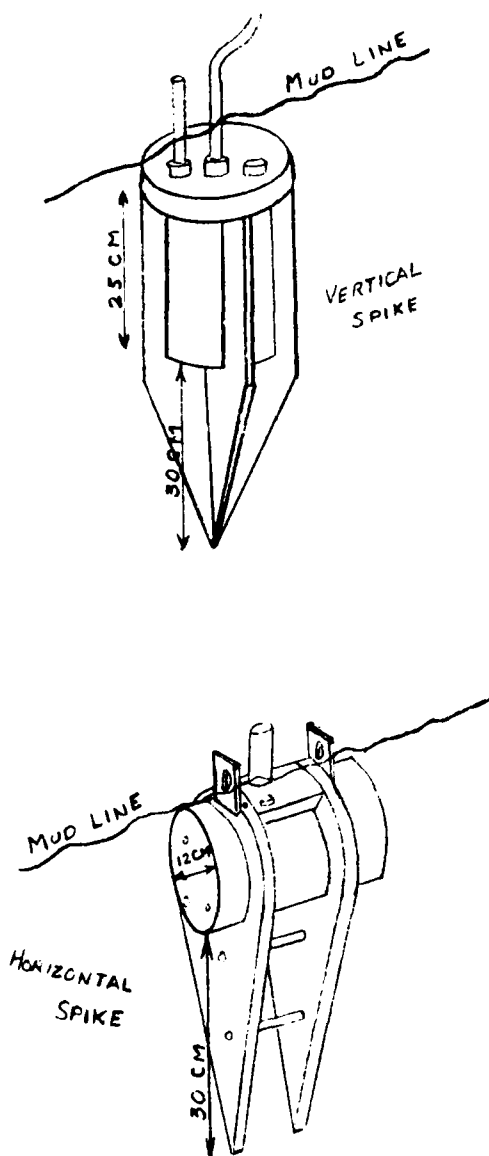
Fig. III-2.

Spike Standards

Two horizontal and one vertical HS-10 1Hz geophones were configured as shown in the sketches. The horizontals were oriented N-S and E-W. All were pushed into the sediment a few CM below the mudline. The spike frames were made of 1/2" aluminum plate.

Weight of vertical in air = 13.6Kg
 Displacement = 4,750CC
 Weight in sediment of $\rho 1.57 = 6.1\text{Kg}$

Weight of horizontal in air = 11.4Kg
 Displacement = 4,950CC
 Weight in sediment of $\rho 1.57 = 3.6\text{Kg}$



Neutral Density Standard

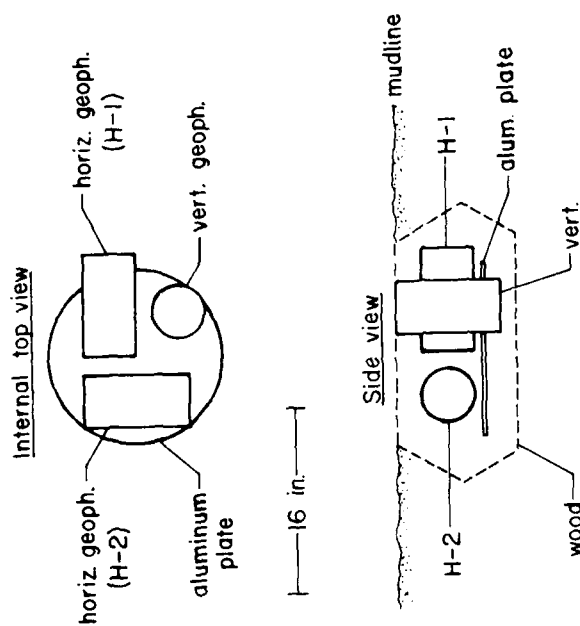


Fig. III-3. Neutral Density Standard

The instrument is a small (14-in. diameter) aluminum disc with three HS-10 1-Hz geophones mounted orthogonally upon it. One horizontal geophone endcap points to the north (NDH-1); the other points to the east (NDH-2). The vertical geophone completes the circular arrangement and keeps the center of mass of the instrument near the midpoint of the plate.

Wood of density 0.5 g/cc surrounds the entire package. The low density of the wood brings the overall density of the instrument to near 1.6 g/cc. (A glass sphere originally planned to enclose the instrument was broken in transit to the test site.) This effectively neutralizes any bearing pressure of the instrument upon the 1.57-g/cc-density sediment in which it is buried. When in position on the bottom of the bay, the mudlevel is even with the top of the vertical geophone.

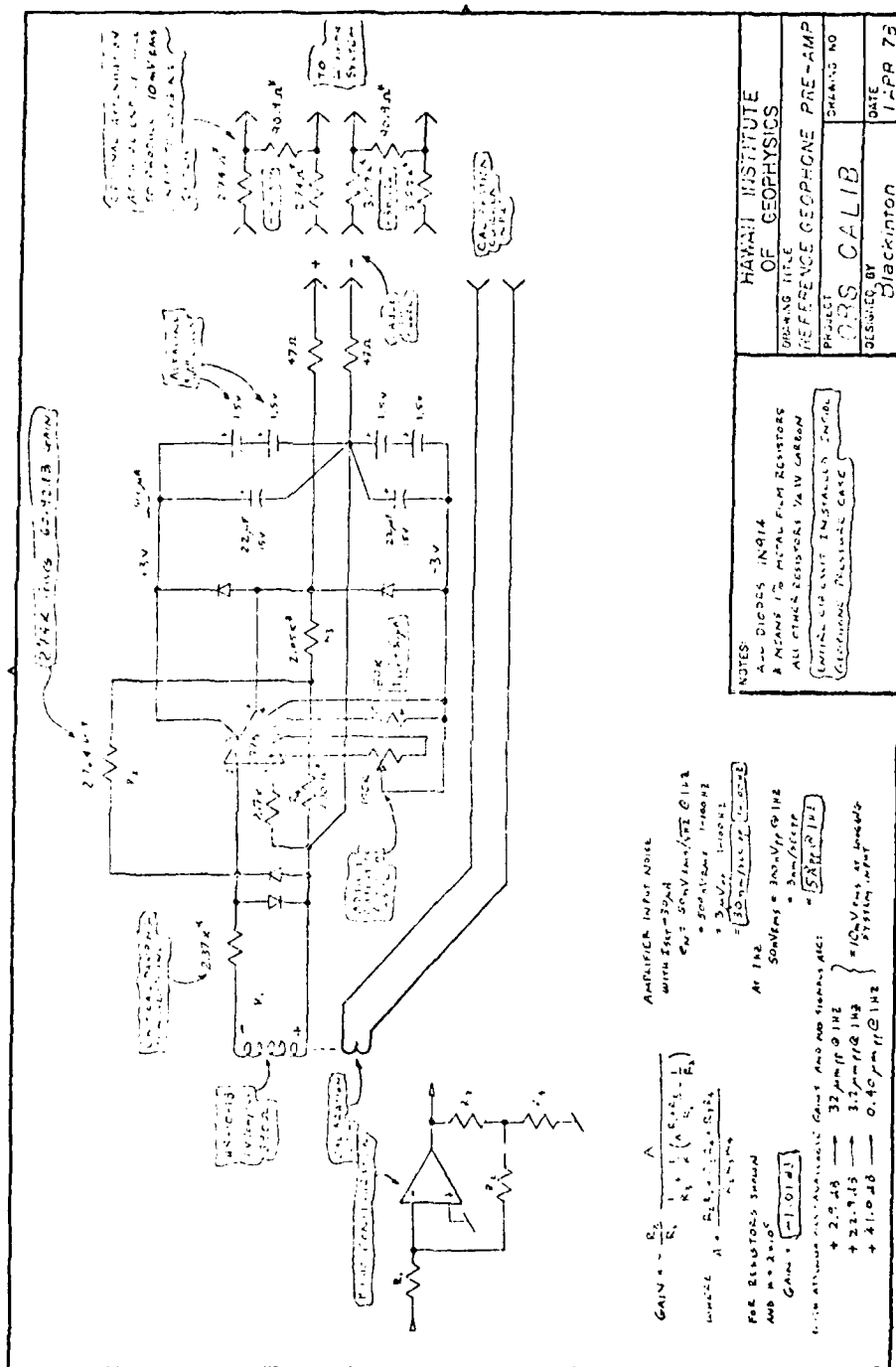


Fig. III-4. Schematic of preamplifier used for Lopez Island standard geophones.

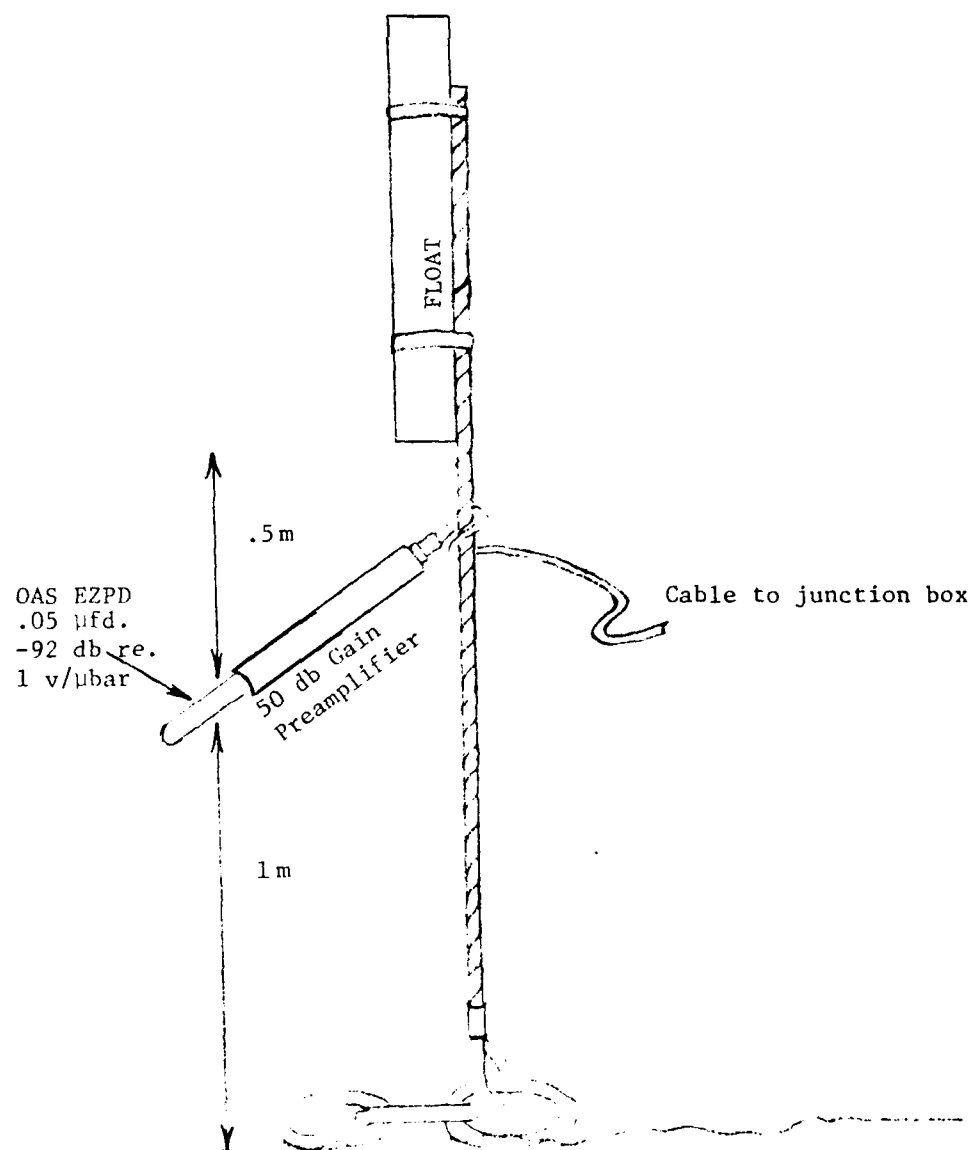


Fig. III-5. Standard hydrophone deployment.

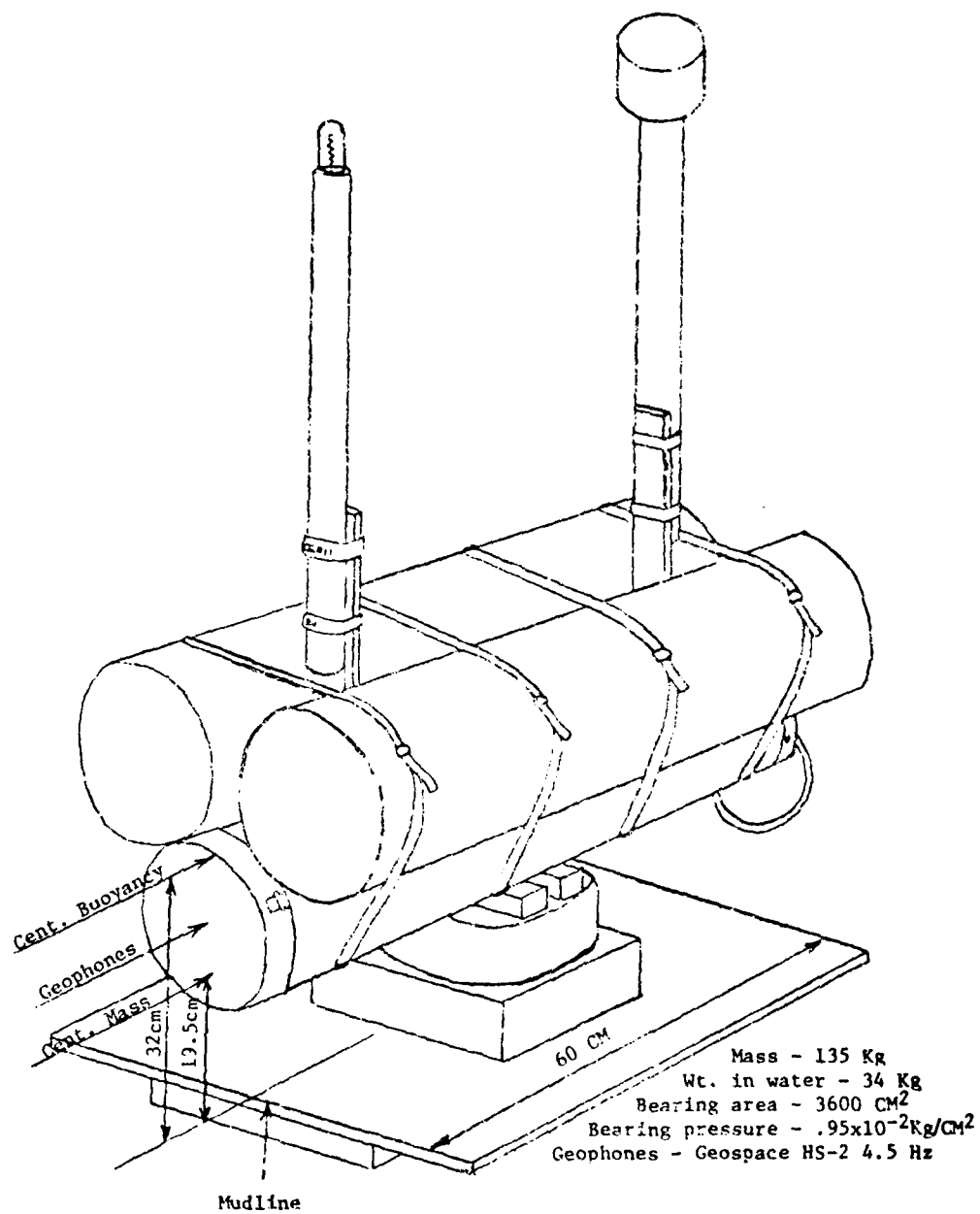


Fig. III-6. Bedford Institute OBS.

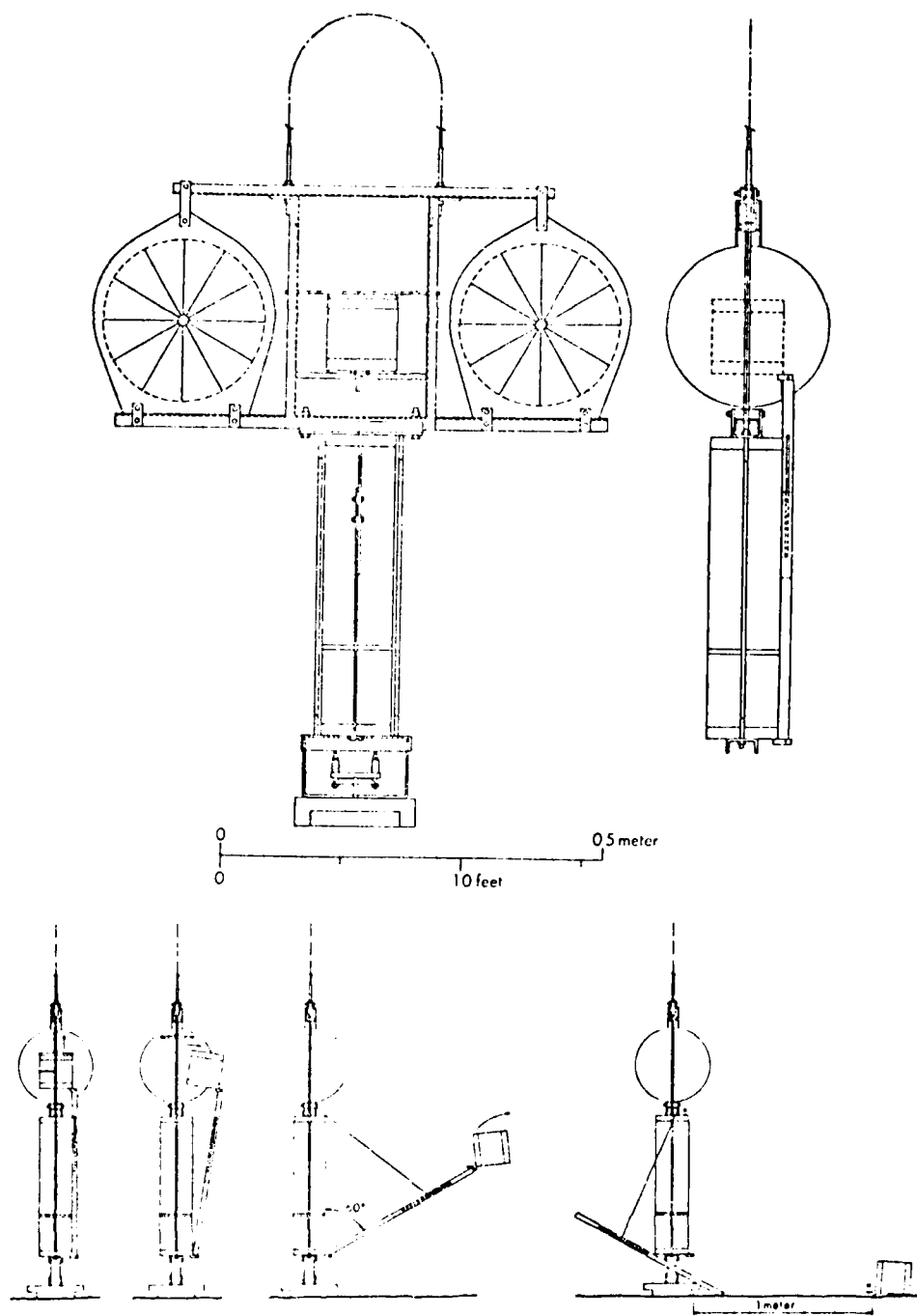


Fig. III-7. Hawaii Institute of Geophysics Burp-Out OBS.

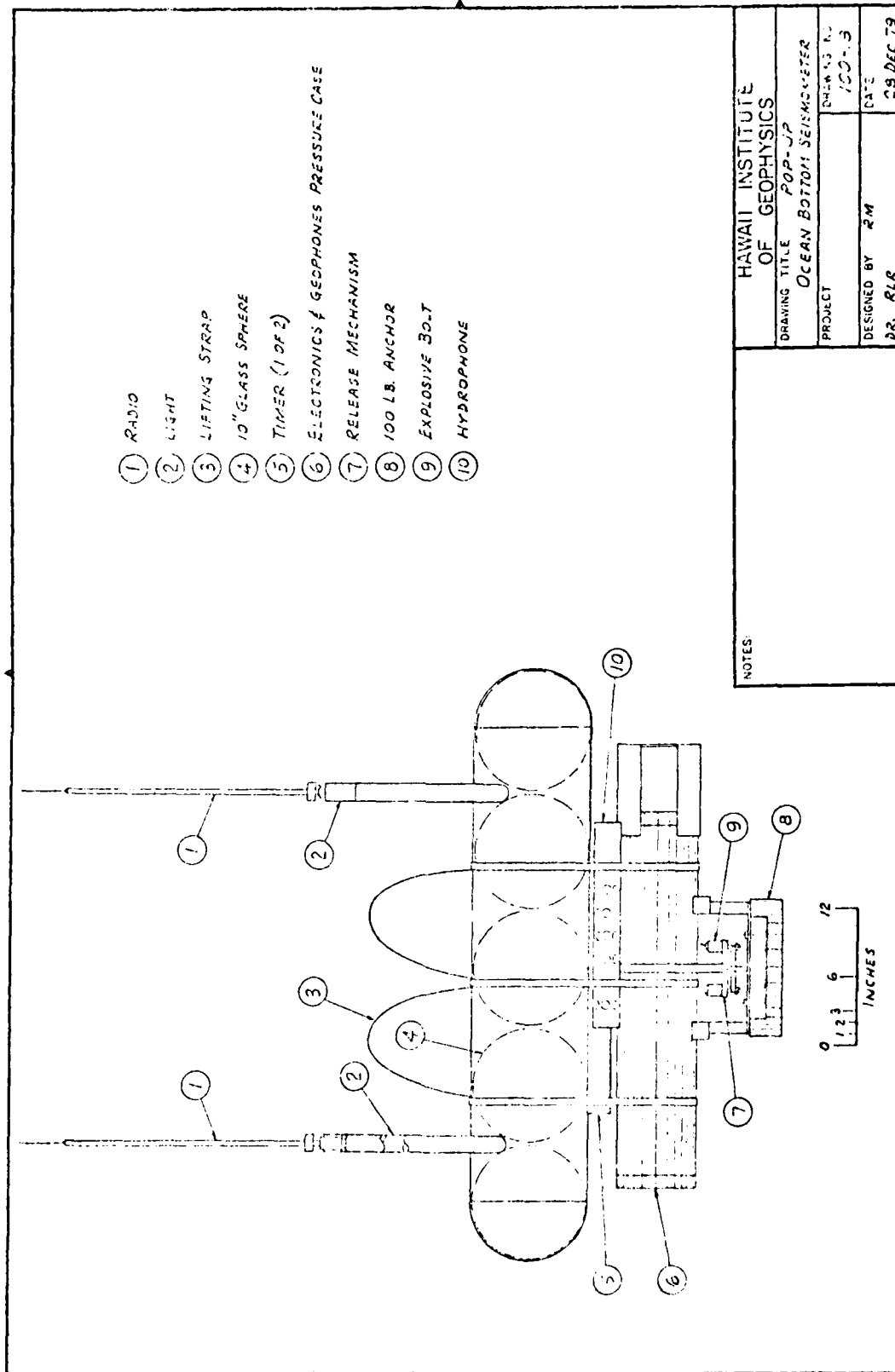


Fig. III-8. Hawaii Institute of Geophysics Standard OBS.

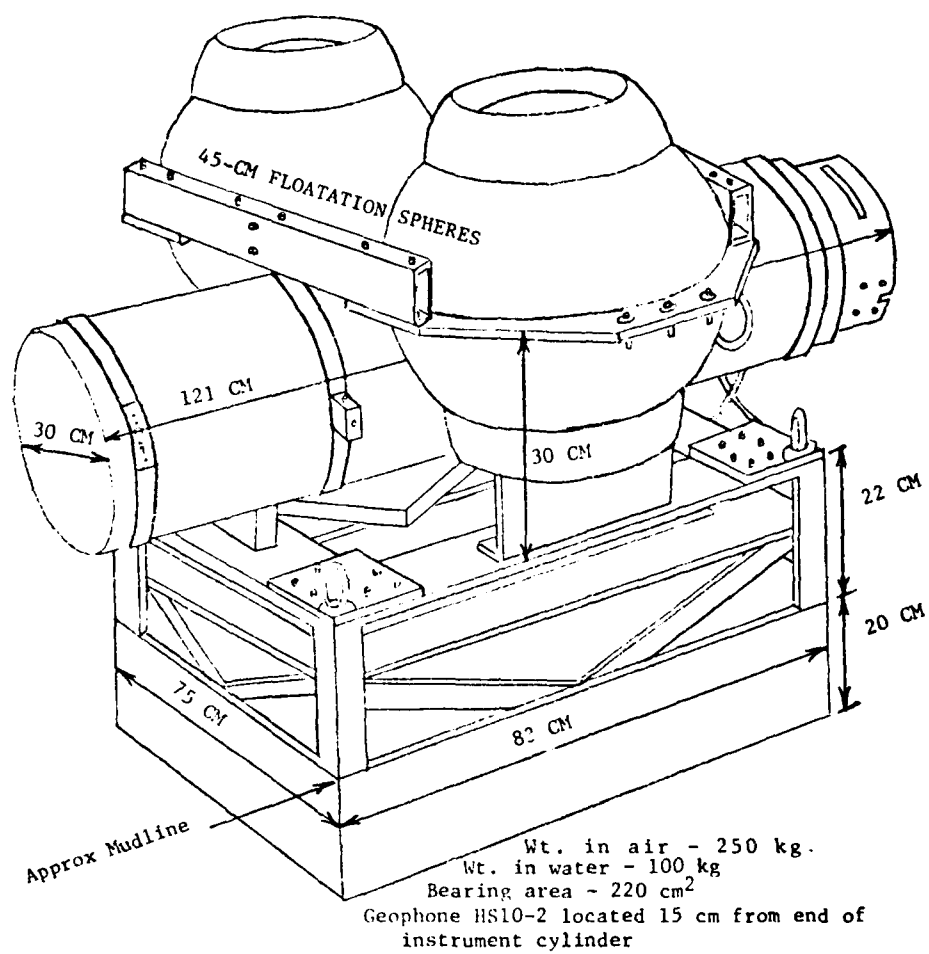
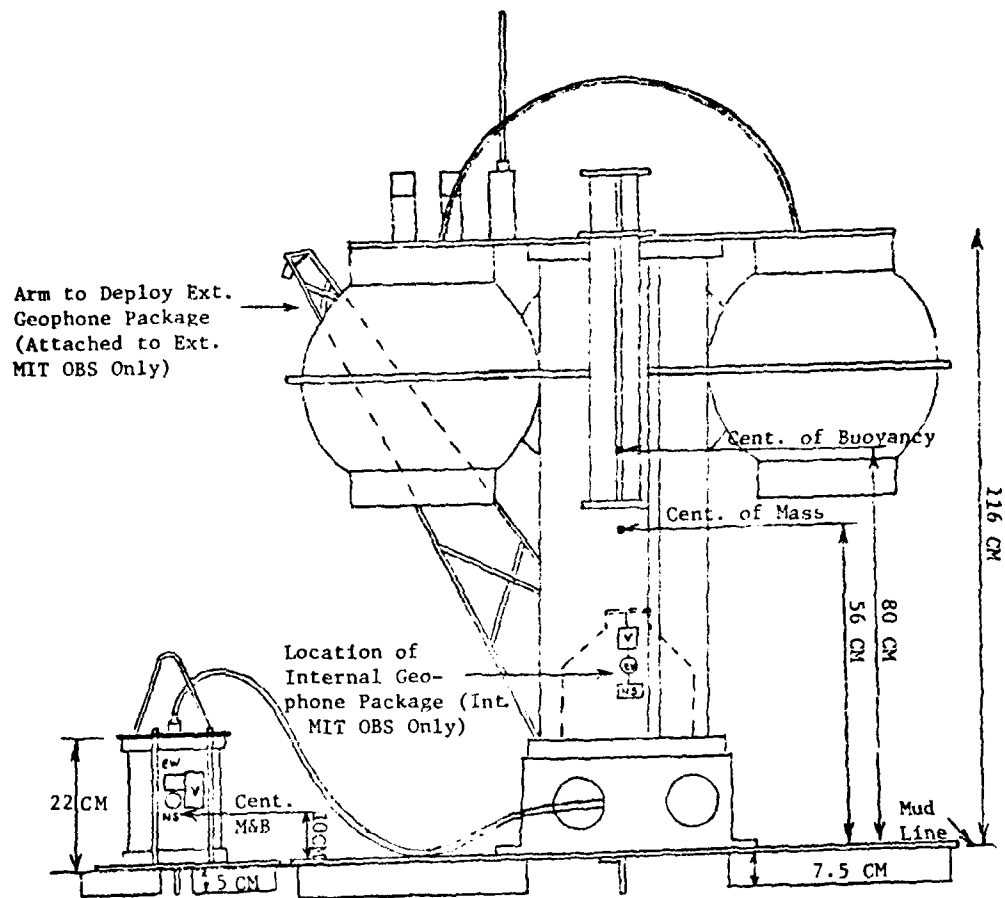


Fig. III-9. Lamont-Doherty Geological Observatory OBS.



<u>MIT OBS</u>	<u>Ext. Package</u>	<u>Int. Package</u>
Total Air Weight	17 Kg	310 Kg
Total Water Weight	9 Kg	52 Kg
Bearing Pressure	70 Kg/m ²	41 Kg/m ²
Coupling Plate Area	.13 m ²	1.27 m ²

Fig. III-10. Massachusetts Institute of Technology OBS.

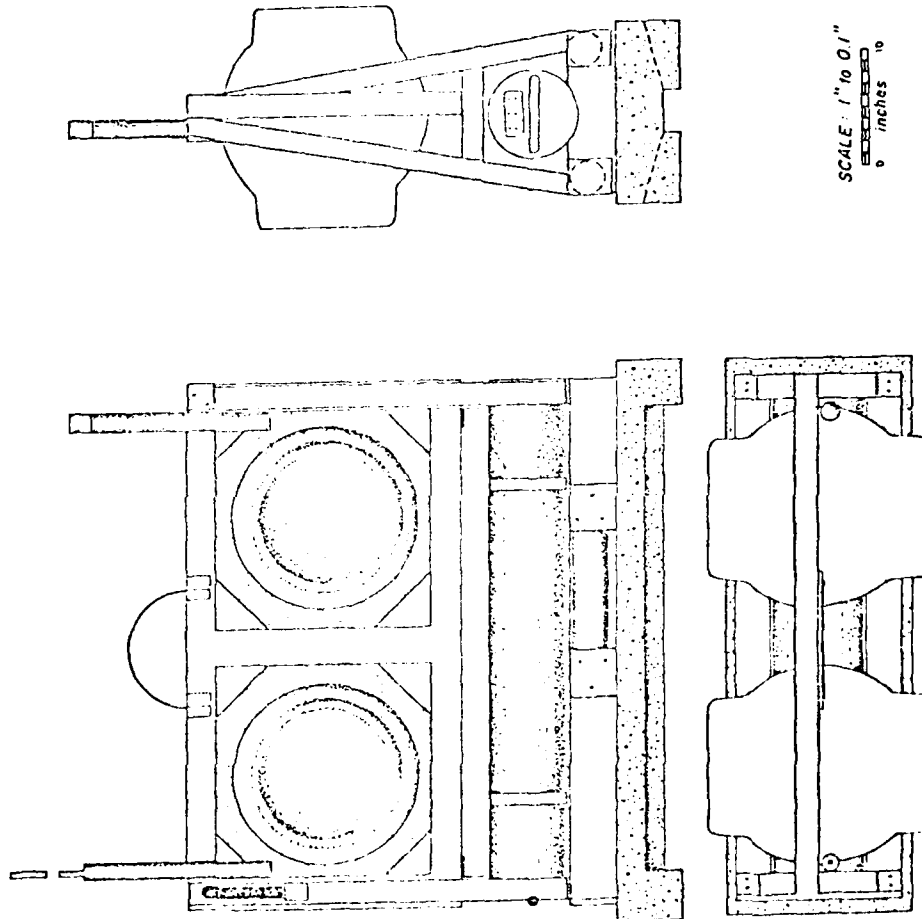


Fig. III-11. Oregon State University OBS.

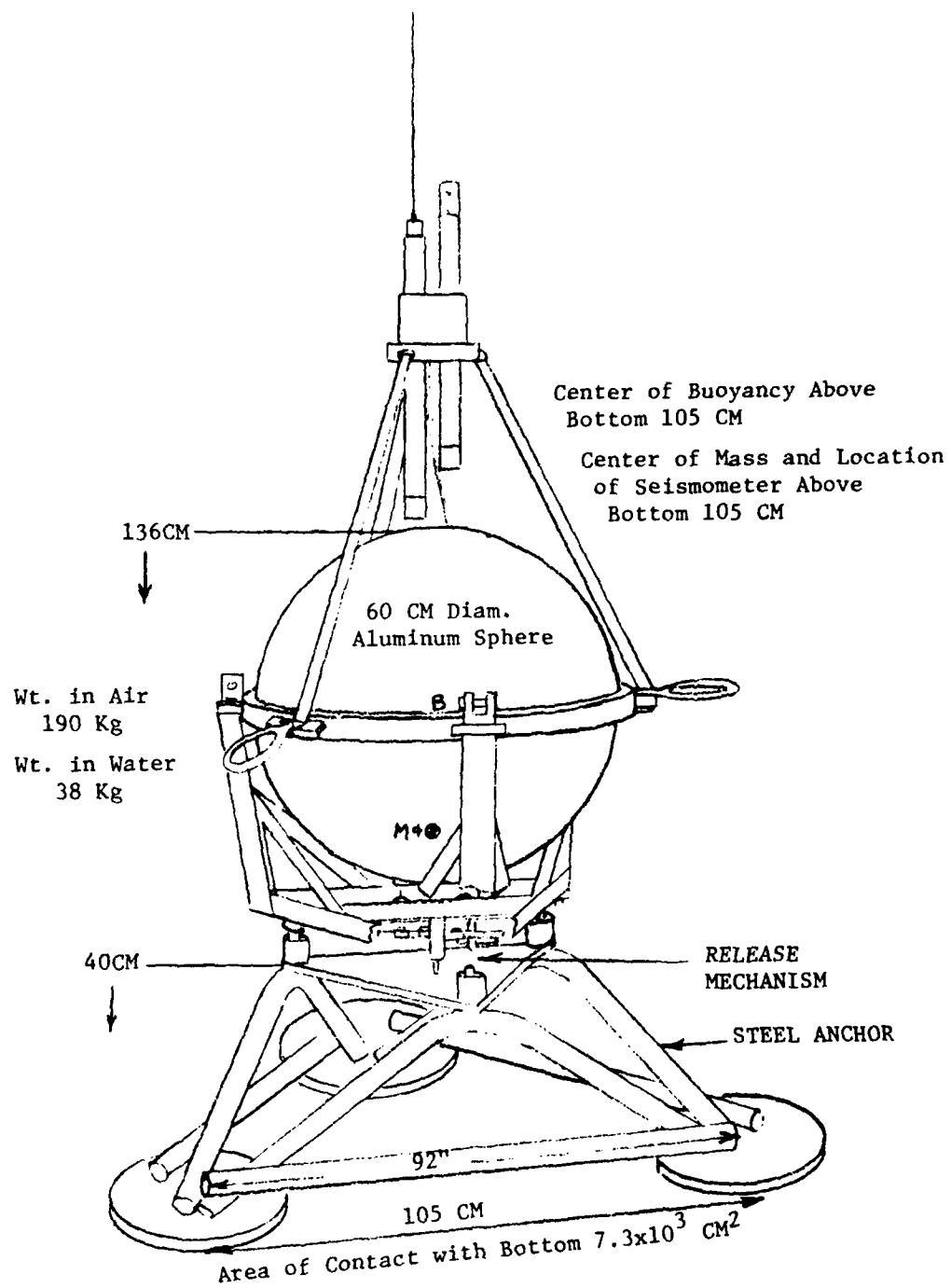


Fig. III-12. Scripps Institution of Oceanography OBS.

UCSB - OBS (Mod 1)

WEIGHT DISTRIBUTION:

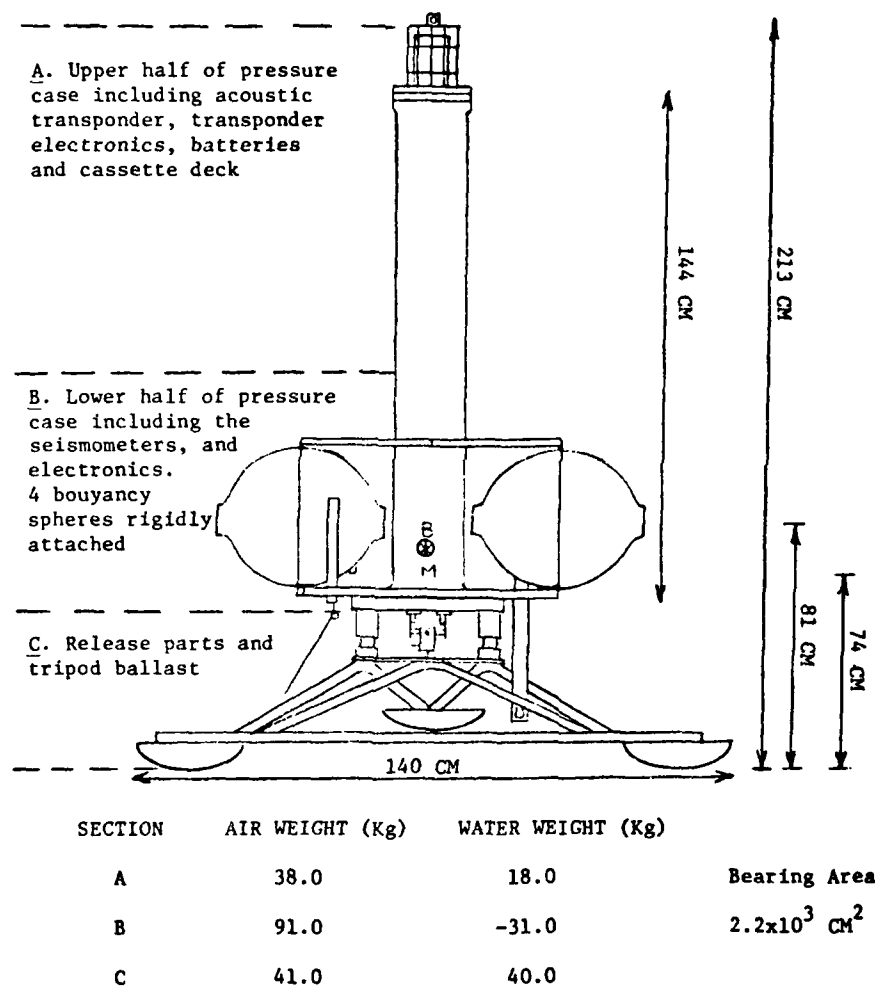


Fig. III-13. University of California at Santa Barbara OBS.

UCSB

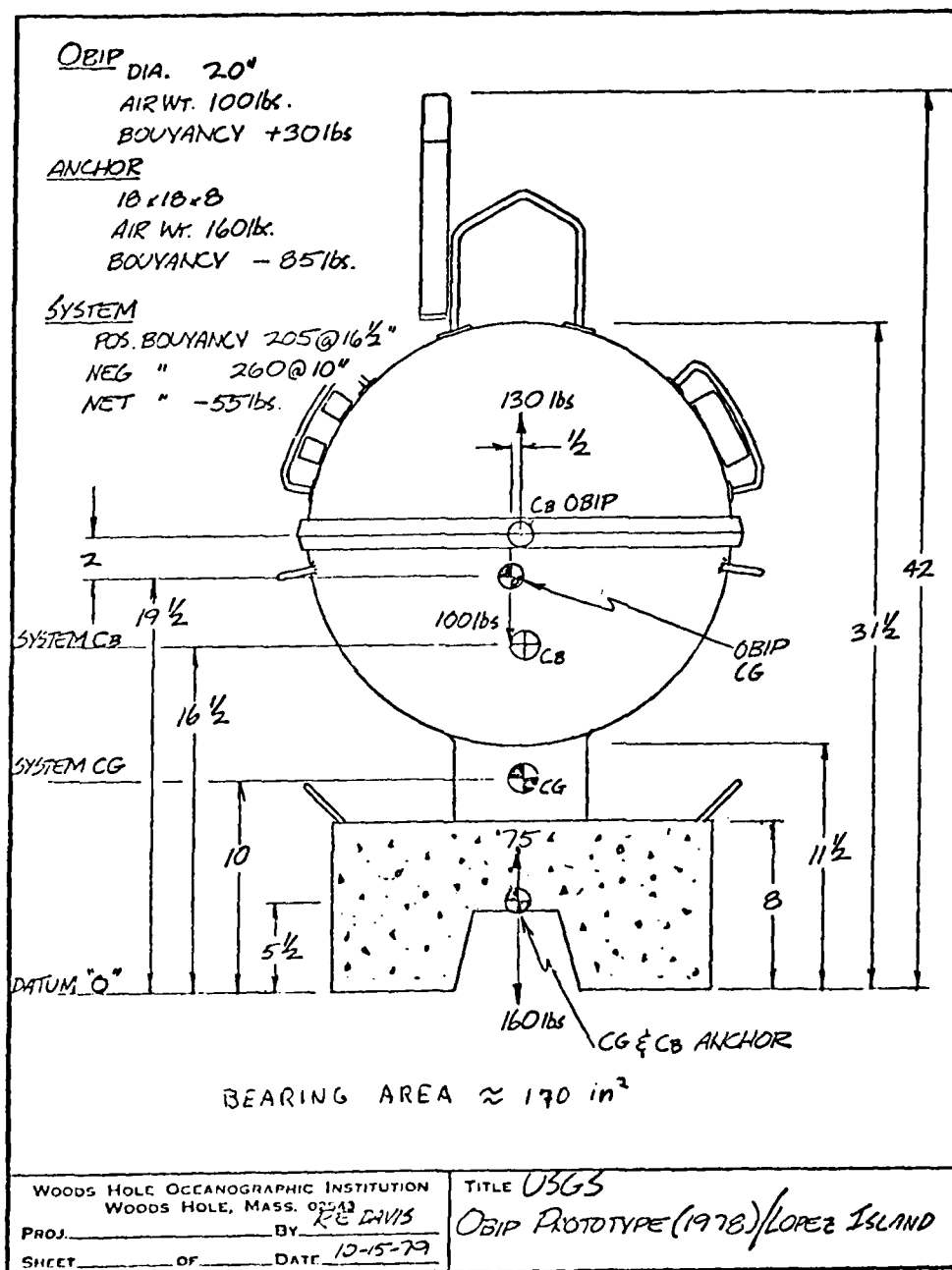


Fig. III-14. U.S. Geological Survey OBS.

TEXAS

Wt. in Air 60 Kg
Wt. in Water 14 Kg
Geophone 4.5 Hz

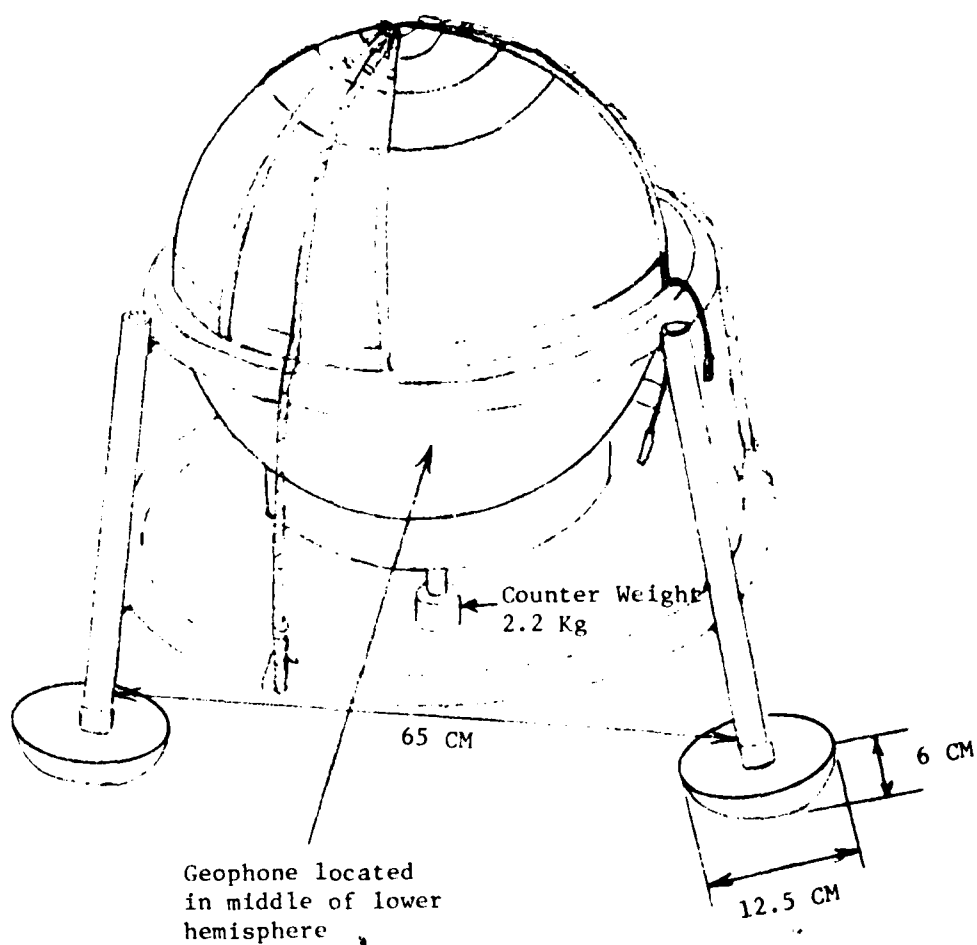


Fig. III-15. University of Texas at Galveston OBS.

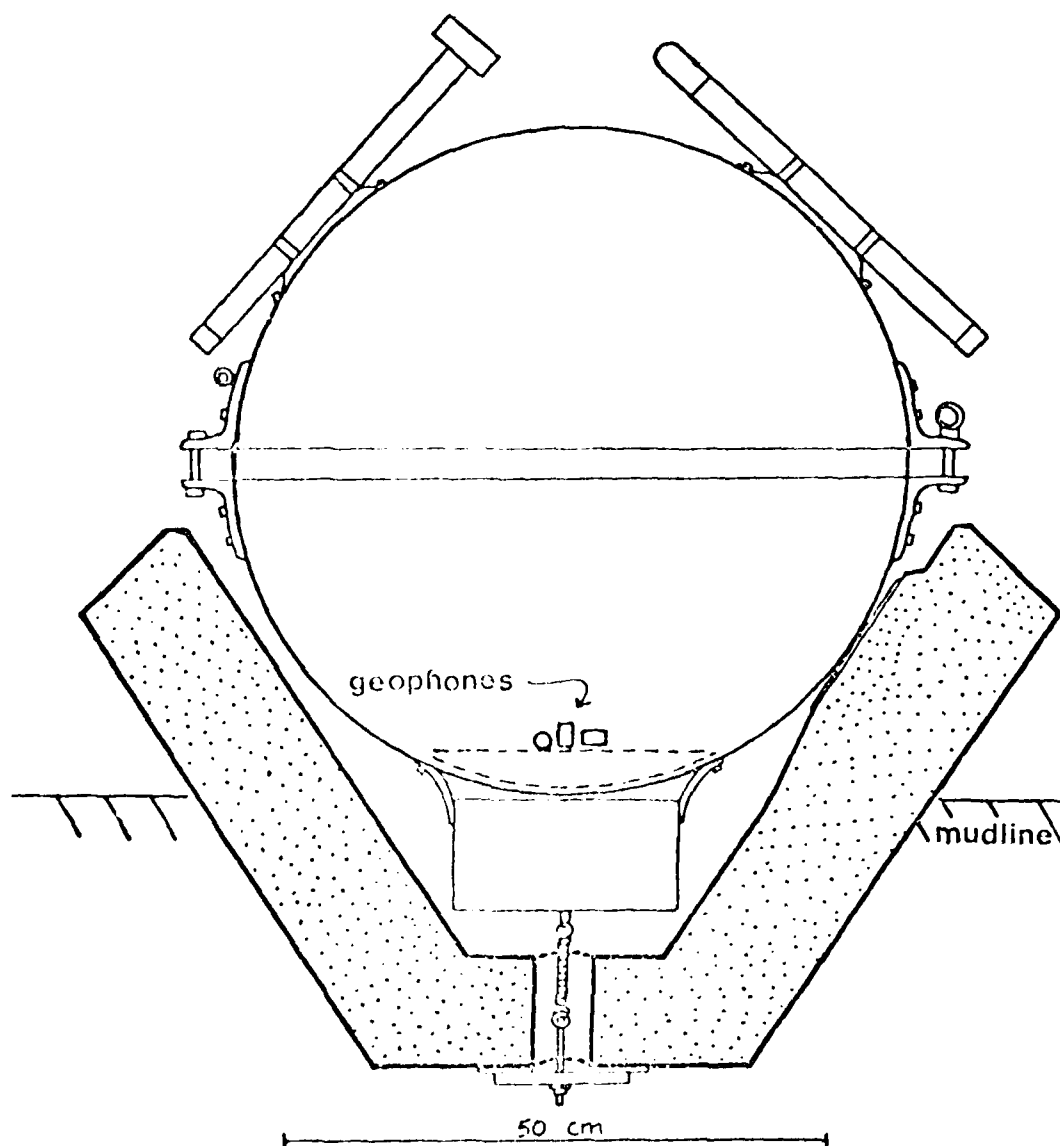


Fig. 111-1b. University of Washington 'Flower Pot' OBS.

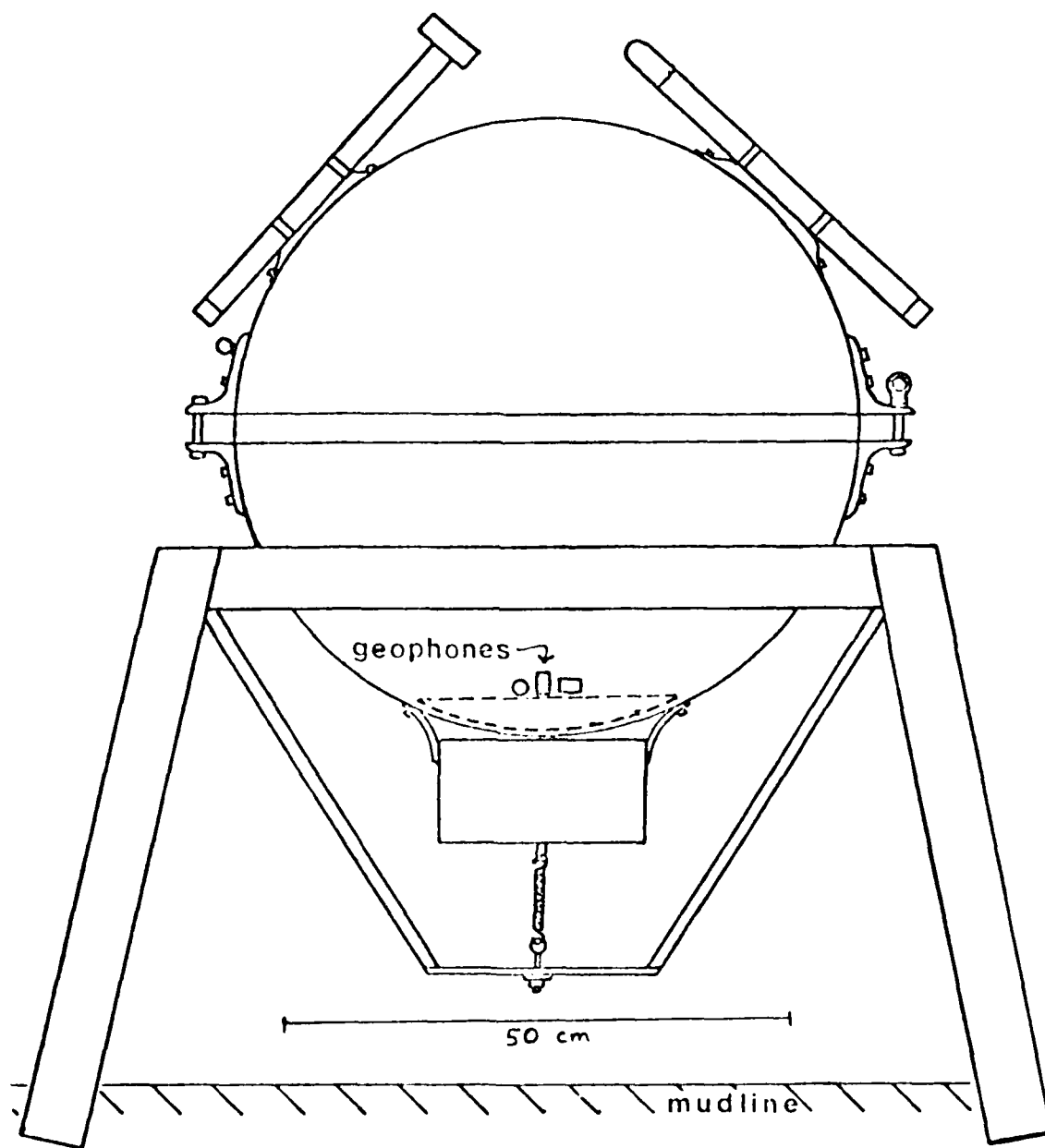


Fig. III-17. University of Washington OBS.

TABLE III-1. Physical Characteristics of Instruments Used at Lopez Island

PACKAGE	SERIAL NO.	MASS g	SEAL IN. VACUUM	CORNER C. MEAN (cm)	HEIGHT (cm)	SENSOR HEIGHT (cm)	BASE WIDTH AVERAGE (cm)	BASE AREA (cm ²)	BEARING PRESSURE (g/cm ²)	CENTER OF BOL. NOY (cm)	PACKAGE DENSITY (g/cm ³)
1	1	17	0.8	10	15	15	36	0.1260	0	-15.0	1.77
2	2	17	0.15	10	5	5	112	0.999	0.20	6.0	2.14
3	3	17	0.8	10	15	15	10	0.0113	53.0	-10.0	2.25
4	4	17	0.8*	10	15	15	10	0.0090	17.2	-5.0	2.29
5	5	17	0.8	10	15	15	66	0.100	9.25	-12.0	1.94
6	6	17	0.8	10	15	15	10	0.0220	15.0	7.0	1.70
7	7	17	0.8	10	15	15	60	0.0730	47.0	41.3	1.43
8	8	17	0.8	10	15	15	70	0.0120	47.15		1.97
9	9	17	0.8	10	15	15	41	0.100	6.7	10.0	2.13
10	10	17	0.16	10	55	55	121	1.2700	4.2	60.0	1.30
11	11	17	0.50	10	50	50	60	0.4740	10.4		1.27
12	12	190	557	105	230	105	105	0.2980	1870	120.0	1.23
13	13	170	265	76	213	76	140	0.2260	1204	81.0	1.19
14	14	170	265	76	167	92	46	0.1400	1770	41.9	1.27
15	15	170	265	76	90	70	85	0.0240	57.3		1.70
16	16	170	265	76	170	45	100	0.0064	265.1	40.0	1.42
17	17	170	265	76	120	85	60	0.1290	175.2	60.0	1.77

* These instruments are buried in the sediments, thus their weight in sediment is given rather than their weight in water ($\rho_s = 1.57 \text{ g/cm}^3$).

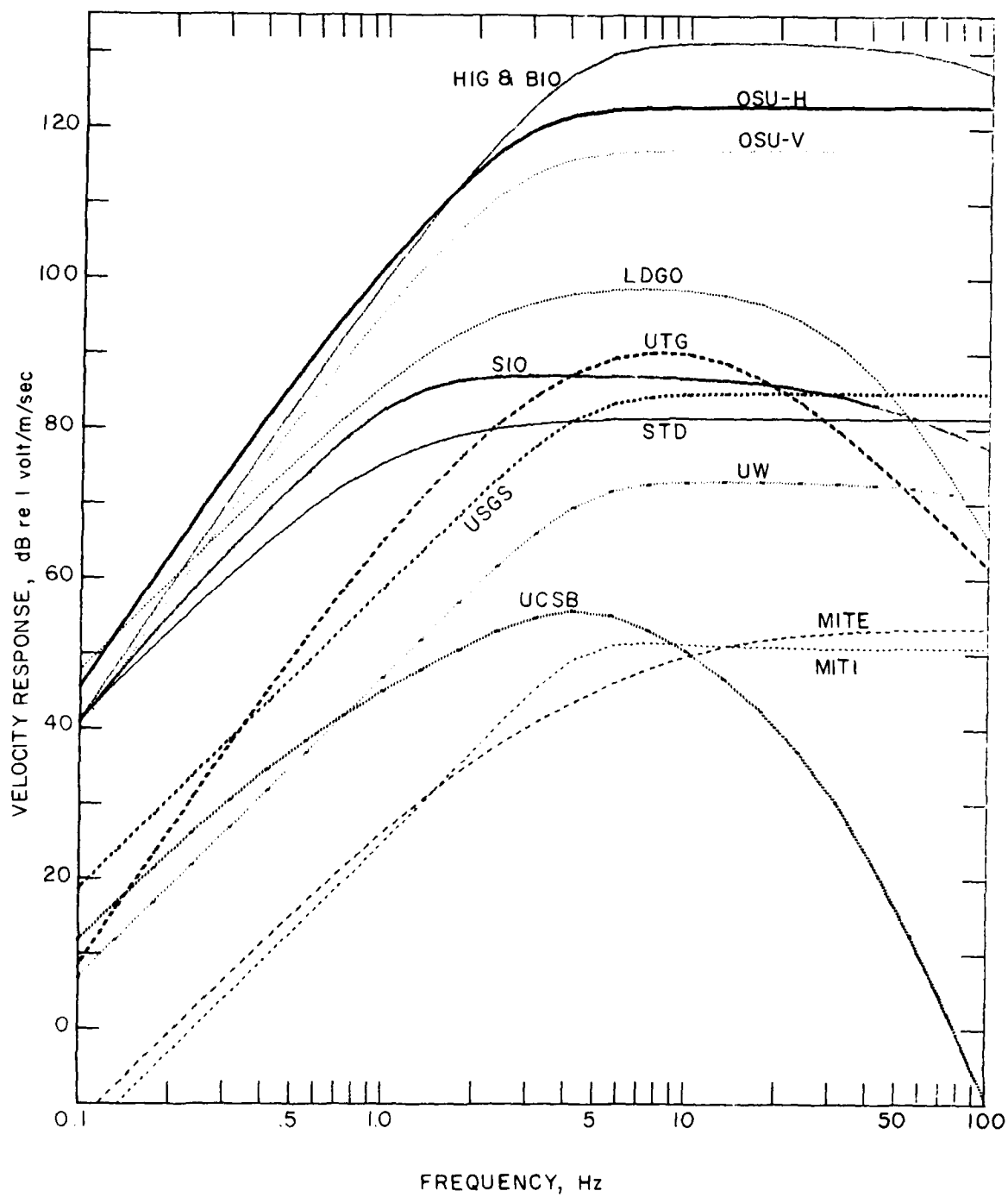


Fig. III-18. Amplitude response of each instrument.

TABLE III-2. Velocity Response Formulae Used to Generate Figure III-18

VELOCITY RESPONSE FORMULAE

OBS	FORMULA	CONSTANTS
STD	$V = \frac{110 (S\tau_1)^2}{1 + 1.45\tau_1 + (S\tau_1)^2} \cdot \frac{1}{1 + S\tau_2}$	$S = i\omega, \quad \tau_1 = 0.159 \text{ sec}$ $\tau_2 = 8 \times 10^{-5} \text{ sec}$
BIOHIG	$V = \frac{38000 (S\tau_1)^2}{1 + 1.45\tau_1 + (S\tau_1)^2} \cdot \frac{S\tau_2}{1 + S\tau_2} \cdot \frac{1}{(1 + S\tau_3)^3}$	$\tau_1 = 0.35 \text{ sec}$ $\tau_2 = 0.1 \text{ sec}$ $\tau_3 = 10^{-3} \text{ sec}$
LDGO	$V = \frac{310 \cdot 316 \cdot (i\omega)^2}{\omega_0^2 - \omega^2 + i\omega\omega_0/Q} \cdot \left(\frac{\omega_1}{\omega_1 + i\omega} \right)^4$	$\omega_0 = 2\pi \cdot 4.5, \quad \omega_1 = 2\pi \cdot 40$
MIT	$V = \frac{A \cdot (i\omega)^2}{\omega_0^2 - \omega^2 + i\omega\omega_0/Q}$	$\omega_0 = 2\pi \cdot 4.5, \quad Q = 0.34 \text{ (MITI)} = 0.90 \text{ (MITI)}$ $A = 472 \text{ (MITI)} = 346 \text{ (MITI)}$
OSU	$V = \frac{66.1 (i\omega)^2}{\omega_0^2 - \omega^2 - i\omega\omega_0/Q} \cdot \frac{i\omega}{1 + i\omega/\omega_1} \cdot \frac{A_1}{1 + i\omega/\omega_2} \cdot \frac{A_2}{1 + i\omega/\omega_3}$	$\omega_0 = 2\pi \cdot 1.15, \quad A_1 = 215 \text{ (vert)} = 420 \text{ (horiz)}$ $\omega_1 = 2\pi \cdot 0.8, \quad \omega_2 = 2\pi \cdot 1260 \text{ (vert)} = 1600 \text{ (horiz)}$ $\omega_3 = 2\pi \cdot 3978,$
SIO	$V = \frac{2 \cdot 81.6 \cdot 275 \cdot i\omega^3}{\omega_0^2 - \omega^2 + i\omega\omega_0/Q} \cdot \frac{1}{\omega_1} \cdot \frac{1}{1 + i\omega/\omega_2} \cdot \frac{1}{(\omega/\omega_2)^2} \cdot \frac{1}{1 + i\omega/\omega_4}$	$\omega_0 = 2\pi \cdot 1.15, \quad \omega_2 = 2\pi \cdot 0.114, \quad \omega_4 = 2\pi \cdot 35.4$ $\omega_1 = 2\pi \cdot 0.227, \quad \omega_3 = 2\pi \cdot 8.68, \quad Q = 0.71$
UCSB	$V = \frac{256 \cdot 50 \cdot (i\omega)^2}{800 + 40 i\omega - \omega^2} \cdot \left(\frac{1}{1 + 0.005 i\omega} \right)^4 \cdot \left(\frac{0.316 i}{1 + 0.316 i\omega} \right)^2$	
USGS	$V = \frac{55 \cdot 316 \cdot (i\omega)^2}{\omega_0^2 - \omega^2 + i\omega\omega_0/Q}$	$\omega_0 = 2\pi \cdot 4.5, \quad Q = 0.7$
UTG	$V = \frac{1000 \cdot 55 \cdot (i\omega)^2}{\omega_0^2 - \omega^2 + i\omega\omega_0/Q} \cdot \frac{i\omega}{\omega_1 + i\omega} \cdot \left(\frac{\omega_2}{\omega_2 + i\omega} \right)^2$	$\omega_0 = 2\pi \cdot 4.5, \quad \omega_2 = 2\pi \cdot 15$ $\omega_1 = 2\pi \cdot 1, \quad Q = 0.5$
UW	$V = \frac{45000 \cdot (S\tau_1)^2}{1 + 1.45\tau_1 + (S\tau_1)^2} \cdot \left[1 + AS\tau_2 + \frac{2}{5}(AS\tau_2)^2 + \frac{1}{15}(AS\tau_2)^3 \right]$	$\tau_1 = 1/(2\pi \cdot 4.5), \quad \tau_2 = 1/(2\pi \cdot 100)$ $A = 1.756$

Response to Vertical Input on Vertical Geophones

The vertical motion of an OBS package (Fig. IV-1) resulting from a vertical seismic input can be approximated by the transfer function given Equation 1 (Appendix E).

$$\frac{I}{Z_s} = (1-C) \left[S^2 + 2h_c \omega_c S / (1-C) + \omega_c^2 / (1-C) \right] / \left[S^2 + 2h_c \omega_c S + \omega_c^2 \right] \quad (1)$$

where

$I = Z_I + X_e$ = displacement of instrument package

X_e = equilibrium value of X

Z_s = displacement of water-sediment interface

ω_c = angular frequency of OBS-bottom coupling

$h_c = \frac{1}{2Q_c}$ = damping coefficient of OBS-bottom coupling

C = coupling constant

Thus, given values for C , h_c , and ω_c , the response can be determined. Response curves for three values of coupling are shown in Figure IV-2.

The coupling constant is given by

$$C = (M_I - \bar{M}_w - \bar{M}_s) / M_I^* \quad (2)$$

where

M_I = instrument mass

\bar{M}_w = mass of displaced water at equilibrium

\bar{M}_s = mass of displaced sediment at equilibrium

$M_I^* = M_I + \bar{M}_w^* + \bar{M}_s^*$, mass of OBS plus water and sediment that move with it.

The value for C can vary from zero at neutral bouyancy where $\frac{1}{Z_s} = 1$ and seismic coupling is perfect for all frequencies, to some value less than one. A maximum value for C , independent of shape, can be calculated from

$$C_{\max} = 1 - (\bar{M}_w + \bar{M}_s) / M_I \quad (3)$$

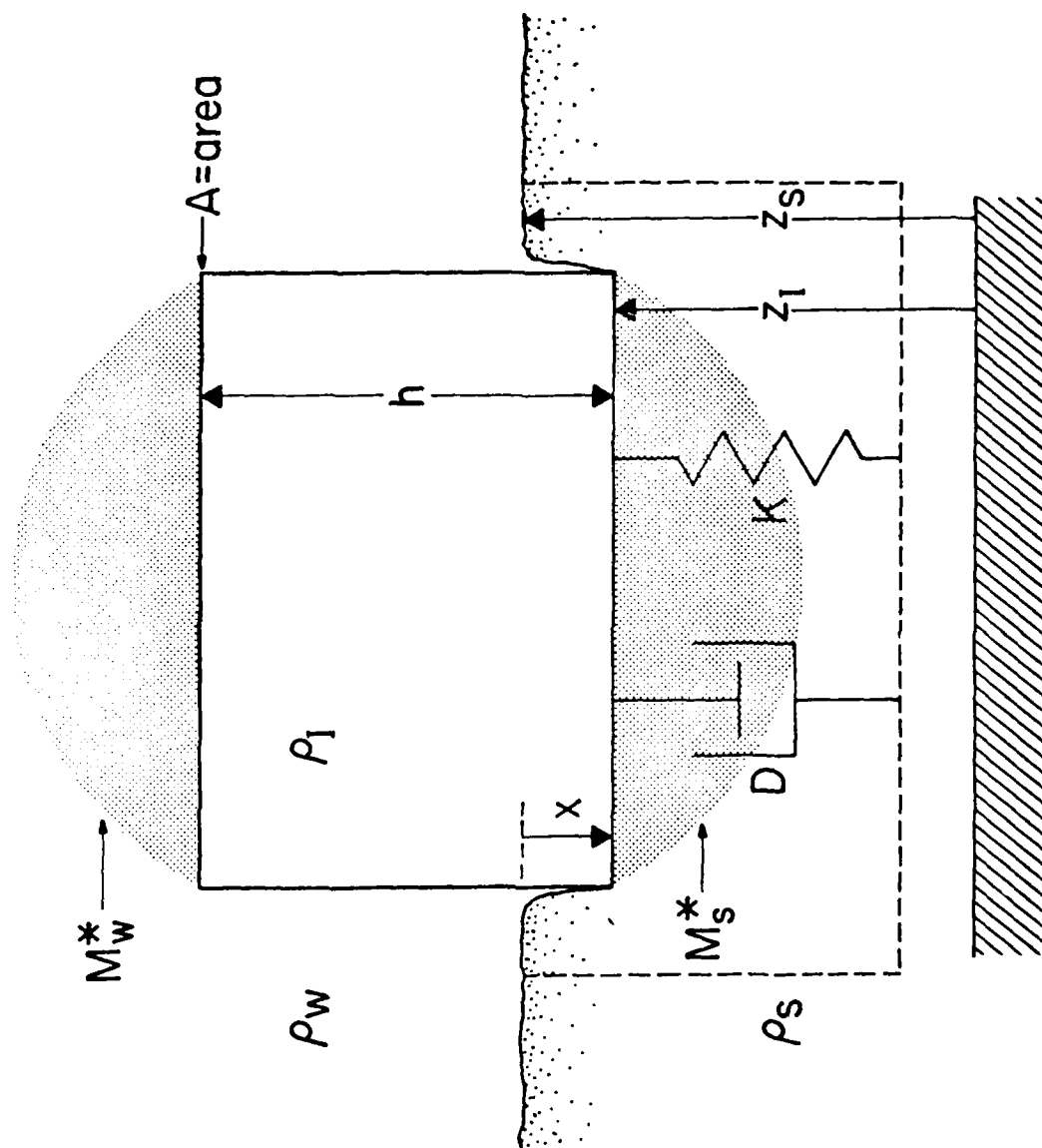


Fig. IV-1. Schematic of OBS coupling to the ocean bottom. From Sutton et al., 1980 (Appendix E).

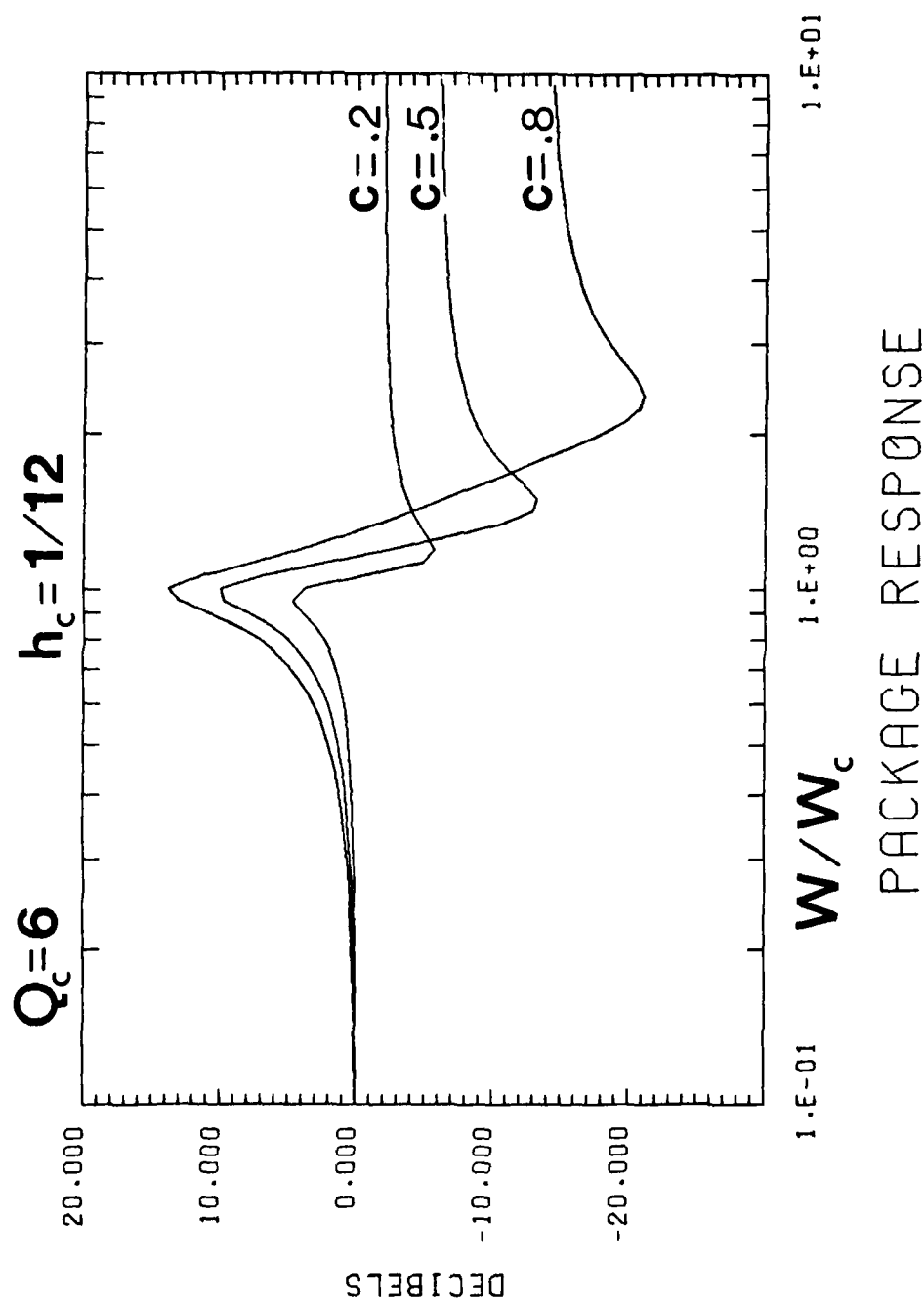


Fig. IV-2. Amplitude response of an OBS package (motion of OBS/motion of bottom) for different values of C . As C approaches zero, the coupling approaches optimum. From Sutton et al., 1980 (Appendix E).

(For most present OBS designs the package is primarily in the water and $\bar{M}_S=0$.) Values of C_{max} calculated for the instruments compared at Lopez Island are given in Table IV-1. The more flat the horizontal surface area, the greater C is overestimated by equation (3).

Experimental values for h_c (or equivalently, Q_c) and ω_c can be obtained from mechanical transient tests such as those described in section II-C. In addition, M_f^* , needed to estimate C , can be obtained from the ratio of applied force to output amplitude. Equations (13) and (14) in Appendix E give the transforms of the output voltage from a critically damped geophone that would be expected from such tests. Theoretical curves are matched to Fourier transforms of transient outputs from three OBS's and the spike standard in Figure IV-3. (A complete set of transient test outputs and spectra for each OBS and the standard instruments is in Appendix C.) Although the observations are degraded by imperfect mechanical testing procedures, we obtained fairly reliable estimates of h_c and ω_c from these comparisons. Estimates of the coupling frequency obtained from the vertical transient tests are listed in Table IV-1.

Theoretical values for Q_c ($Q_c=1/2h_c$) and ω_c can be obtained from Figure 1 in Appendix E and the data in Table III-2. Calculated mass factors, F_m , which provide an estimate of Q_c , and calculated coupling frequencies are listed in Table IV-1. These values are based on a single estimate of sediment rigidity and density, do not include any entrained sediment or water ($M_S^*, M_W^*=0$), neglect the effect of buoyancy on ω_c , and do not take into account large differences in the configuration of the areas in contact with the bottom (only the horizontal component of the contact area is considered).

Observed and calculated coupling frequencies are compared in Figure IV-4. Most of the operational OBS's show fairly good agreement for an assumed sediment shear velocity $V_S=10\text{m/s}$ and density $\rho_S=1/57\text{g/cm}^3$. LDGO, UW, and UWF, however, fall well off the line with a higher observed than calculated frequency. From Table III-I we see that these packages apply a bearing pressure to the bottom sediment more than three times greater than that of the next greatest. Therefore, it is likely that they are coupled to a stiffer bottom; e.g., as shown in Figure IV-4, an increase in V_S to 33 m/s would bring theory and observation together for LDGO; smaller increases are required for UW and UWF.

All three of the standard instruments show considerably lower observed than calculated coupling frequencies. All three instruments are tightly coupled to the bottom sediment and it is likely that there is considerable error in neglecting M_S^* . As indicated in Figure IV-4, calculated frequencies could be reduced to observed by addition of reasonable amounts of sediment to the instrument mass, as follows: a 2-cm-thick layer surrounding the roughly spherical, buried ND; a 3-cm-thick layer under the flat, circular PL; two hemispheres of radius equal to that of the (horizontal) bearing area of the buried spike. The reader is referred to Appendix F for an alternative investigation of these parameters.

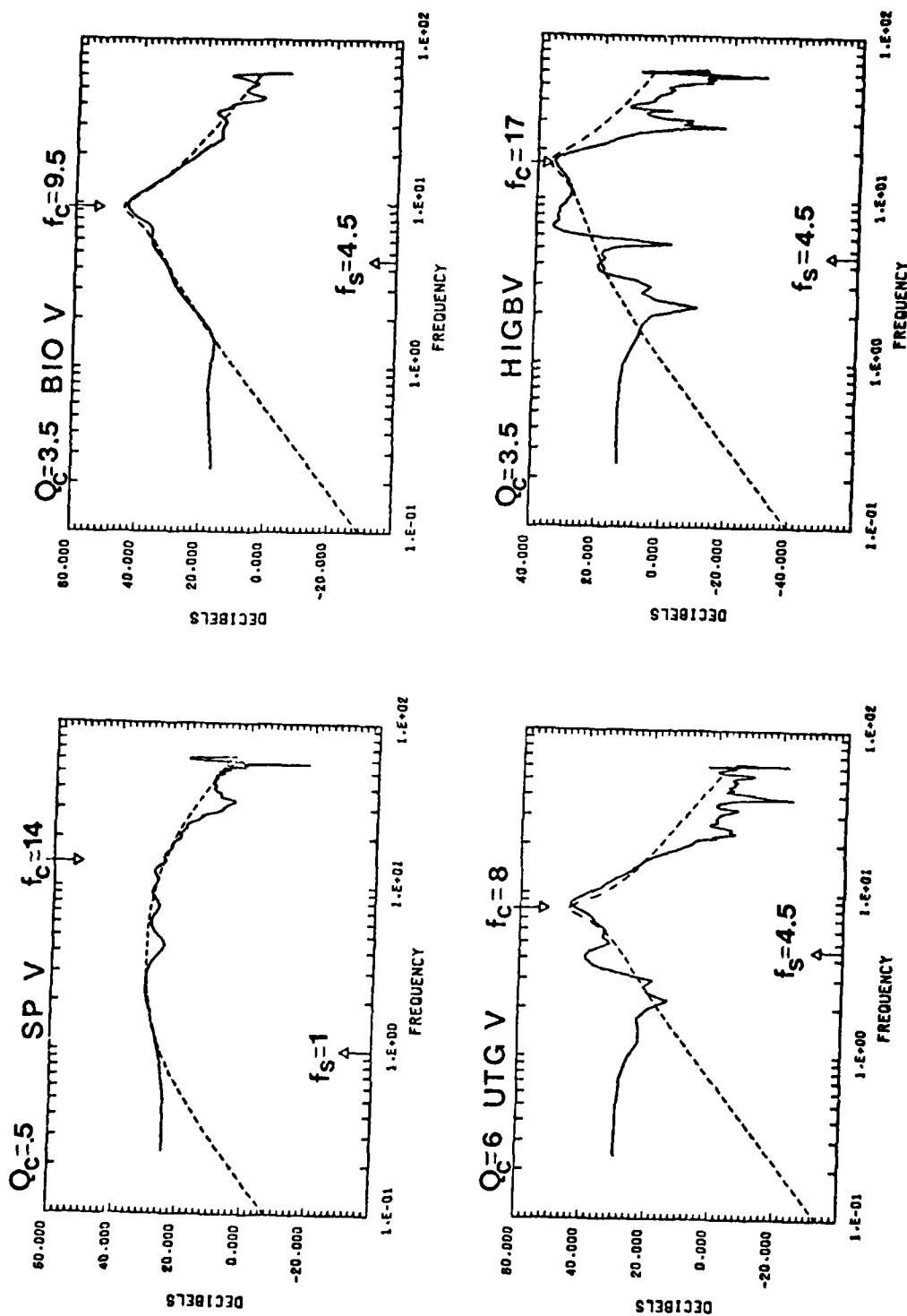


Fig. IV-3. Theoretical response curves (dashed line) compared to transient test data (solid line) for several instruments. The vertical dB scales have an arbitrary reference for the theoretical curves and are referenced to 1 digital unit for the data. From Sutton et al., 1980 (Appendix E).

TABLE IV-1. OBS Coupling Parameters

	(2)	(3)	(4)	(5)	(6)
OBS	C_{\max}	$V_s/R(s^{-1})$	F_m	f_c (Hz)	f_o (Hz)
ND	0	56	2.7	17	14
PL	.53/.27	18	0.22	19	14
SP	.17	100	5.1	22	14
BIO	.25	29	2.2	9.9	9.5
HIGE	.41	120	8.9	20	17
HIGS	.30	67	28	7.1	8
LDGO	.40	120	270	3.6	12
MITE	.53	50	1.4	21	22
OSU	.21	26	2.5	8.1	10
SI0 ⁽¹⁾	.19	56	6.9	11	11
UCSB ⁽¹⁾	.16	65/100	10/36	10/8.3	8 1/2
USGS	.21	48	8.1	8.4	8-9
UTC ⁽¹⁾	.23	200	100	9.9	8 1/2
UW ⁽¹⁾	.11	380	1700	4.6	8
UWF	.44	50	42	3.9	8 1/2

(1) OBS's having three foot pads; others have a single base area

(2) Calculated from equation (3)

(3) $V_s = 10$ m/s; $R = (\text{area of one footpad}/\pi)^{1/2}$

(4) $F_m = M_I/n \rho_s R^3$; n =number of footpads; $\rho_s = 1.57$ g/cm³

(5) $f_c = (n R n_s / 4 M_I)^{1/2}$; $\mu_s = V_s^2$

(6) f_o = observed coupling frequency estimated from spectra of vertical transient tests

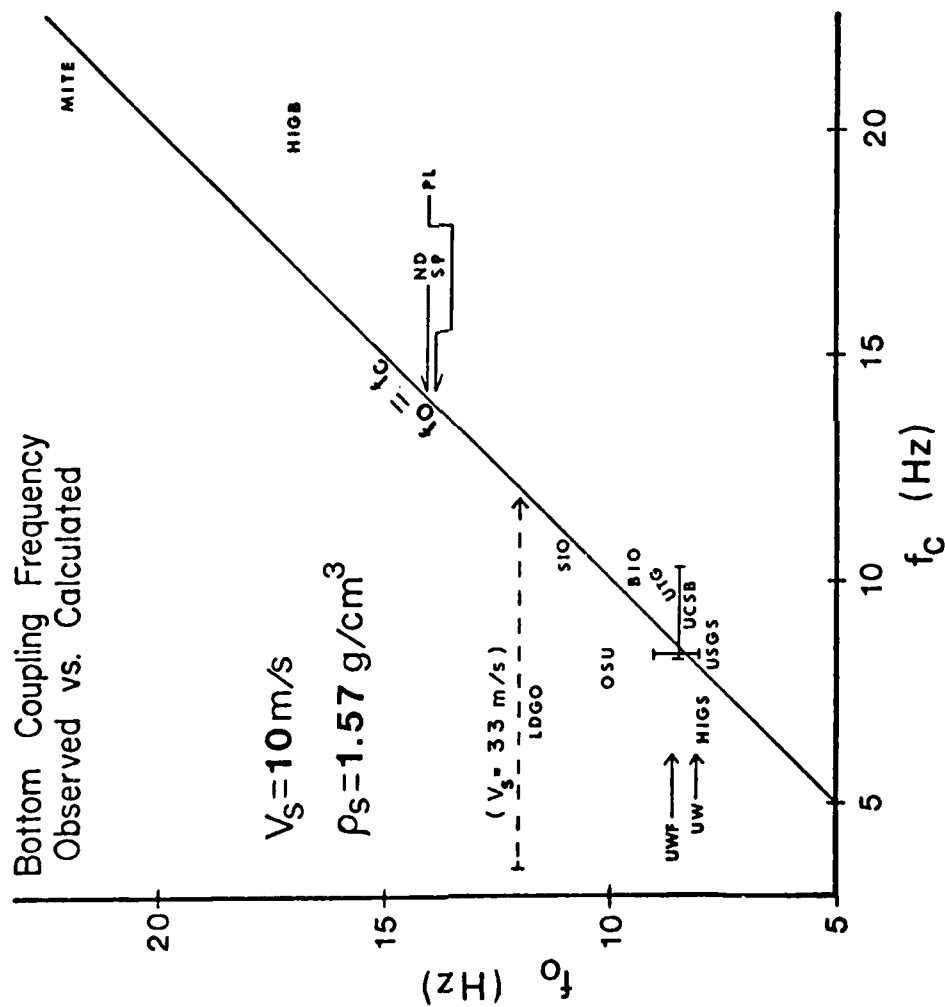


Fig. IV-4. Bottom coupling frequency, observed versus calculated. If the theory is perfect, all values could be on the straight line. Deviations from the line are discussed in the text.

The Q of the coupling resonance, theoretically, is proportional to $F_m^{1/2}$. F_m , the mass factor, is listed in Table IV-1; a comparison with the value for Q_c shown in Figure IV-3 indicates rough agreement with expectations. Transient test results in Appendix C can be used for more thorough comparisons.

Signals from controlled source and transient tests can be compared in both the time and the frequency domains. Some of the comparisons are discussed here (see also Appendix E) and the remainder are presented in Appendix C. Data are processed and presented in as similar a format as possible to aid in comparison. The reader is referred to Appendix C for the format of the figures.

Some may question what is learned from the transient test, in that it does not force the instrument to move in the same way as a seismic wave, and the resulting motions can be complicated. The validity of using the mechanical transient tests for obtaining the parameters f_c and Q_c is shown in Figures IV-5 and IV-6. The time signals and spectra obtained for the early arrivals from airgun shot 182 on PL, SP, and SIO verticals are shown in Figure IV-5 together with the vertical transient tests of SIO. Note that the spectra for PL and SP are similar, especially at frequencies below 20 Hz. The SIO test, however, shows extra energy near 12 Hz and a flattening of the spectrum above 12 Hz. The vertical transient test for SIO (bottom of Fig. IV-5) shows a peak near 11 Hz; thus it appears that modification of the signal because of coupling causes the spectral differences. A similar situation is shown in Figure IV-6 for a cap shot. Here the SIO test again shows amplification relative to SP near 11-12 Hz. HIGS, however, shows amplification near 8 Hz. As shown at the bottom of Figure IV-6, the HIGS transient has a peak near 8 Hz, again suggesting that the effects of coupling are being observed in the seismic response.

Examples of good coupling are shown in Figure IV-7. Transient tests that yield a sharp spike in the time domain, such as SP and MITE, yield relatively flat spectral responses and good seismic response to both high and low frequencies. Two examples of good coupling (SP and MITE) and two of poor coupling (USGS and UTG) are shown in Figure IV-8 for the same CAP shot. (The low sensitivity of MITE for frequencies below about 10 Hz is of internal origin and is not related to coupling.) Near 11 Hz the USGS instrument shows a strong resonance and UTG shows a somewhat weaker resonance. Spectra for both cap and background noise for both OBS's fall off above the resonance frequencies. By comparison, the SP and MITE verticals show relatively flat spectra.

Response to Vertical Input on Horizontal Geophones. Cross coupling between vertical seismic input and horizontal geophones does not appear to be a serious problem. If a package is made reasonably symmetrical around a vertical axis, then horizontal resonances will not be excited by vertical inputs. Quantitative data are available from vertical transient tests on OBS's containing horizontal component sensors, but they have not been analyzed.

Horizontal Input Recorded on Vertical Geophones. A particularly good example of this type of cross coupling can be seen in Figure IV-9.

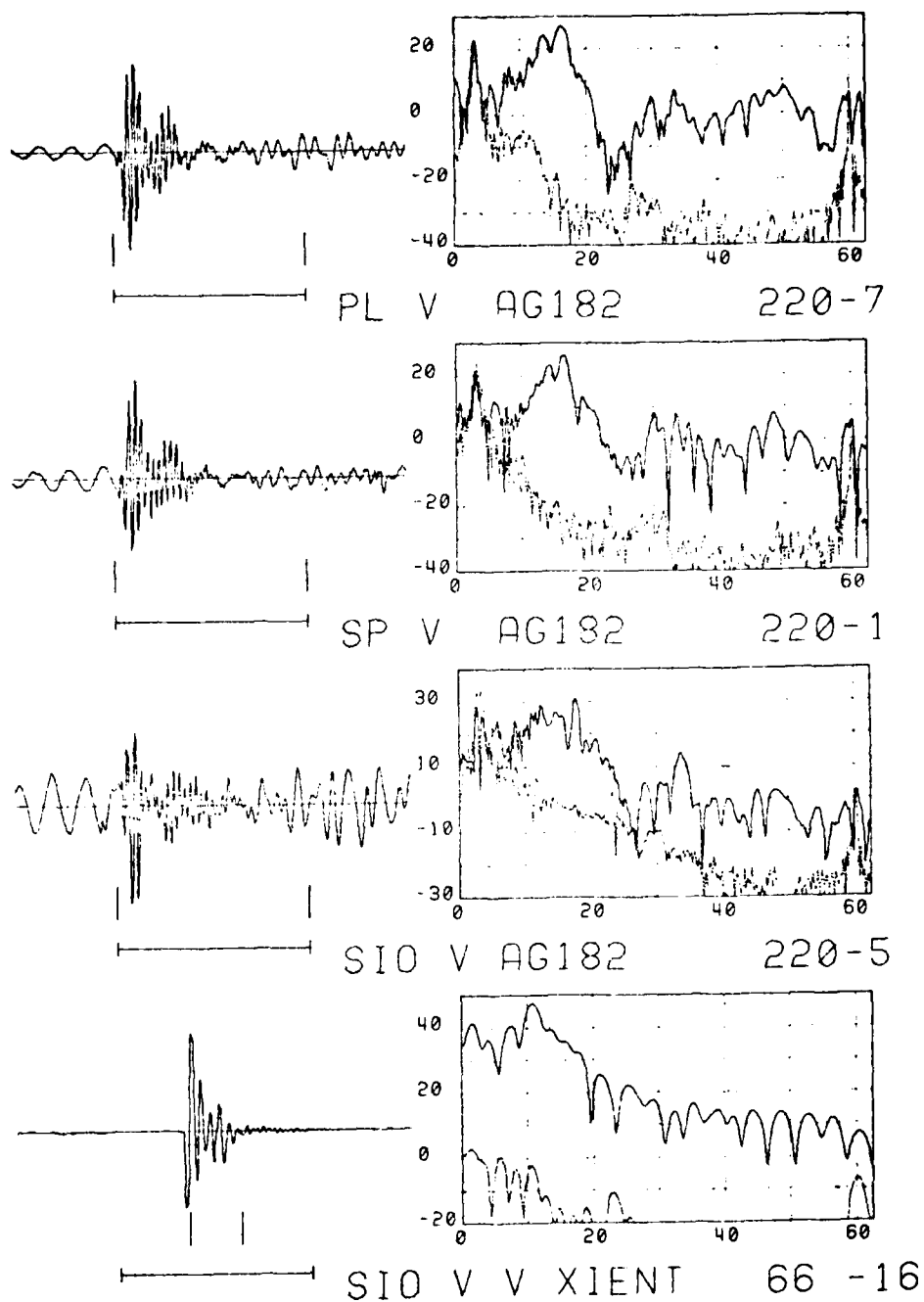


Fig. IV-5. Time and frequency domain recordings of airgun shot 182. The format for these figures is explained in Appendix C.

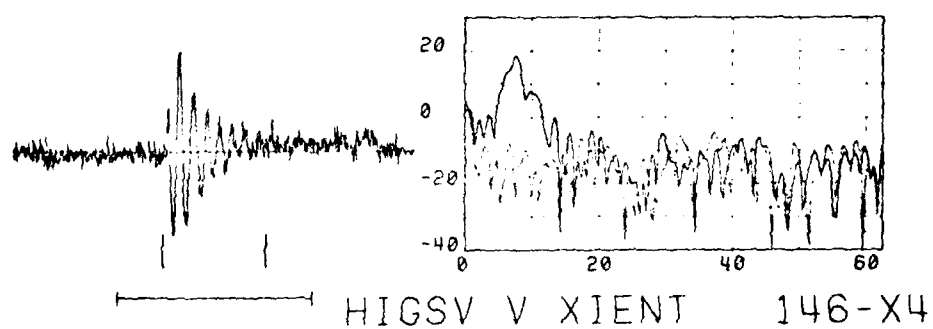
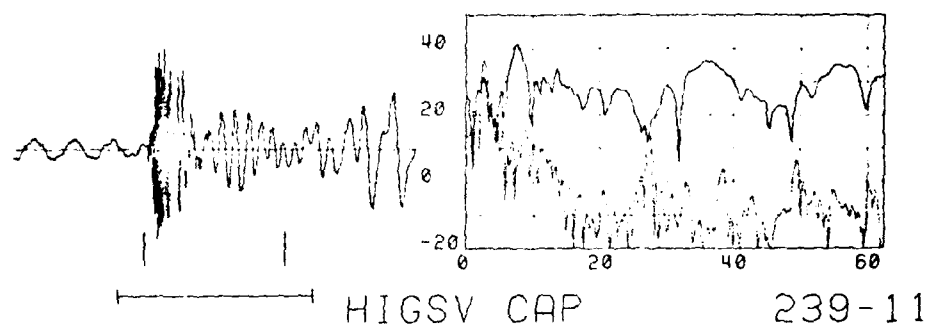
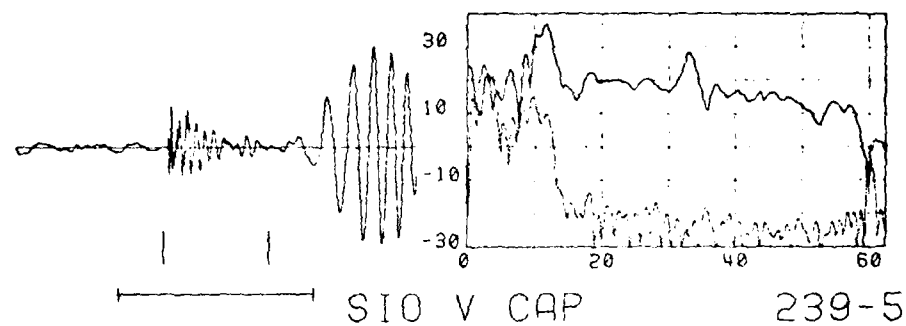
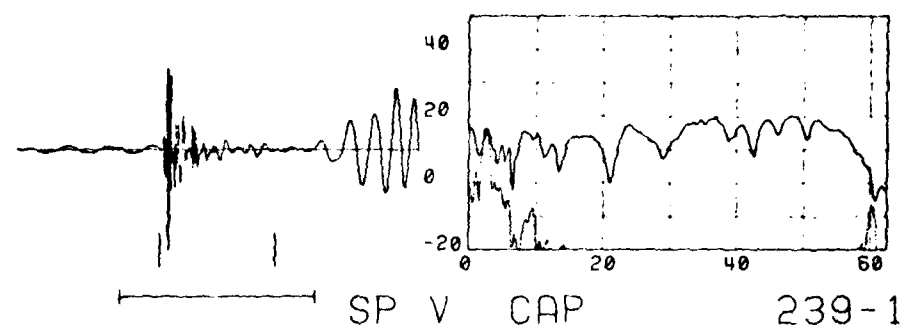


Fig. IV-6. Recordings showing the correlation between seismic response and transient test response.

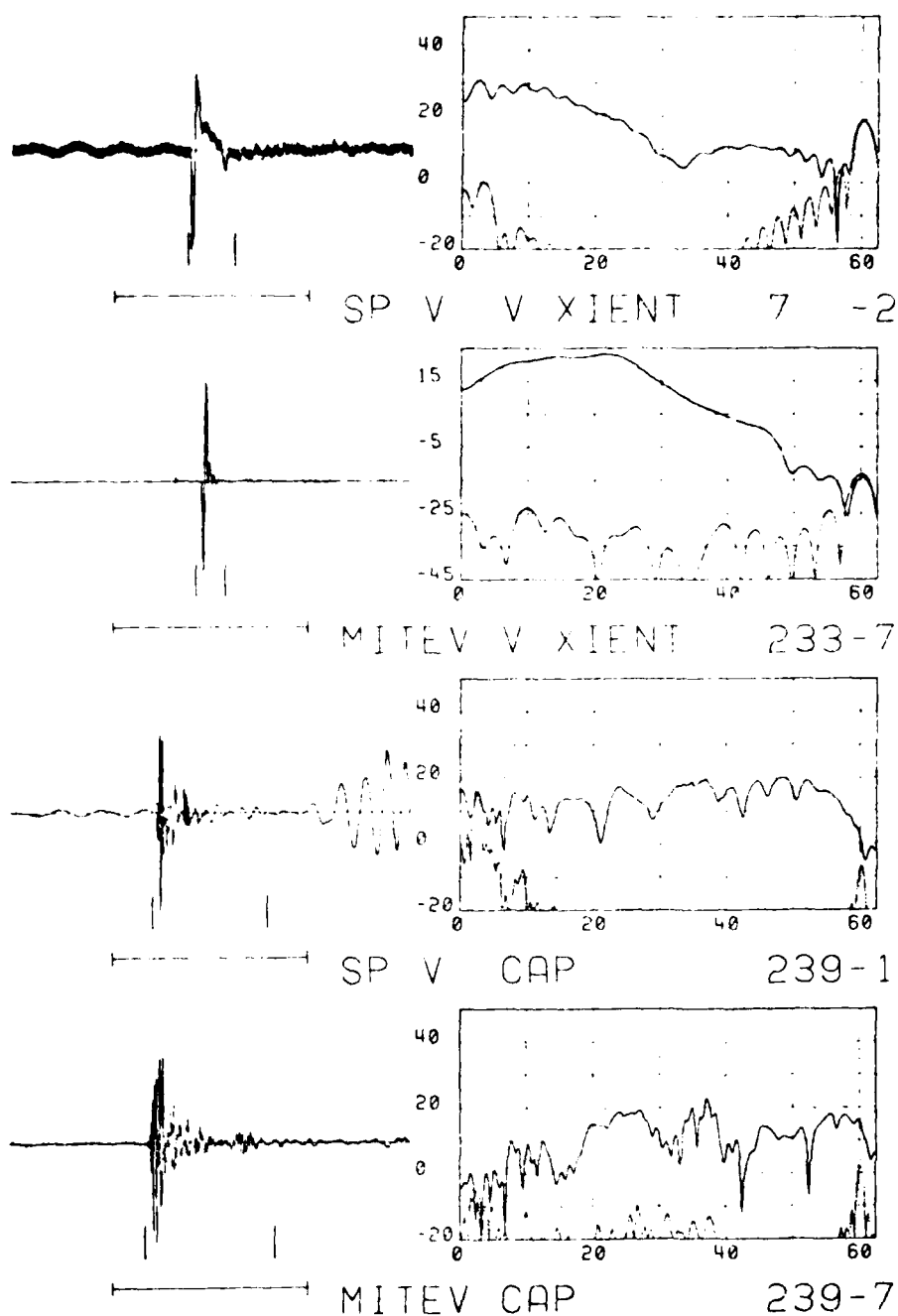


Fig. IV-7. Recordings showing good response characteristics. Note that spike response in the time domain yields the desirable flat response in the frequency domain.

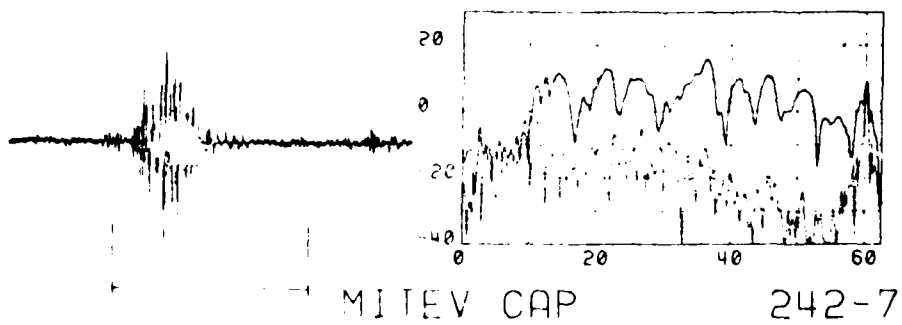
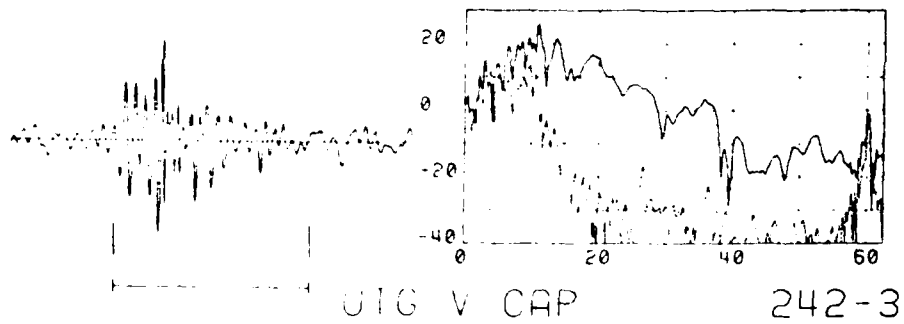
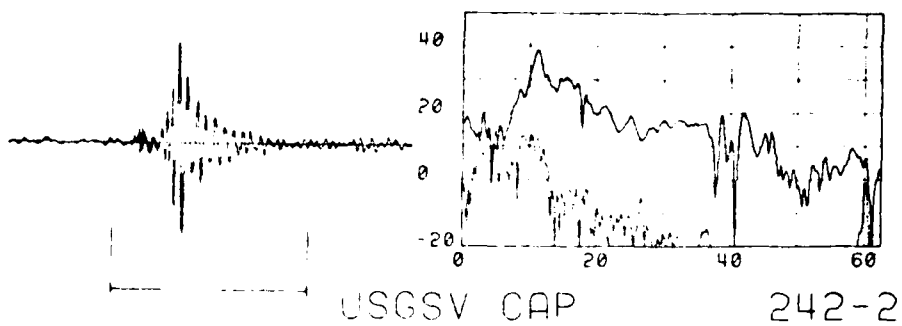
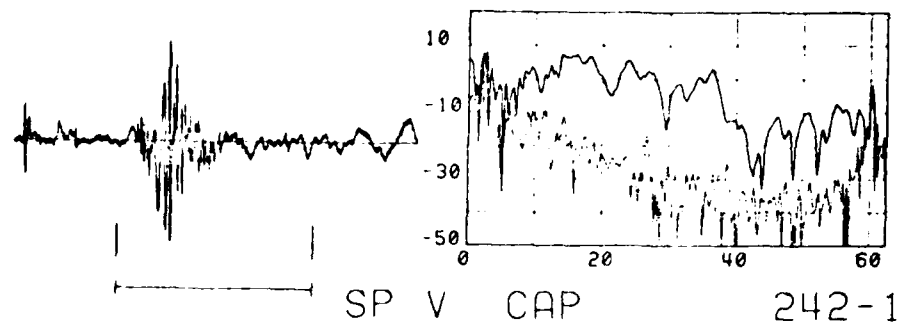


Fig. IV-8. Comparison of desirable and undesirable responses of various instruments to the same source.

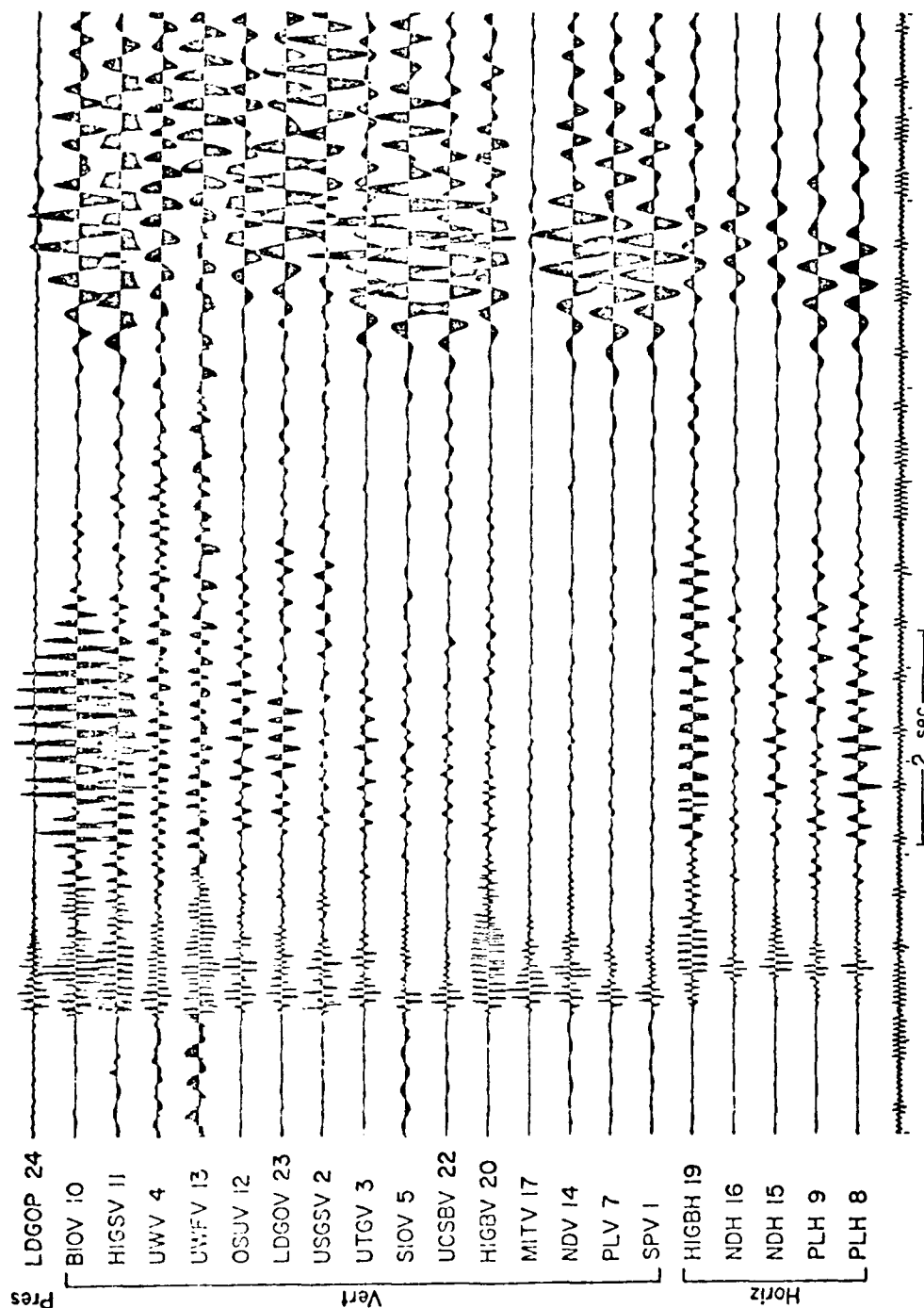


Fig. IV-9. Airgun shot 182. This figure contains a wealth of information pertinent to coupling. The energy arriving between 1.5 and 5 sec after the first arrival is discussed in the text. Note that the hydrophone (LDGOP) sees very little after the first arrival. All records were adjusted to have approximately equal amplitudes early in the record. From Sutton et al., 1980 (Appendix E).

In this figure the signals from all components recorded for airgun shot 182 are displayed. The horizontal geophones shown at the bottom show a strong 6-Hz arrival from about 1.5 to 5 sec after the first arrivals. The vertical standards and vertical MITE and HIGB sensors show very little of this arrival, indicating that it is horizontally polarized. Vertical geophones from other packages, however, show varying amounts of signal arriving during this period which has been transformed by the instruments from horizontal motion into vertical motion. This type of cross coupling is undesirable in that it would be extremely hard to predict, and it represents a severe distortion of true ground motion. This problem is discussed more thoroughly in Appendix H.

The horizontal transient test recorded on the vertical geophones indicate the possible severity of this problem. Figure IV-10 (also Figs. 5-10 in Appendix C) shows results of these tests. Note that in the horizontal tests a second signal is observed. This signal is believed to be generated when the electromagnet armature hits the pulley rod (Fig. II-5).

In Figure IV-10 the PL standard shows a relatively sharp response and flat spectrum, indicating that cross coupling should not severely affect this instrument. BIO, however, shows a very strong resonance near 6 Hz. This resonance indicates a possibly severe horizontal-to-vertical cross-coupling problem, which is indeed seen in Figure IV-9. The transient tests for UCSB are interesting in that the tests were done at two different levels rather than two different azimuths, and the resulting transients excited two different resonances that differ in frequency by a factor of 2 (4 and 8 Hz). Note, however, that UCSB did not exhibit a severe cross-coupling problem in Figure IV-9, indicating that the wave train observed in Figure IV-9 did not contain sufficient energy at 4 or 8 Hz to excite either of these resonances.

Response to Horizontal Input on Horizontal Geophones. Transient tests were conducted in two horizontal directions or at two different elevations on each package. The resulting signals are shown in Figures 11 to 13 in Appendix C. In most cases a resonance was observed that indicates motion in at least one horizontal mode, either lateral sliding or rotation around a horizontal axis. The complexity reflects both the difficulty in obtaining reliable horizontal transient data and the true complexity of the motion of the package, each with its own peculiarities and symmetries that modify this type of coupling.

V. NOISE MEASUREMENTS

Two types of noise studies were made: a description of the ambient background noise and its mode of propagation and an evaluation of noise induced in the OBS's by water currents.

To describe the ambient background noise we used the frequency spectra, the particle vector motion as determined from the three components

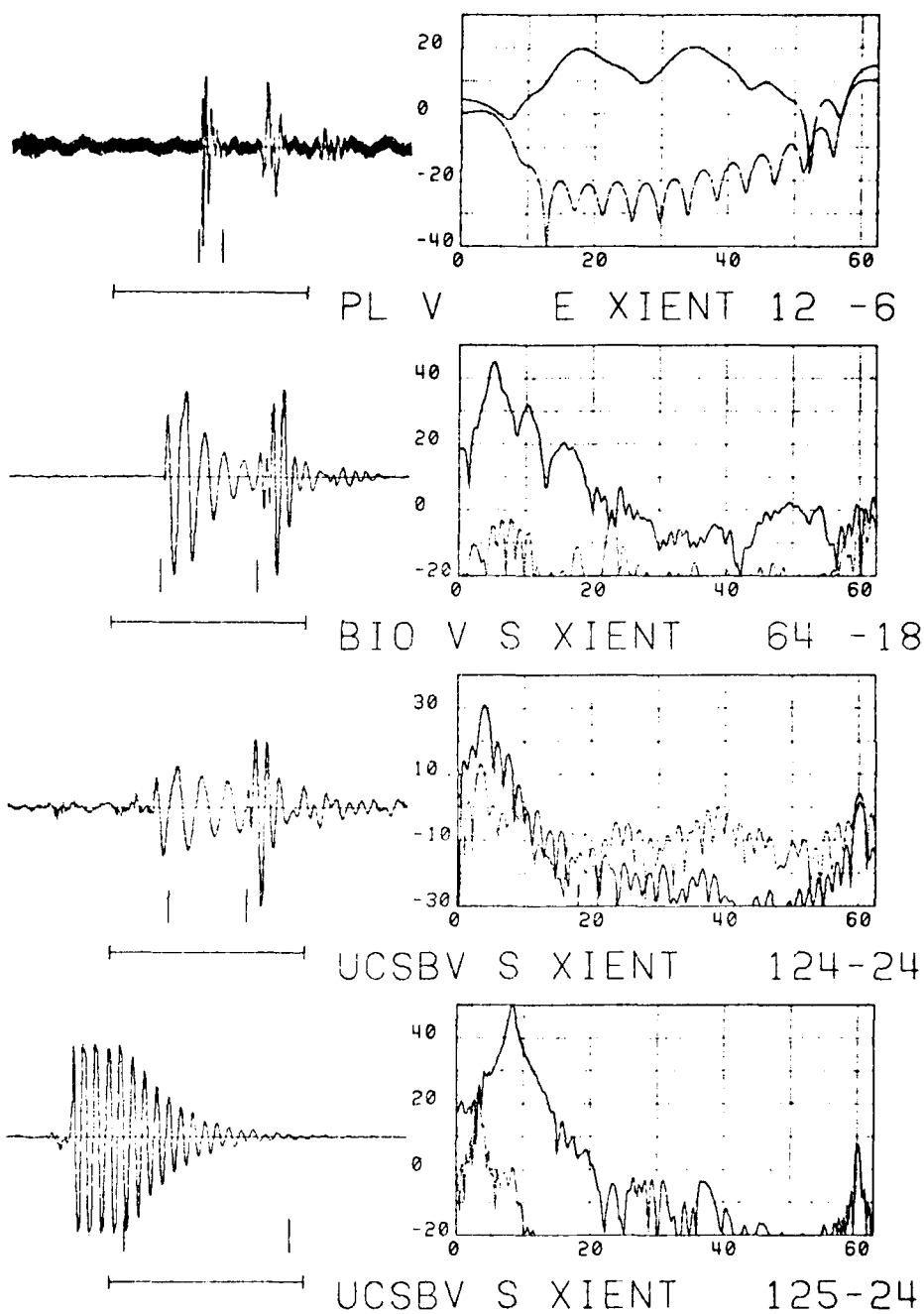


Fig. IV-10. Horizontal transient tests recorded on vertical geophones. The severity of this type of cross coupling for some instruments is obvious. From Sutton et al., 1980 (Appendix E).

of motion, and the frequency-wave number spectra determined from the array of OBS's. We found that the noise spectra peaked very strongly around 2.5 to 3 Hz and in this frequency band the particle motion was elliptical and had phase velocities of about 20 to 50 m/sec; these parameters are consistent with the propagation of the noise as surface waves. We also found that shot-generated, dispersed surface waves have properties similar to the background noise, supporting the contention that the mode of generation, propagation, and attenuation of the noise can be understood in terms of dispersed surface waves. Further, and possibly of greatest practical importance, we established that these surface waves are highly attenuated in the water and weakly recorded on a hydrophone. This implies that hydrophones in deep-sea sediment environments are likely to be substantially quieter and give less complicated seismograms than geophones. The determination of current-induced noise on the OBS's was evaluated by comparing the spectra of several instruments against current speed. The results from this comparison are not definitive.

A more detailed discussion of these results is given below.

Characteristics of Ambient Seismic Noise

An example of ambient noise and its amplitude spectrum as recorded on the plate vertical is shown in Figure V-1, from record 210. The spectrum shows that the noise is dominated by energy in the 2- to 4-Hz band. A vector plot of the particle motion is shown in Figure V-2. In these plots the vertical axis is one component of motion and the horizontal axis is an orthogonal component. In these graphs rectilinear, or body-wave motion, would appear in the vertical-horizontal plots as vectors of constant slope, whereas elliptical particle motion would appear as fan-shaped patterns. It is clear from Figure V-2 that the predominant motion is elliptical. Another example is noise preceding airgun shot 182. The three components of motion as recorded on the plate and the associated particle motion are shown in Figures V-3 and 4.

In this experiment the two-dimensional array can be used to determine the coherency and phase velocity of the noise by taking the three-dimensional Fourier transform, or frequency-wave number spectrum of the array data. An example of the wave number spectrum taken at 2 Hz is shown in Figure V-5. From this spectrum the phase velocity at 2 Hz is found to be about 30 m/sec. For a more detailed discussion of this analysis see Appendix G.

Comparison of Noise with Shot-Generated Surface Waves

Nearly all the cap and airgun shots generated low-velocity surface waves in the 2- to 4-Hz band. An example, airgun shot 182, as recorded by the array is shown in Figure V-6. (See also Fig. IV-9.) The spectrum of this wave as recorded on the plate vertical for airgun shot 131 is

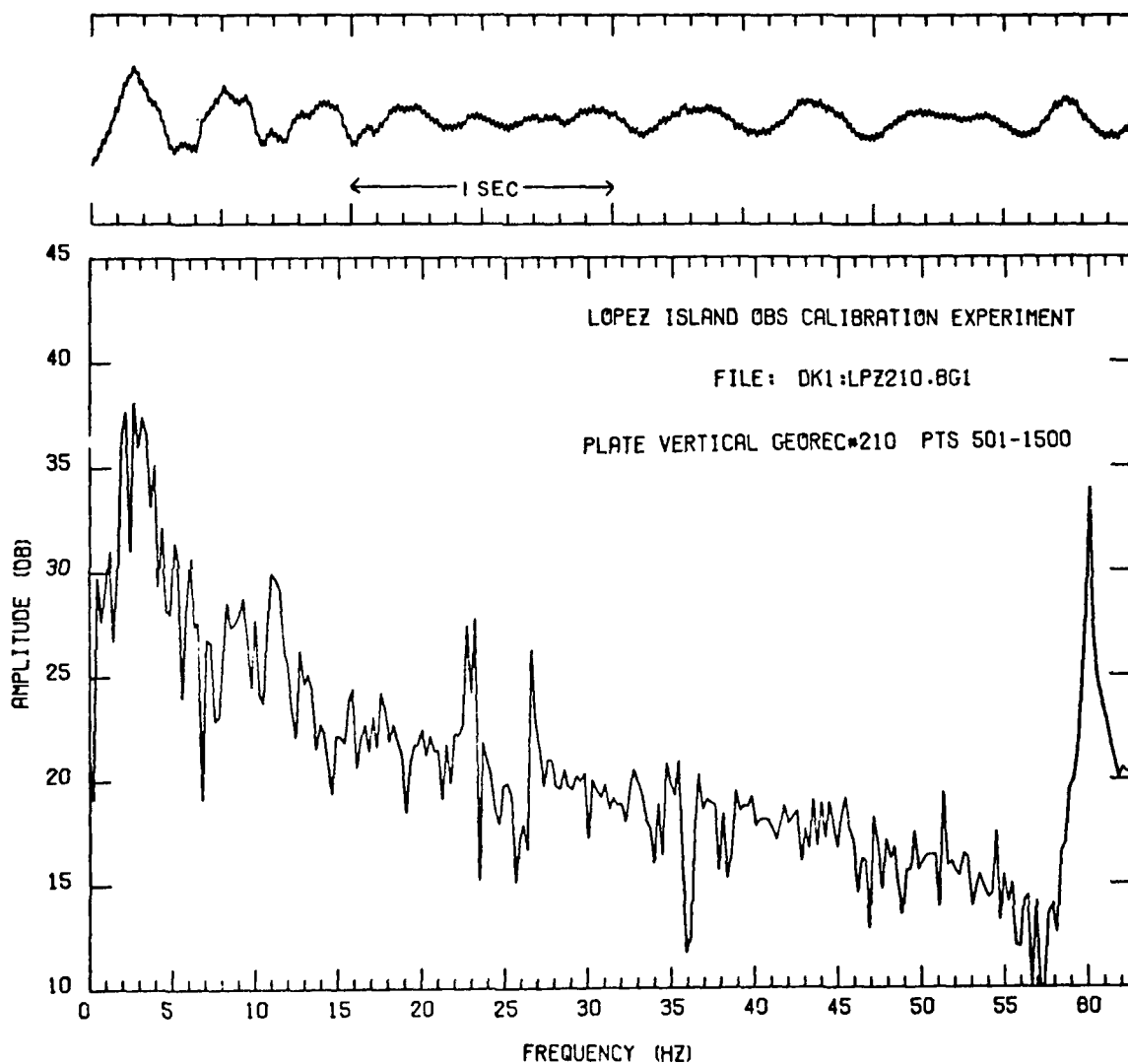


Fig. V-1. Noise record 210; time series and spectrum for plate vertical.

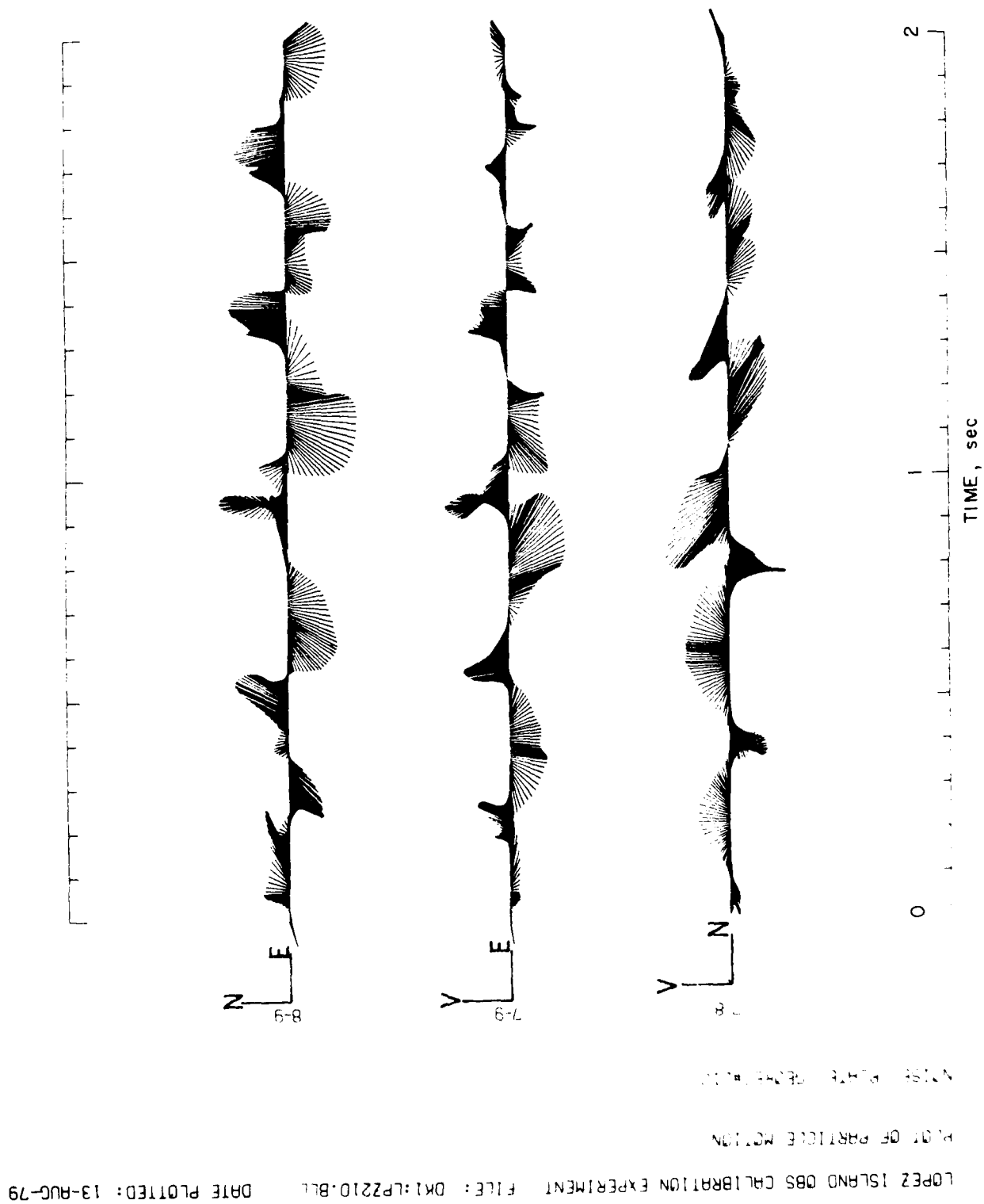


Fig. V-2. Particle motion for noise record 210 using the plate data.

LOPEZ ISLAND OBS CALIBRATION EXPERIMENT FILE: DK1:LPZ182.L40 DATE PLOTTED: 10-AUG-79

NOISE PLATE A/G SHOT 182 GEOREC#220 PTS 1001-2000

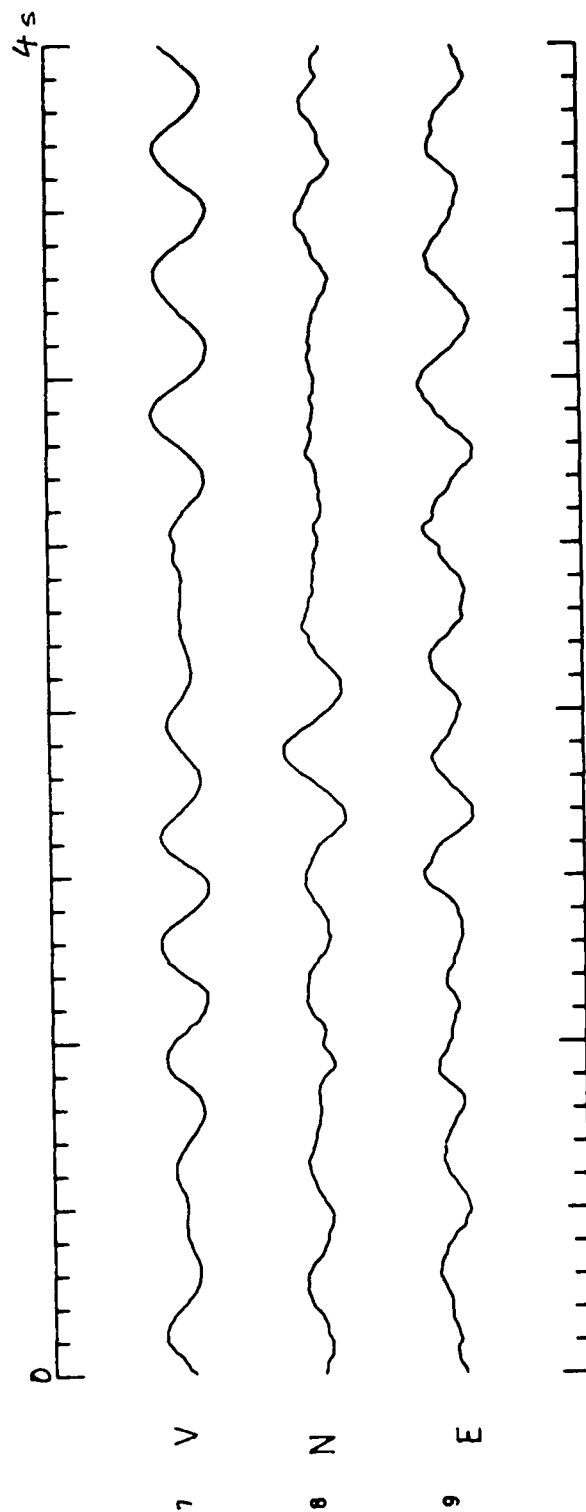


Fig. V-3. Noise record preceding airgun shot 182 showing vertical and horizontal components of motion on the plate.

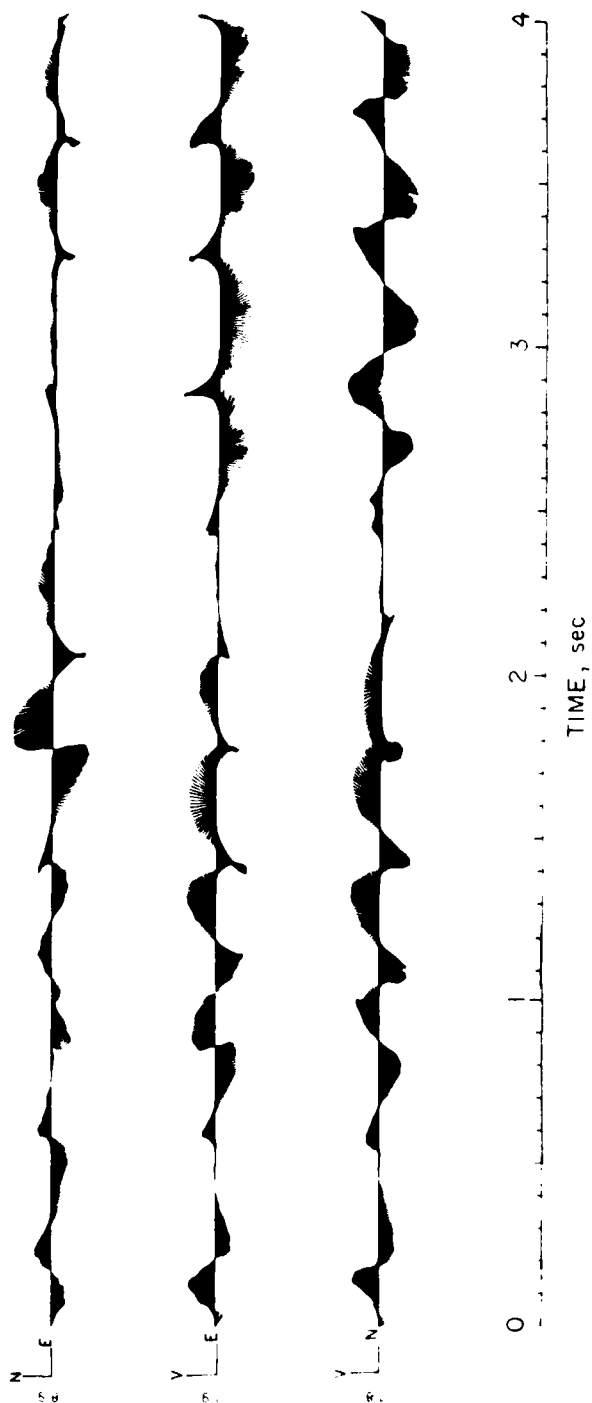


Fig. V-4. Particle motions for the noise record in Figure V-3.

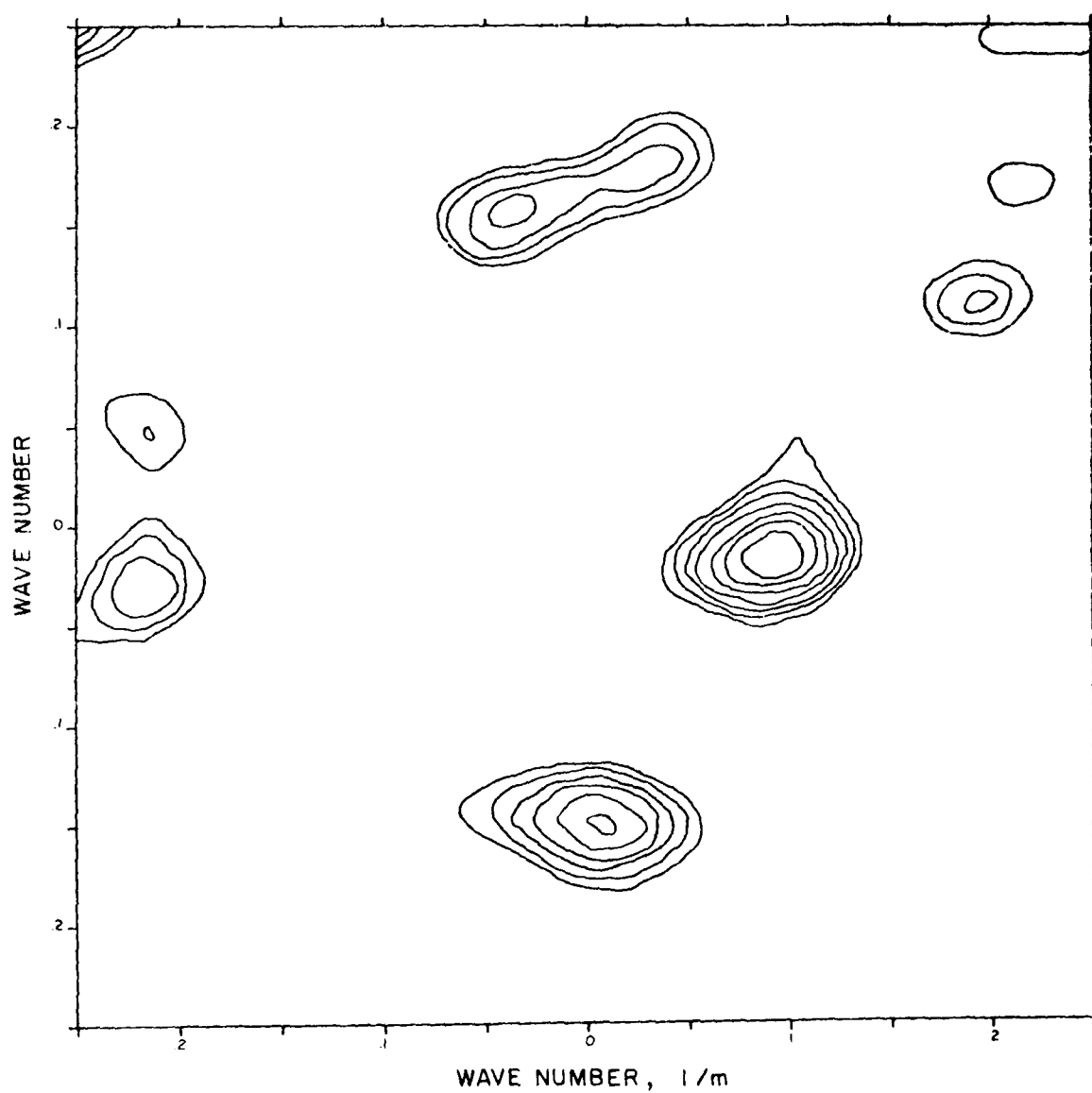


Fig. V-5. Wavenumber spectrum at 2 Hz of noise. from eleven instruments.

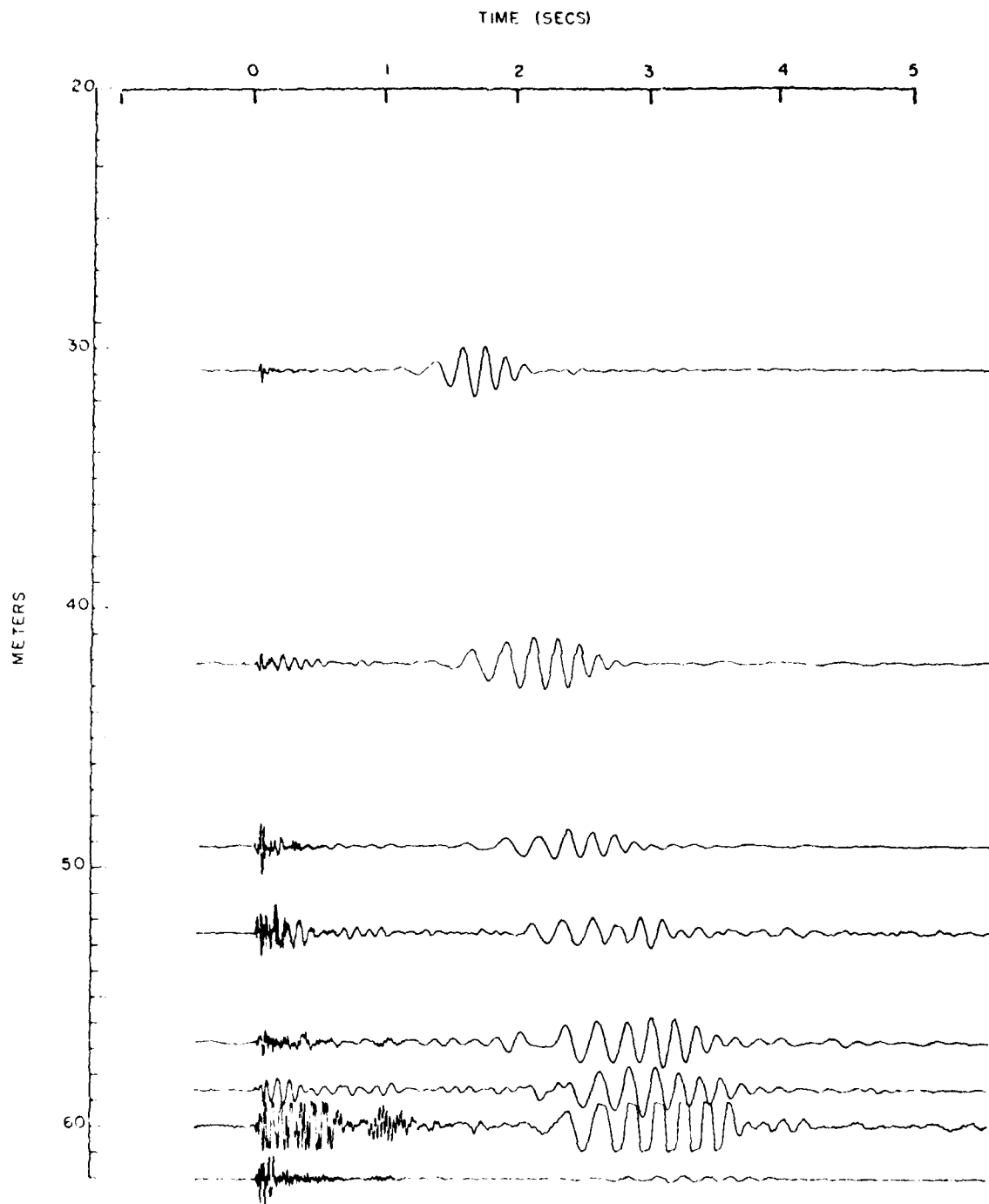


Fig. V-6. Record section showing recordings of the array for a cap shot; note the large-amplitude surface wave.

shown in Figure V-7 and is very similar to the noise spectrum in Figure V-1. The particle motion for this wave packet is elliptical, as shown in Figure V-8. A group velocity and phase velocity dispersion curve for this wave packet is shown in Figure V-9 (from Tuthill et al., 1980, Appendix G).

The similarity of the spectra, dispersion curves, and particle motion for the noise and the shot-generated surface waves strongly suggests that the noise is propagating as short-wavelength dispersive surface waves. The wavelengths in the 2- to 4-Hz band are found from the corresponding phase velocities to be about 15 m to 6 m.

Comparison Between Hydrophone and Seismometer Data

Figure V-10 shows a comparison between the LDGO hydrophone, the plate vertical and the plate horizontal for airgun shot 182. It is clear from this figure that the surface wave train is only weakly recorded on the hydrophone. This is to be expected since this motion is caused by short-wavelength surface waves that are highly attenuated in the water. The previous discussion also implies that the 2- to 4-Hz noise should be greatly reduced on the hydrophone. This implication is verified in Figure V-11, a comparison of noise spectra from the LDGO hydrophone and the HIGS vertical. This result alone implies that hydrophone records should be quieter and simpler than geophone records because they will be contaminated by short-wavelength ambient noise and short-wavelength signal-induced noise. This is particularly important in crustal refraction profiles because wavelengths of about 10 m will contain information about the immediate neighborhood of the instrument only and is of no use in determining average crustal properties. Worse than this, the short-wavelength noise will greatly degrade the long-wavelength signals.

Correlation of Background Noise with Currents

The purpose of this section is to investigate the possibility that (a) currents cause shaking of the instruments and hence noise; or alternatively, (b) that water currents traversing the array couple noise into the bottom the propagates across the array.

During one 13-hour period, hourly samples (of approximately 1-min. duration) of background noise were digitized. Water currents recorded on each of the four current meters for 15 min preceding and following each noise sample were averaged and ranked and are plotted in Figure V-12. During this time period the currents ranged from 1 to 4-1/2 cm/sec. This range is about as great as was observed during the entire experiment. The larger standard deviations for the higher current levels suggest a greater amount of irregularity in current across the OBS array during these times.

Noise spectral estimates were obtained for each 1-min sample by dividing the record into N 4-sec-long records (where N=30) and averaging

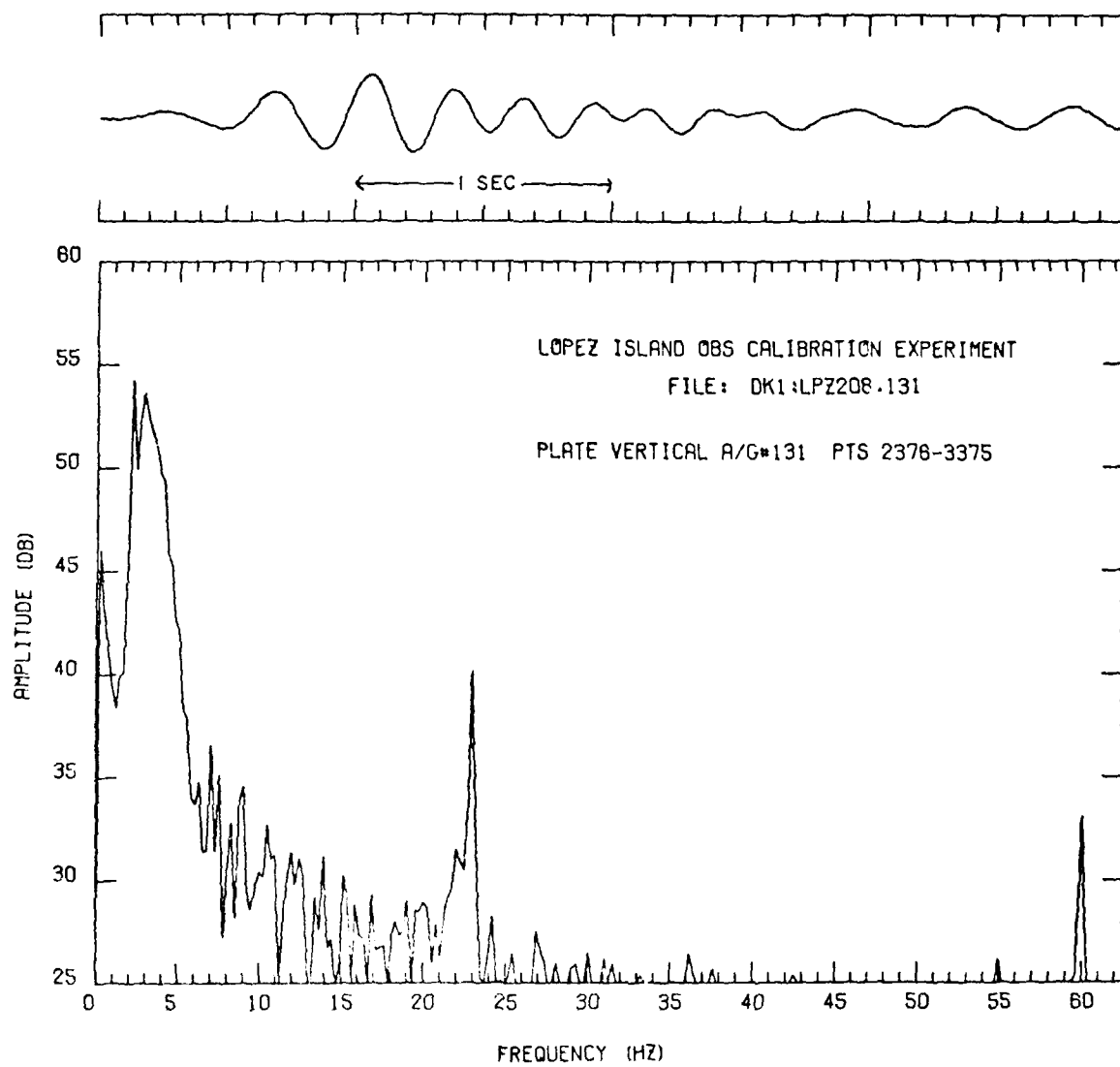


Fig. V-7. Time series and spectrum of the surface wave from a gun shot 131 on the plate vertical.

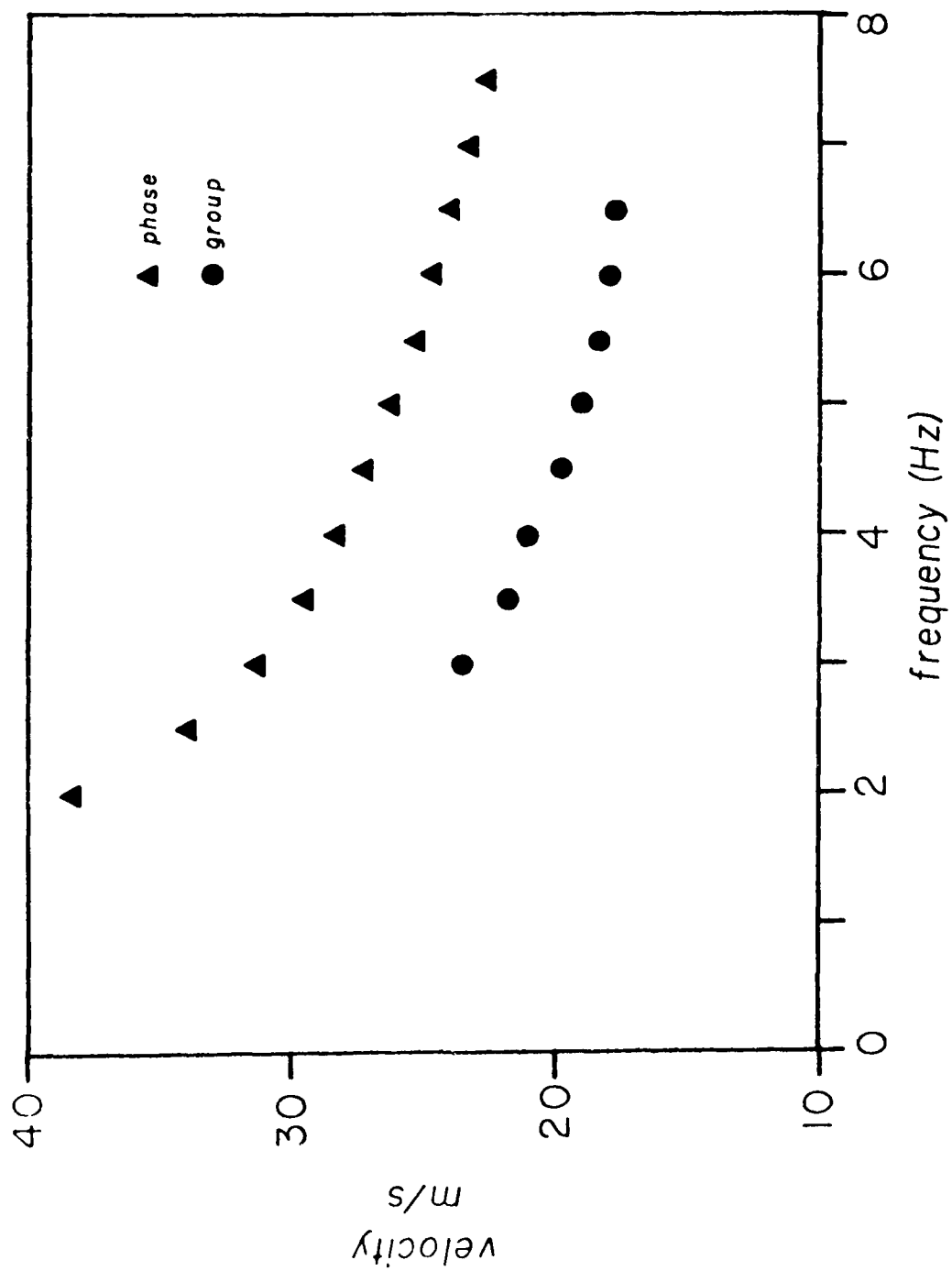


Fig. V-9. Phase and group velocity dispersion data for the surface waves.

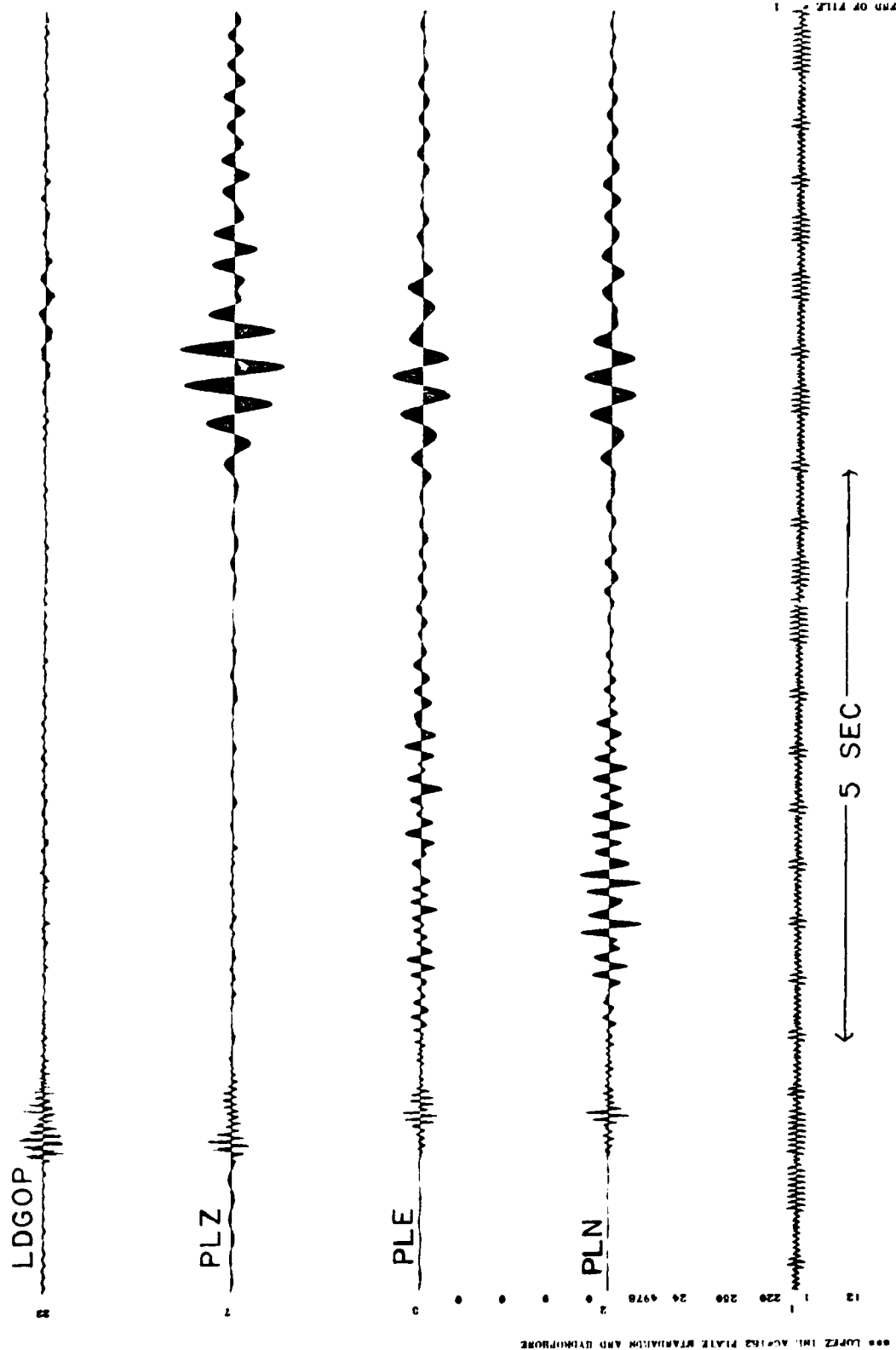
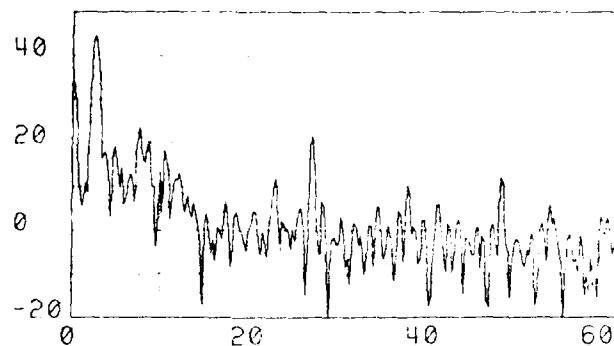
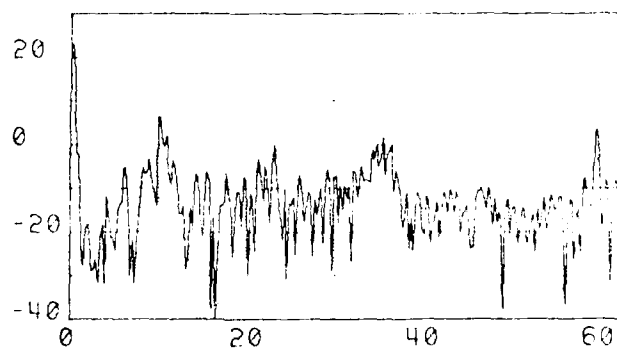


Fig. V-10. Comparison of recordings by the plate and the LDGO hydrophone of airgun shot 182. Note the high attenuation of the surface waves and horizontal motion on the hydrophone.



HIGSV NOISE

214-11



LDG P NOISE

214-24

Fig. X-11. Comparison of noise spectra from the HIGS vertical and the LDG0 hydrophone. Note the absence of the 2-HZ noise peak on the hydrophone.

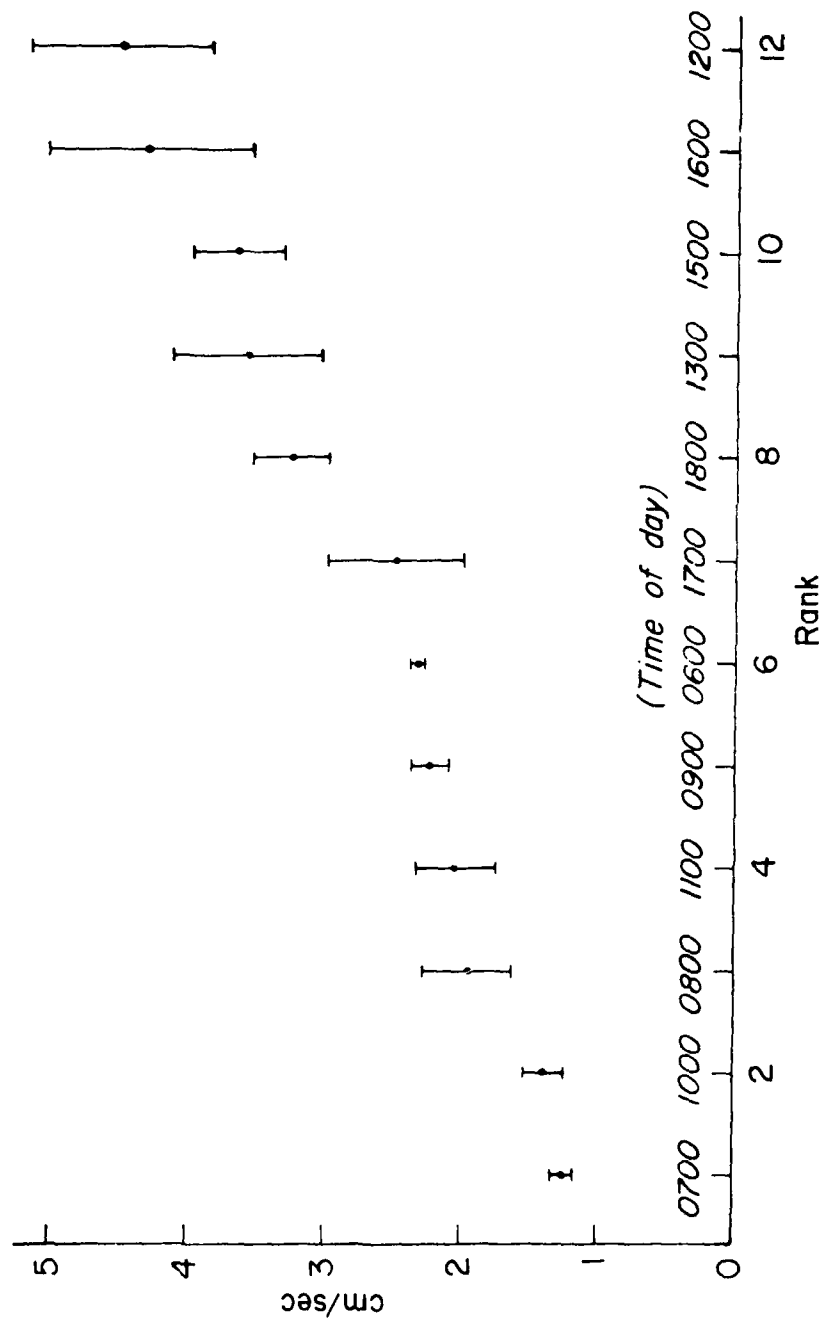


Fig. V-12. Water currents plotted by rank. Note that the current speed is not plotted against time.

the N spectra. For each frequency the mean \bar{X} and the 2-sigma confidence limits were obtained. In addition, the normalized variance, defined by

$$\frac{1}{N} \left[\sum_{i=1}^N (X_i - \bar{X})^2 \right] / (N-1)$$

was determined. For a stochastic or random process the variance will be proportional to the mean, whereas for a deterministic process the variance will be zero. An additional statistic, the fractional standard deviation, was also calculated and is defined by

$$\left[\frac{1}{N} \sum_{i=1}^N (X_i - \bar{X})^2 \right]^{1/2} / \bar{X}$$

For a gaussian process this statistic will be equal to a constant, whereas for a deterministic process this statistic will tend to zero.

Examples of these spectra and their statistics are shown in Figure V-13 for the Spike V and the UCSB V. It can be seen from these figures that the 60-Hz noise and noise peaks between 20 and 30 Hz have low standard errors, indicating that they are deterministic, as expected for the 60-Hz noise. Also, the 20 to 30 Hz may have a mechanical source (for example, from a motorboat.) The predominant noise at 2 Hz is more nearly stochastic.

Interpretation of these spectra is made difficult because of the several possible ways in which currents could induce noise. For example, currents might shake one instrument (such as the moored current meters) more than the others and this energy could be coupled to the bottom and radiate across the array as surface waves in the 2- to 4-Hz band, or the shaking of individual instruments might stimulate coupling resonances observed in the lift tests and these resonances would occur at frequencies peculiar to each OBS.

To test whether current-related noise is coupled into the ground and radiated across the array we have plotted the height of the 2- to 4-Hz spectral peak on the Spike V versus current speed in Figure V-14. The correlation between these two parameters is low, suggesting that there is little current-induced noise propagating across the array. (Note that the Spike V was chosen for this test because it was buried and should be insensitive to current-induced shaking.)

To test whether individual instruments were sensitive to current shaking we used as an example the UCSB V data.

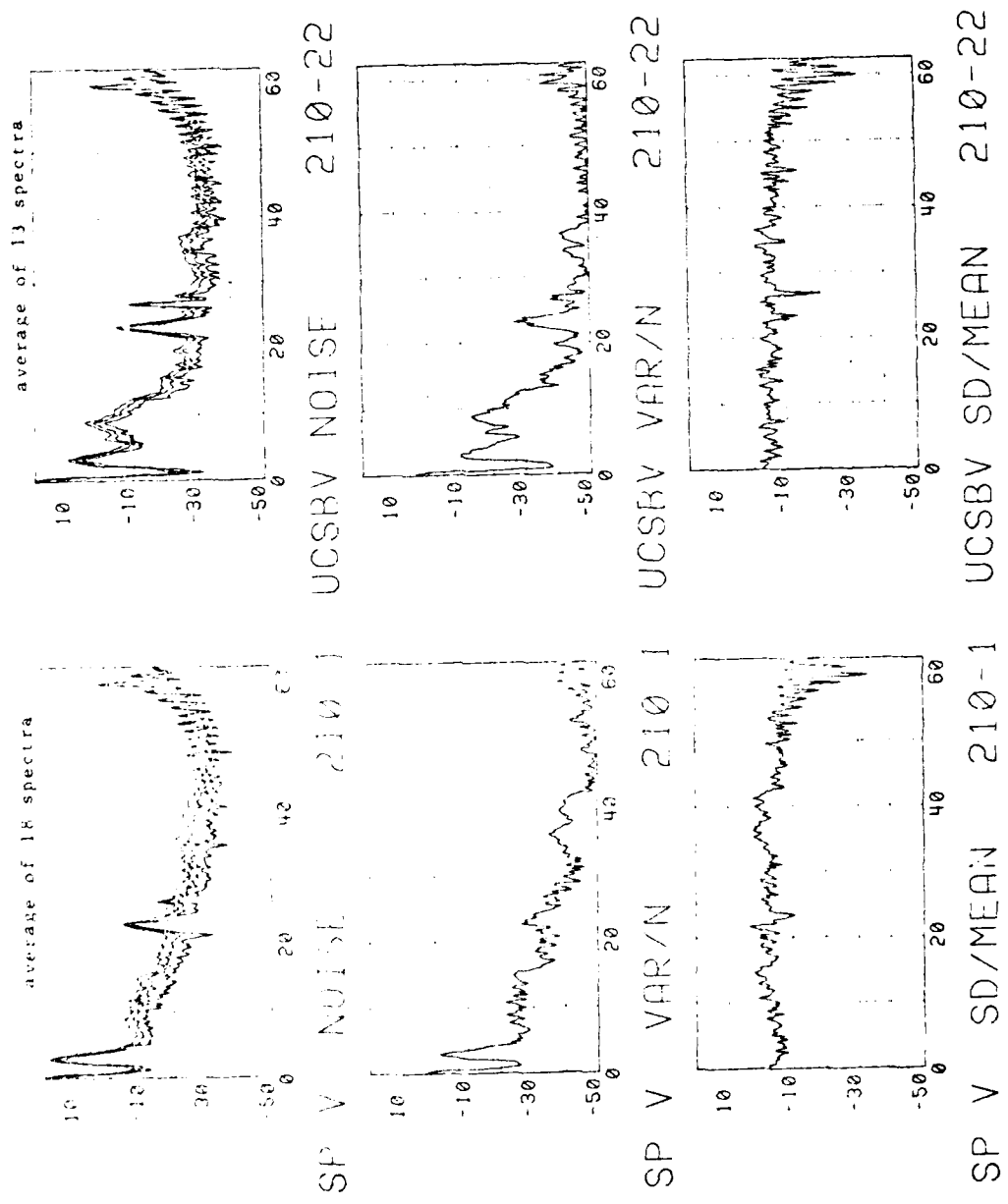


Fig. V-13. Noise spectra and spectral statistics for the Spike V and UCSB V. See text for explanation of the statistics.

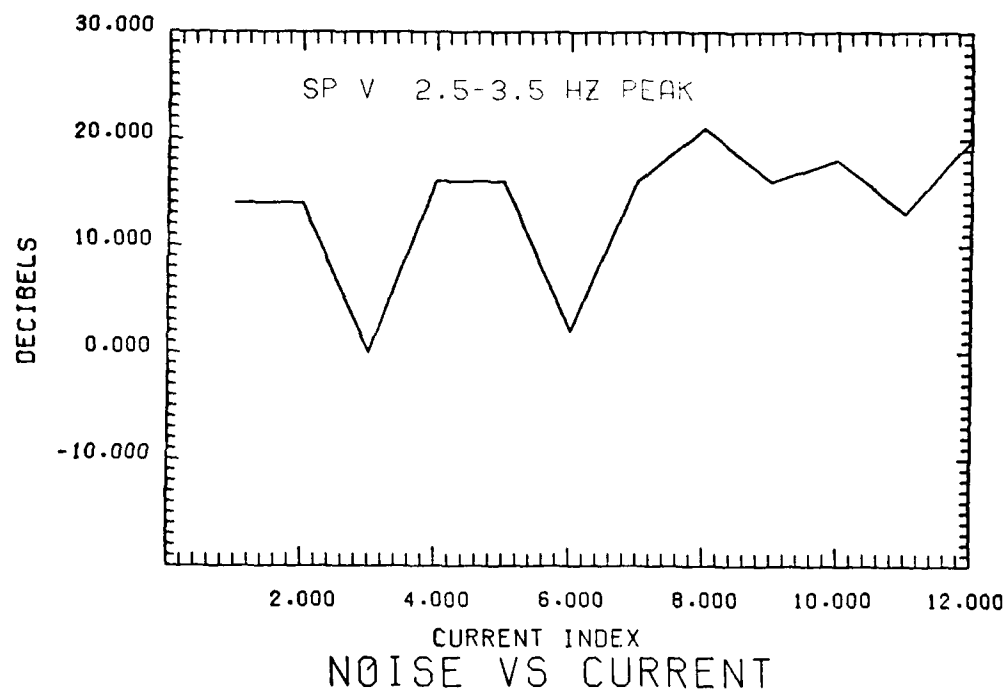


Fig. V-14. Plot of the amplitude of the 3-Hz noise peak on the Spike V versus current index. There does not appear to be a strong correlation between noise level at 3 Hz and current speed. The current index is the same as in Figure V-12.

It can be seen on Figure V-13 that the UCSBV has a noise peak at about 9 Hz that is not seen by the Spike V. The horizontal pull lift tests showed this instrument to have a strong resonance at this frequency and it is clear that this resonance is being induced by the noise. To evaluate whether this instrument was sensitive to the currents we plotted the amplitude of the 2- to 4-Hz and 9-Hz noise peaks versus current speed in Figure V-15. The lack of correlation suggests that the currents are not causing the noise.

We conclude that in this range of current speed (1 to 4 cm/sec) the currents are not the source of the noise. At this time we have no idea what is causing the noise.

Additional noise data are presented in Appendix D.

VI. CONCLUSIONS

On the basis of the preceding discussions we arrive at recommendations for the design criteria for ocean bottom seismic systems. Although none of these recommendations is absolutely necessary for obtaining high-fidelity seismic signals at any particular site, if the recommendations are followed, OBS systems can be built that will be able to obtain high-fidelity seismic signals anywhere.

The primary purpose of an OBS is to record the motion of the ground. If a record of this motion cannot be obtained with reasonable fidelity because of either (1) high noise, (2) poor coupling, (3) lack of dynamic range, (4) lack of storage capacity, or (5) lack of reliability, then the OBS has at least partially failed. This test addressed the first two of these problems. Indeed, if coupling and noise problems are serious, no amount of dynamic range or storage capability will help.

Several observations from the Lopez Experiment are important when considering modifications to present systems or design of new OBS's:

(1) The geophone standards produced generally consistent results and seemed to record true ground motion. A design goal might be to build an OBS similar to one of the standards--either plate-like, with neutral density in the sediment, or shoved into the sediment. None of the standards however, was built to record data internally, free-fall to the bottom, and return to the surface. Adding hydrodynamic stability during drop, buoyancy for return, and recording capability would change the basic features of these units unless the sensors were carefully located in the package or mechanically decoupled from the recording-retrieval unit. Indeed, the MITF and HIGB instruments, which showed good coupling characteristics, have characteristics similar to the plate standard. An OBS with characteristics similar to the neutral density or spike standards would not be suitable for hard-bottom applications, nor would emplacement and retrieval be a simple matter in soft sediment.

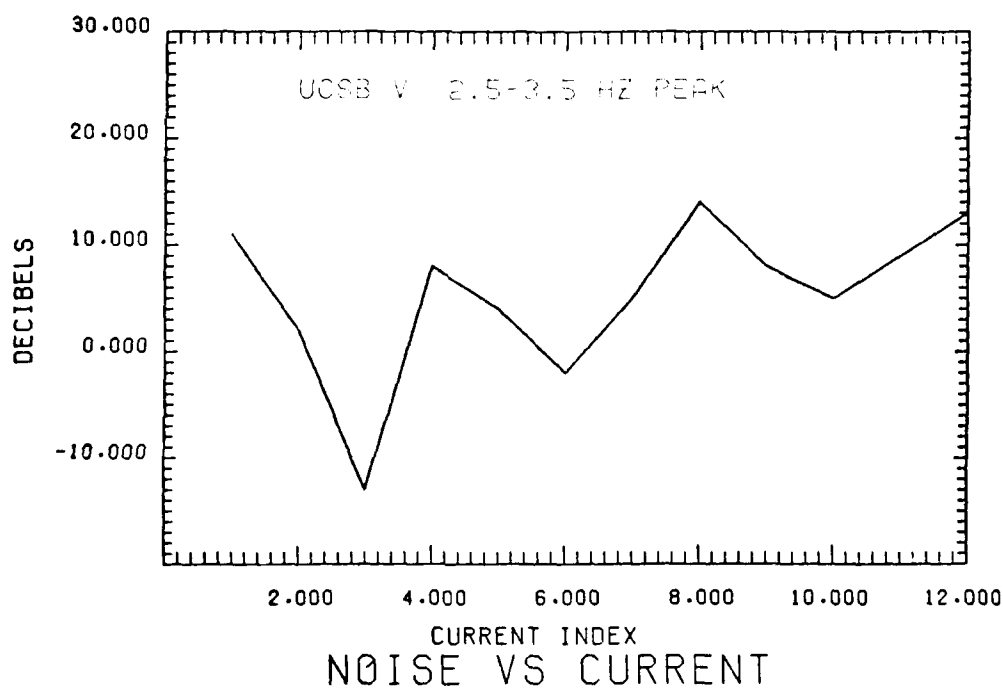
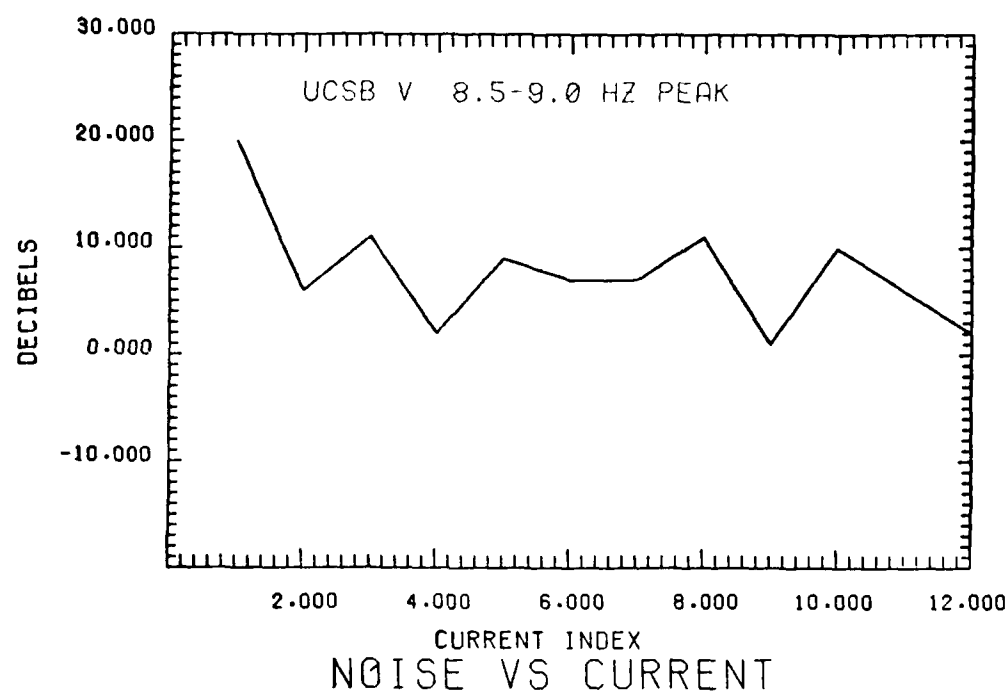


Fig. V-15. Plots of the amplitude of the 3-Hz and 9-Hz noise peaks versus current index for the UCSB V. There is not a strong correlation between current speed and noise levels. The current index is the same as in Figure V-12.

(2) Hydrophones yield records that are not distorted by coupling problems or complicated by low-velocity shear arrivals. However, the failure to record (near normally incident) shear arrivals can be a curse as well as a blessing in some applications. This is easily seen in Figure IV-9, where the hydrophone sees very little signal after the first arrivals. Although hydrophones may be adequate for most refraction work and are useful for earthquake studies, the loss of shear wave data in either application can be considered a serious shortcoming. Hydrophones should be considered a valuable sensor in OBS's, but not a replacement for geophones.

(3) Maximizing base dimensions relative to height of the package appears to reduce cross coupling caused by rocking. Placing geophones near the center of cross-coupling rotation should also lessen this effect, especially for the vertical component. Reducing the cross section in water would certainly also lessen possible problems with bottom currents. Although current-generated noise was not observed at Lopez, the highest currents observed during the experiment are often exceeded in the deep ocean (Kasahara et al., 1979). There is some published evidence for correlation of current-generated noise with OBS package configuration (Bradner et al., 1965 ; Kasahara et al., 1979 ; Kasahara et al., in press ; and Duennebier et al., 1980.) Intuitively one would expect a squat, low-profile instrument design to be preferable; this intuitive argument may extend even to the flotation and recording packages of the instruments with externally deployed sensor packages.

(4) First order theory, assuming a damped harmonic oscillator, suggests that increasing the surface area in contact with the sediment increases the coupling frequency and the damping. This effect forces the OBS motion to be closer to that of the sediment. In addition, more sediment and water are likely to be entrained with the OBS, thus causing a drop in the coupling coefficient, C , and improved response to frequencies above the coupling frequency. In general, the Lopez observations support this theory.

The incorporation of an in situ transient test device on existing OBS's appears feasible. In addition to providing a good check on overall system operation, it would give two of the three principal coupling parameters, f_c and Q_c , needed for calculating coupling response. The third, the coupling coefficient, C , can be estimated, as discussed in section IV.

(5) Adjusting the density of the package to be slightly greater than that of water also would decrease the value of C , decreasing the effects of coupling. This would make the instrument more sensitive to high frequencies and reduce the resonant amplification. Special care must be taken in this case to keep a low profile and good contact with the bottom to reduce cross coupling and current problems.

One problem not discussed in this report is horizontal-to-horizontal coupling. Unlike vertical-to-vertical coupling, it is much more

susceptible to torques and asymmetries in package configuration and emplacement. Asymmetry can cause considerable azimuthal variation in response to horizontal motion. The complexity of the horizontal coupling problem makes it difficult to understand, although following basic principles such as keeping asymmetries to a minimum and decreasing the cross section in the water should help considerably.

In the Lopez tests the amplitude responses of the spike and plate standard instruments were generally within 2 dB of each other and the waveforms were well duplicated. We judge from the similarity of the responses that these instruments were responding accurately to the motion of the upper few centimeters of the sediment layer. We believe that we now know enough about problems with noise and coupling to design an OBS system that will sense true ground motion with fidelity equal to that of the standards. We also know that in some places geophones will be particularly noisy because of short-wave length signals in the sediments. In these areas, particularly, the addition of a hydrophone to the OBS is highly desirable.

Knowing how to sense the motion is only one problem. Recording and retrieving the data deserve equal study and effort. Numerous technological options are available: analog or digital recording; acoustic or timed releases; spherical or cylindrical pressure cases; motor or explosive bolt releases and so forth. Unlike the problems with coupling and noise, we can anticipate that more and better solutions will become available for these problems as technology advances.

VII. FUTURE DEVELOPMENTS

The coupling and noise problems in existing instruments can be reduced significantly by modifications suggested by the results of this experiment. With such modifications these instruments will be adequate to continue fruitful research in marine seismology over the next few years. This research not only will result in significant progress in seismology, but also will provide additional valuable data on design parameters, particularly if collaborative field work continues in which the performance of instruments of different design can be compared.

The above notwithstanding, new instrumentation should be designed and tested. Ocean bottom seismology is far too new a field to permit stagnation in the development of instrumentation.

Three systems appear desirable for the foreseeable future: (1) a simple, inexpensive (hydrophone ?) system that will allow use of a large number of units for dense arrays; (2) a somewhat more expensive system with a hydrophone and three geophones to augment arrays of the simpler systems, to be used in detailed micro-earthquake studies, and (3) a relatively expensive system capable of handling a variety of sensor systems including hydrophone arrays, geophones, and long-period sensors.

The simple arrays could be easily deployed and retrieved and would be cheap enough so that large number of units could be used in any

experiment. These units would be of primary value in refraction experiments and could be used to provide dense coverage in micro-earthquake studies.

The four component units would supply sediment and shear velocity information for refraction lines and shear wave arrival times, particle motion, and surface wave information in earthquake studies. These units would require more care in emplacement and recovery and would be more costly. The "expensive system" would be the experimental unit used in special studies and for testing of new ideas.

Certain ocean bottom seismological research is also expected to require instruments capable of very long deployment times. Development in this area also should be supported.

ACKNOWLEDGMENTS

We thank all of the support personnel involved in LOPEZ for their help in making the experiment a success. The University of Washington was a great help with finding a location for the experiment and with the logistics of the experiment itself. We thank the Quinney family for the use of their house on Lopez Island as a base of operations during the experiment. Rita Pujalec of HIG edited and prepared the final report for publication. We thank ONR for recognizing the need for this experiment and for funding it, the subsequent meetings, and this report.

REFERENCES

- Bradner, H., J. Dodds, and R. Foulks, 1965. Coherence measurements with time sampling ocean bottom seismometers. *Proc. IEEE*, v. 53, no. 13, p. 1906-1908.
- Duennebier, F. K., G. Blackinton, and G. H. Sutton, 1980. Current-generated noise recorded on ocean bottom seismometers. This report, Appendix J.
- Kasahara, J., S. Nagumo, S. Koresawa, and T. Daikubara, 1980. Experimental results of vortex generation around ocean bottom seismometers due to bottom currents. *Bull. Earthq. Res. Inst.* (In press.)
- Kasahara, J., S. Koresawa, S. Nagumo, T. Daikuhara, T. Hara, and S. Ando, 1979. Pop-up OBS (ERI type P-79). *Bull. Earthq. Res. Inst.*, v. 54, p. 515-530.
- Sutton, G. H., F. K. Duennebier, and B. Iwatake, 1980. Coupling of ocean bottom seismometers to soft bottoms. This report, Appendix E.
- Tuthill, J. D., 1980. The propagation of Stoneley waves in unconsolidated sediments. Masters thesis, University of Washington, Seattle.
- Tuthill, J. D., B. T. R. Lewis, and J. D. Garmany, 1980. Stoneley waves, Lopez Island noise, and deep sea noise from 1 to 5 Hz. This report, Appendix G.

Appendix A

CONTRIBUTORS TO THE LOPEZ ISLAND
OCEAN BOTTOM SEISMOMETER INTERCOMPARISON EXPERIMENT

The following individuals and organizations participated in the
Lopez Island OBS Intercomparison Experiment:

A. Burkhalter and R. L. Moe
(Digital Data Acquisition System)
Shipboard Computer Group
SIO/UCSD
La Jolla, California 92093

BIO D. Heffler
Bedford Institute of Oceanography
Box 1006
Dartmouth, Nova Scotia
Canada

HIG E. Saade and G. H. Sutton
Hawaii Institute of Geophysics
University of Hawaii
Honolulu, Hawaii 96822

LDGO R. G. Bookebinder, W. McDonald, and P. Pomeroy
Lamont-Doherty Geological Observatory
Palisades, New York 10964

MIT P. J. Mataboni and S. Solomon
Massachusetts Institute of Technology
Building 37-484
Cambridge, Massachusetts 02139

OSU S. H. Johnson and R. McAlister
School of Oceanography
Oregon State University
Corvallis, Oregon 97331

SIO J. Orcutt and D. F. Willoughby
Geological Research Division
Scripps Institution of Oceanography
La Jolla, California 92093

UCSB W. Prothero and S. Zelikovitz
Department of Geological Sciences
University of California, Santa Barbara
Santa Barbara, California 93106

USGS B. Ambuter
U. S. Geological Survey
Woods Hole, Massachusetts 02543

UTG	A. K. Ibrahim and P. Roper Marine Science Institute University of Texas 700 The Strand Galveston, Texas 77550
UW	L. Bond and B. Lewis Department of Oceanography WB-10 University of Washington Seattle, Washington 98195
WHOI	R. E. Davis, J. Dushenes, J. Ewing, and D. Koelch Woods Hole Oceanographic Institution Woods Hole, Massachusetts 02543

Appendix B

CATALOG OF LOPEZ ISLAND
EXPERIMENT DIGITIZED EVENTS

CATALOG OF LOPEZ ISLAND EXPERIMENT DIGITIZED EVENTS

On the following pages is a catalog of the seven digital tapes produced by the SIO Geospace recording system. Each component of each instrument is identified by a code number described on the next page. Catalog entries are listed according to Geospace record number. The code numbers for all components recorded during an event are listed next to each Geospace record number.

Record number 500 was not recorded digitally and was hand-digitized from a paper recording. Records 146 to 148 were not recorded correctly. Data for these events were re-digitized from the HIGS analog tapes recorded inside the OBS. These records are not in this index but are found elsewhere in the report (Appendix E, Fig. E-5).

LIST OF LOPEZ COMPONENTS

Code Number	SIO Digital Log Book	Present Notation	Description
1	SP 1	SP V	Spike standard vertical
2	SP 2	SP N	Spike standard horizontal
3	SP 3	SP E	Spike standard horizontal
4	ND 1	ND V	Neutral density standard vertical
5	ND 2	ND N	Neutral density standard horizontal
6	ND 3	ND E	Neutral density standard horizontal
7	PL 1	PL V	Plate standard vertical
8	PL 2	PL N	Plate standard horizontal
9	PL 3	PL E	Plate standard horizontal
10	UW 1	UW V	Univ. of Washington vertical
11	UW 2	UW H	Univ. of Washington horizontal
12	UWFP	UWF V	Univ. of Washington Flower Pot vertical
13	SIO 1	SIO V	Scripps Institute vertical
14	BIO 1	BIO V	Bedford Institute vertical
15	BIO 2	BIO H	Bedford Institute horizontal
16	BIO 3	BIO P	Bedford Institute hydrophone
17	WHOI	WHOI P	Woods Hole hydrophone
18	OSU 1	OSU V	Oregon State vertical
19	OSU 2	OSU H	Oregon State horizontal
20	OSU 3	OSU P	Oregon State hydrophone
21	MITV	MITE V	M.I.T. vertical
22	MITH 1	MITE H	M.I.T. horizontal
23	MITH 2	MITN H	M.I.T. horizontal

Code Number	SIO Digital Log Book	Present Notation	Description
24	HIGBV	HIGB V	H.I.G. burp out vertical
25	HIGBH	HIGB H	H.I.G. burp out horizontal
26	HIGBP	HIGB P	H.I.G. hydrophone
27	UTG 1	UTG V	Univ. of Texas vertical
28	UCSB 3	UCSB V	Univ. of California vertical
29	UCSB 1/2	UCSB H	Univ. of California horizontal
20	LDGO 1	LDG V	Lamont-Dogherty vertical
31	LDGO 2	LDG P	Lamont-Dogherty hydrophone
32	HIGSV	HIGS V	H.I.G. standard vertical
33	HIGSH	HIGS H	H.I.G. standard horizontal
34	HIGSP	HIGS P	H.I.G. standard hydrophone
35	UTGS	USGS V	U.S. Geological Survey vertical
36		LAND	Land base station vertical

LOPEZ DIGITIZED EVENTS

RECORD	DESCRIPTION	CHANNELS																								TIME	JUNE DAY	TAPE REEL
		1	2	3	4	5	6	7	8	9	10	11	12	13	14	15	16	17	18	19	20	22	23	24				
3	ND V XIENT	1	2	3		7	8	9		4	5	6														1638	18	1
4	ND CAL	1	2	3		7	8	9		4	5	6														1646	18	1
5	ND CAL	1	2	3		7	8	9		4	5	6														1653	18	1
7	SP V XIENT	1	2	3		7	8	9		4	5	6														1720	18	1
9	SP V XIENT	1	2	3		7	8	9		4	5	6														1728	18	1
10	PL V XIENT	1	2	3		7	8	9		4	5	6														1744	18	1
11	PL N XIENT	1	2	3		7	8	9		4	5	6														1816	18	1
12	PL E XIENT	1	2	3		7	8	9		4	5	6														1847	18	1
6	SP V XIENT	1	2	3		7	8	9		4	5	6														18	1	
8	SP V XIENT	1	2	3		7	8	9		4	5	6														18	1	
13	PL V XIENT	1	2	3		7	8	9		4	5	6														18	1	
48	UV V XIENT	1	2	3		7	8	9		4	5	6	10	11												1619	19	2
49	UV V XIENT	1	2	3		7	8	9		4	5	6	10	11												1635	19	2
50	UV N XIENT	1	2	3		7	8	9		4	5	6	10	11												1643	19	2
52	CAL TRACK 3																									19	2	
54	SIO TURN ON	1	2	3		7	8	9		4	5	6					13									0900	20	2
61	BIO V XIENT	17	1	2	3		7	8	9	4	5	6	10	11	13											1645	20	2

RECORD	DESCRIPTION	CHANNELS																								JUNE DAY	TAPE REEL
		1	2	3	4	5	6	7	8	9	10	11	12	13	14	15	16	17	18	19	20	22	23	24	TIME		
62	CAL TRACK 4																								20	1	
63	BIO E XIENT	17	1	2	3		7	8	9	4	5	6		10	11	13		14	15	16				1658	20	1	
64	BIO S XIENT	17	1	2	3		7	8	9	4	5	6		10	11	13		14	15	16				1707	20	1	
65	SIO V XIENT	17	1	2	3		7	8	9	4	5	6		10	11	13		14	15	16				1804	20	1	
66	SIO V XIENT	17	1	2	3		7	8	9	4	5	6		10	11	13		14	15	16				1809	20	1	
67	SIO E XIENT	17	1	2	3		7	8	9	4	5	6		10	11	13		14	15	16				1821	20	1	
68	CAL TRACK 4																							1824	20	1	
70	NOISE	17	1	2	3		7	8	9	4	5	6		10	11	13		14	15	16				0942	21	3	
71	CAL TRACK 5																							0945	21	1	
73	NOISE	17	1	2	3		7	8	9	4	5	6		10	11	13		14	15	16	29	29	28	0959	21	1	
75	SIO TRANSDUCER	17	1	2	3		7	8	9	4	5	6		10	11	13		14	15	16	29	29	28	1035	21	1	
76	SIO TRANSDUCER	17	1	2	3		7	8	9	4	5	6		10	11	13		14	15	16	29	29	28	1039	21	1	
77	SIO UCSB TRANS	17	1	2	3		7	8	9	4	5	6		10	11	13		14	15	16	29	29	28	1043	21	1	
80	LDC N XIENT	17	1	2	3	30	7	8	9	31	4	5	6		10	11	13		14	15	16	29	29	28	1532	21	1
86	CAL TRACK 5																							1700	21	3	
88	NOISE		1	18	19	30	7	8	9	31	4		20	10	11	13		14	15	16	29	29	28	0854	22	3	
89	CAL TRACK 6																							0859	22	3	
99	UTC V XIENT		1	18	19	30	7	24	25	27	4	21	22	20	10	11	13	23	14	15	16	29	29	28	1243	22	3

RECORD	DESCRIPTION	CHANNELS												TIME	JUNE DAY	TAPE REEL										
		1	2	3	4	5	6	7	8	9	10	11	12				13	14	15	16	17	18	19	20	22	23
100	UTC V XIENT	1	18	19	30	7	24	25	27	4	21	22	20	10	11	13	23	14	15	16	29	29	28	1247	22	3
101	UTC V XIENT	1	18	19	30	7	24	25	27	4	21	22	20	10	11	13	23	14	15	16	29	29	28	1256	22	3
102	UTC V XIENT	1	18	19	30	7	24	25	27	4	21	22	20	10	11	13	23	14	15	16	29	29	28	1306	22	3
103	UTC S XIENT	1	18	19	30	7	24	25	27	4	21	22	20	10	11	13	23	14	15	16	29	29	28	1313	22	3
104	UTC E XIENT	1	18	19	30	7	24	25	27	4	21	22	20	10	11	13	23	14	15	16	29	29	28	1322	22	3
105	UTC E XIENT	1	18	19	30	7	24	25	27	4	21	22	20	10	11	13	23	14	15	16	29	29	28	1327	22	3
107	HICB V XIENT	1	18	19	30	7	24	25	27	4	21	22	20	10	11	13	23	14	15	16	29	29	28	1401	22	3
108	HICB V XIENT	1	18	19	30	7	24	25	27	4	21	22	20	10	11	13	23	14	15	16	29	29	28	1410	22	2
109	HICB E XIENT	1	18	19	30	7	24	25	27	4	21	22	20	10	11	13	23	14	15	16	29	29	28	1418	22	2
110	HICB N XIENT	1	18	19	30	7	24	25	27	4	21	22	20	10	11	13	23	14	15	16	29	29	28	1425	22	2
111	HICB N XIENT	1	18	19	30	7	24	25	27	4	21	22	20	10	11	13	23	14	15	16	29	29	28	1431	22	2
112	UV V XIENT	1	18	19	30	7	24	25	27	4	21	22	20	10	11	13	23	14	15	16	29	29	28	1634	22	2
113	UV W XIENT	1	18	19	30	7	24	25	27	4	21	22	20	10	11	13	23	14	15	16	29	29	28	1643	22	2
114	UV W XIENT	1	18	19	30	7	24	25	27	4	21	22	20	10	11	13	23	14	15	16	29	29	28	1650	22	2
115	UV W XIENT	1	18	19	30	7	24	25	27	4	21	22	20	10	11	13	23	14	15	16	29	29	28	1657	22	2
116	UV S XIENT	1	18	19	30	7	24	25	27	4	21	22	20	10	11	13	23	14	15	16	29	29	28	1704	22	2
119	SIO V XIENT	1	18	19	30	7	24	25	27	4	21	22	20	10	11	13	23	14	15	16	29	29	28	1723	22	2
120	SIO E XIENT	1	18	19	30	7	24	25	27	4	21	22	20	10	11	13	23	14	15	16	29	29	28	1733	22	2

RECORD	DESCRIPTION	CHANNELS																								TIME	JUNE DAY	TAPE REEL
		1	2	3	4	5	6	7	8	9	10	11	12	13	14	15	16	17	18	19	20	22	23	24				
121	SIO S XIENT	1	18	19	30	7	24	25	27	4	21	22	20	10	11	13	23	14	15	16	29	29	28	1741	22	3		
122	SIO S XIENT	1	18	19	30	7	24	25	27	4	21	22	20	10	11	13	23	14	15	16	29	29	28	1747	22	3		
123	UCSB V XIENT	1	18	19	30	7	24	25	27	4	21	22	20	10	11	13	23	14	15	16	29	29	28	1006	22	3		
124	UCSB S XIENT	1	18	19	30	7	24	25	27	4	21	22	20	19	11	13	23	14	15	16	29	29	28	1017	22	3		
125	UCSB S XIENT	17	1	18	19	30	7	24	25	27	4	21	22	20	10	11	13	23	14	15	16	29	29	28	1046	22	3	
126	CAL TRACK 7																							1049	22	3		
141	OSU V XIENT	17	1	18	19	30	7	24	25	27	4	21	22	20	10	12	13	23	14	33	34	29	29	28	1325	23	4	
142	OSU V XIENT	17	1	18	19	30	7	24	25	27	4	21	22	20	10	12	13	23	14	33	34	29	29	28	1331	23	4	
143	OSU V XIENT	17	1	18	19	30	7	24	25	27	4	21	22	20	10	12	13	23	14	33	34	29	29	28	1340	23	4	
144	OSU E XIENT	17	1	18	19	30	7	24	25	27	4	21	22	20	10	12	13	23	14	33	34	29	29	28	1350	23	4	
154	CAL TRACK 3																							0931	24	2		
155	AC SHOT 1	1	2	20	4	5	18	26	7	24	32	17	31	13	14	21	34	28	16	30	10	27	3	6931	24	2		
156	AC SHOT 2	1	2	20	4	5	18	26	7	24	32	17	31	13	14	21	34	28	16	30	10	27	3	1000	24	2		
158	AC SHOT 3	1	2	20	4	5	18	26	7	24	32	17	31	13	14	21	34	28	16	30	10	27	12	1102	24	2		
159	AC SHOT 5	1	2	20	4	5	18	26	7	24	32	17	31	13	14	21	34	28	16	30	10	27	12	1136	24	2		
160	AC SHOT 9	1	2	20	4	5	18	26	7	24	32	17	31	13	14	21	34	28	16	30	10	27	12	1140	24	2		
161	AC SHOT 13	1	2	20	4	5	18	26	7	24	32	17	31	13	14	21	34	28	16	30	10	27	12	1144	24	2		
162	AC SHOT 16	1	2	20	4	5	18	26	7	24	32	17	31	13	14	21	34	28	16	30	10	27	12	1147	24	2		

RECORD	DESCRIPTION	CHANNELS																								JUNE DAY	TIME	TAPE REEL
		1	2	3	4	5	6	7	8	9	10	11	12	13	14	15	16	17	18	19	20	22	23	24				
163	AC SHOT 21	1	2	20	4	5	18	26	7	24	32	17	31	13	14	21	34	28	16	30	10	27	12			1152	24	2
164	AC SHOT 25	1	2	20	4	5	18	26	7	24	32	17	31	13	14	21	34	28	16	30	10	27	12			1156	24	2
165	AC SHOT 32	1	2	20	4	5	18	26	7	24	32	17	31	13	14	21	34	28	16	30	10	27	12			1203	24	2
166	AC SHOT 37	1	2	20	4	5	18	26	7	24	32	17	31	13	14	21	34	28	16	30	10	27	12			1208	24	2
167	AC SHOT 43	1	2	20	4	5	18	26	7	24	32	17	31	13	14	21	34	28	16	30	10	27	12			1214	24	2
168	CAL TRACK 3																									1234	24	2
169	CAP 2	1	2	20	4	5	18	26	7	24	32	17	31	13	14	21	34	28	16	30	10	27	12			1452	24	2
191	AC SHOT 112	1	2	3	10	11	17	7	8	9	14	15	18	19	4	5	6	21	22	25	24	28	29	29		1934	24	3
192	AC SHOT 114	1	2	3	10	11	17	7	8	9	14	15	18	19	4	5	6	21	22	25	24	28	29	29		1938	24	3
194	AC SHOT 117	1	2	3	10	11	17	7	8	9	14	15	18	19	4	5	6	21	22	25	24	28	29	29		1944	24	3
195	CAL TRACK 4																									1946	24	4
201	NOISE	1	2	3	10	11	17	7	8	9	14	15	18	19	4	5	6	21	22	25	24	28	29	29		0602	25	3
202	CAL TRACK 5																									0637	25	3
203	NOISE	1	2	3	10	11	17	7	8	9	14	15	18	19	4	5	6	21	22	25	24	28	29	29		0700	25	3
204	NOISE	1	2	3	10	11	17	7	8	9	14	15	18	19	4	5	6	21	22	25	24	28	29	29		0800	25	7
205	NOISE	1	2	3	10	11	17	7	8	9	14	15	18	19	4	5	6	21	22	25	24	28	29	29		0900	25	4
206	NOISE	1	2	3	10	11	17	7	8	9	14	15	18	19	4	5	6	21	22	25	24	28	29	29		1000	25	4
207	AC 119-126	1	2	3	10	11	17	7	8	9	14	15	18	19	4	5	6	21	22	25	24	28	29	29		1017	25	4

RECORD	DESCRIPTION	CHANNELS																								JUNE DAY	TAPE REEL
		1	2	3	4	5	6	7	8	9	10	11	12	13	14	15	16	17	18	19	20	22	23	24	TIME		
200	AC 127-133	1	2	3	10	11	17	7	8	9	14	15	18	19	4	5	6	21	22	25	24	28	29	29	1037	25	4
210	NOISE	1	2	3	10	11	17	7	8	9	14	15	18	19	4	5	6	21	22	25	24	28	29	29	1102	25	3
211	NOISE	1	2	3	10	11	17	7	8	9	14	15	18	19	4	5	6	21	22	25	24	28	29	29	1200	25	3
212	NOISE	1	2	3	10	11	17	7	8	9	14	15	18	19	4	5	6	21	22	25	24	28	29	29	1300	25	3
213	NOISE	1	35	27	10	13	17	7	8	9	14	32	18	12	4	5	6	21	34	25	24	28	30	31	1500	25	3
214	NOISE	1	35	27	10	13	17	7	8	9	14	32	18	12	4	5	6	21	34	25	24	28	30	31	1600	25	3
215	AC 150-159	1	35	27	10	13	17	7	8	9	14	32	18	12	4	5	6	21	34	25	24	28	30	31	1615	25	5
216	AC 160-167	1	35	27	10	13	17	7	8	9	14	32	18	12	4	5	6	21	34	25	24	28	30	31	1641	25	6
217	NOISE	1	35	27	10	13	17	7	8	9	14	32	18	12	4	5	6	21	34	25	24	28	30	31	1700	25	6
218	CAL TRACK 2																								1702	25	6
220	AC 180-185	1	35	27	10	13	17	7	8	9	14	32	18	12	4	5	6	21	34	25	24	28	30	31	1737	25	7
221	CAL																								1744	25	7
222	NOISE	1	35	27	10	13	17	7	8	9	14	32	18	12	4	5	6	21	34	25	24	28	30	31	1800	25	7
226	UWF V XIENT	1	35	27	10	13	17	7	8	9	14	32	18	12	4	5	6	21	34	25	24	28	30	31	0813	26	7
227	UWF W XIENT	1	35	27	10	13	17	7	8	9	14	32	18	12	4	5	6	21	34	25	24	28	30	31	0822	26	7
228	UWF N XIENT	1	35	27	10	13	17	7	8	9	14	32	18	12	4	5	6	21	34	25	24	28	30	31	0822	26	7
229	MUTH V XIENT	1	35	27	10	13	17	21	22	23	14	32	18	12	4	5	6		34	25	24	28	30	31	0936	26	7
230	MUTH W XIENT	1	35	27	10	13	17	21	22	23	14	32	18	12	4	5	6		34	25	24	28	30	31	0951	26	7

RECORD	DESCRIPTION	CHANNELS																								TIME	JUNE DAY	TAPE REEL
		1	2	3	4	5	6	7	8	9	10	11	12	13	14	15	16	17	18	19	20	22	23	24				
231	CAL TRACK 4																								0934	26	7	
233	MITE V XIENT	1	35	27	10	13	17	21	22	23	14	32	18	12	4	5	6		34	25	24	28	30	31		1009	26	7
234	MITE H XIENT	1	35	27	10	13	17	21	22	23	14	32	18	12	4	5	6		34	25	24	28	30	31		1021	26	7
235	UTC V XIENT	1	35	27	10	13	17	21	22	23	14	32	18	12	4	5	6		34	25	24	28	30	31		1045	26	5
236	UTC E XIENT	1	35	27	10	13	17	21	22	23	14	32	18	12	4	5	6		34	25	24	28	30	31		1037	26	5
238	CROSS TALK																								1242	26	5	
239	CAP	1	35	27	10	13	20	21	22	36	14	32	18	12	2	3	19	29	15	11	24	28	30	33		1419	26	6
240	QUARRY BLAST?	1	35	27	10	13	20	21	22	36	14	32	18	12	2	3	19	29	15	11	24	28	30	33		1442	26	6
241	CAP	1	35	27	10	13	20	21	22	36	14	32	18	12	2	3	19	29	15	11	24	28	30	33		1638	26	6
242	CAP	1	35	27	10	13	20	21	22	36	14	32	18	12	2	3	19	29	15	11	24	28	30	33		1554	26	6
243	CAP	1	35	27	10	13	20	21	22	36	14	32	18	12	2	3	19	29	15	11	24	28	30	33		1702	26	6
244	CAL TRACK 5	1	35	27	10	13	20	21	22	36	14	32	18	12	2	3	19	29	15	11	24	26	30	33		1739	26	6
248	USCB NE XIENT	1	35	27	10	13	20	21	22	36	14	32	18	12	29	23	19	29	15	11	17	28	30	33		1219	27	4
249	CROSS COUPLING	1	35	27	10	13	20	21	22	36	14	32	18	12	29	23	19	29	15	11	17	28	30	33		1235	27	4
250	USCS V XIENT	1	35	27	10	13	20	21	22	36	14	32	18	12	29	23	19	29	15	11	17	28	30	33		1326	27	4
251	USCS S XIENT	1	35	27	10	13	20	21	22	36	14	32	18	12	29	23	19	29	15	11	17	28	30	33		1337	27	4
252	USCS S XIENT	1	35	27	10	13	20	21	22	36	14	32	18	12	29	23	19	29	15	11	17	28	30	33		1344	27	4
253	USCS V XIENT	1	35	27	10	13	20	21	22	37	14	32	18	12	29	23	19	29	15	11	17	28	30	33		1353	27	4

RECORD	DESCRIPTION	CHANNELS																											JUNE DAY	TIME	TAPE REEL
		1	2	3	4	5	6	7	8	9	10	11	12	13	14	15	16	17	18	19	20	22	23	24							
254	USGS V XIENT	1	35	27	10	13	20	21	22	36	14	32	18	12	29	23	19	29	15	11	17	28	30	33	1405	27	5				
255	AC 186-195	1	35	27	10	13	20	21	22	36	14	32	18	12	29	23	19	29	15	11	17	28	30	33	1429	27	5				
256	AC 196-202	1	35	27	10	13	20	21	22	36	14	32	18	12	29	23	19	29	15	11	17	28	30	33	1452	27	7				
257	CAL TRACK 2																								1507	27	7				
260	CAL TRACK 3																								1237	28	5				
261	LAND TEST	30	10	27																					1310	28	5				
262	LAND TEST	30	10	27																					1310	28	5				
263	LAND TEST	30	10	27																					1310	28	5				
264	LAND TEST	30	10	27																					1310	28	5				
265	CAL TRACK 3																								1328	28	5				

Appendix C

SELECTED DIGITIZED EVENTS RECORDED
DURING THE LOPEZ ISLAND EXPERIMENT

SELECTED DIGITIZED EVENTS RECORDED DURING THE LOPEZ ISLAND EXPERIMENT

This appendix contains 111 records of signals recorded on ocean bottom seismometers at Lopez Island. Each recording was processed identically within the bounds discussed below. Records are presented four per page with time domain recordings on the left and frequency domain on the right. Each time domain recording is 1024 samples long; the horizontal line under each recording is 2 sec (500 samples) long. The vertical lines under each record show the section of the recording that was transformed into the frequency domain (power spectrum) shown on the right. In each case, the section to be transformed was convolved with a 10% cosine taper window and placed in the middle of a 512-point window after decimation by a factor of 2. No corrections are made for possible aliasing. The resulting 512-point time series was then fourier transformed and the "periodogram" was computed to obtain an estimate of the power spectrum. In addition to the signal, a section of noise (the same length as the signal) was transformed and plotted (lighter line). This makes it possible to distinguish energy generated by signal from noise. The vertical scale for each spectrum is dB referenced to 1 digital unit. The horizontal scale is in Hertz. Under each spectrum is the information necessary to identify each event. The first two to four letters are the instrument identifier used throughout this report followed by the component designation (V, H, or P, for vertical geophone, horizontal geophone, or pressure). Then given are the type of source, Geospace record number, and channel number from Appendix B.

INDEX TO APPENDIX C

DATA SAMPLES

PAGE	SENSOR	RECORD-CHANNEL	TEST
1	ND V	3-10	Vertical pull on vertical sensor
	PL V	10-6	
	SP V	7-2	
	BIO V	61-18	
2	HIGB V	108-7	Vertical pull on vertical sensor
	HIGS V	146-X4*	
	LDGO V	500-2**	
	MITE V	233-7	
3	OSU V	141-3	Vertical pull on vertical sensor
	SIO V	66-16	
	UCSB V	123-24	
	USGS V	254-2	
4	UTG V	102-9	Vertical pull on vertical sensor
	UW V	49-14	
	UWF V	226-13	
5	PL V	12-6	Horizontal pull on vertical sensor
	BIO V	64-18	
	BIO V	63-18	
	HIGS V	110-7	

* Records 146-148 were digitized from analog tapes. The channel refers to the OBS channel.

** Record 500 was hand digitized from paper recordings.

AD-A094 355

HAWAII INST OF GEOPHYSICS HONOLULU

F/6 8/11

LOPEZ ISLAND OCEAN BOTTOM SEISMOMETER INTERCOMPARISON EXPERIMENT--ETC(U)

OCT 80 G H SUTTON, B T LEWIS, J EWING

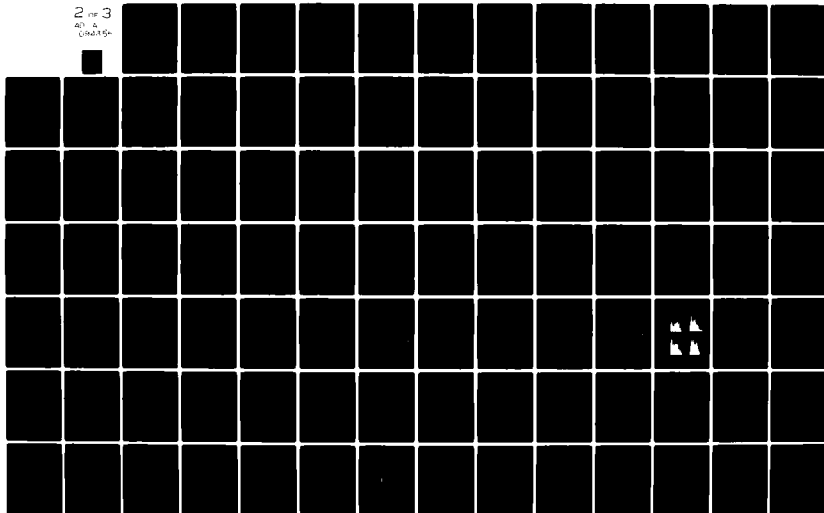
N00014-75-C-0209

HIG-80-4

NL

UNCLASSIFIED

2 of 3
AD-A
00015-



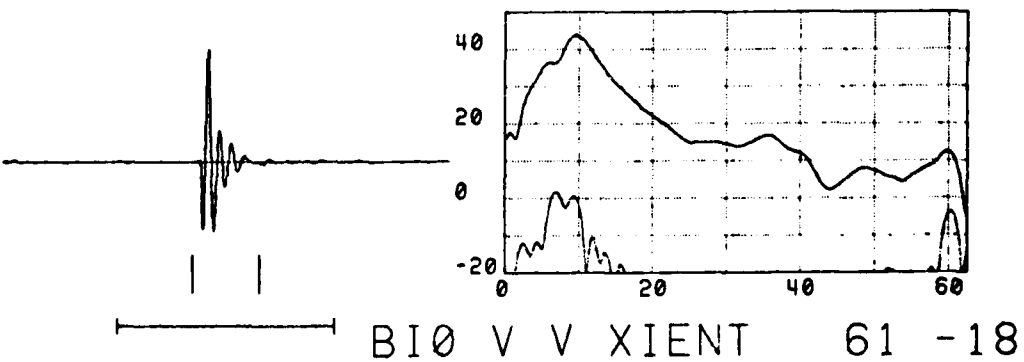
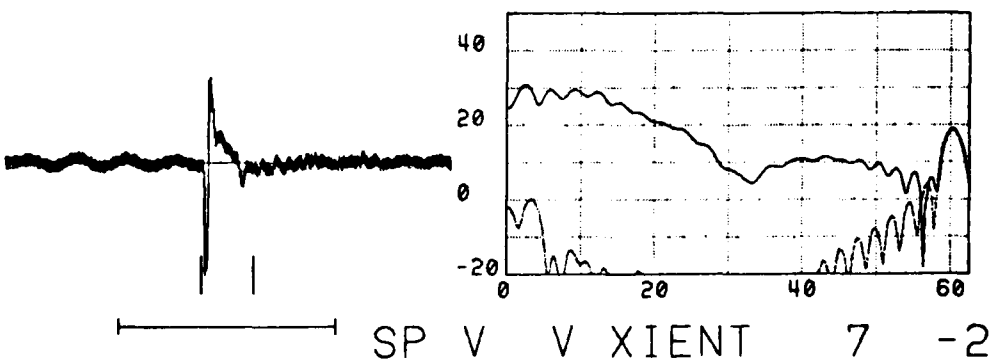
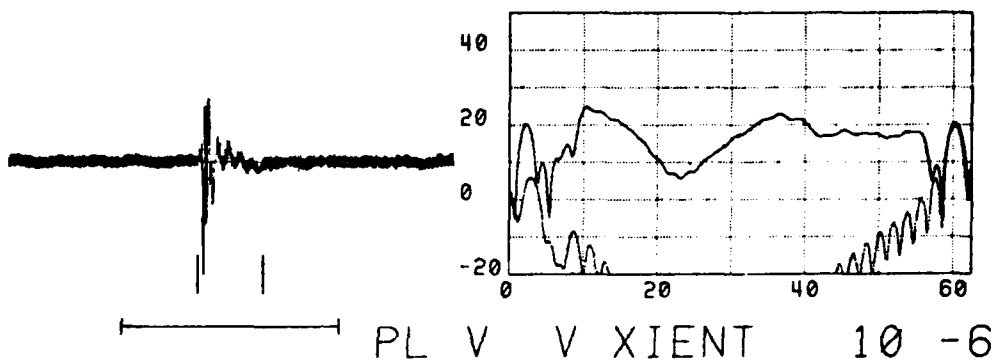
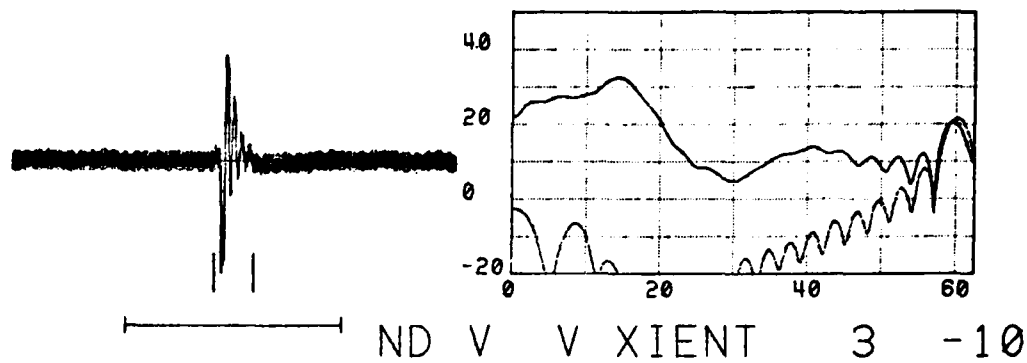
PAGE	SENSOR	RECORD-CHANNEL	TEST
6	HIGB V	111-7	Horizontal pull on vertical sensor
	HIGS V	147-X4	
	HIGS V	148-X4	
	LDG V	80-5	
7	LDG V	501-2	Horizontal pull on vertical sensor
	LDG V	501-2	
	MITE V	234-7	
	SIO V	67-16	
8	SIO V	120-16	Horizontal pull on vertical sensor
	UCSB V	248-22	
	UCSB V	124-24	
	UCSB V	125-24	
9	USGS V	252-2	Horizontal pull on vertical sensor
	USGS V	253-2	
	UTG V	236-3	
	UTG V	105-9	
10	UW V	50-14	Horizontal pull on vertical sensor
	UW V	115-14	
	UWF V	228-13	
	UWF V	227-13	
11	PL N	11-7	Horizontal pull on horizontal sensor
	PL E	12-8	
	BIO H	64-19	
	BIO H	63-19	

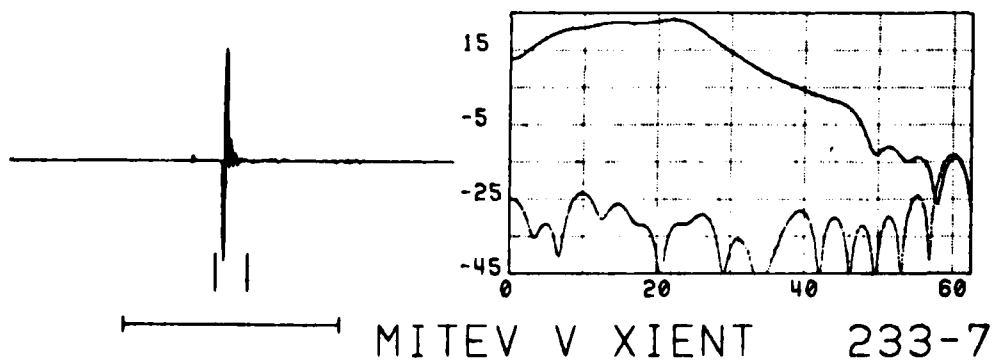
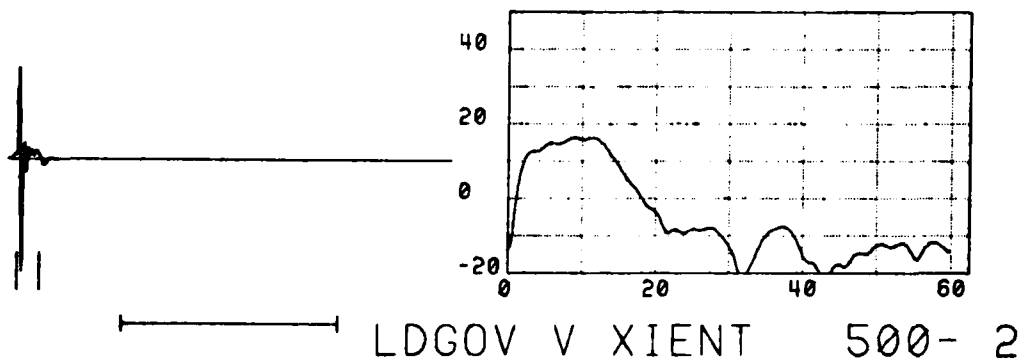
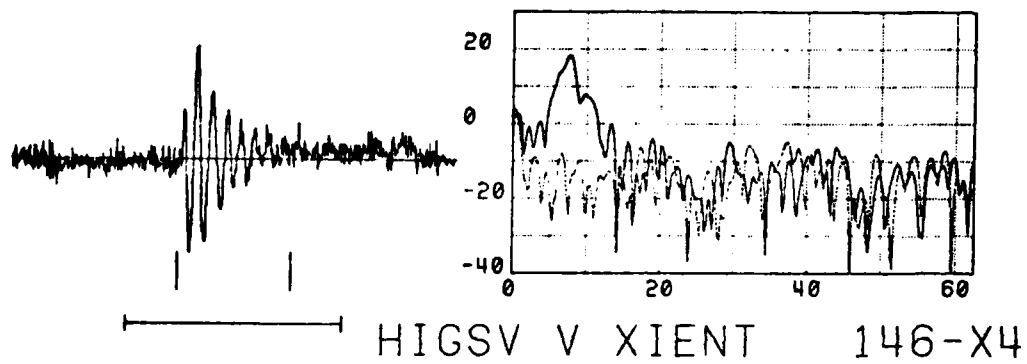
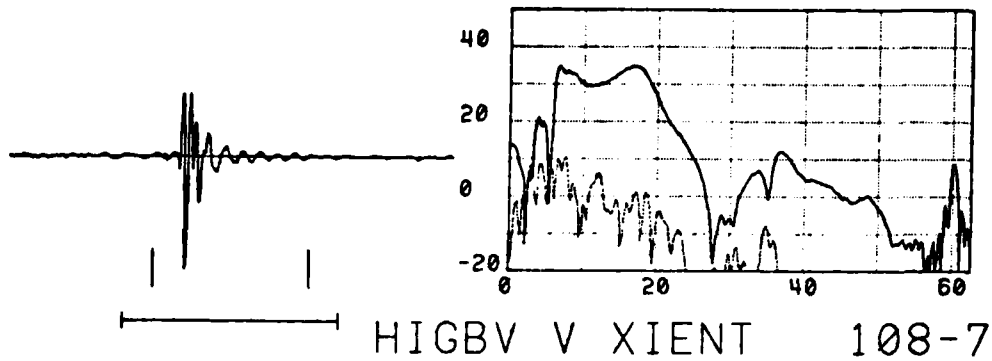
PAGE	SENSOR	RECORD-CHANNEL	TEST
18	LDG V CAP	239-23	Lopez seismic on vertical sensor
	LDG V CAP	242-23	
	MITE V AG 182	220-17	
	MITE V CAP	239-7	
19	MITE V CAP	242-7	Lopez seismic on vertical sensor
	OSU V AG 182	220-12	
	OSU V CAP	239-12	
	OSU V CAP	242-12	
20	SIO V AG 182	220-5	Lopez seismic on vertical sensor
	SIO V CAP	239-5	
	SIO V CAP	242-5	
	UCSB V AG 182	220-22	
21	UCSB V CAP	239-22	Lopez seismic on vertical sensor
	UCSB V CAP	242-22	
	USGS V AG 182	220-2	
	USGS V CAP	239-2	
22	USGS V CAP	242-2	Lopez seismic on vertical sensor
	UTG V AG 182	220-3	
	UTG V CAP	239-3	
	UTG V CAP	242-3	
23	UW V AG 182	220-4	Lopez seismic on vertical sensor
	UW V CAP	239-4	
	UW V CAP	242-4	
	UWF V AG 182	220-13	

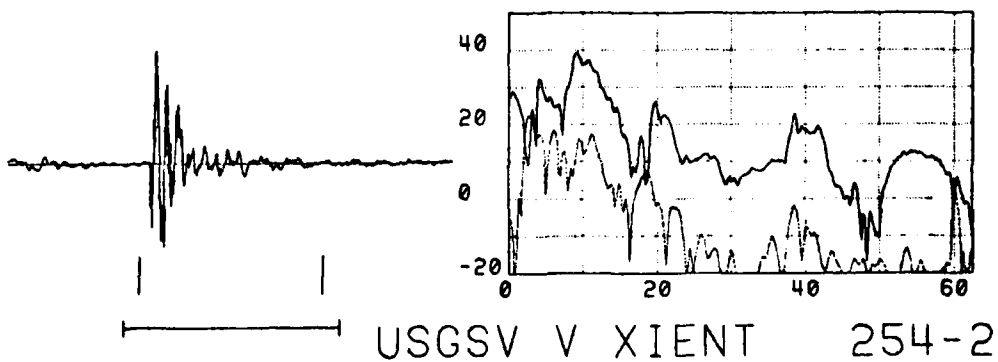
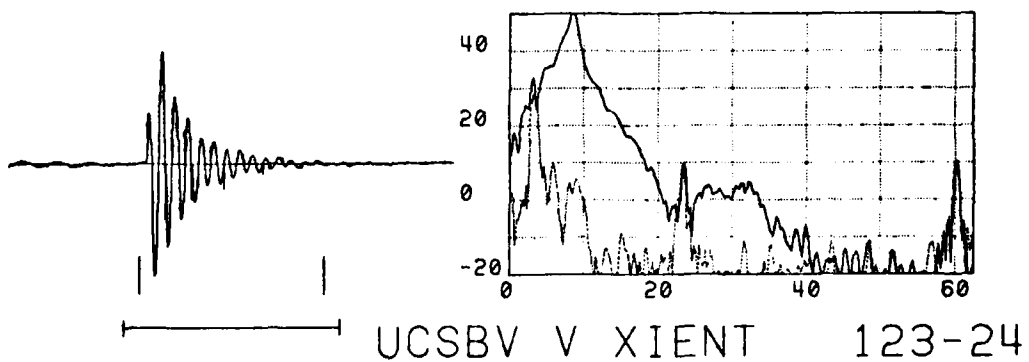
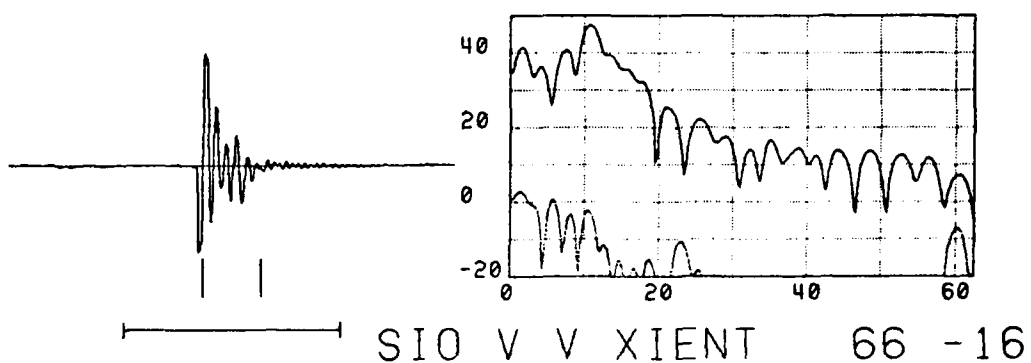
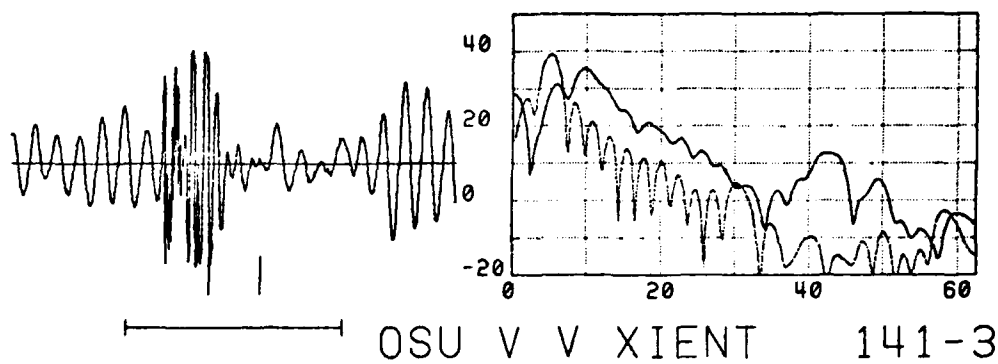
PAGE	SENSOR	RECORD-CHANNEL	TEST
12	HIGB H	110-8	Horizontal pull on horizontal sensor
	HIGB H	109-8	
	HIGS H	147-X1	
	HIGS H	148-X1	
13	MITE H	234-8	Horizontal pull on horizontal sensor
	MITM H	230-9	
	OSU H	144-4	
	UW H	116-15	
14	ND V AG 182	220-14	Lopez seismic on vertical sensor
	PL V AG 182	220-7	
	SP V AG 182	220-1	
	SP V CAP	239-1	
15	SP V CAP	242-1	Lopez seismic on vertical sensor
	BIO V AG 182	220-10	
	BIO V CAP	239-10	
	BIO V CAP	242-10	
16	HIGB V AG 9	160-9	Lopez seismic on vertical sensor
	HIGB V AG 182	220-20	
	HIGB V CAP	239-20	
	HIGB V CAP	242-20	
17	HIGS V AG 182	220-11	Lopez seismic on vertical sensor
	HIGS V CAP	239-11	
	HIGS V CAP	242-11	
	LDG V AG 182	220-23	

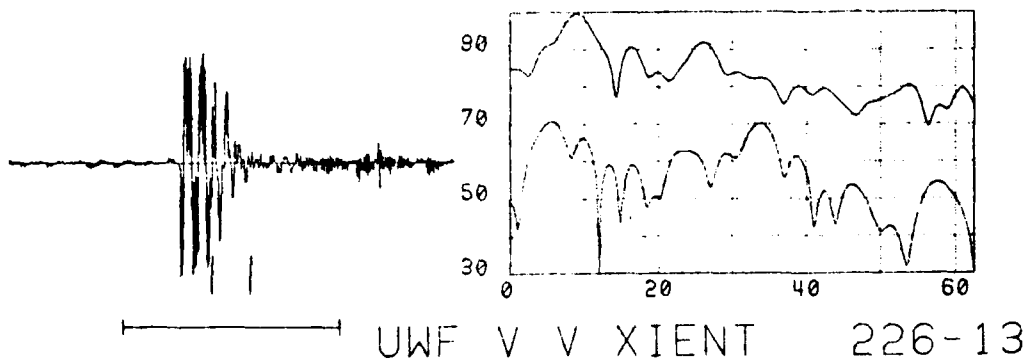
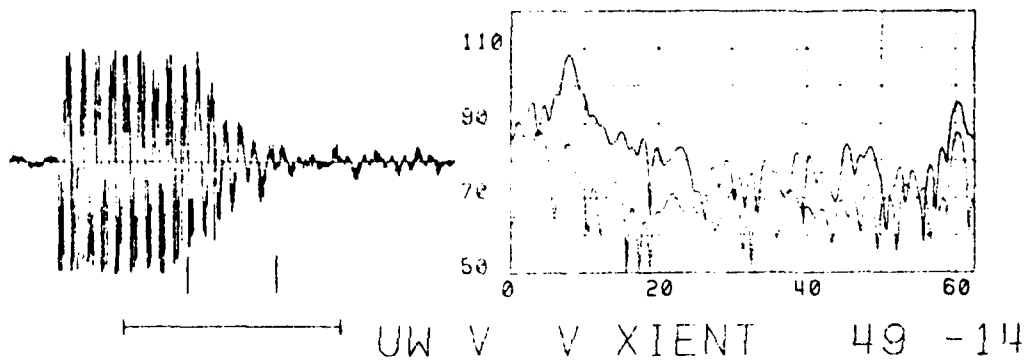
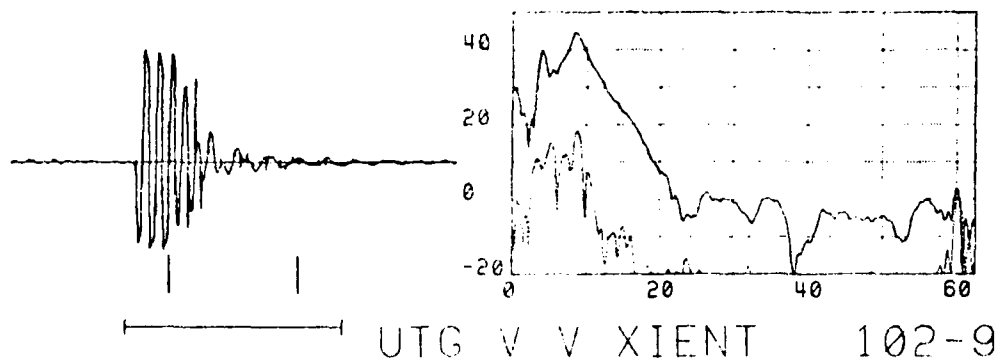
PAGE	SENSOR	RECORD-CHANNEL	TEST
24	UWF V CAP	239-13	Lopez seismic on vertical sensor
	UWF V CAP	242-13	
	LAND V CAP	239-9	
	LAND V CAP	242-9	
25	ND N AG 182	220-15	Lopez seismic on horizontal channel
	ND E AG 182	220-16	
	PL N AG 182	220-8	
	PL E AG 182	220-9	
26	SP N CAP	239-14	Lopez seismic on horizontal channel
	SP E CAP	239-15	
	SP N CAP	242-14	
	SP E CAP	242-15	
27	BIO H CAP	239-18	Lopez seismic on horizontal channel
	BIO H CAP	242-18	
	HIGB H AG 182	220-19	
	HIGS H CAP	239-24	
28	HIGS H CAP	242-24	Lopez seismic on horizontal channel
	MITE H CAP	239-8	
	MITE H CAP	242-8	
	OSU H CAP	239-16	
29	OSU H CAP	242-16	Lopez seismic on horizontal channel
	UCSB H CAP	239-17	
	UCSB H CAP	242-17	
	UW H CAP	239-19	

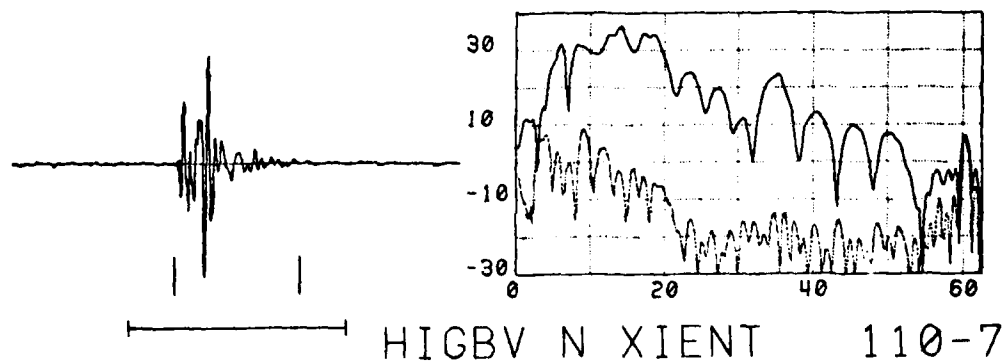
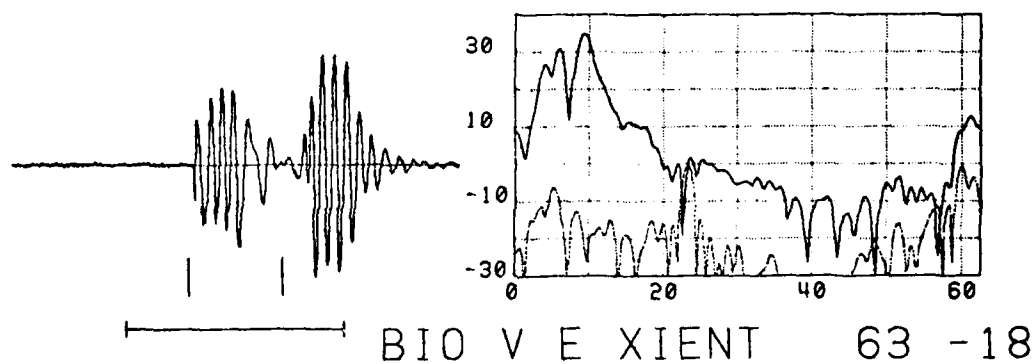
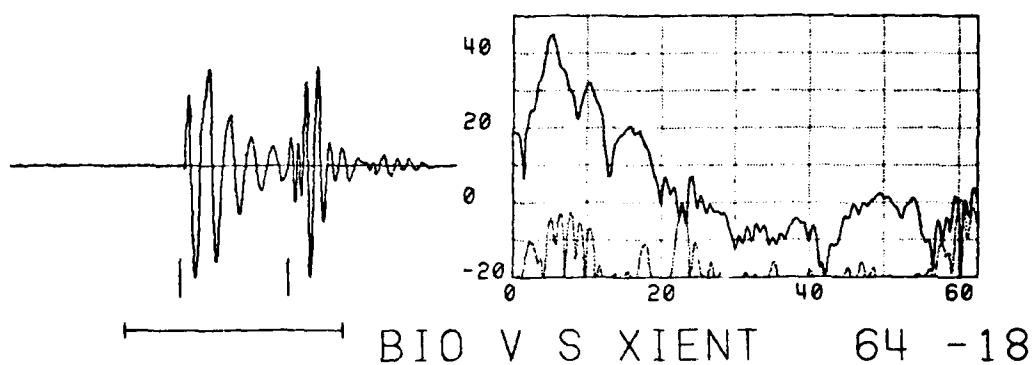
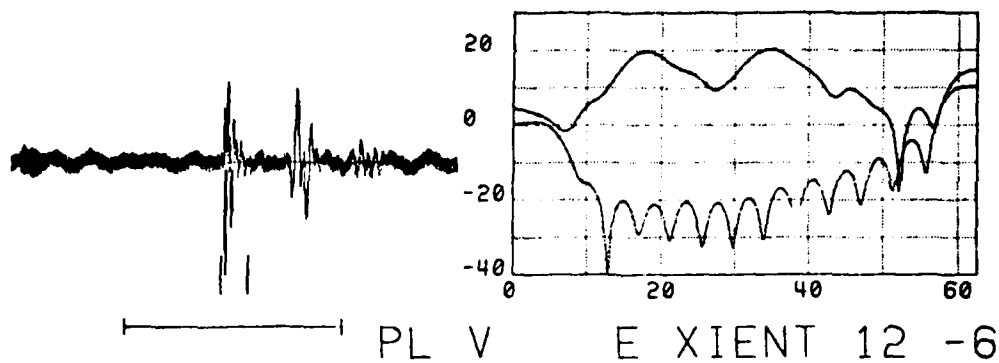
PAGE	SENSOR	RECORD-CHANNEL	TEST
30	UW H CAP	242-19	Lopez seismic on hydrophone
	WHOI P AG 182	220-6	
31	HIGB P AG 9	160-7	Lopez seismic on hydrophone
	LDG P AG 182	220-24	
	OSU P CAP	239-6	
	OSU P CAP	242-6	

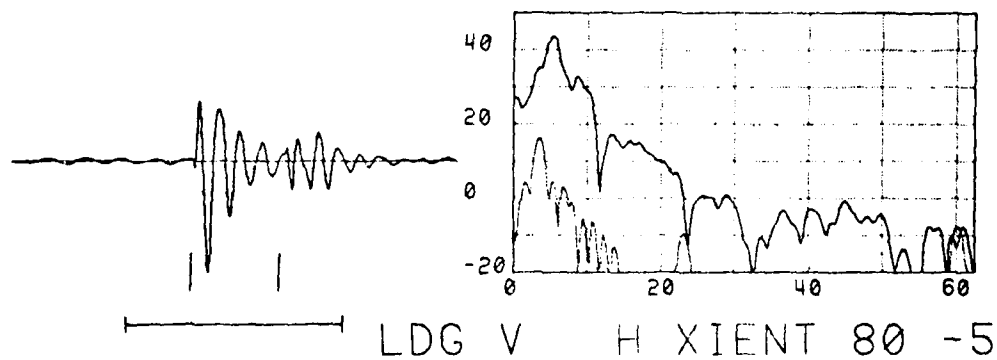
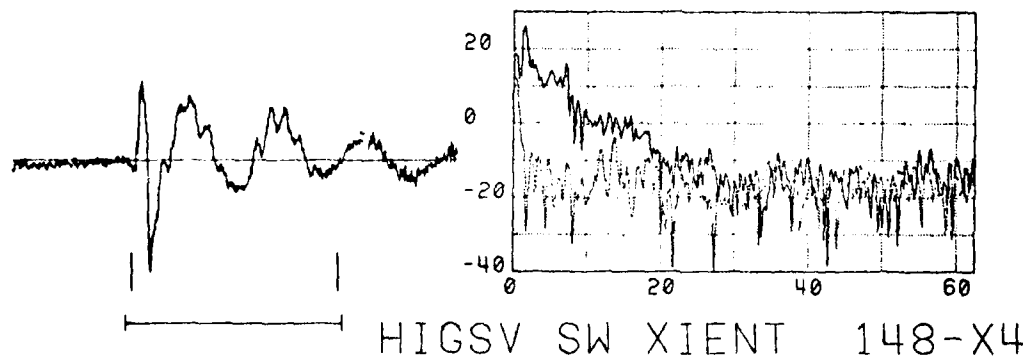
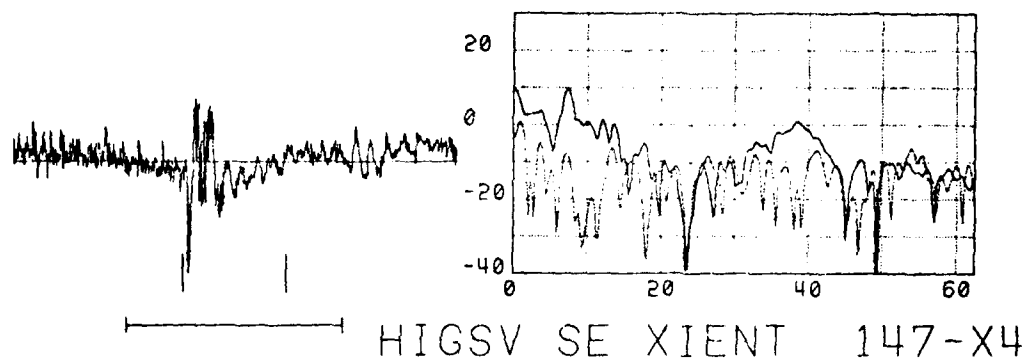
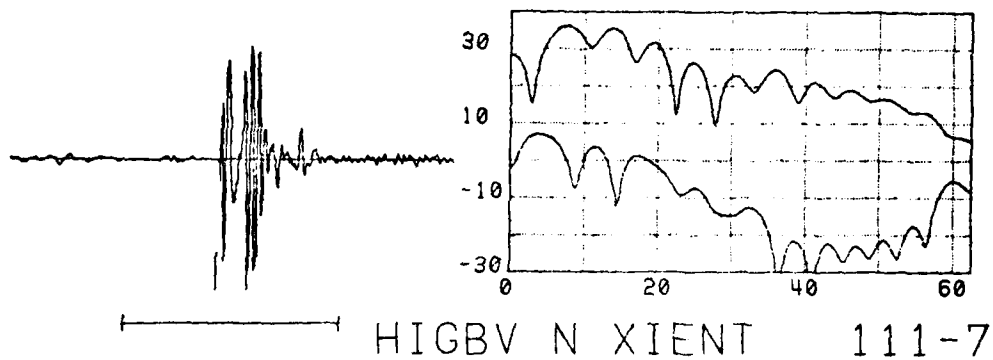


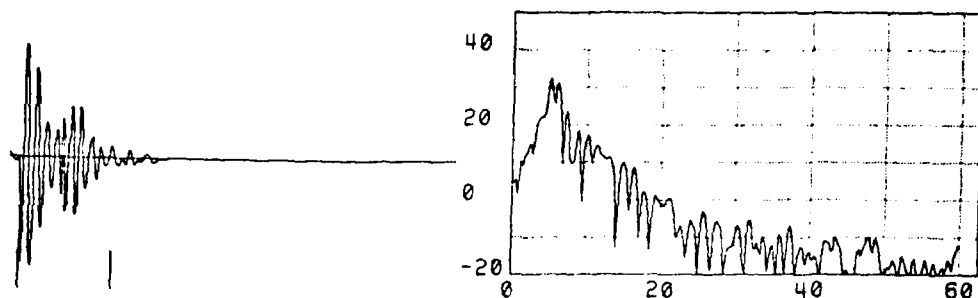




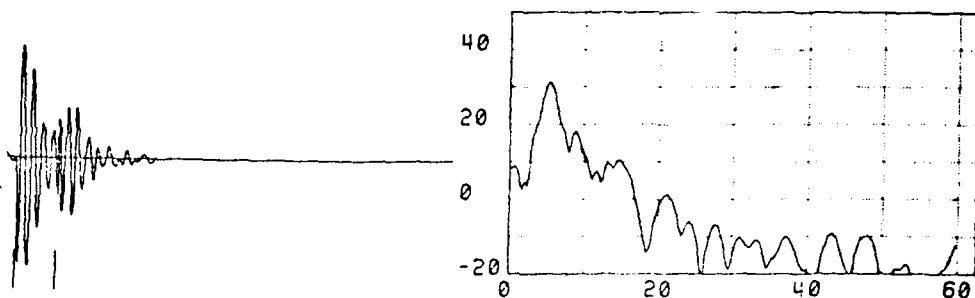




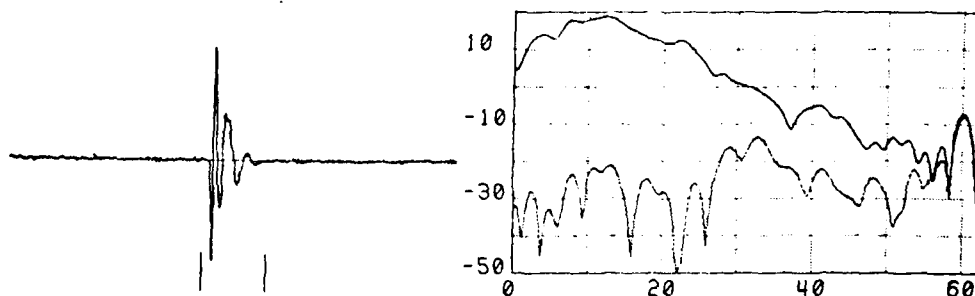




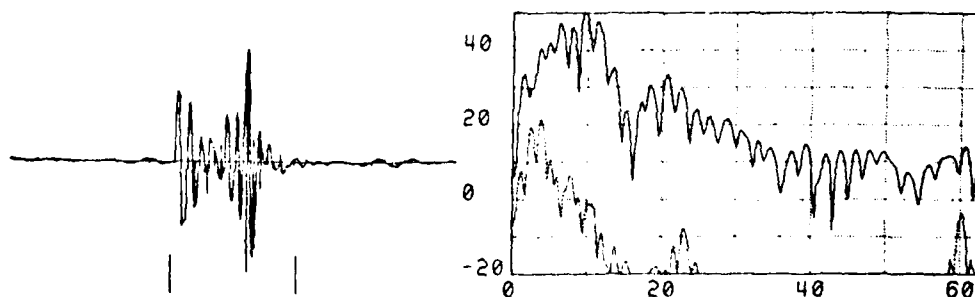
LDG V N XIENT 501-2



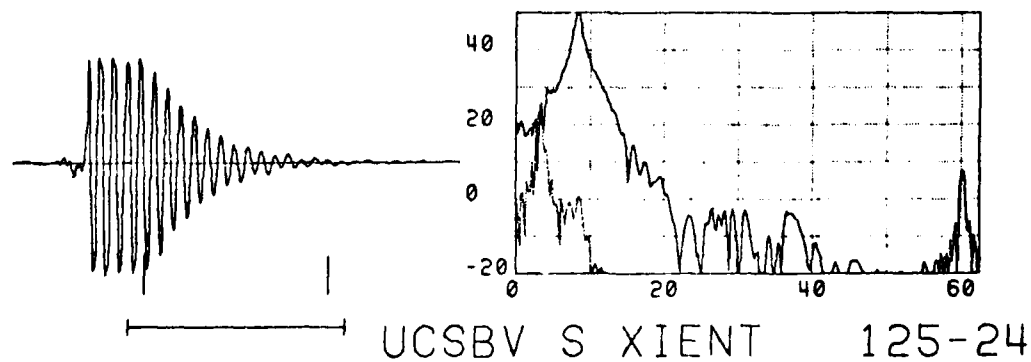
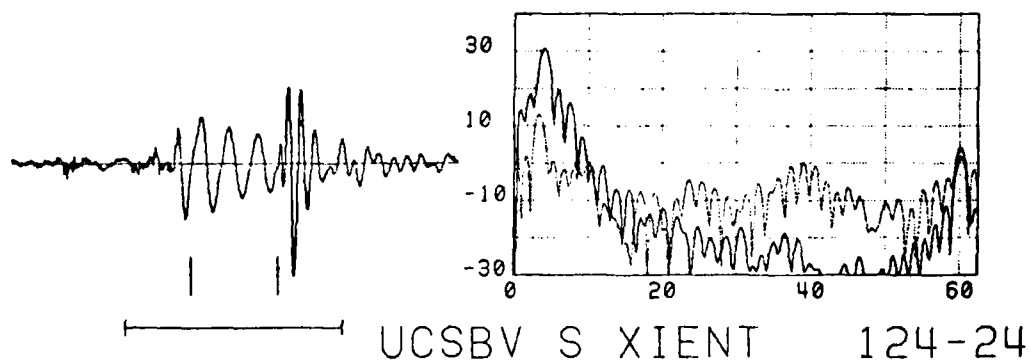
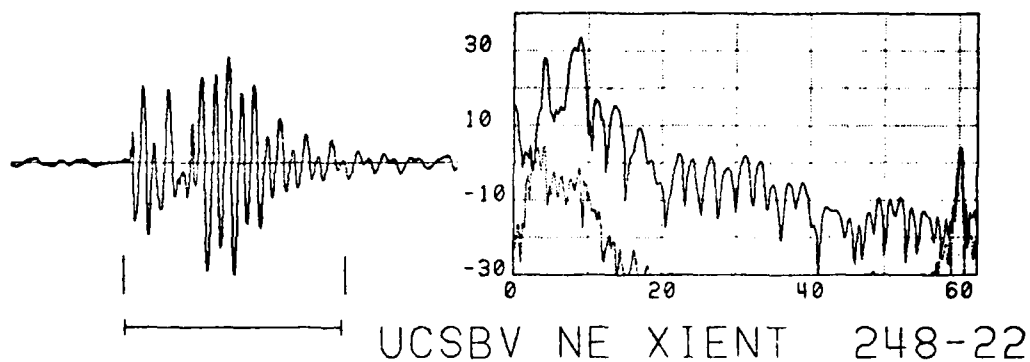
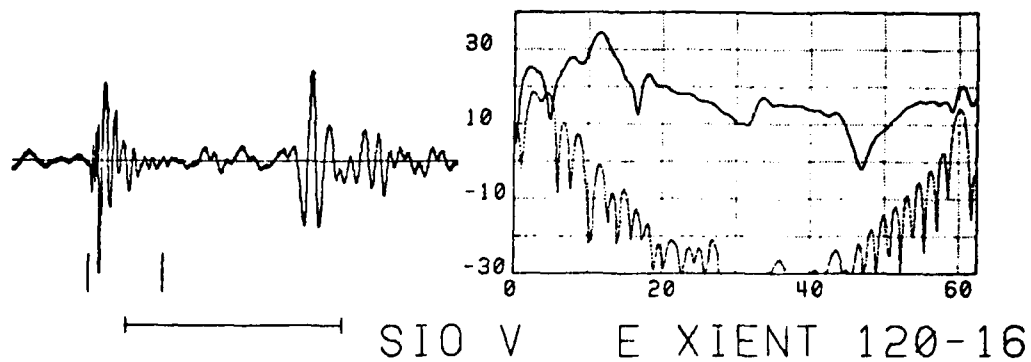
LDG V N XIENT 501-2

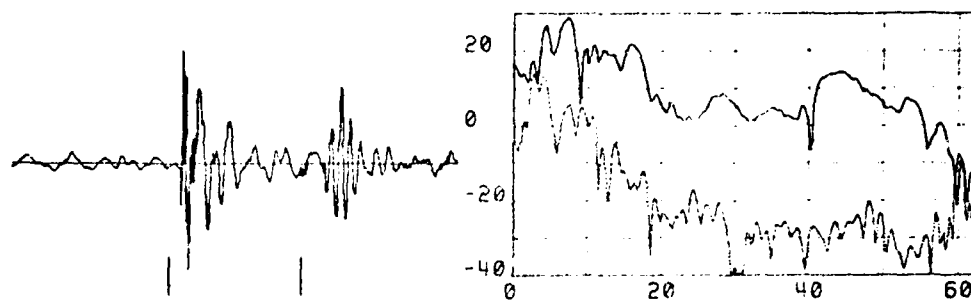


MITEV H XIENT 234-7

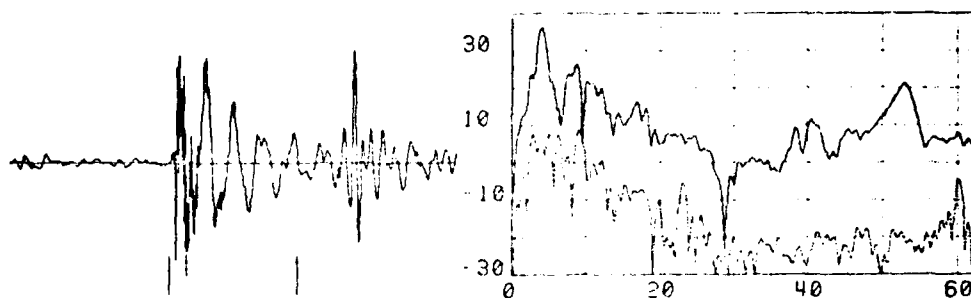


SIO V E XIENT 67-16

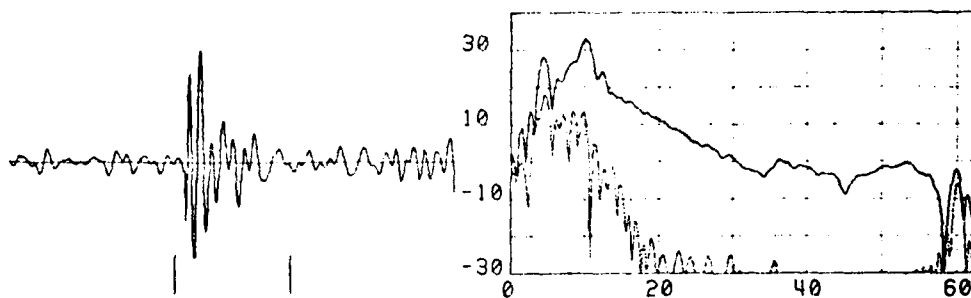




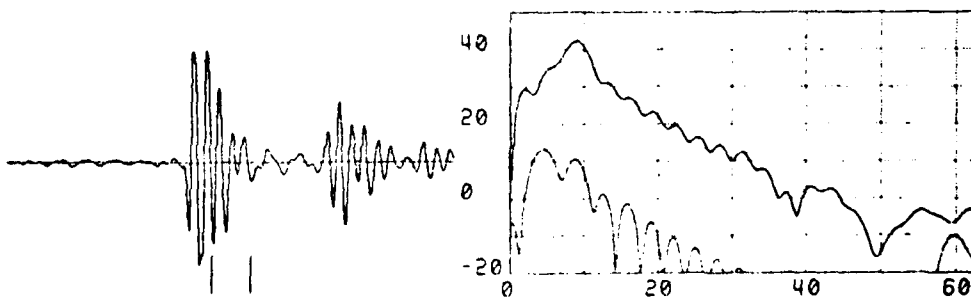
USGSV S XIENT 252-2



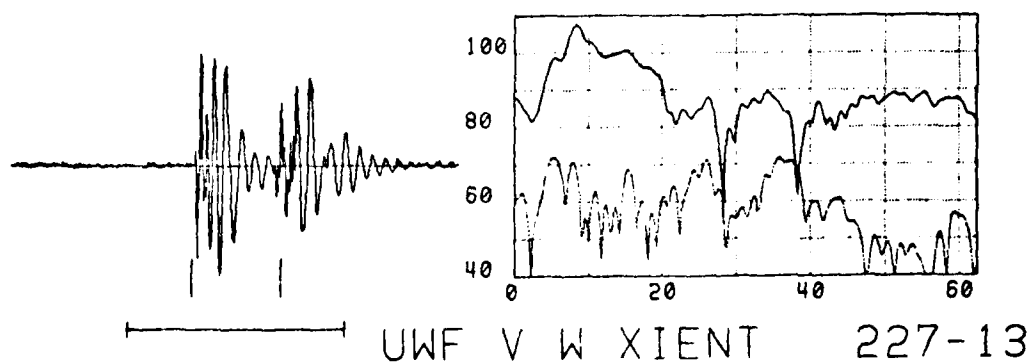
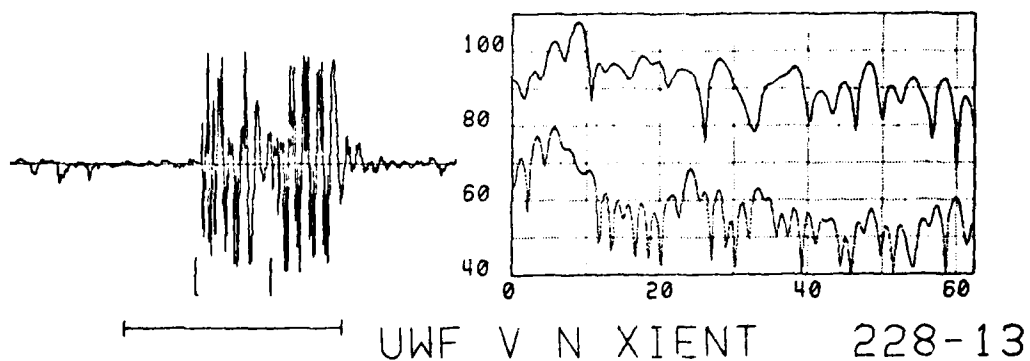
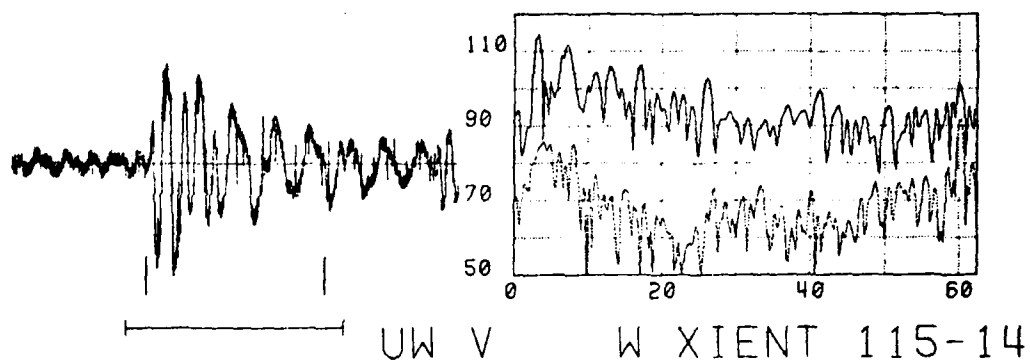
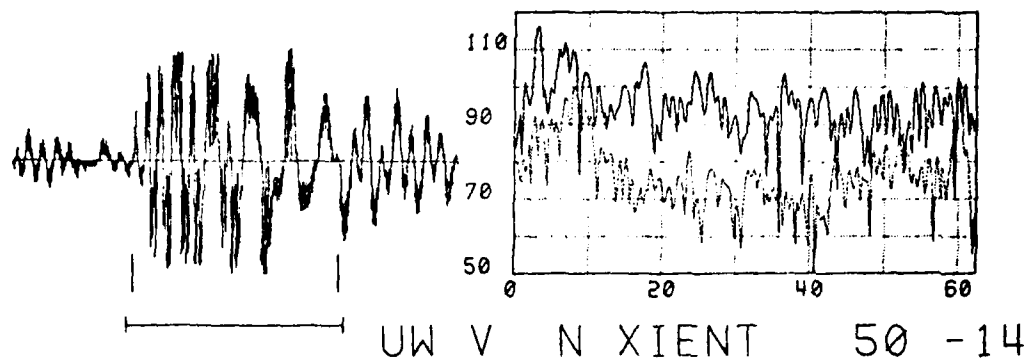
USGSV W XIENT 253-2

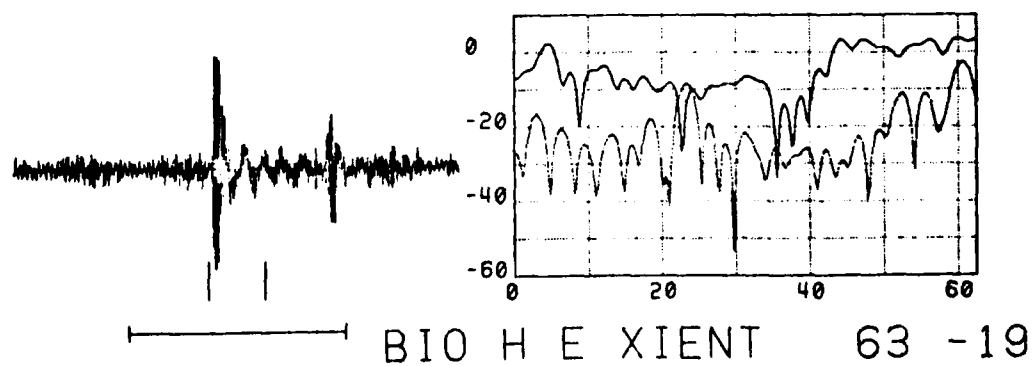
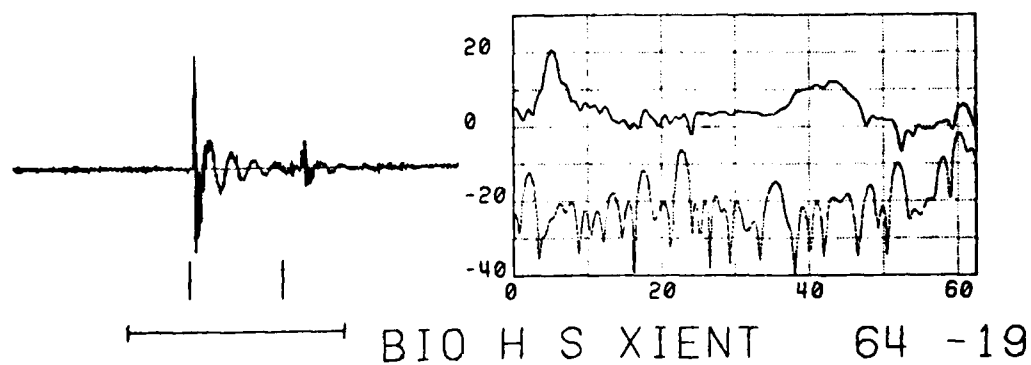
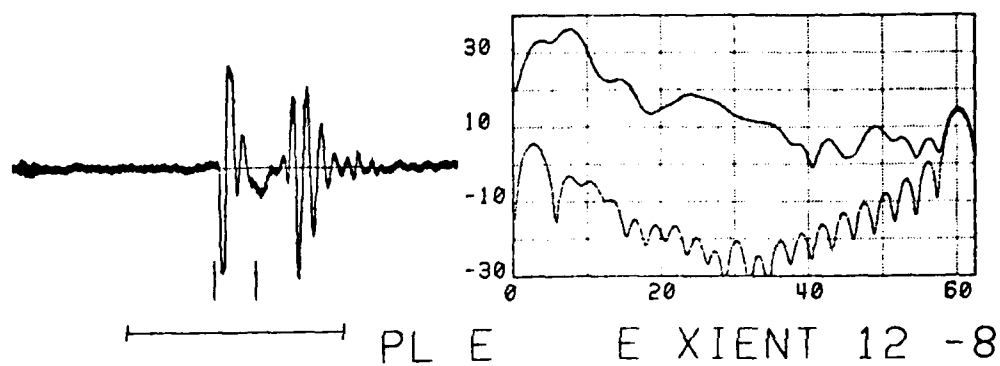
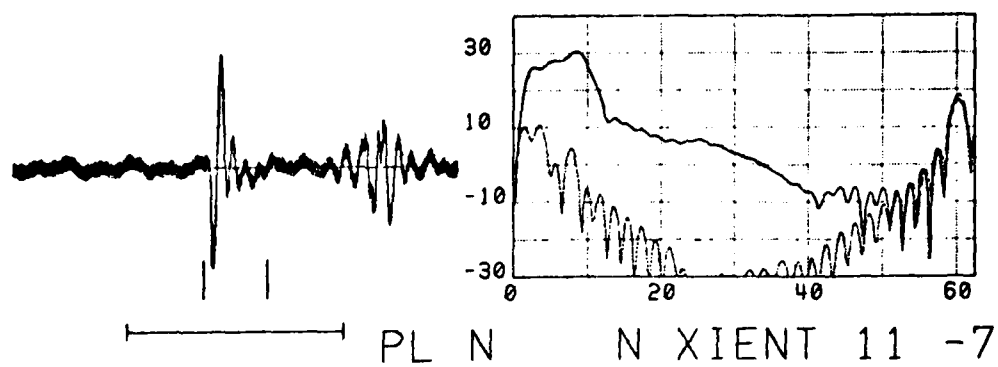


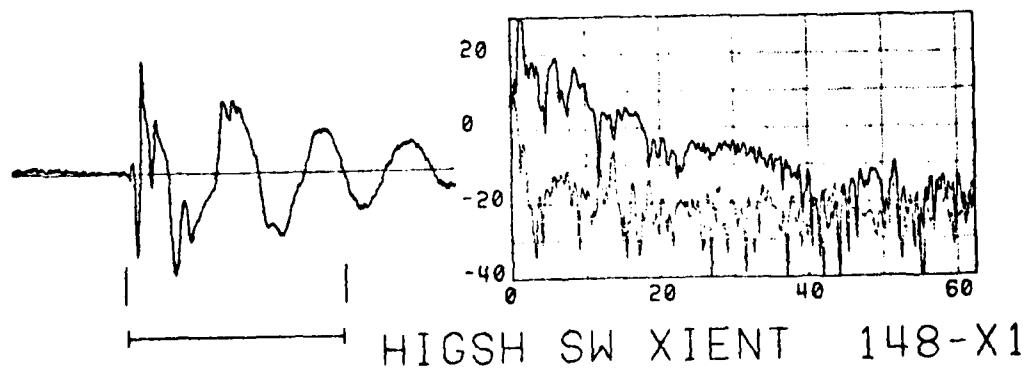
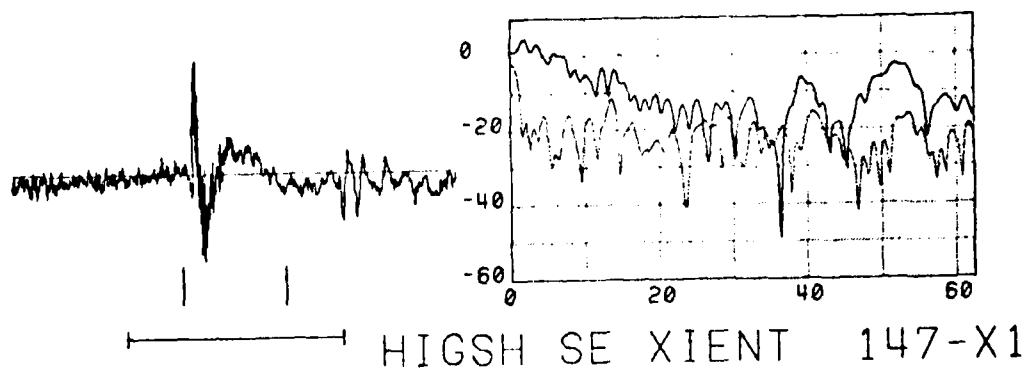
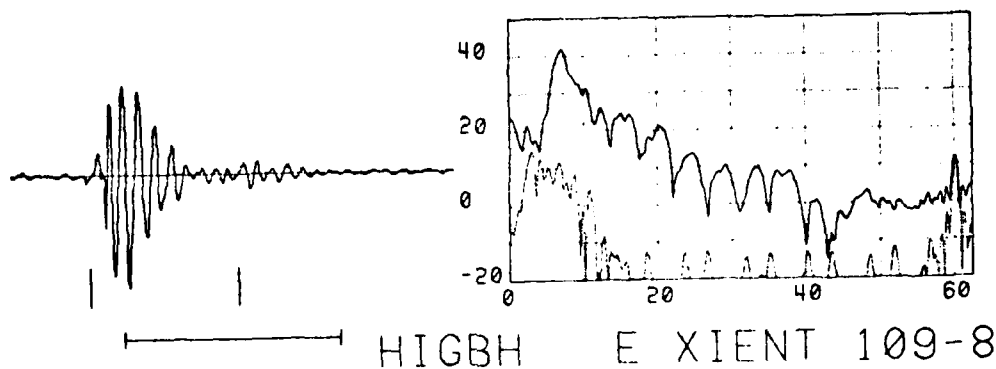
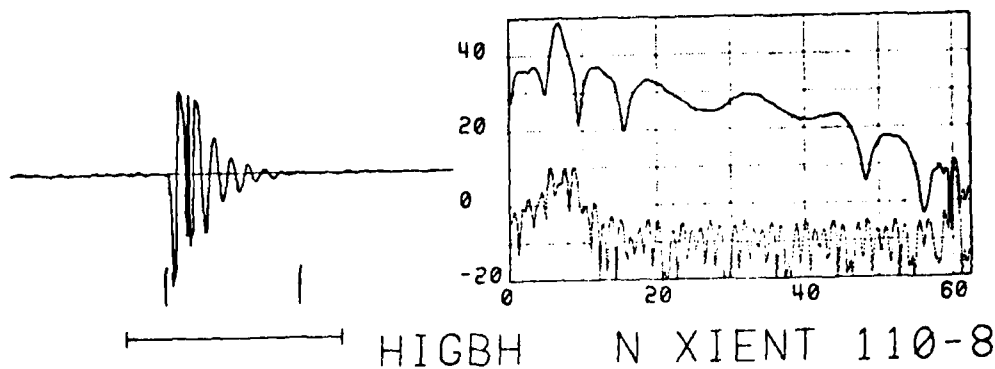
UTG V E XIENT 236-3

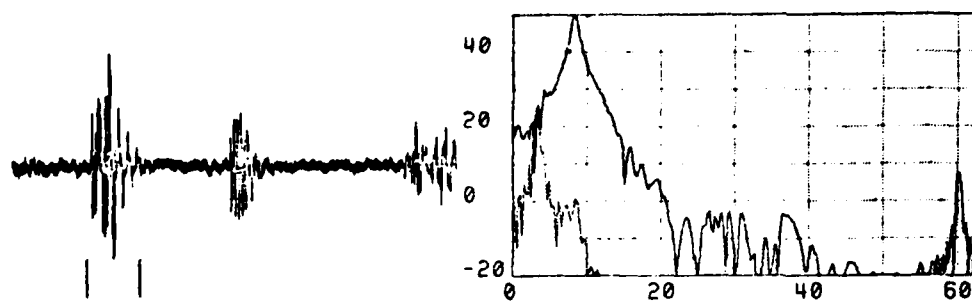


UTG V E XIENT 105-9

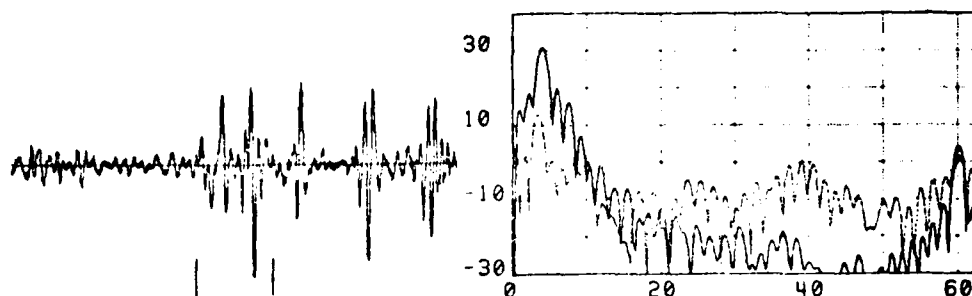




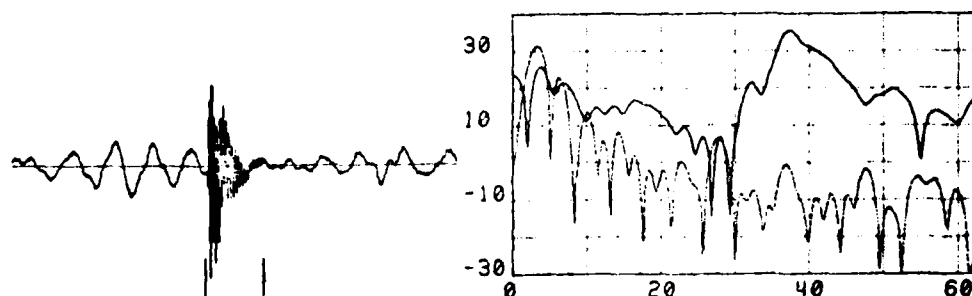




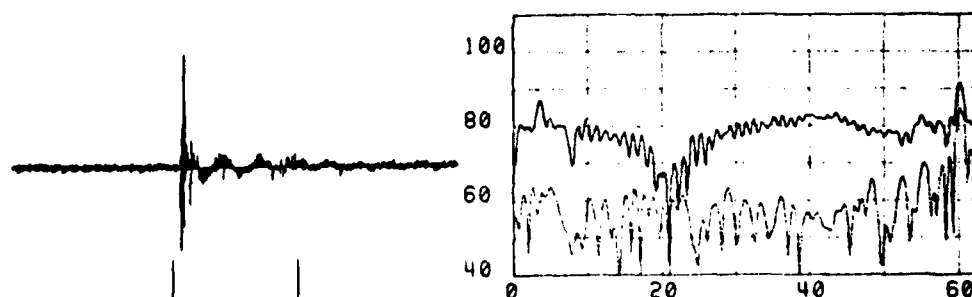
MITEH H XIENT 234-8



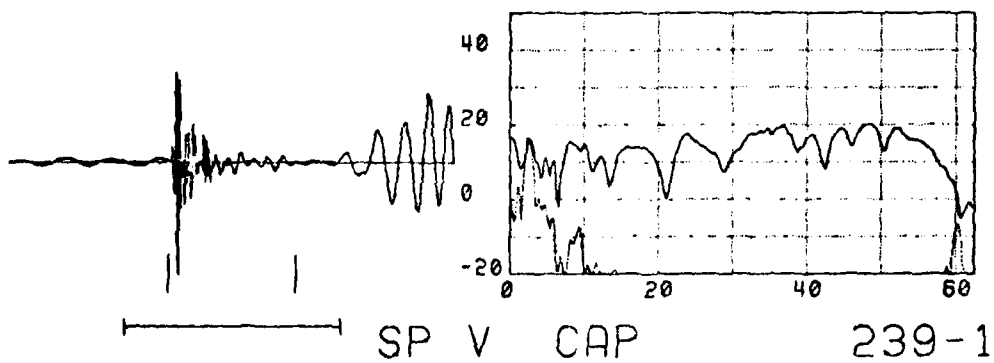
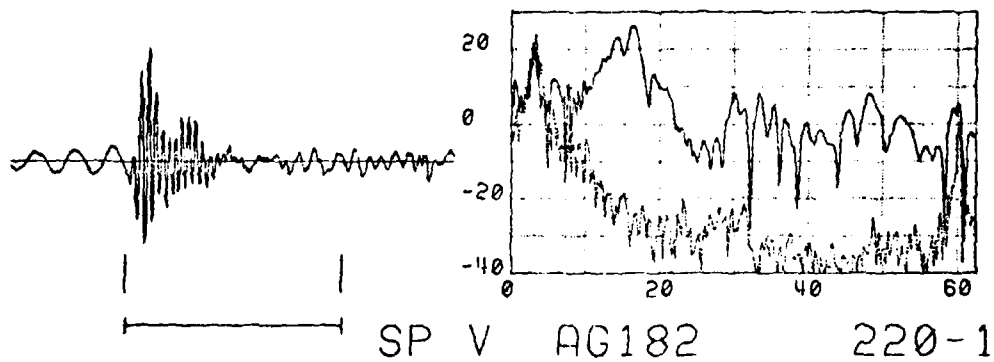
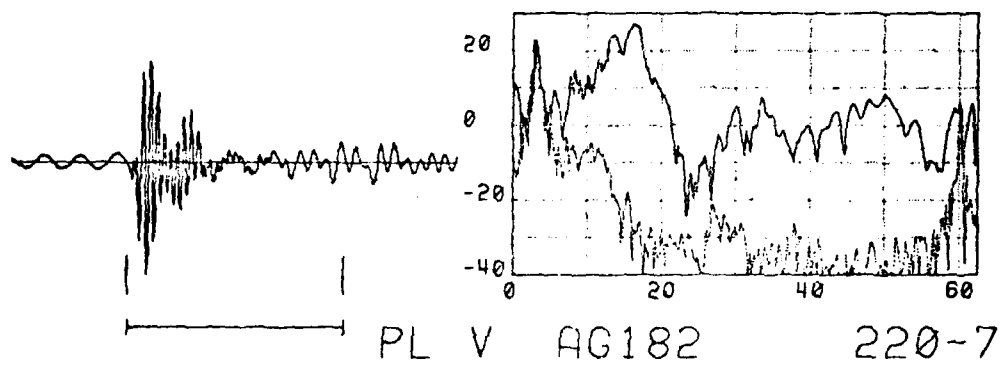
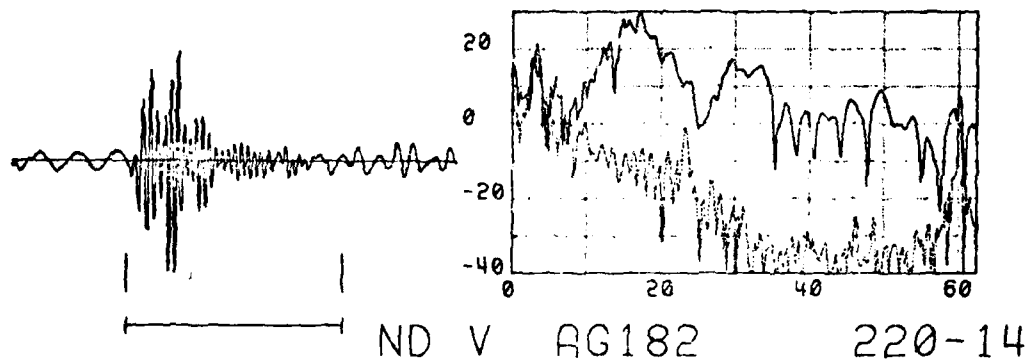
MITMH H XIENT 230-9

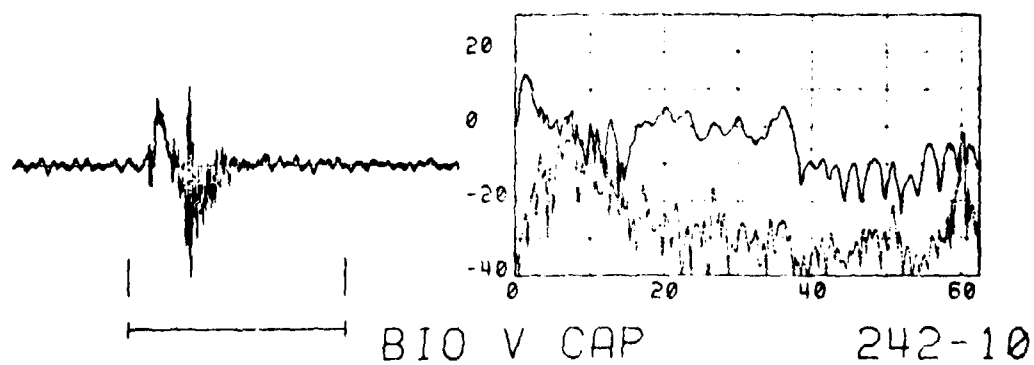
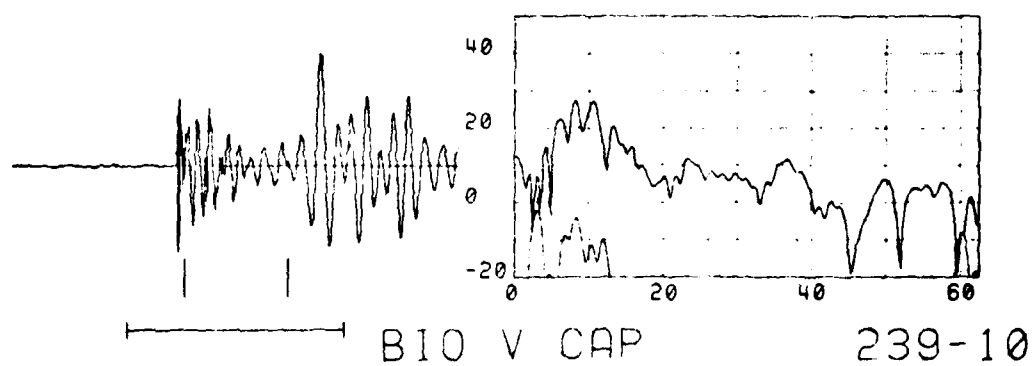
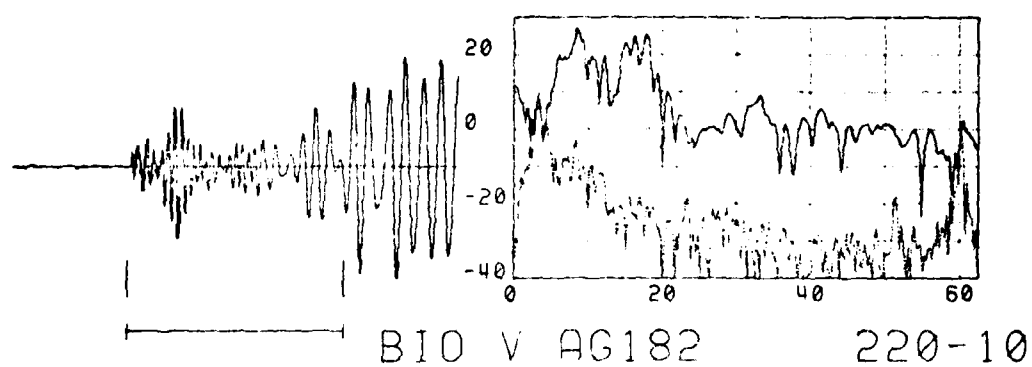
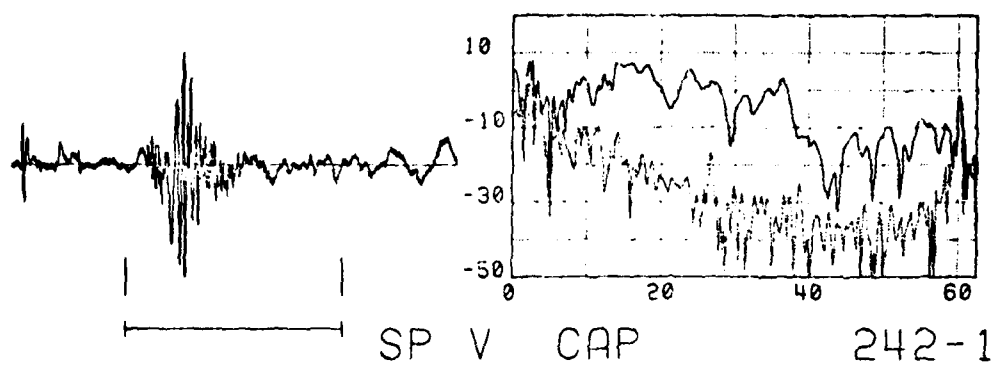


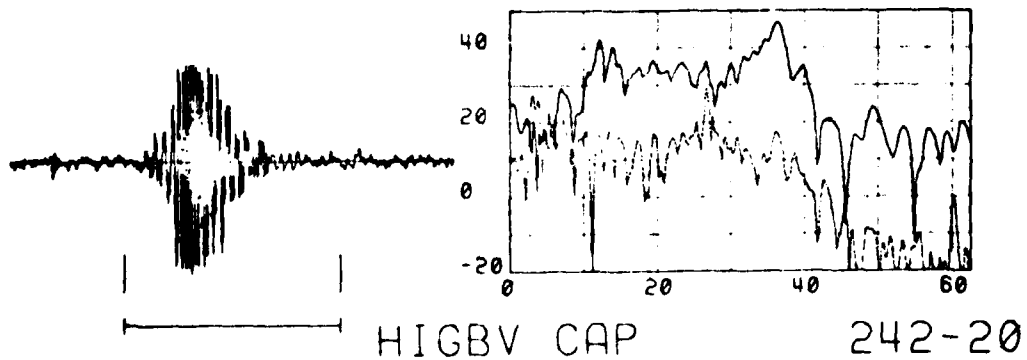
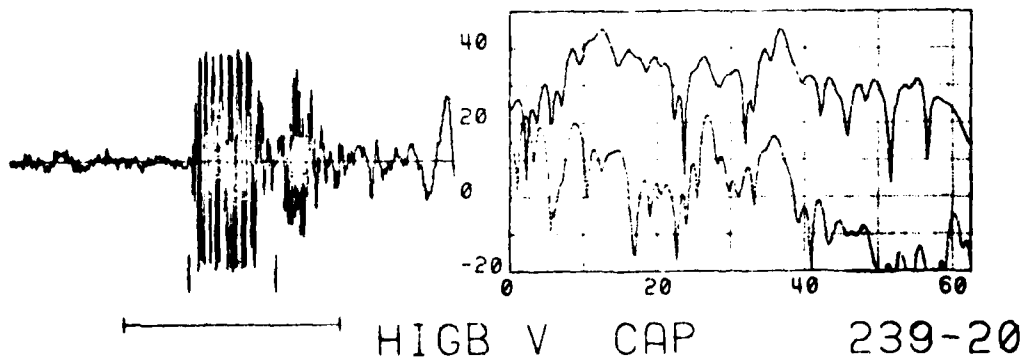
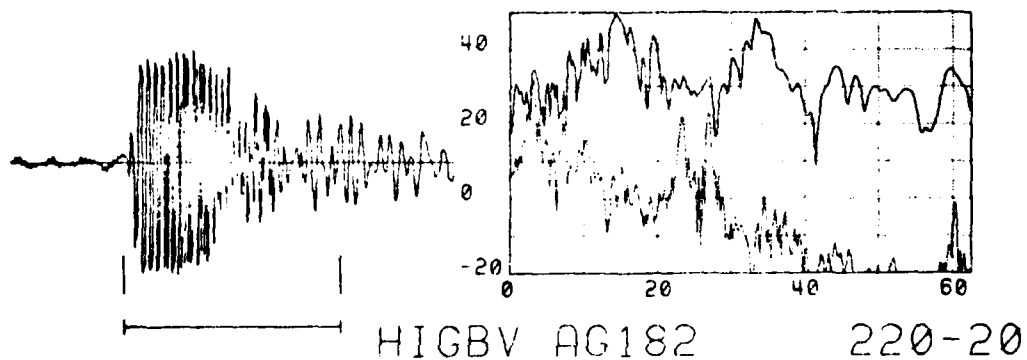
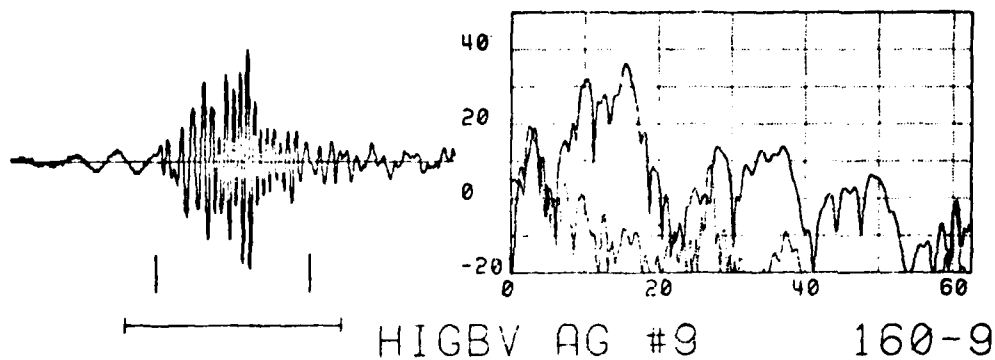
OSU H E XIENT 144-4

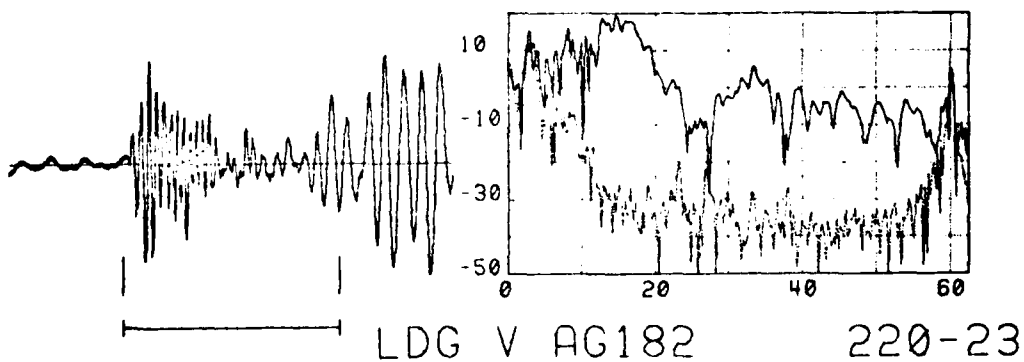
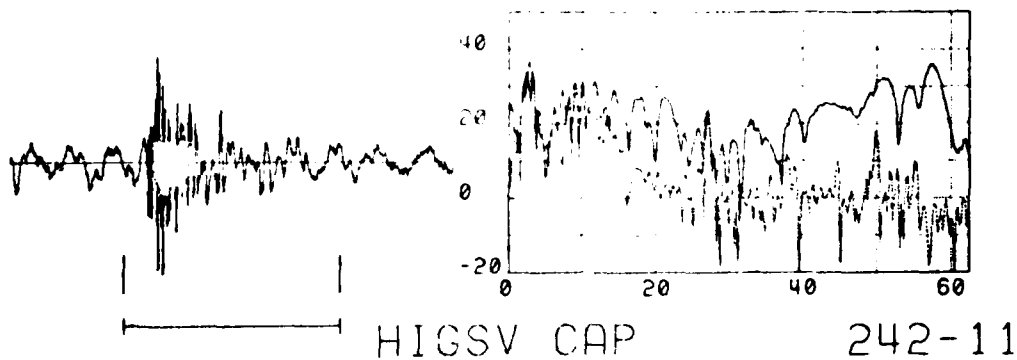
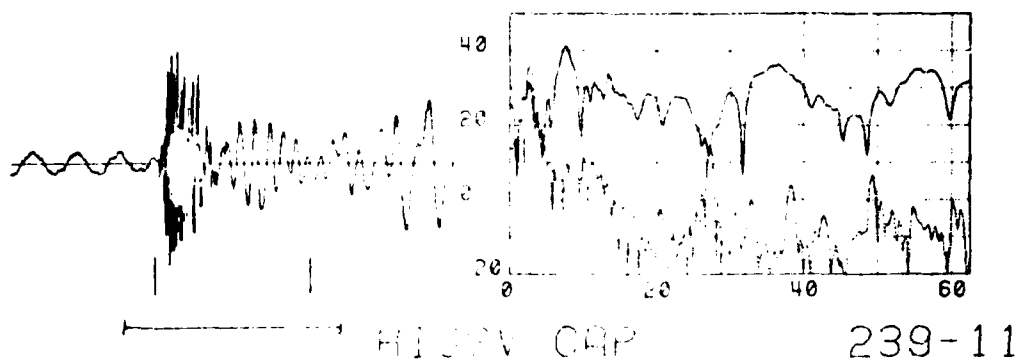
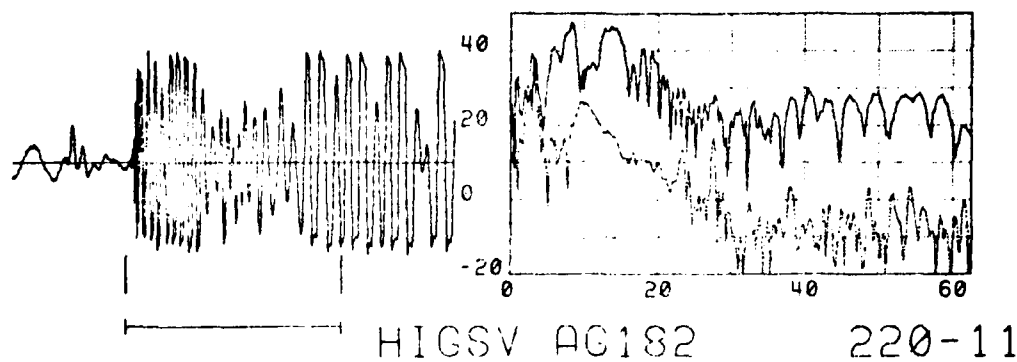


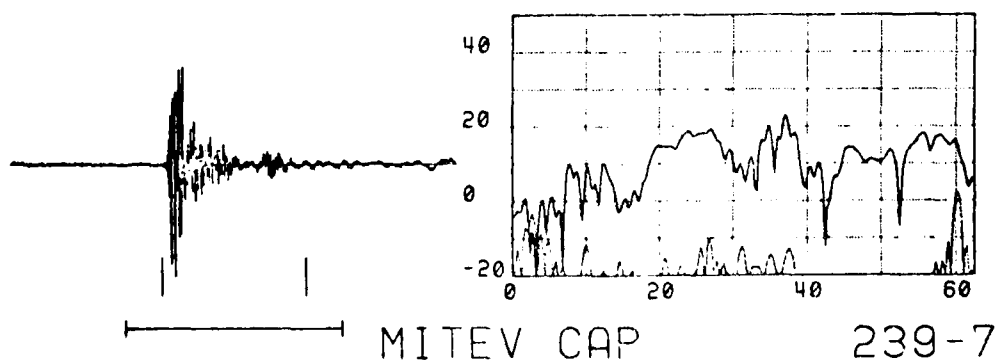
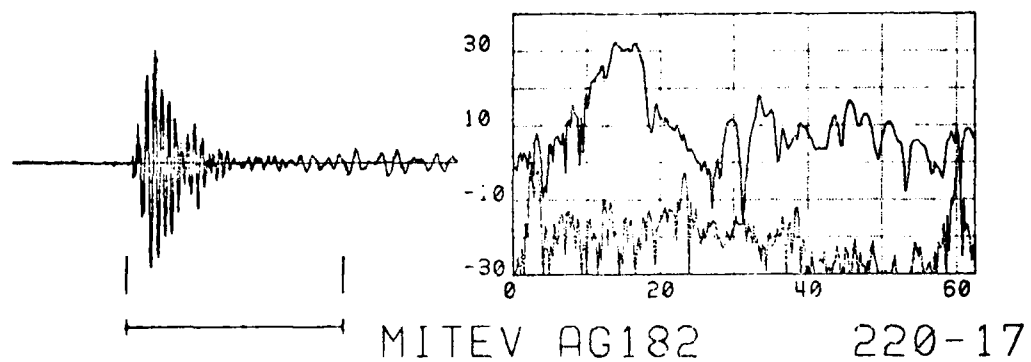
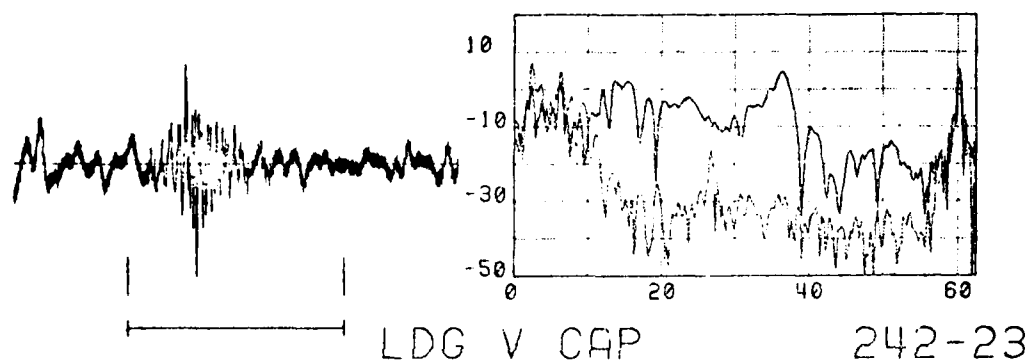
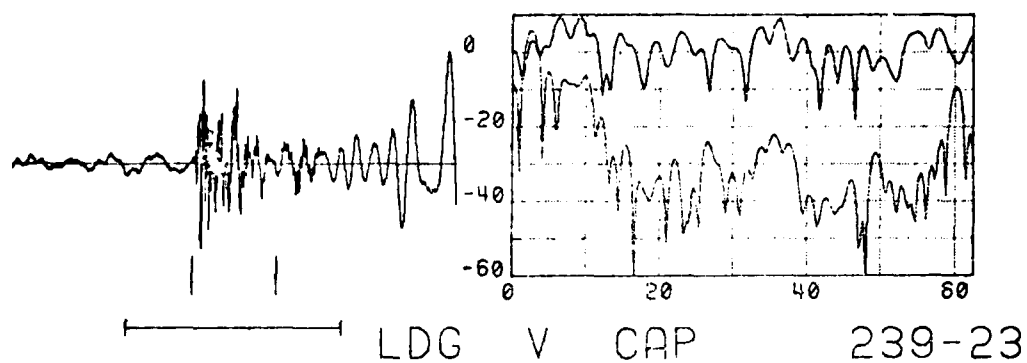
UW H H XIENT 116-15

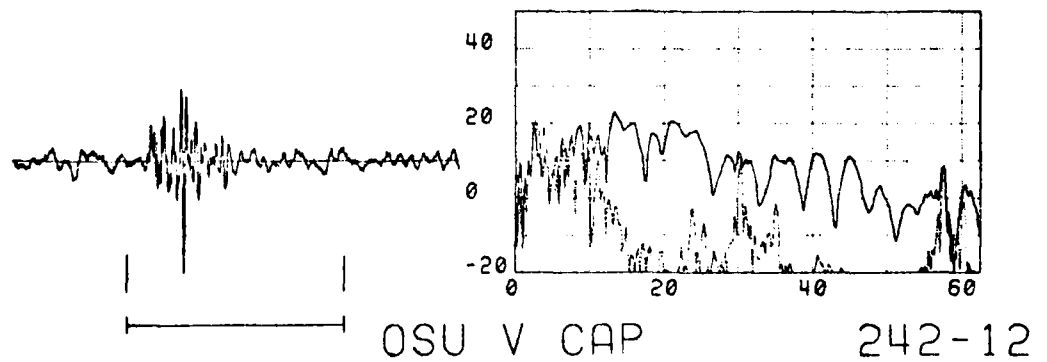
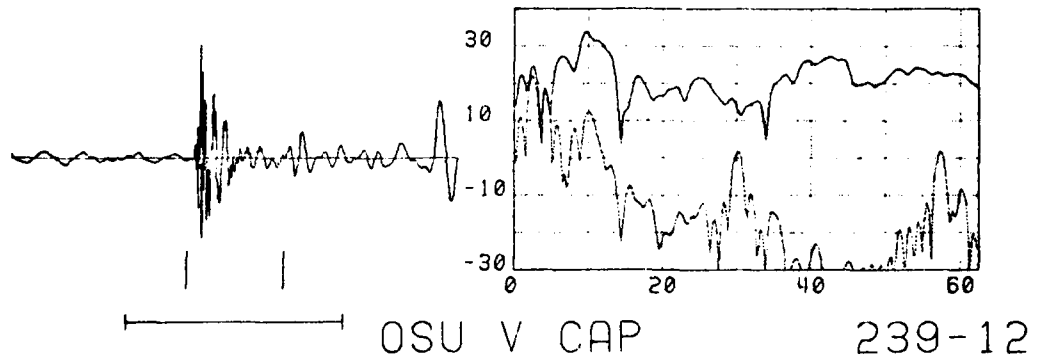
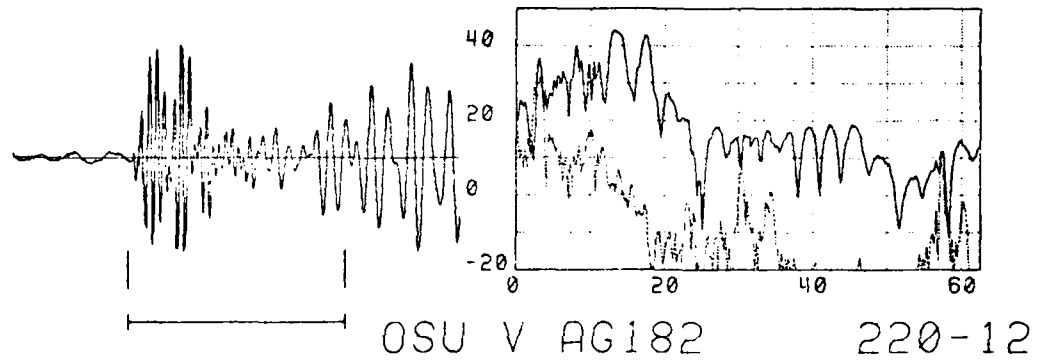
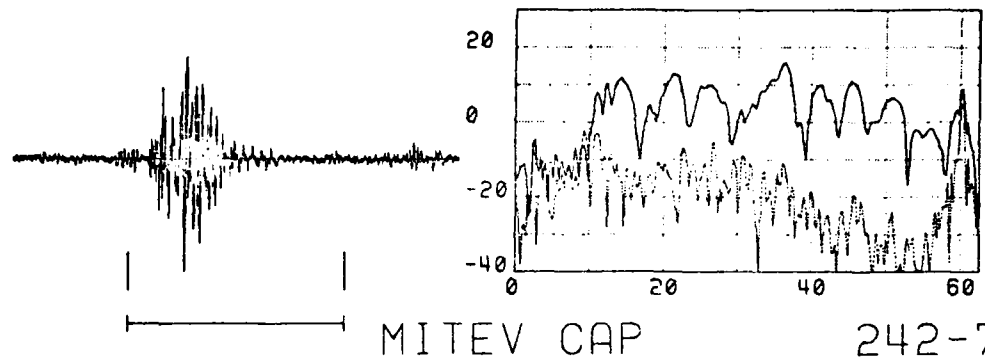


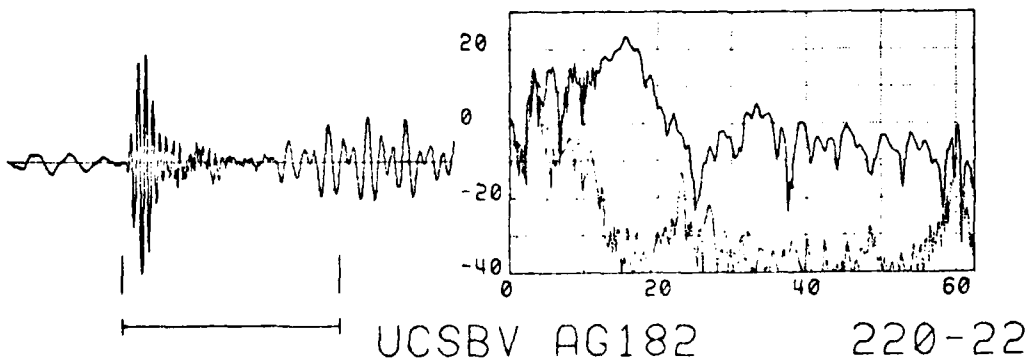
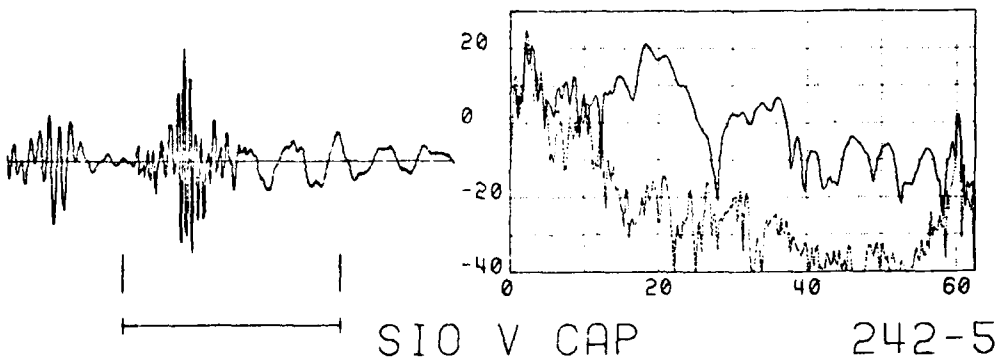
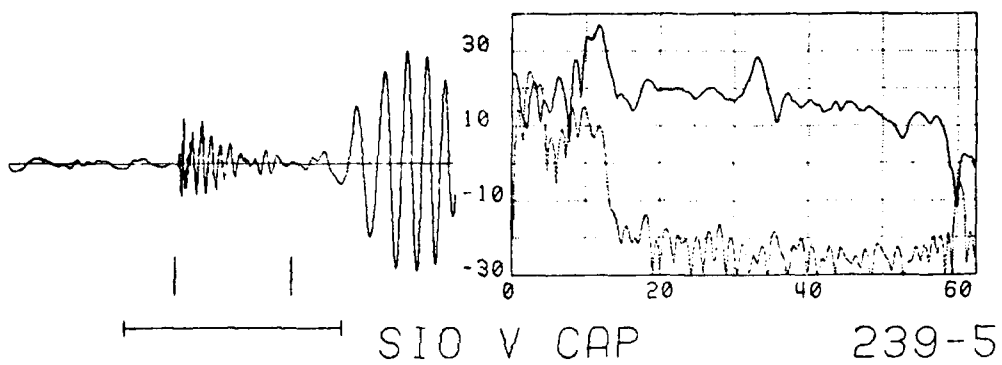
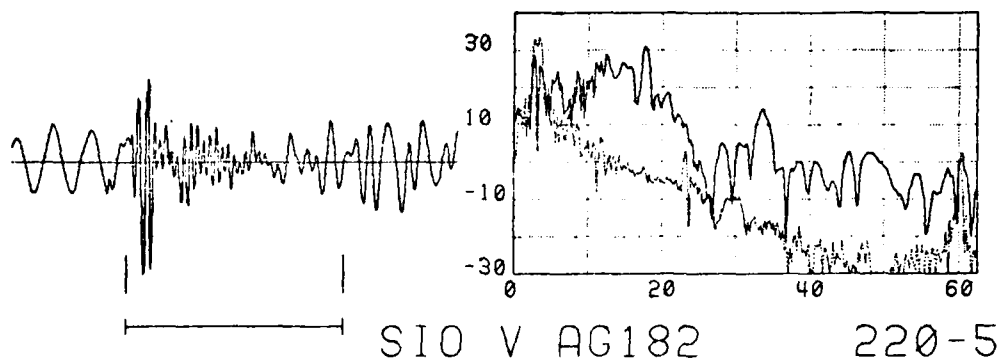


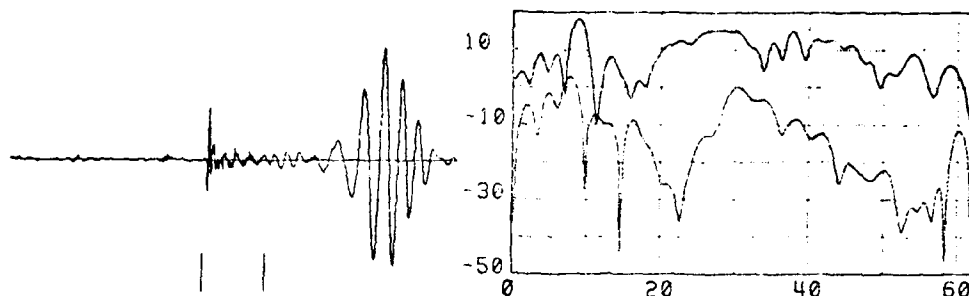






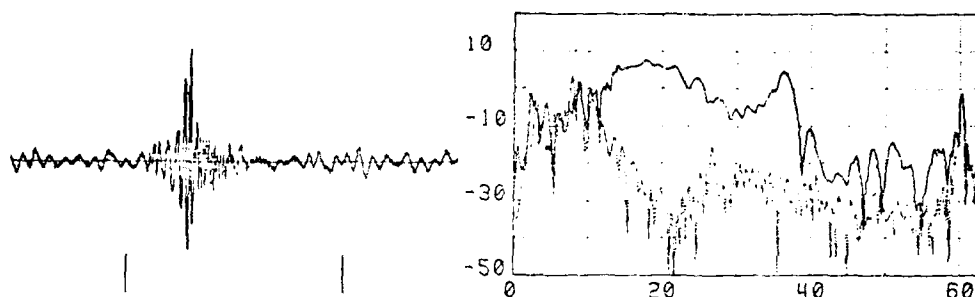






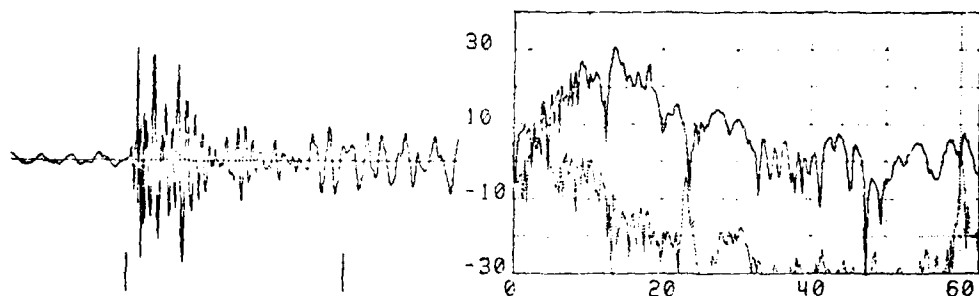
UCSBV CAP

239-22



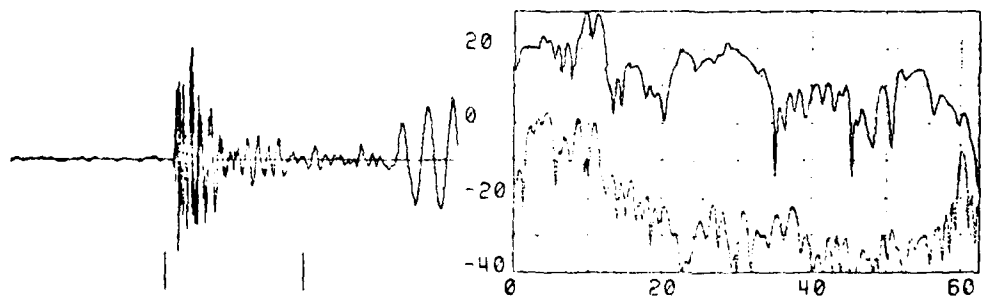
UCSBV CAP

242-22



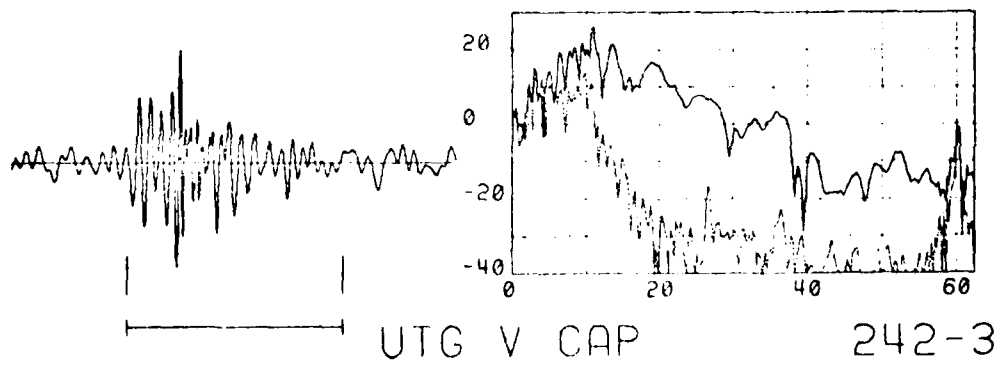
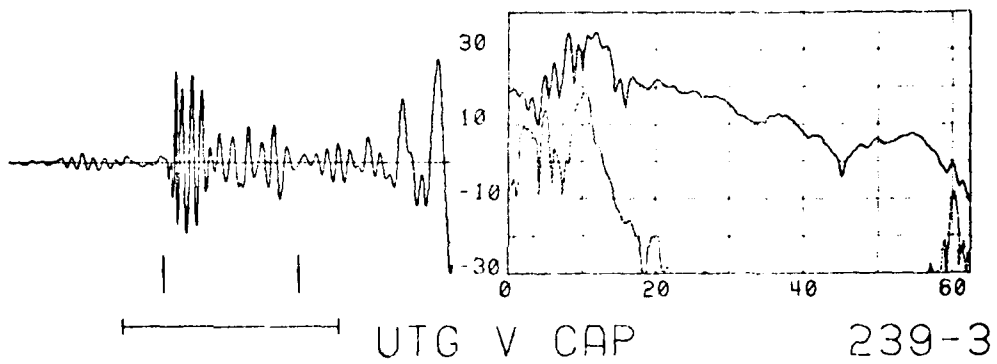
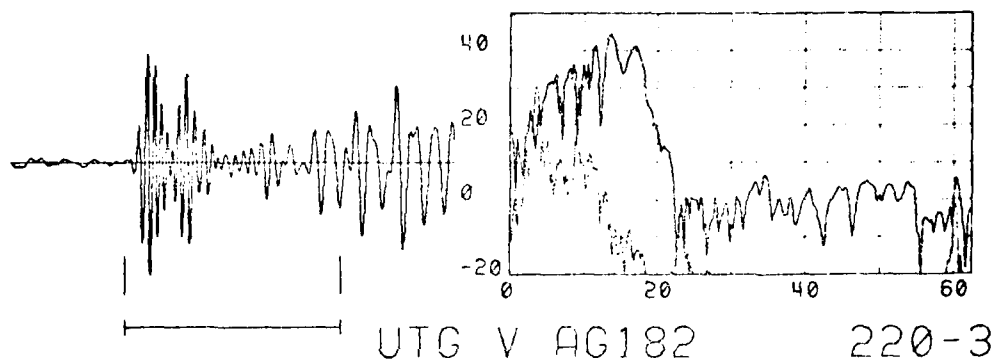
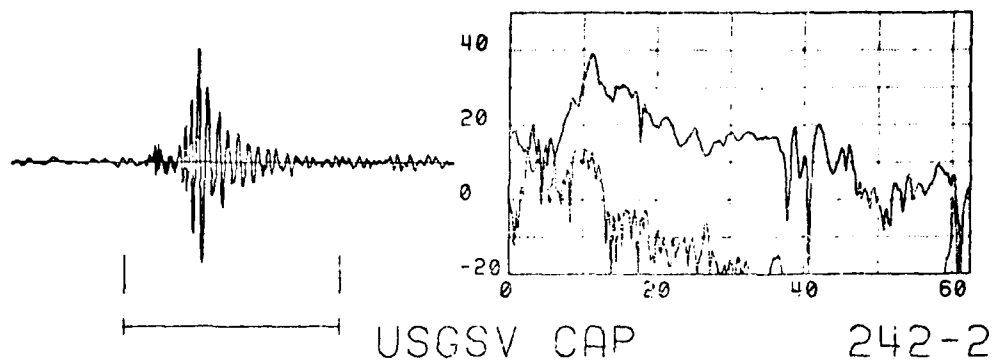
USGSV AG182

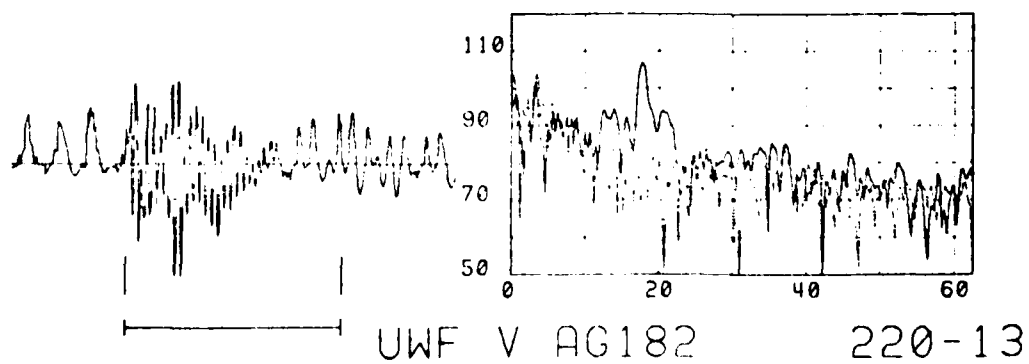
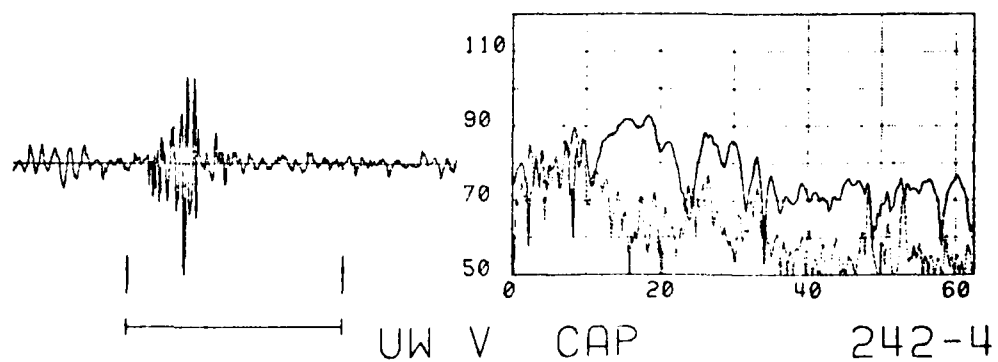
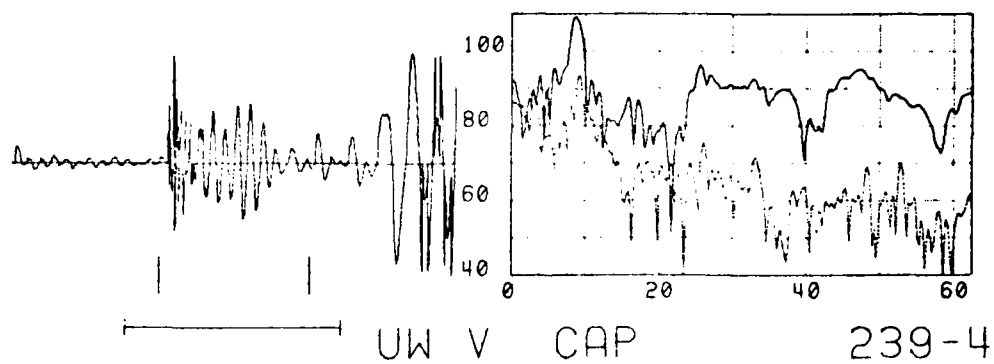
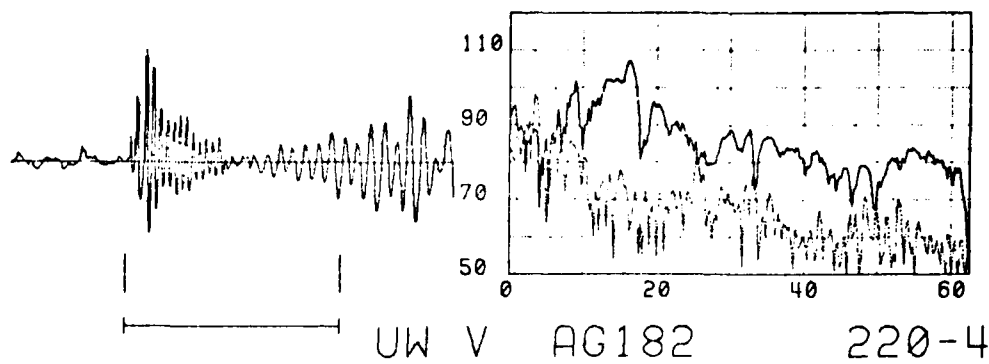
220-2

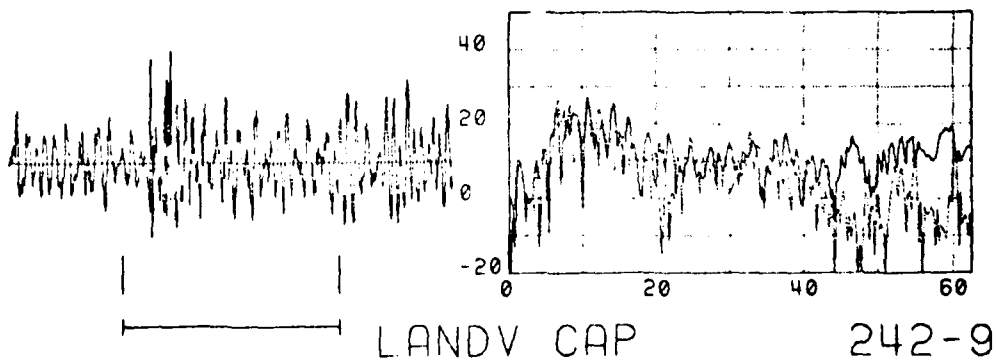
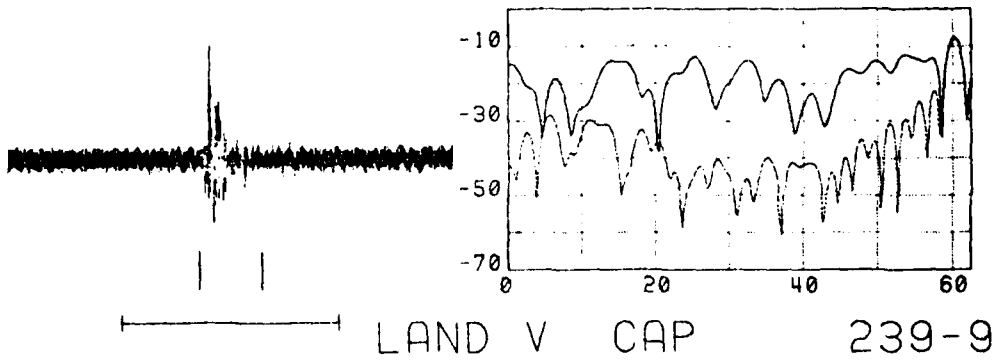
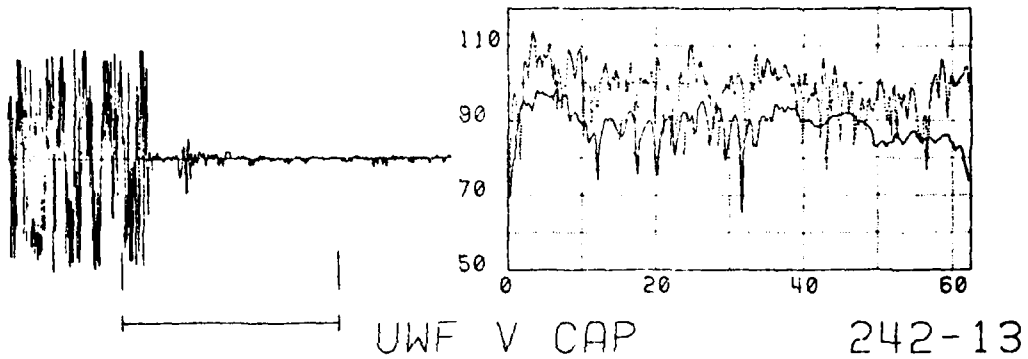
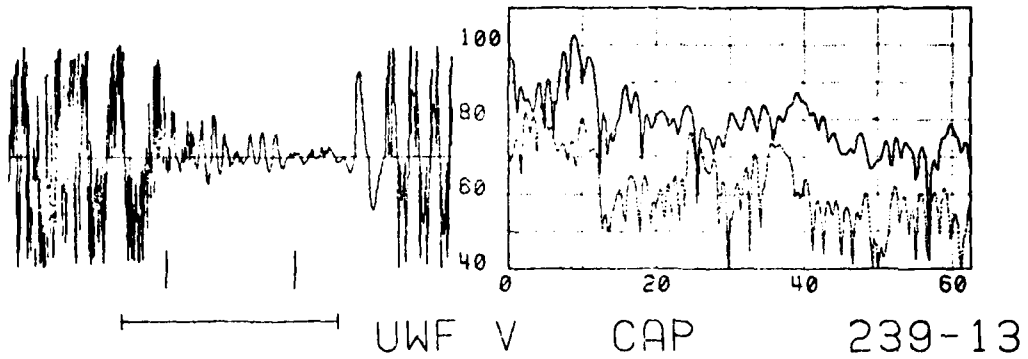


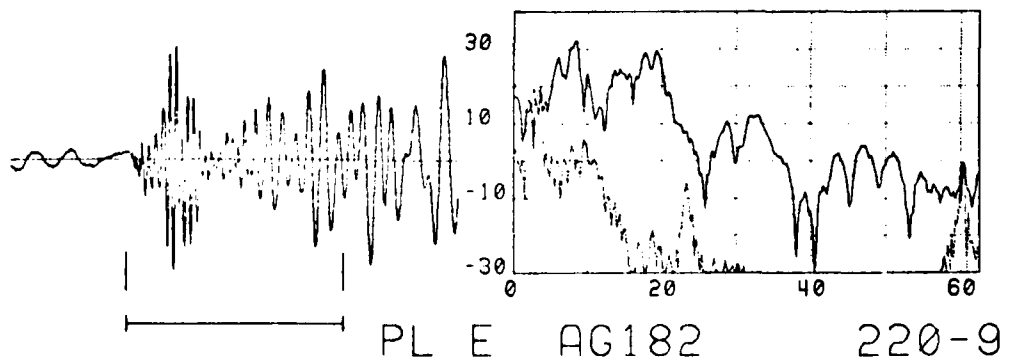
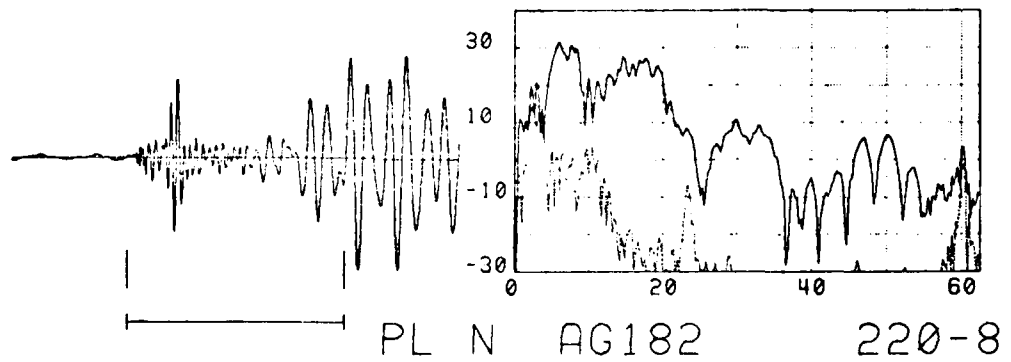
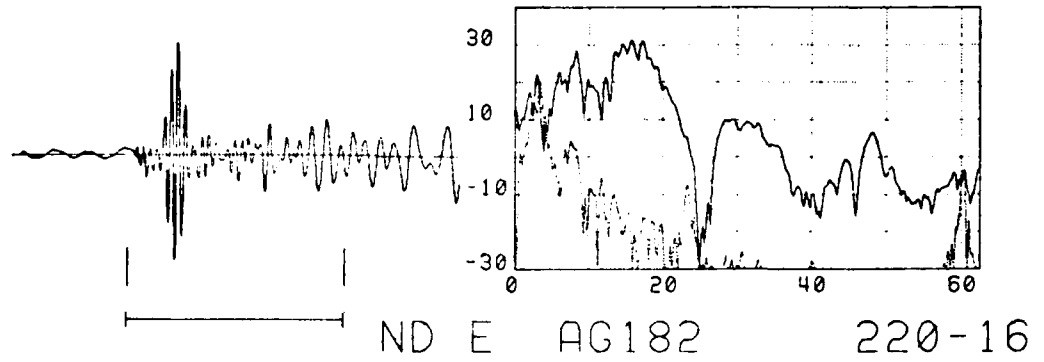
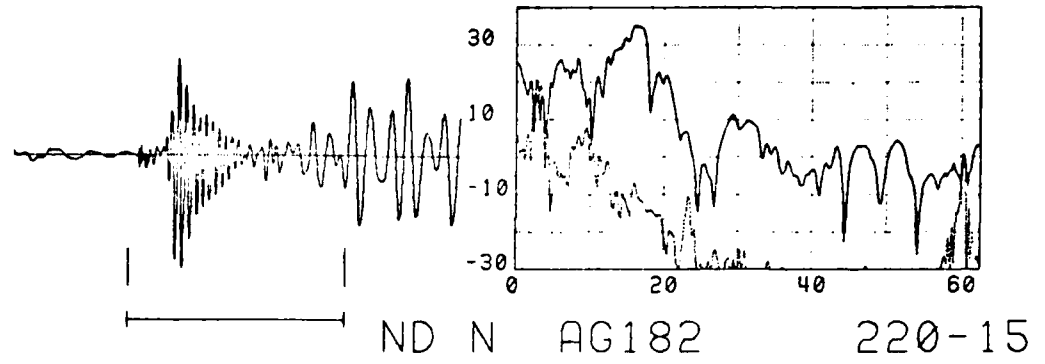
USGSV CAP

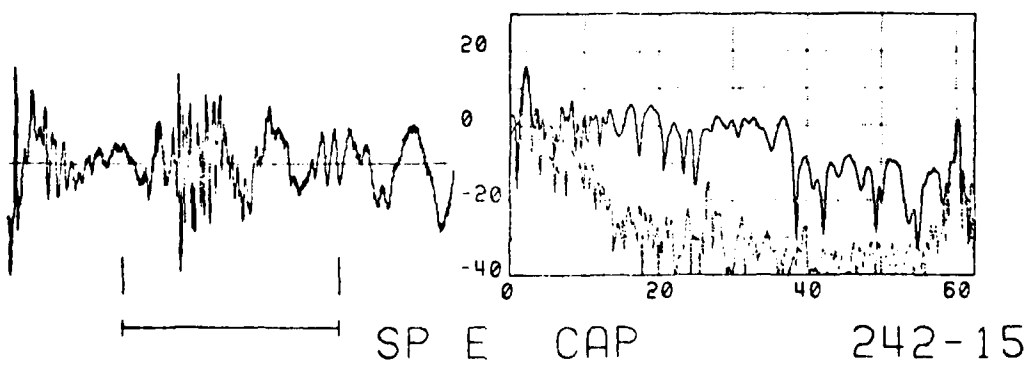
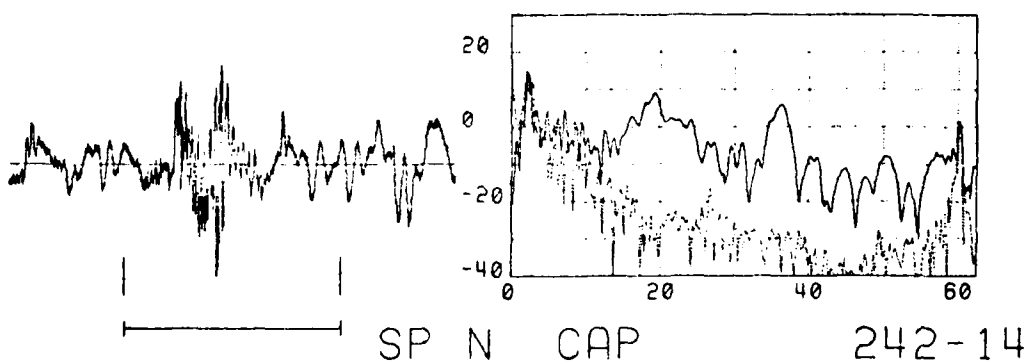
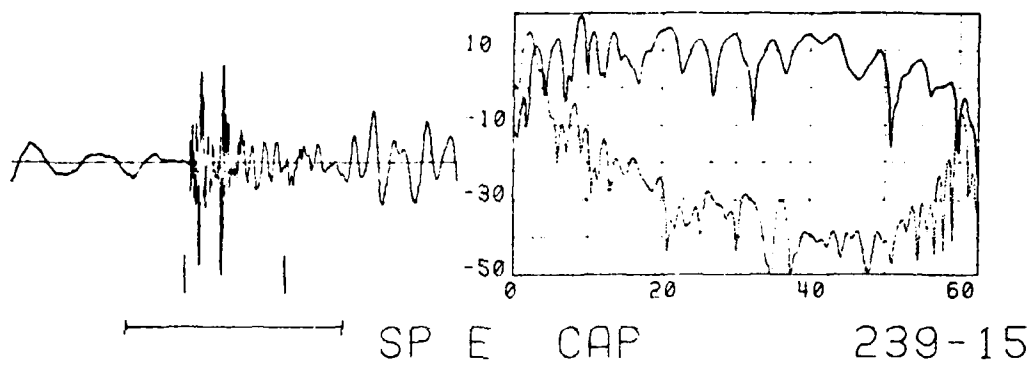
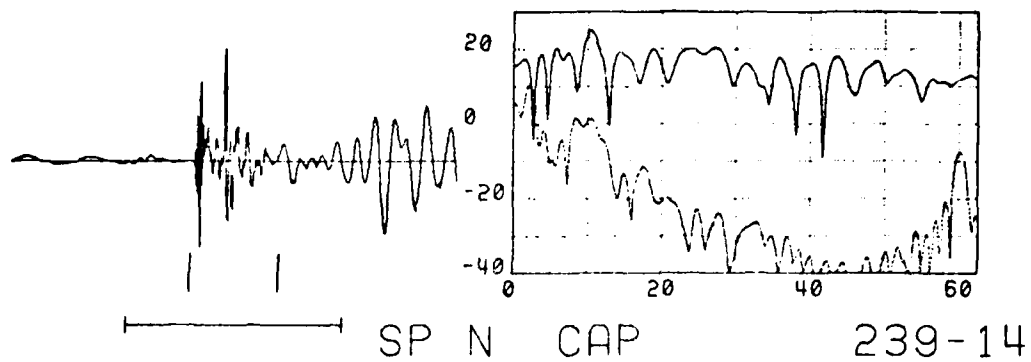
239-2

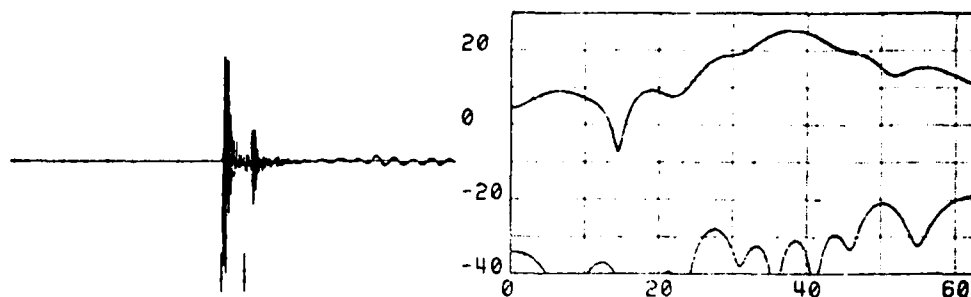






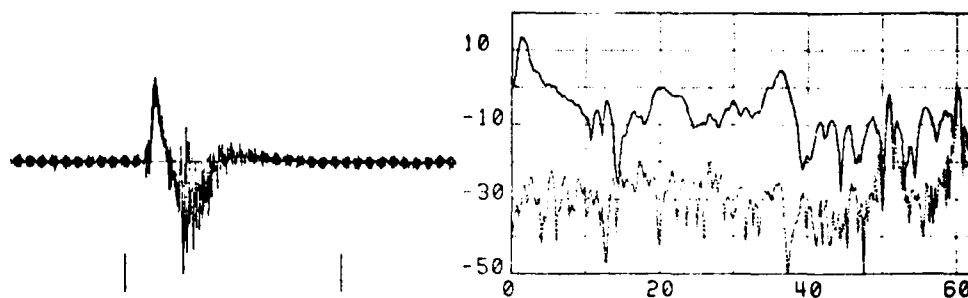






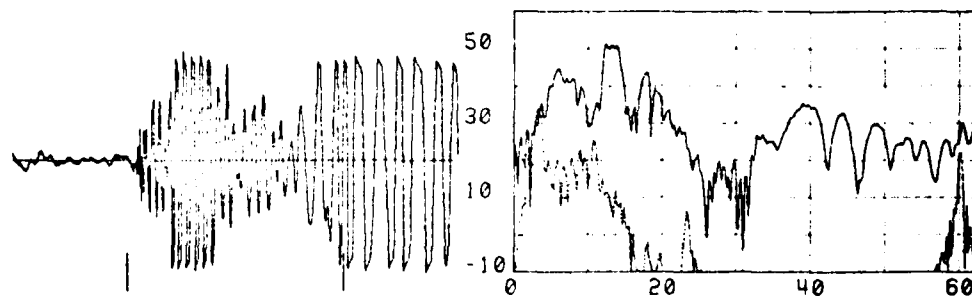
BIO H CAP

239-18



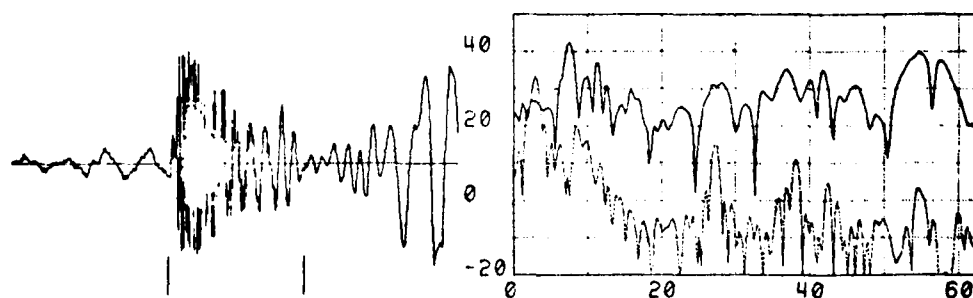
BIO H CAP

242-18



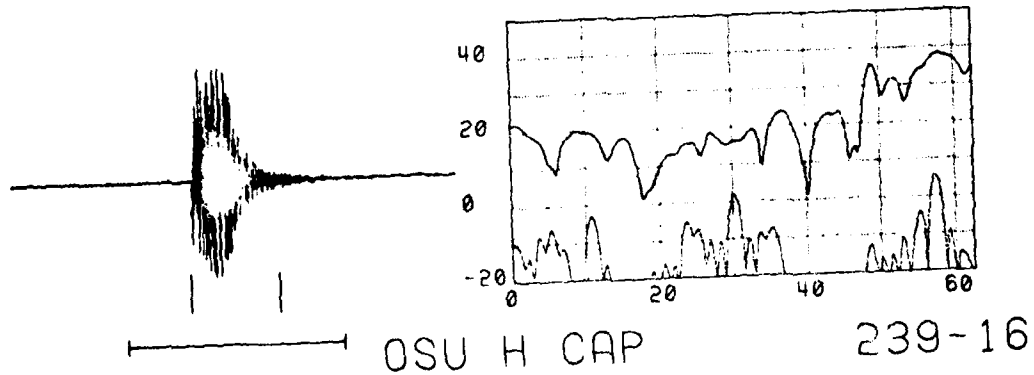
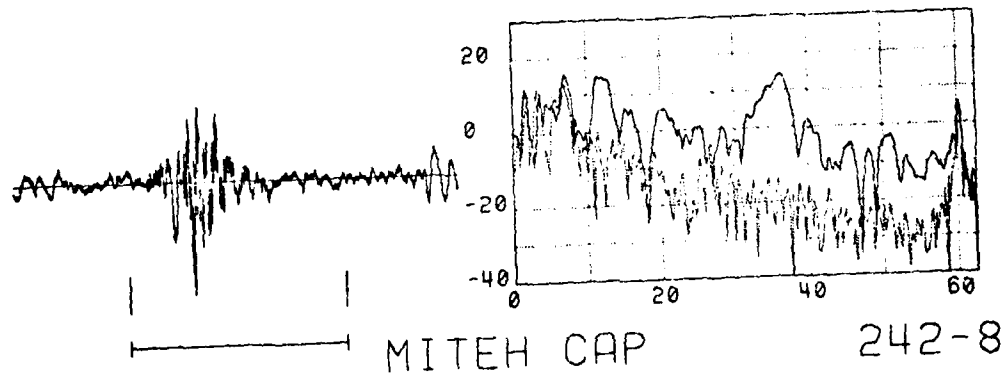
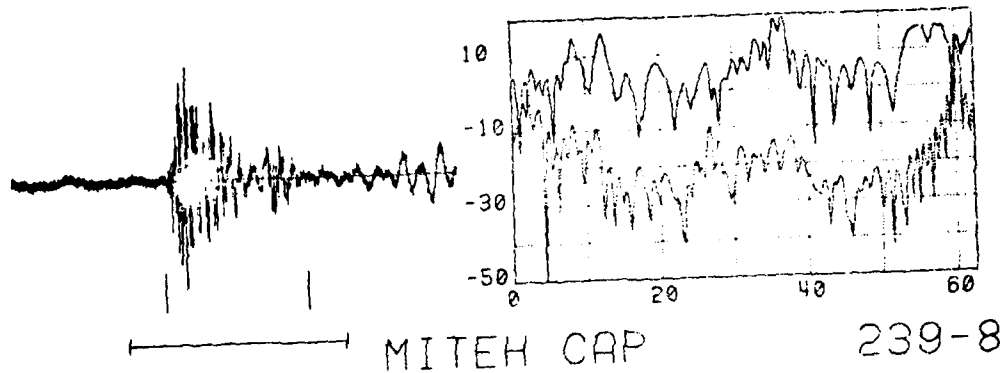
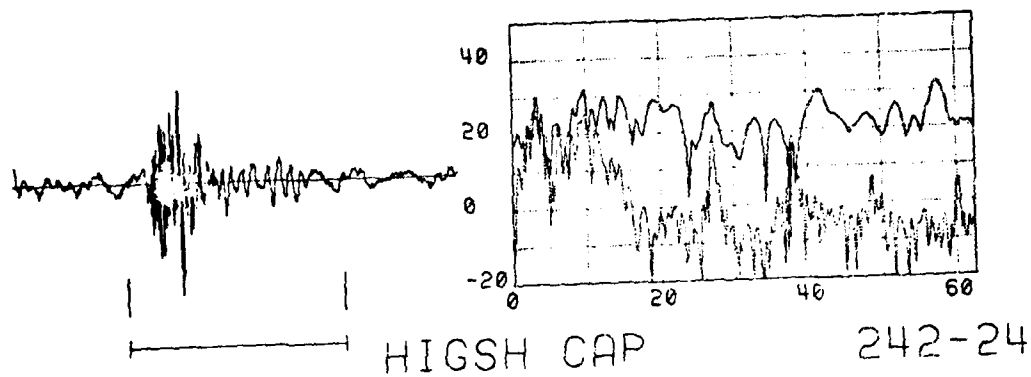
HIGBH AG182

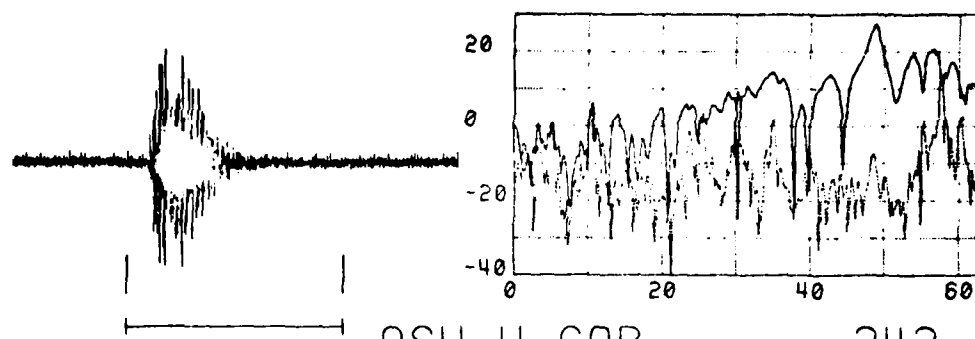
220-19



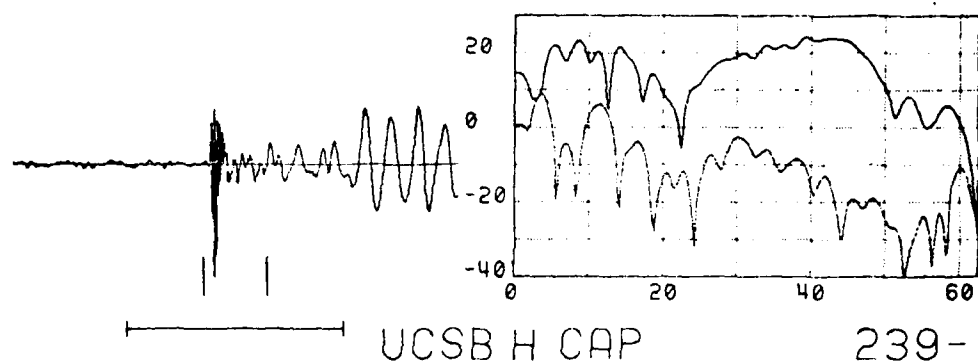
HIGSH CAP

239-24

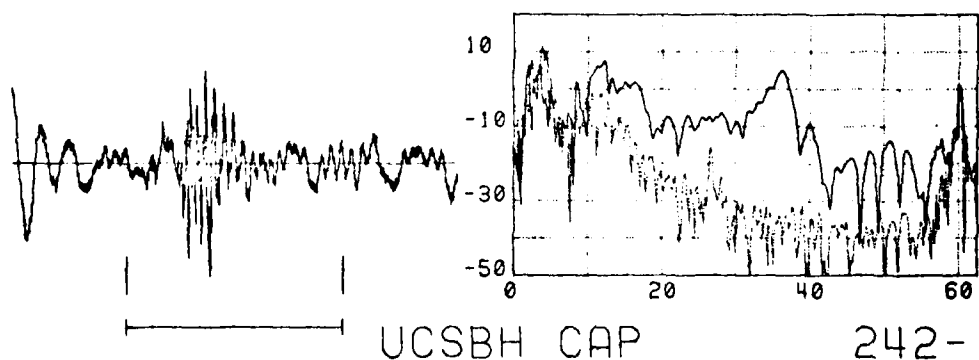




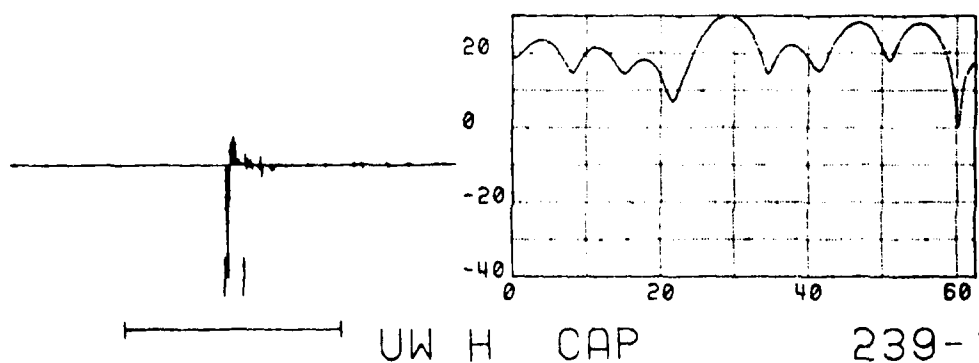
242-16



239-17

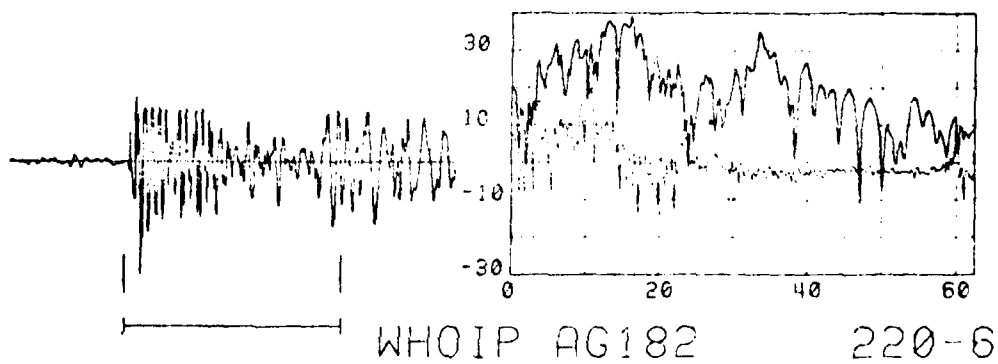
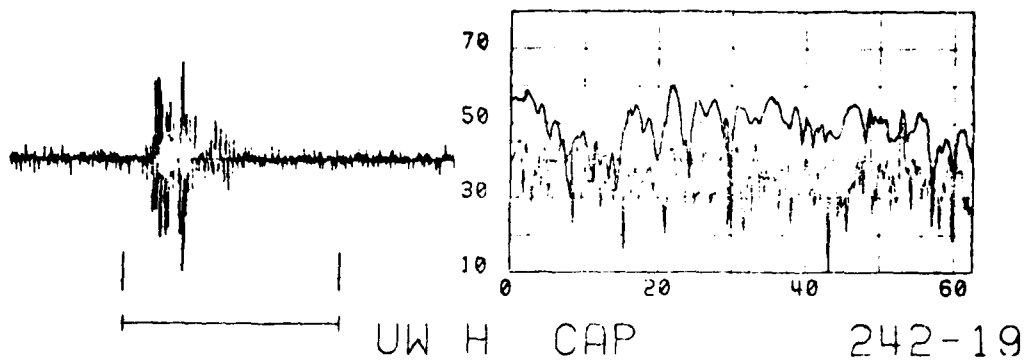


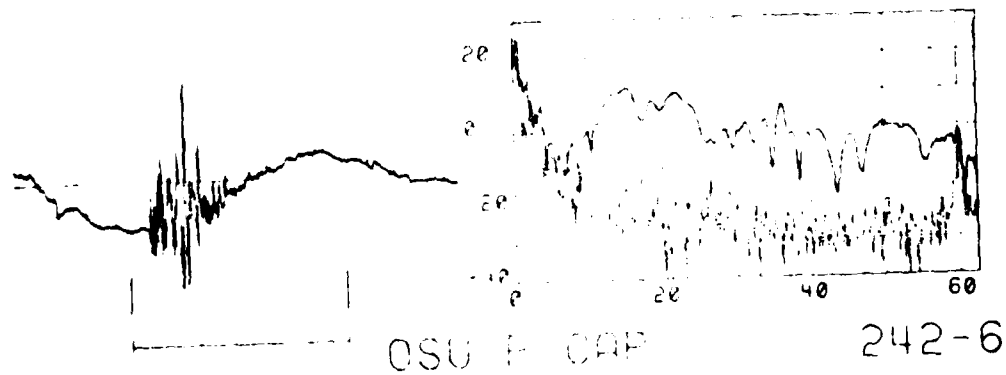
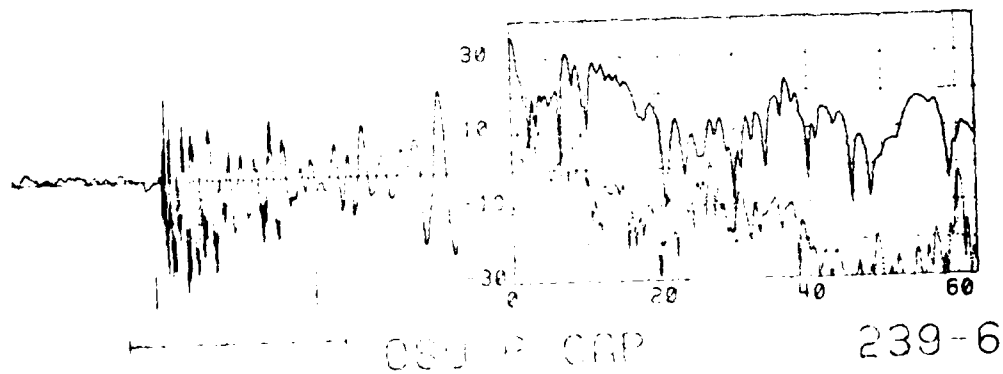
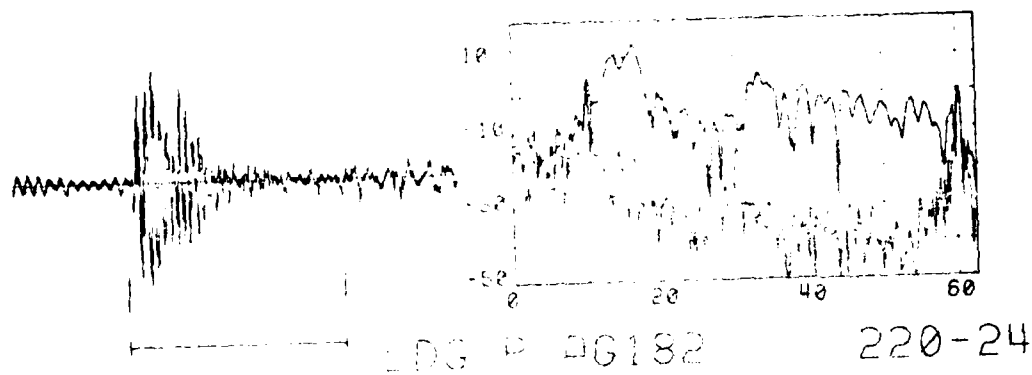
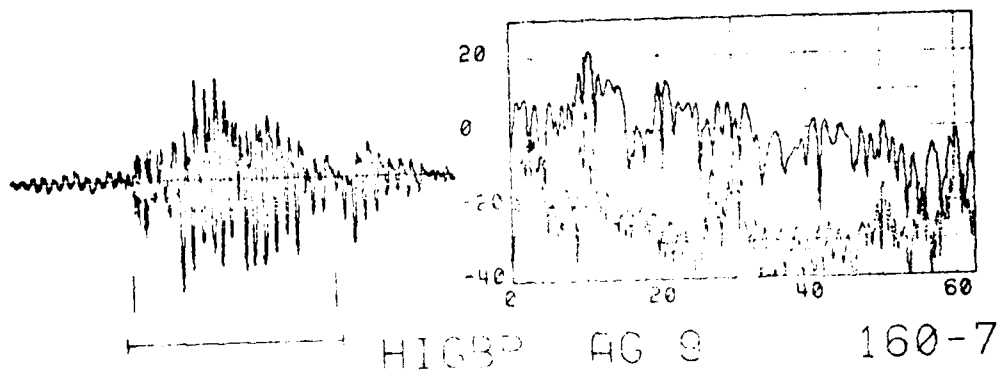
242-17



239-19

C-30





Appendix D

NOISE STUDIES

NOISE STUDIES

The figures in this appendix are discussed in section V of this report. Figures D4 to D5 were computed from the hourly noise samples of June 25, 1978. The spectra are listed according to the current rank from Figure V-12. The number 1 represents a noise sample from the hour in which the weakest current was measured and 12 corresponds to the strongest current. The spectra are labeled with the sensor name and digital record number from Appendix B. For LDCO and HIGS components, noise samples were taken during the last four sampling periods only.

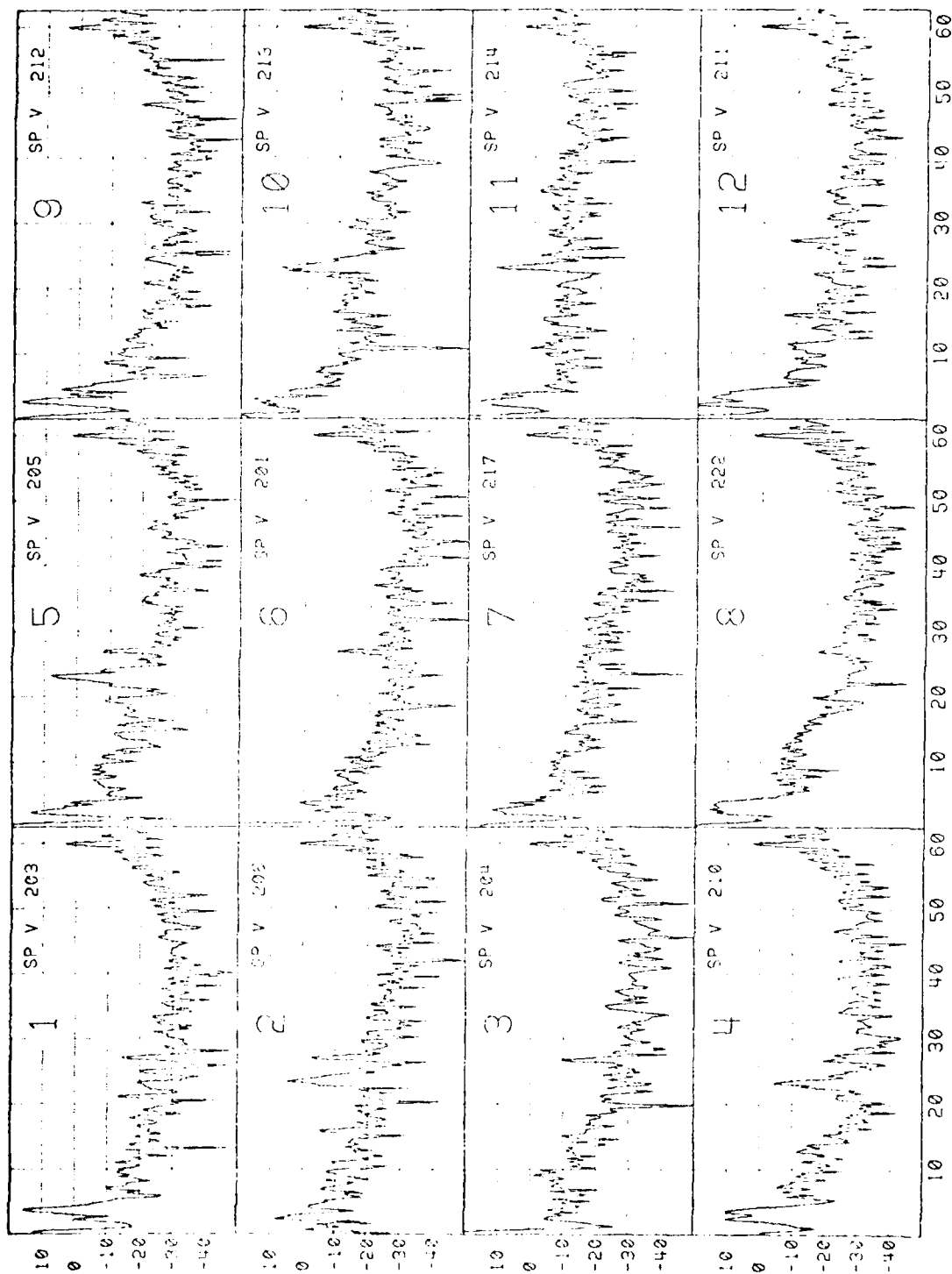
Details of the spectral analysis are given here. The hourly noise samples were about 1 or 2 min long. From these samples, the "most quiet" 10% digital sample block (about 4 sec) was decimated to 512 sample points and windowed with a 10% cosine window. A Fast Fourier Transform was used to produce a 256-point power spectrum with a Nyquist frequency of 62.5 Hz. The power spectral estimates are plotted in dB referenced to one digital unit.

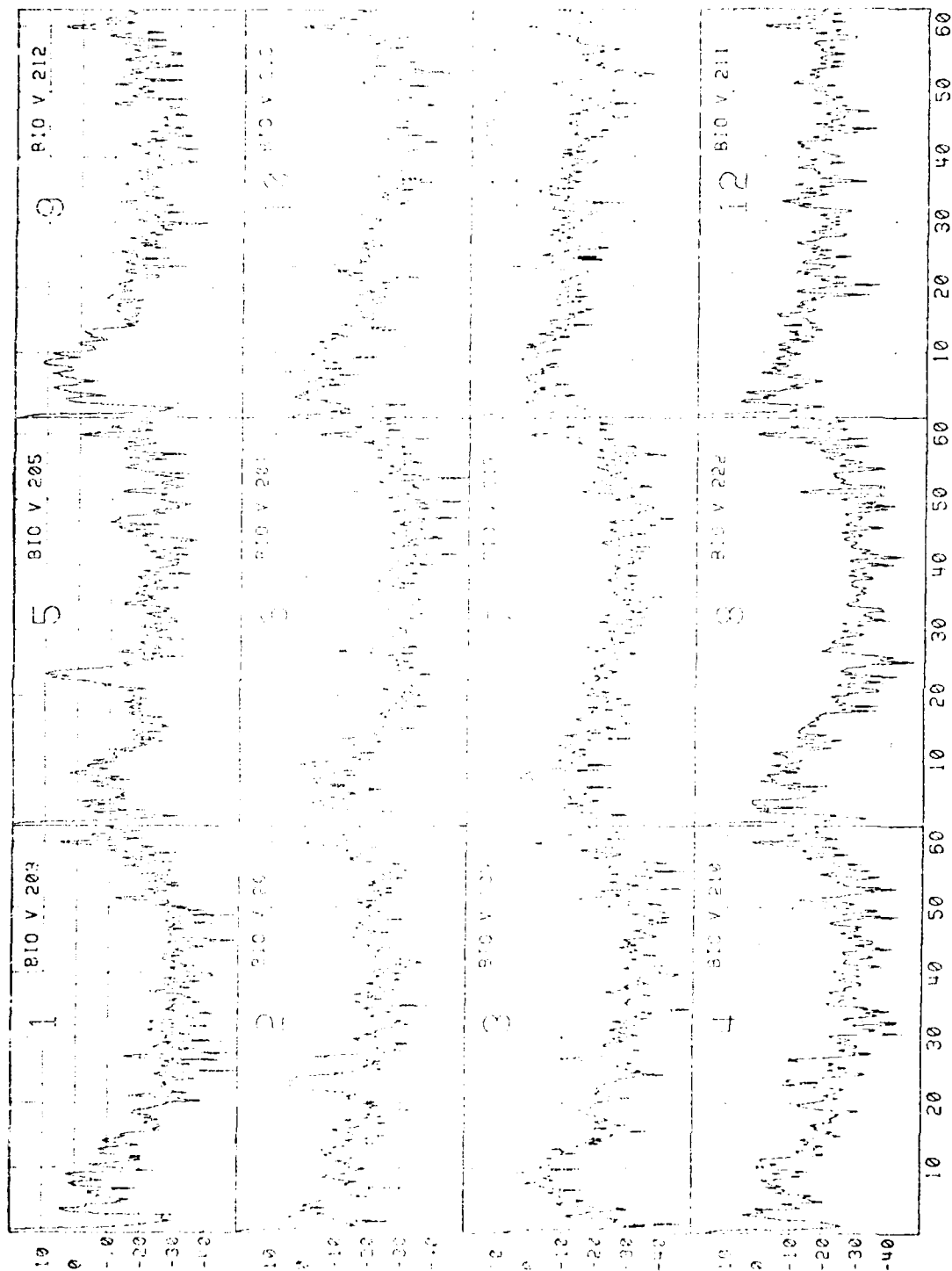
Figures D6 to D17 contain averaged spectra for each current rank from Figure V-12. These averaged spectra were computed in order to verify the statistical reliability of the previous spectra, each of which was computed from just one 4-sec data block.

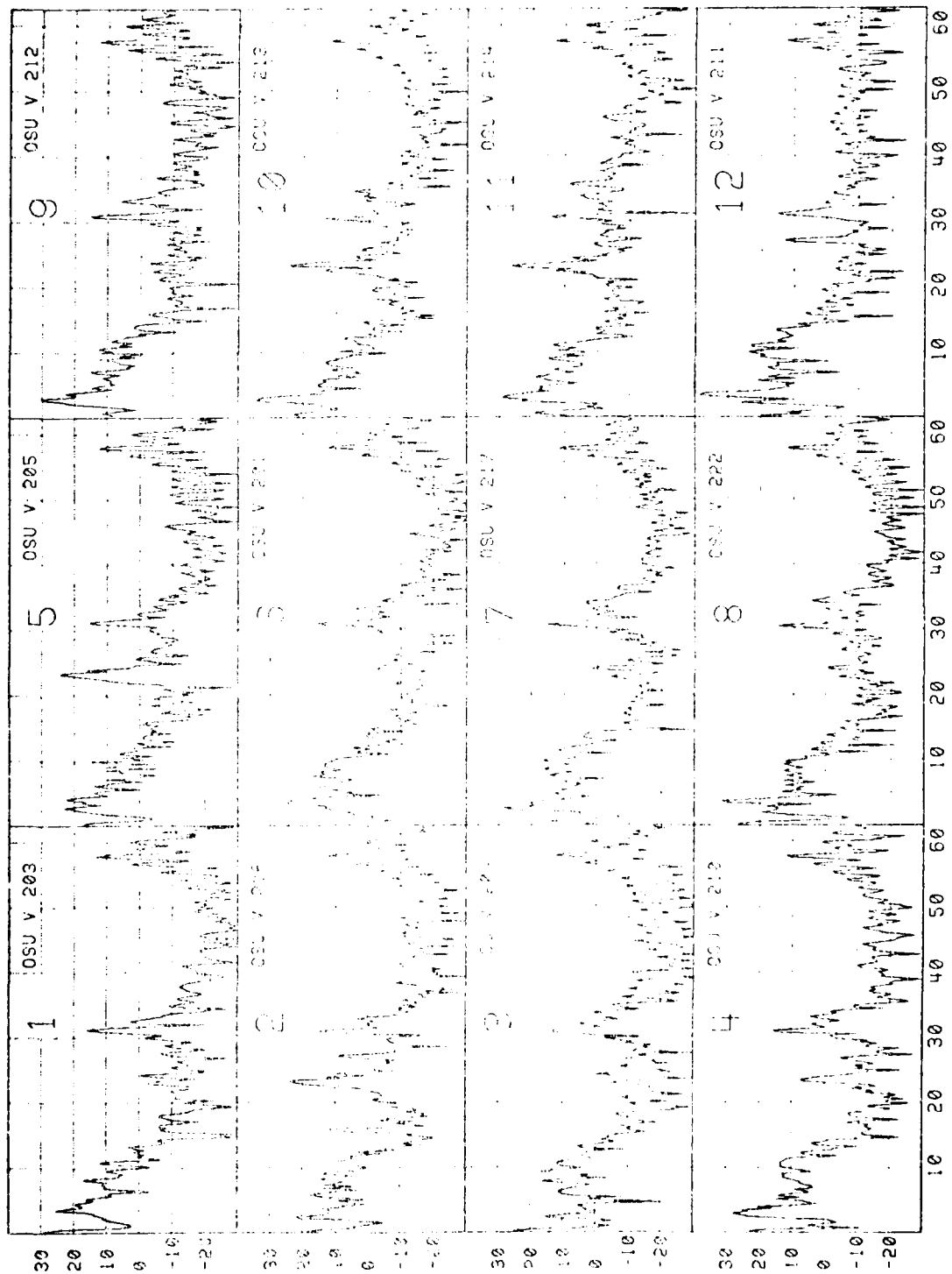
For each hourly noise sample three plots were made for the SPV and QASPV components. The topmost plot is the average of N amplitude spectra with upper and lower two-sigma confidence intervals. Each such spectrum represents an interval of $N \times 4$ sec, where N is the number of spectra averaged. The middle plot is of the sample variance divided by N . The bottom plot shows the sample standard deviation at each spectral frequency divided by the mean spectral estimate at each frequency. There are 256 spectral frequencies covering the range 0.24 to 62.5 Hz. In all three plots the vertical scale is in decibels and the horizontal scale is in Hertz. The last two plots may be used to examine the amount of randomness in signals producing spectral peaks.

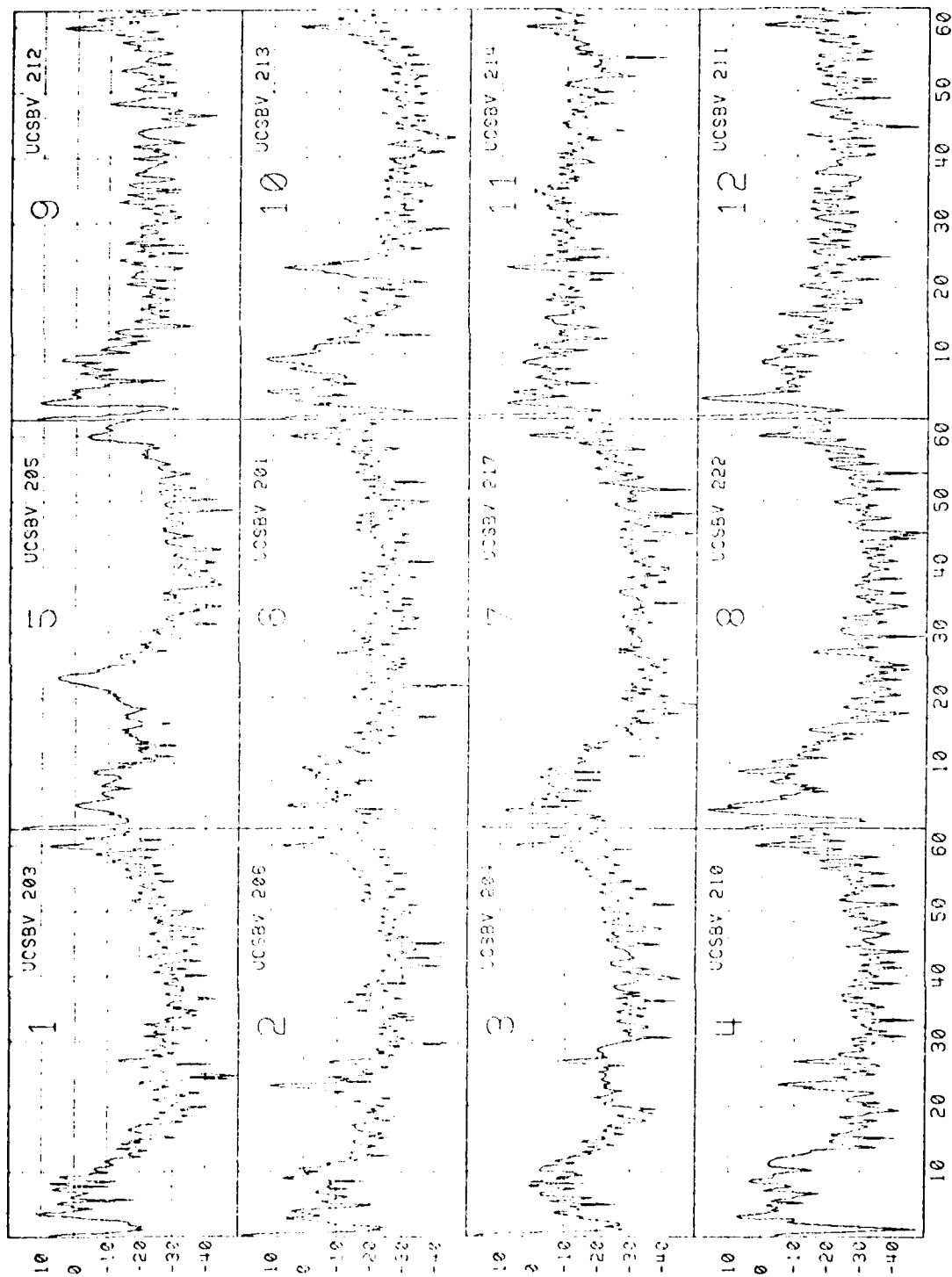
INDEX TO APPENDIX D

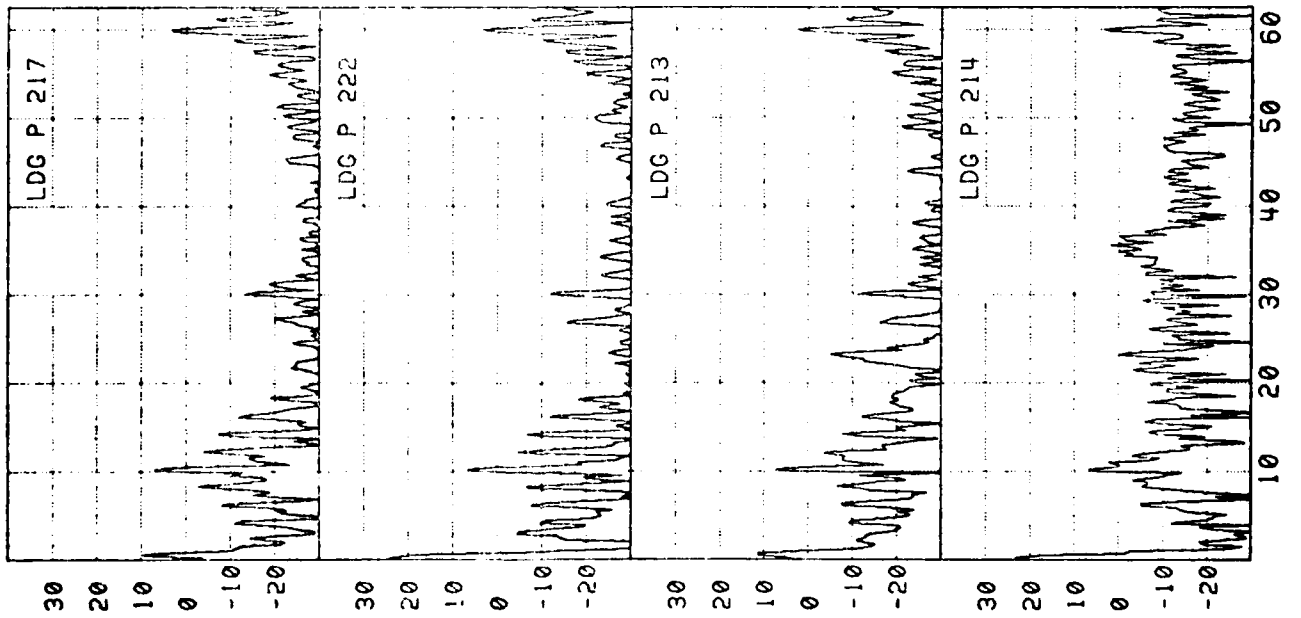
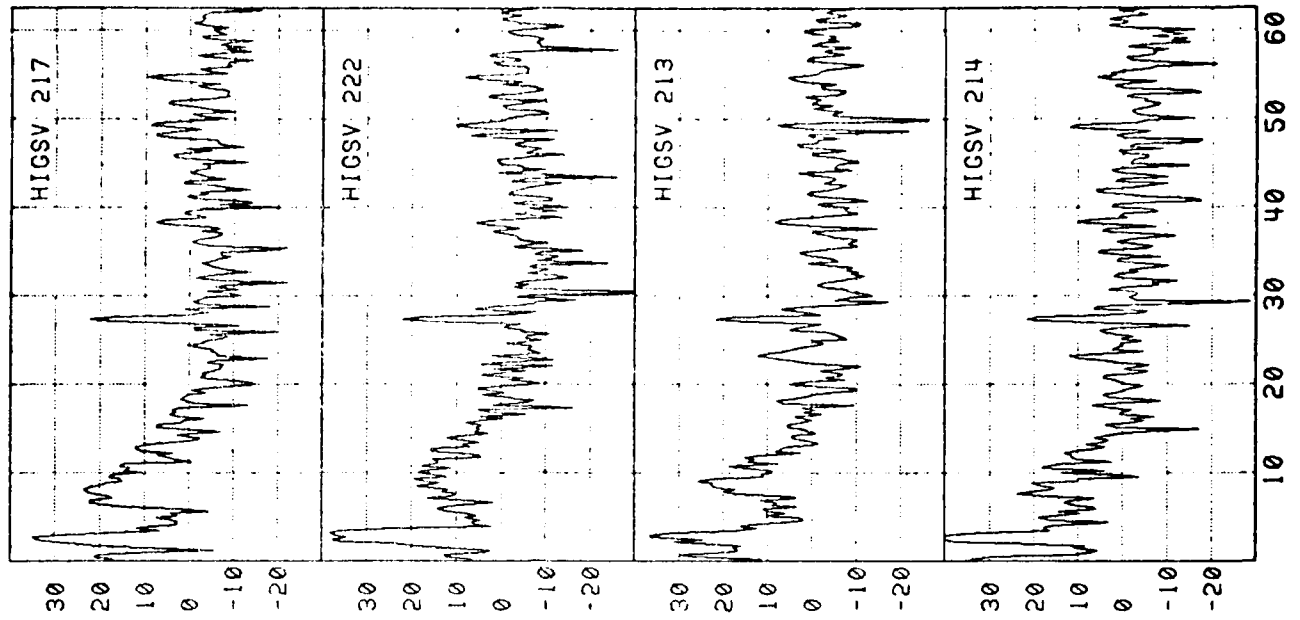
<u>Page</u>	<u>Sensor</u>	<u>Data</u>
D-1	SPV	Noise spectra
D-2	BIOV	"
D-3	OSUV	"
D-4	UCSBV	"
D-5	LDGOP and HIGSV	Noise spectra comparison
D-6 to D-17	SPV and UCSBV	Noise statistics comparison

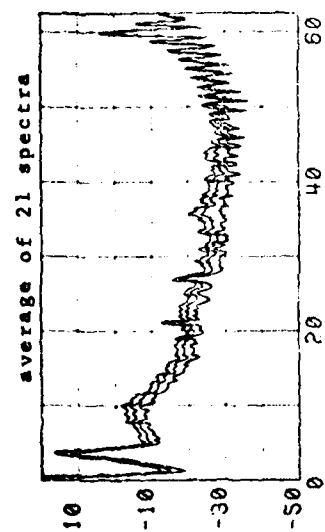




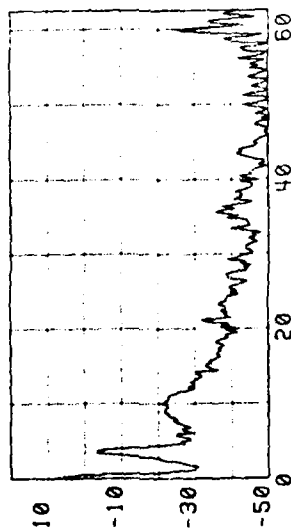




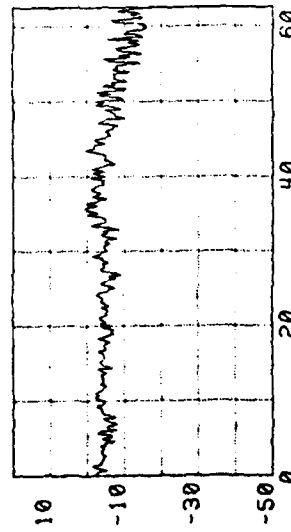




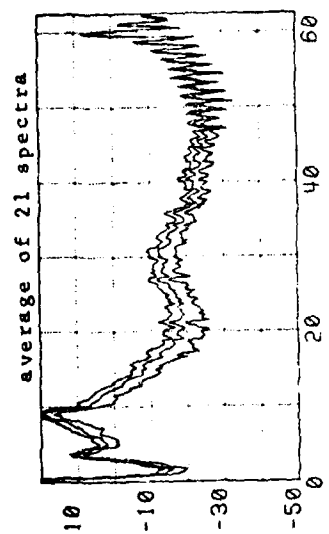
SP V NOISE 203-1



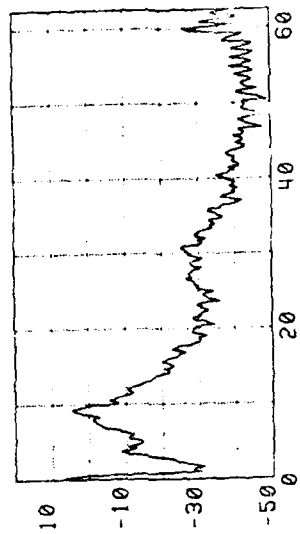
SP V VAR/N 203-1



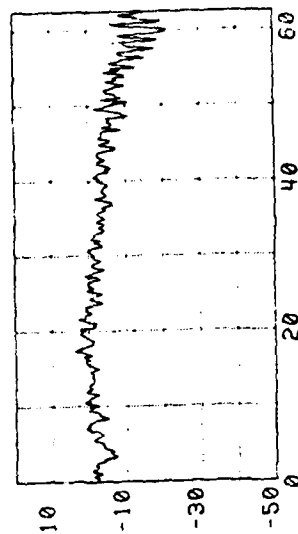
SP V SD/MEAN 203-1



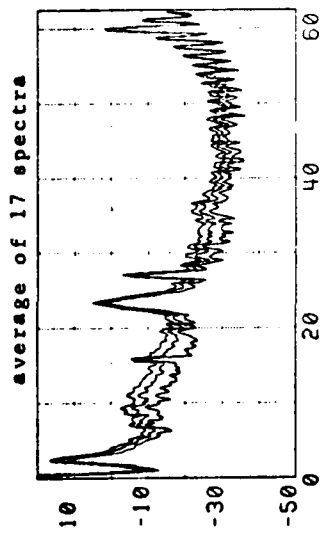
UCSBV NOISE 203-22



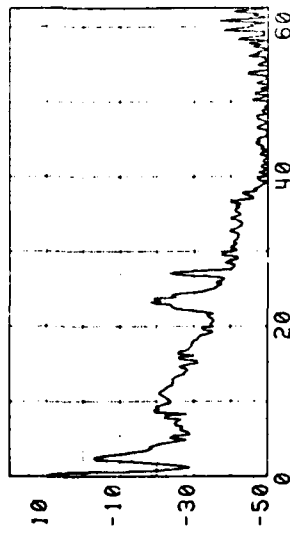
UCSEV VAR/N 203-22



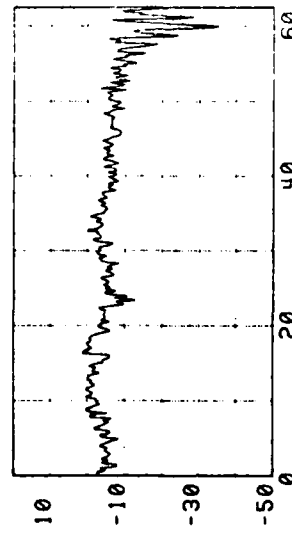
UCSBV SD/MEAN 203-22



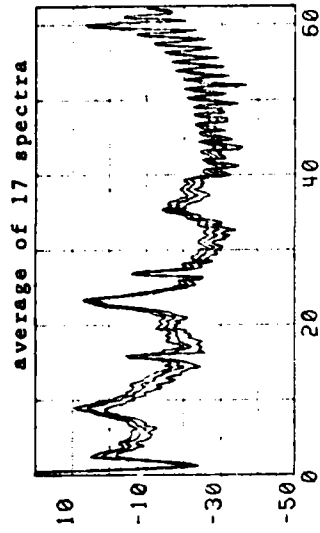
SP V NOISE 206-1



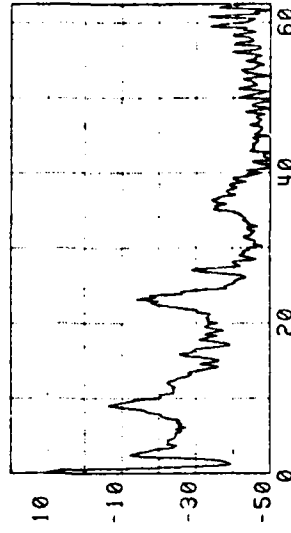
SP V VAR/N 206-1



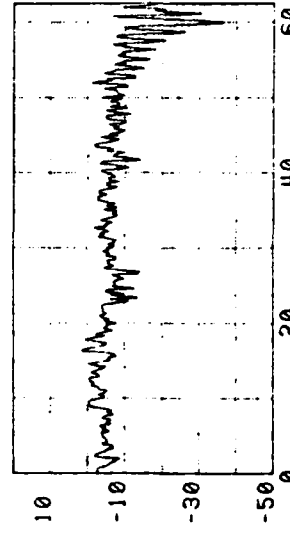
SP V SD/MEAN 206-1



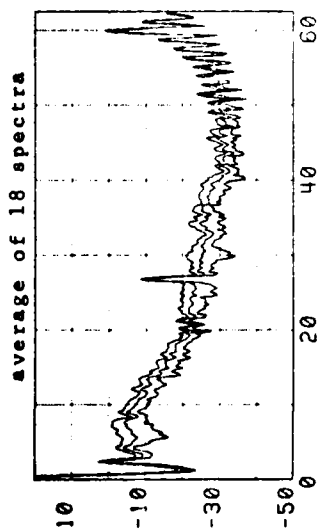
UCSBV NOISE 206-22



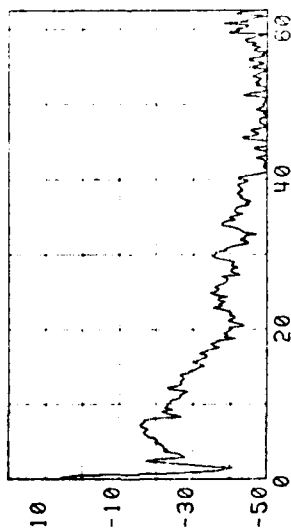
UCSBV VAR/N 206-22



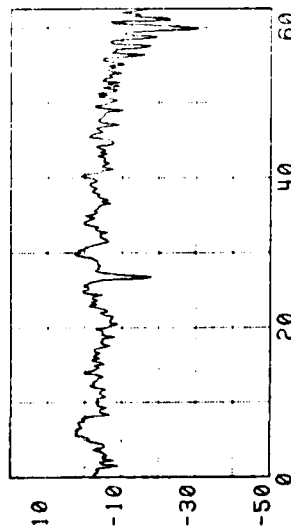
UCSBV SD/MEAN 206-22



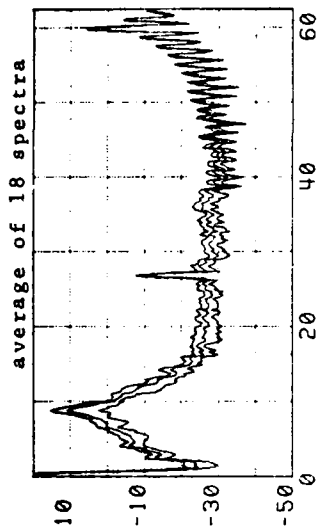
SP V NOISE 204-1



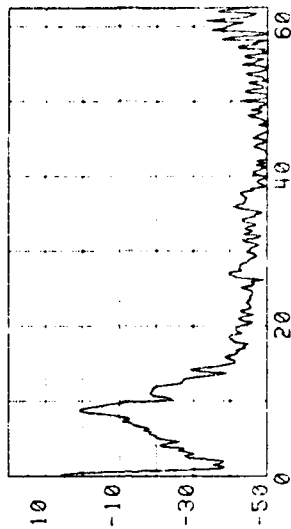
SP V VAR/N 204-1



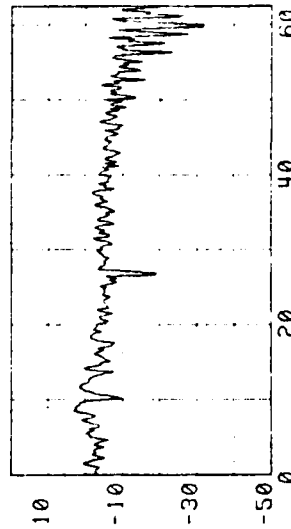
SP V SD/MEAN 204-1



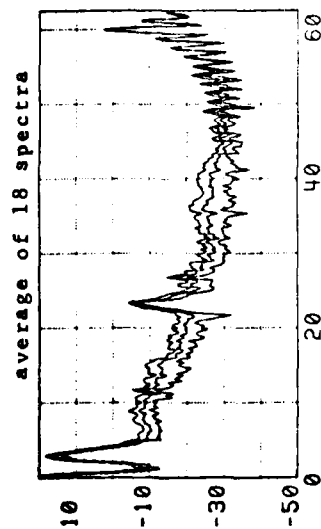
UCSBV NOISE 204-22



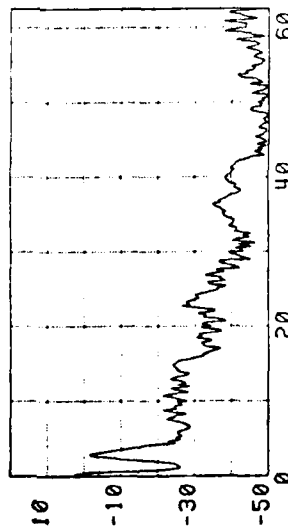
UCSBV VAR/N 204-22



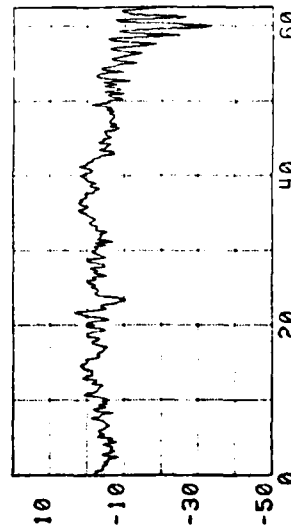
UCSBV SD/MEAN 204-22



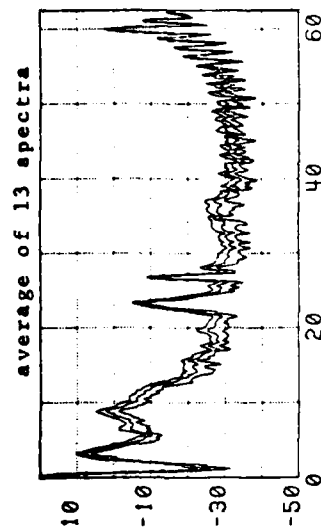
SP V NOISE 210-1



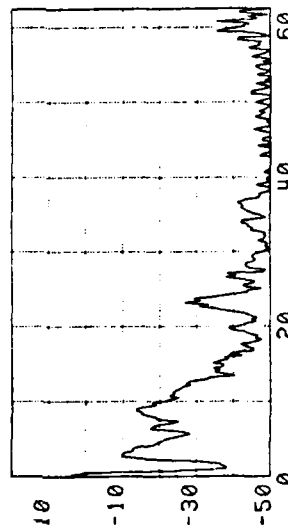
SP V VARIANCE 210-1



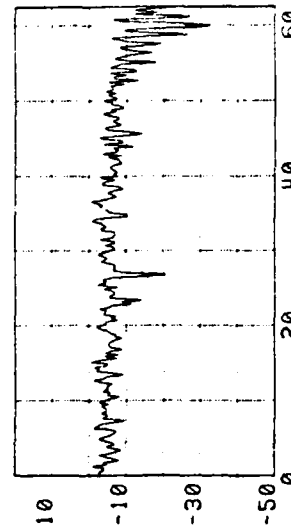
SP V SD/MEAN 210-1



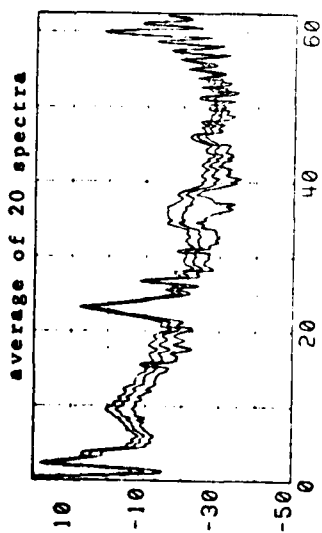
UCSBV NOISE 210-22



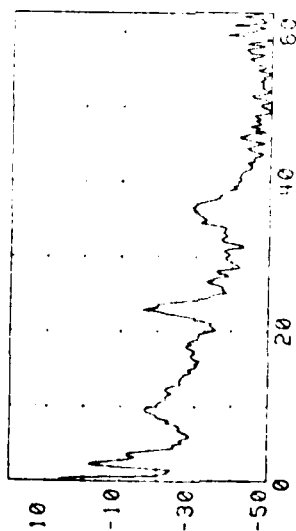
UCSBV VARIANCE 210-22



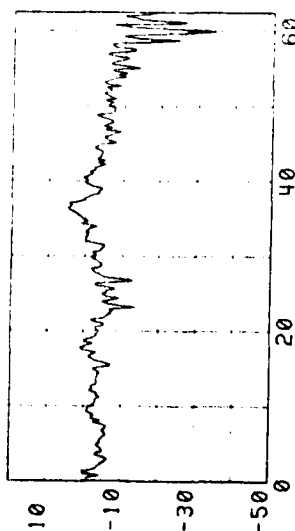
UCSBV SD/MEAN 210-22



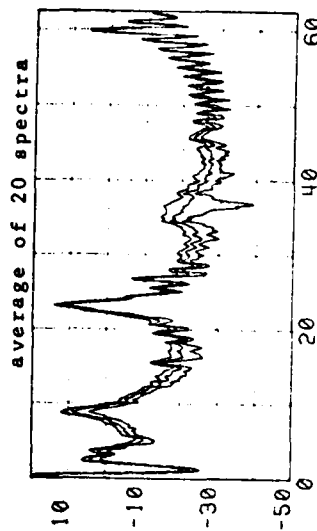
SP V NOISE 205-1



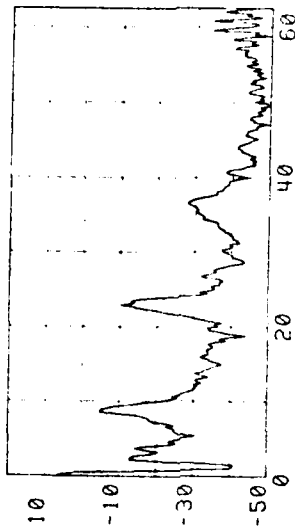
SP V VAR/N 205-1



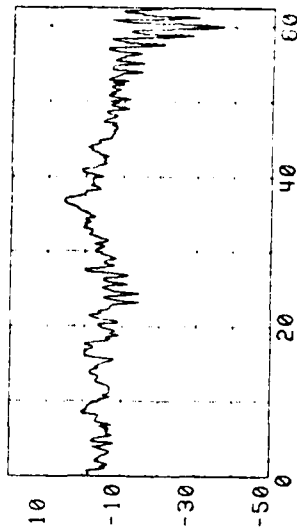
SP V SD/MEAN 205-1



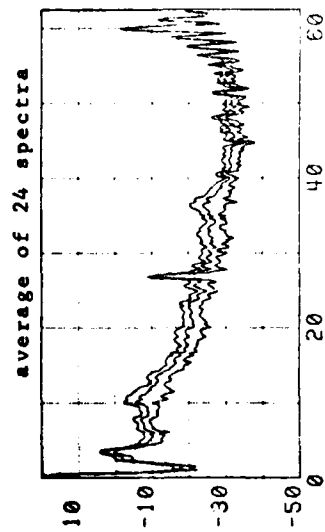
UCSBV NOISE 205-22



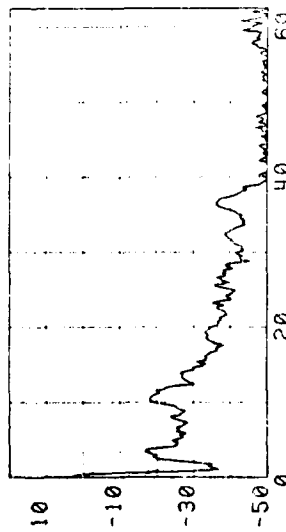
UCSBV VAR/N 205-22



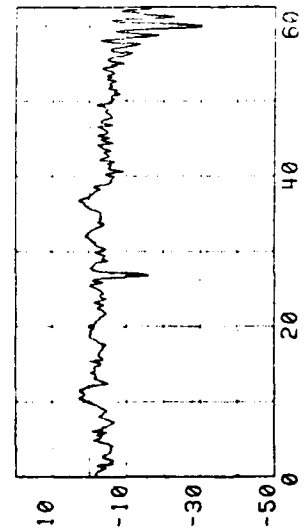
UCSBV SD/MEAN 205-22



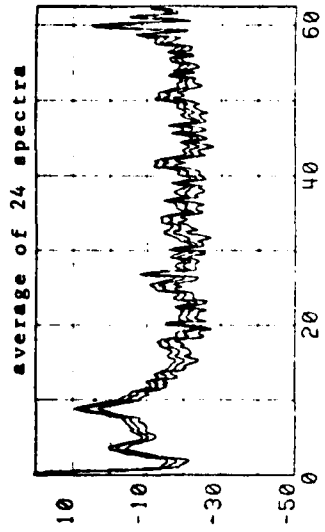
SP V NOISE 201-1



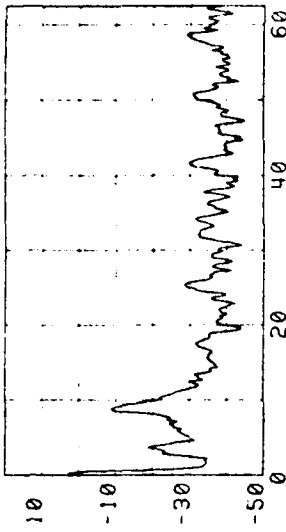
SP V VAR/N 201-1



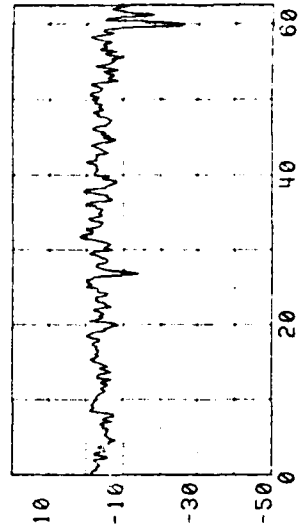
SP V SD/MEAN 201-1



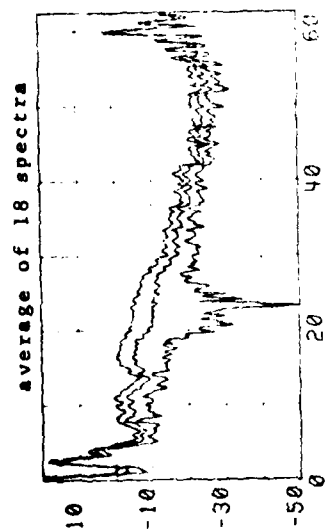
UCSBV NOISE 201-22



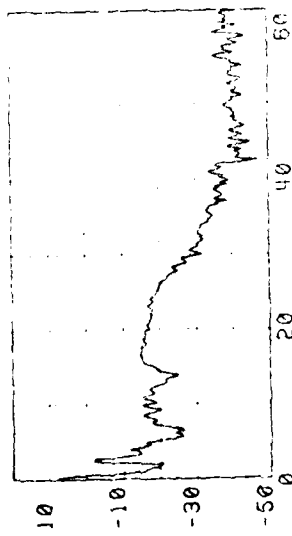
UCSBV VAR/N 201-22



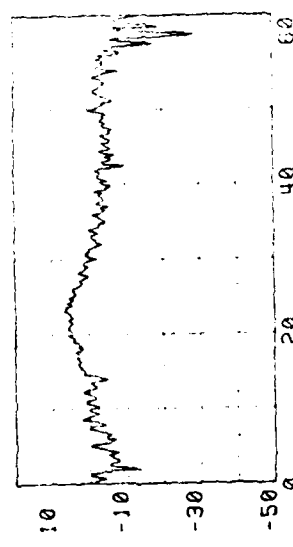
UCSBV SD/MEAN 201-22



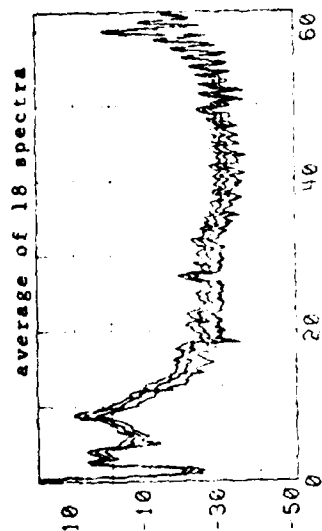
SP V NOISE 217-1



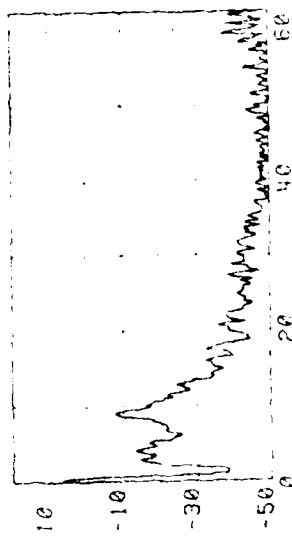
SP V VAR/N 217-1



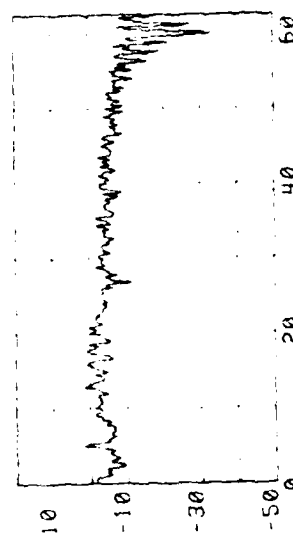
SP V SD/MEAN 217-1



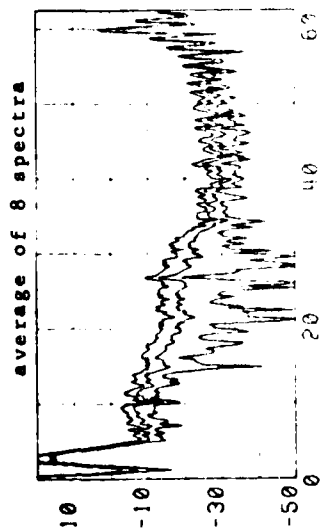
UCSBV NOISE 217-22



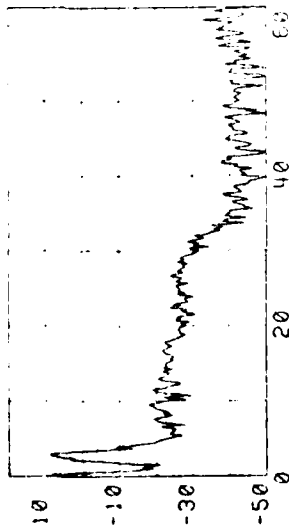
UCSBV VAR/N 217-22



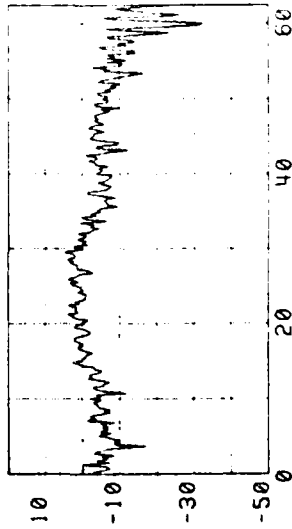
UCSBV SD/MEAN 217-22



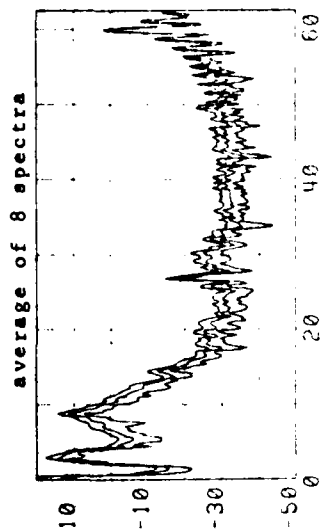
SP V NOISE 222-1



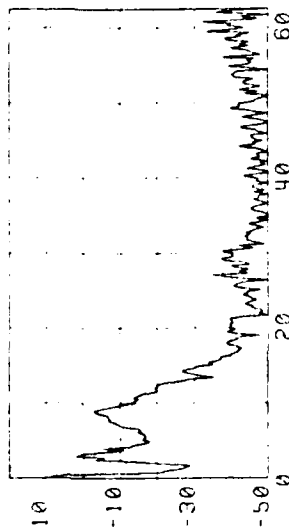
SP V VAR/N 222-1



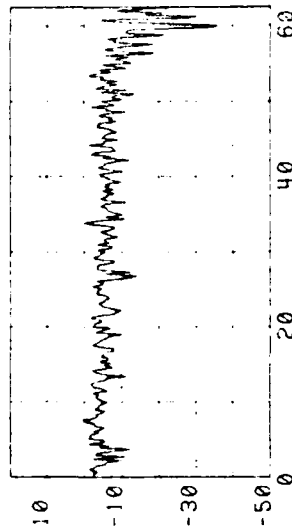
SP V SD/MEAN 222-1



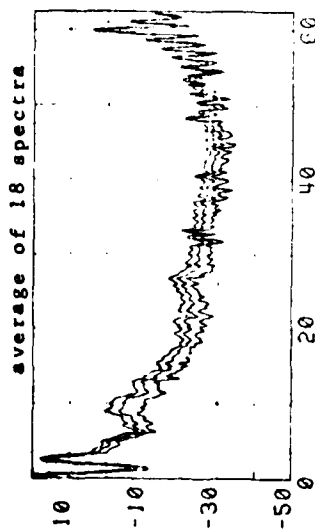
UCSBV NOISE 222-22



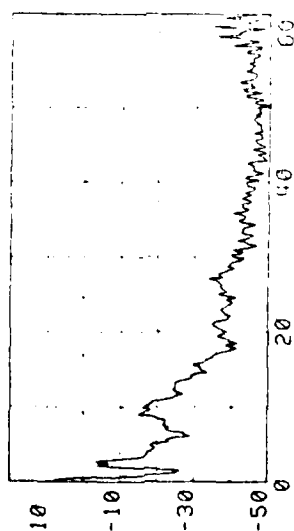
UCSBV VAR/N 222-22



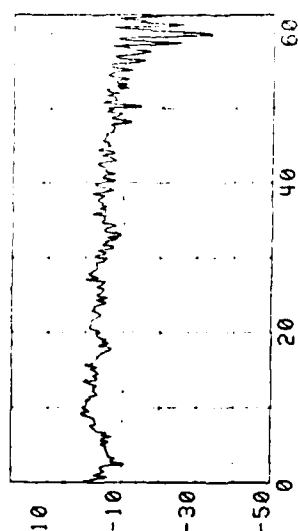
UCSBV SD/MEAN 222-22



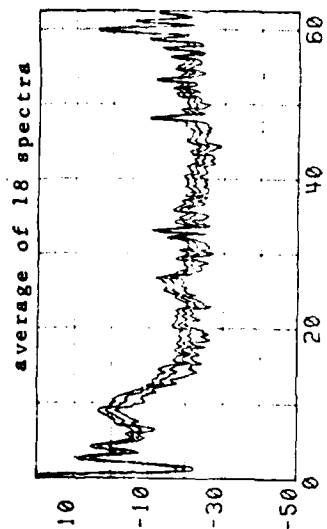
SP V NOISE 212-1



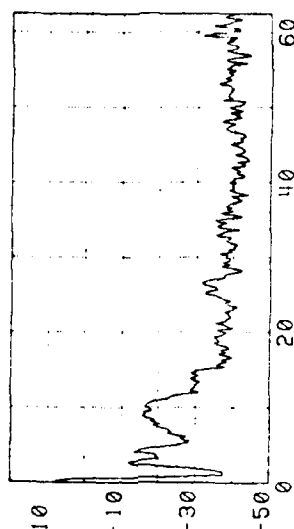
SP V VAR/N 212-1



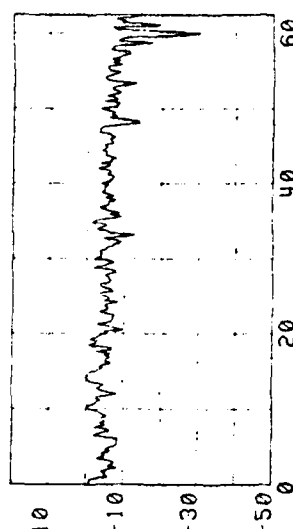
SP V SD/MEAN 212-1



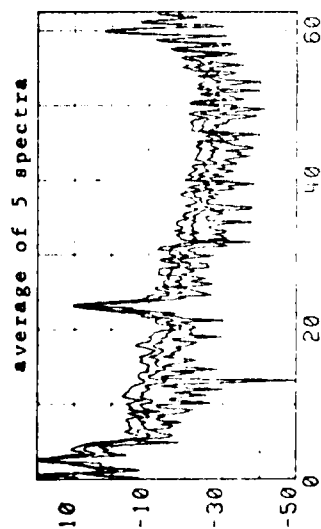
UCSBV NOISE 212-22



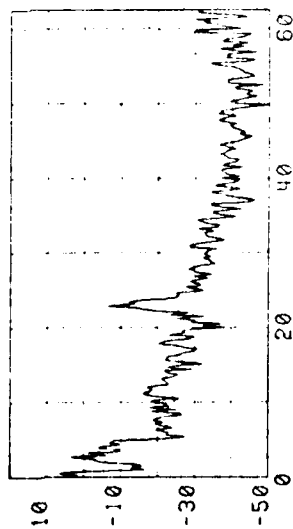
UCSBV VAR/N 212-22



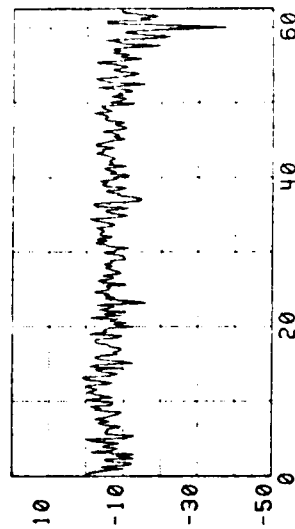
UCSBV SD/MEAN 212-22



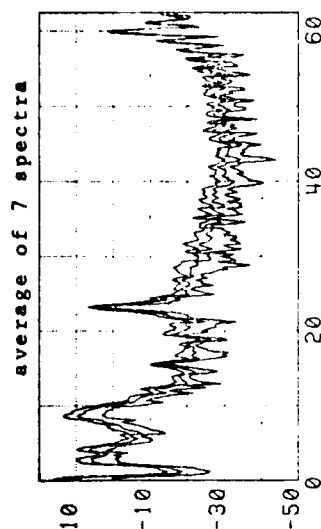
SP V NOISE 213-1



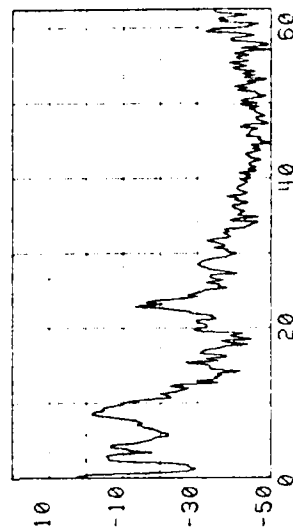
SP V VAR/N 213-1



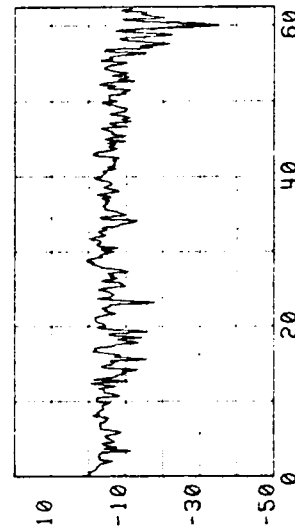
SP V SD/MEAN 213-1



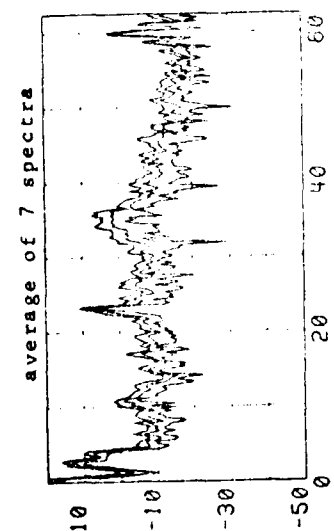
UCSBV NOISE 213-22



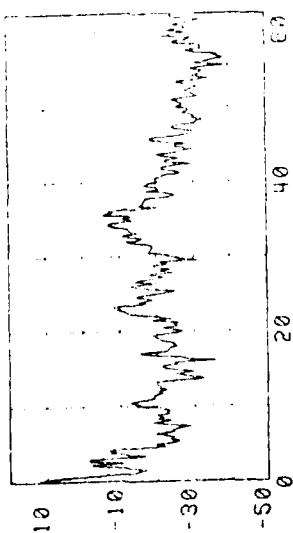
UCSBV VAR/N 213-22



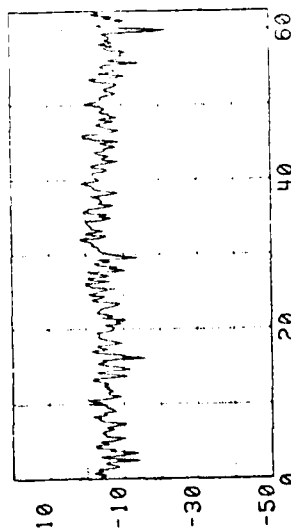
UCSBV SD/MEAN 213-22



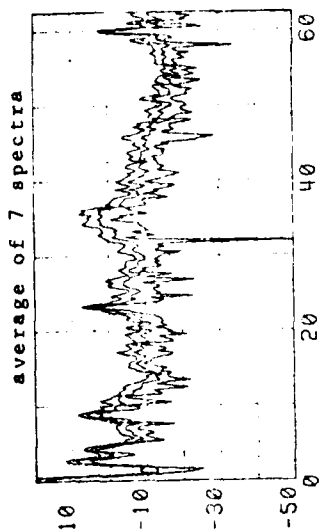
SP V NOISE 214-1



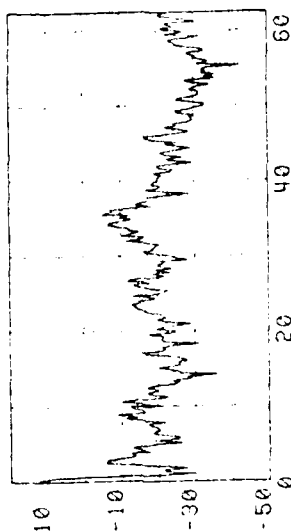
SP V VAR/N 214-1



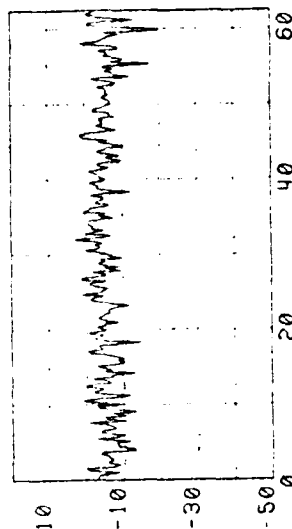
SP V SD/MEAN 214-1



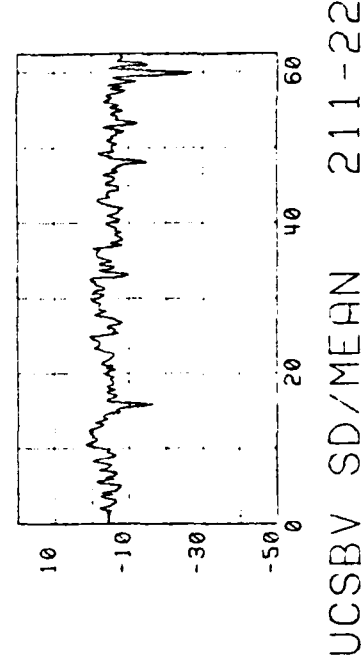
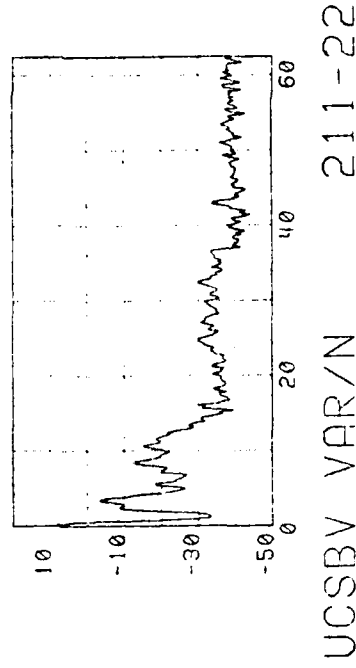
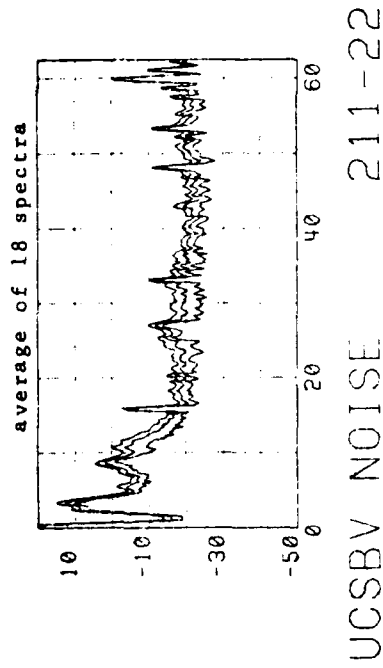
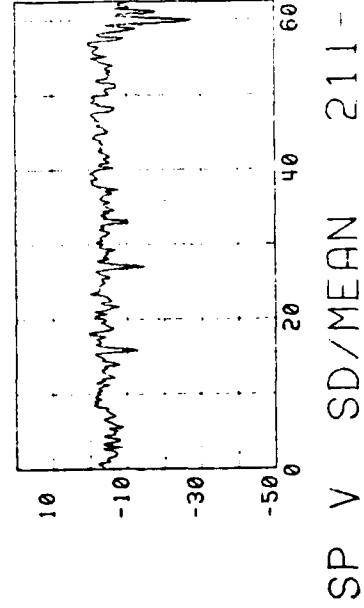
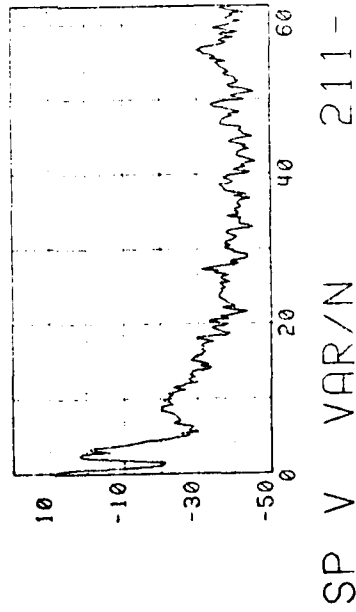
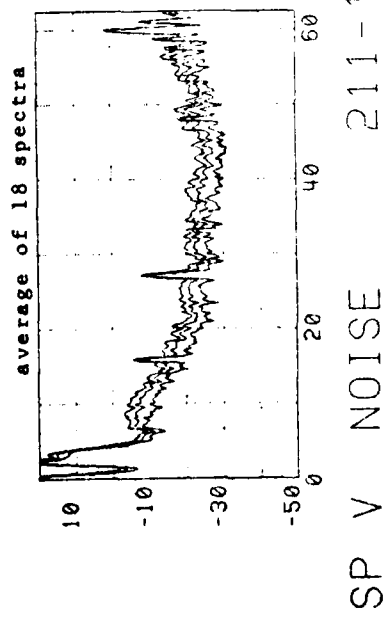
UCSBV NOISE 214-22



UCSBV VAR/N 214-22



UCSBV SD/MEAN 214-22



Appendix E

COUPLING OF OCEAN BOTTOM SEISMOMETERS
TO SOFT BOTTOMS

COUPLING OF OCEAN BOTTOM SEISMOMETERS
TO SOFT BOTTOMS

G. H. Sutton, F. K. Duennebier, and B. Iwatake

Hawaii Institute of Geophysics
University of Hawaii
Honolulu, Hawaii 96822

Abstract

Unlike response of seismometers resting on hard rock where the seismometer case moves with the rock to high frequencies, the response of ocean bottom seismometers (OBS) can be strongly affected by the low mechanical strength of ocean sediments. The motion as measured by the seismometer will not follow the expected relationships between pressure and particle motion for different wave types. Cross coupling between horizontal and vertical motions can occur, especially when there is differential motion between water and sediment. Resonant amplification and attenuation of higher frequencies also occur. Secondary seismic arrivals are especially subject to distortion. Overall response is strongly dependent upon the mass and configuration of the OBS and the rigidity and density of the bottom material. Tests at Lopez Island, Puget Sound using both directly applied mechanical transients and seismic signals with various instrument configurations demonstrate the above effects and provide some guidance for improved designs.

Introduction

The usual reason for placing a seismometer anywhere is to measure free-field particle motion in response to some seismic source. The presence of the seismometer does not usually modify the particle motion at seismic frequencies if care is taken to emplace the instrument on a relatively rigid spot. On the ocean floor, however, the most common plant is thick, soft, low-velocity sediment. For this case, the presence of the seismometer can severely distort the free-field motion. In addition, the seismometer is emplaced at a boundary between a liquid and a solid, unlike land emplacement, and the effects of buoyancy can strongly affect the observed motion. The boundary also complicates the situation because strong differential motion can occur across it.

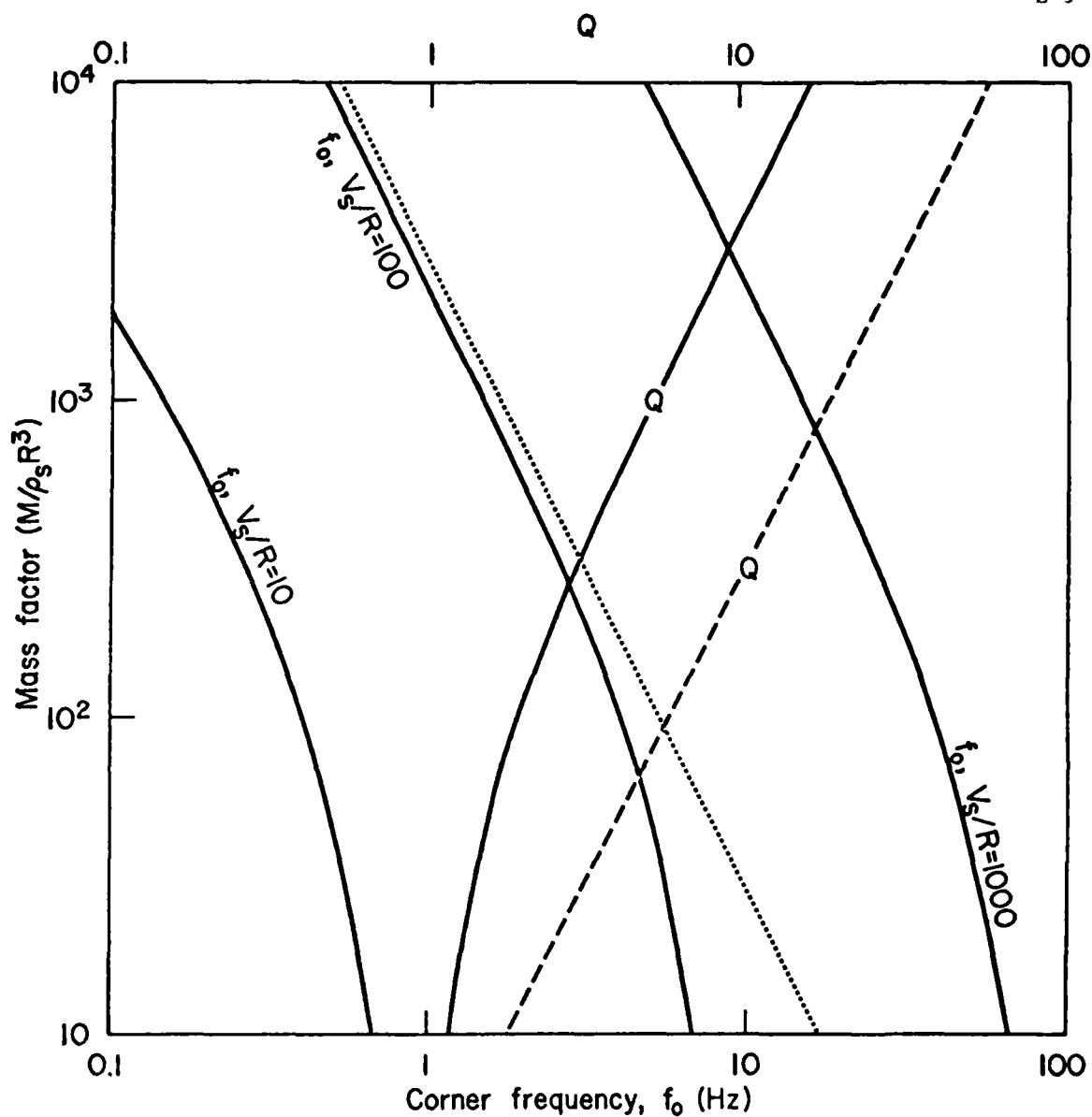
The problem to determine the response of an OBS to bottom motion is similar to that faced a number of years ago by geophysicists concerned with the response of prospecting geophones placed on compliant materials, with the additional complication of water motion and buoyancy forces (Washburn and Wiley, 1941; Wolf, 1944; Bycroft, 1956; Lamer, 1969).

For the prospecting case, the response depends principally on rigidity and density of soil and mass and bearing area of geophone. Damping results from reradiation of seismic energy as well as from internal dissipation (the latter is generally ignored) and depends upon the ratio of instrument radius to a (shear) wavelength. With low rigidities of ocean bottom sediments, these wavelengths can be shorter than we might first guess, e.g., for $V_s = 10$ m/s and $f = 100$ Hz, $\lambda = 10$ cm. The curves in Figure E-1 show corner (resonance) frequency and resonance amplification, Q , as functions of dimensionless instrument mass and ratio of shear velocity to instrument radius. For a given uniform bottom sediment, corner (resonance) frequency increases approximately as $(R/M)^{1/2}$ and Q increases as $(M/R^3)^{1/2}$ where R is the radius of the cross section in contact with the sediment and M is the instrument mass.

In this paper we provide a simple extension of the theory to include buoyancy forces (for vertical motion only), present the theory for a mechanical transient test designed to excite coupling resonances, and compare theoretical expectations with observational results obtained from special tests in Shoal Bay, Lopez Island, Puget Sound. Sutton et al. (1980), Zelikovitz and Prothero (1980), Tuthill et al. (1980), Lewis and Tuthill (1980), and Johnson and McAlister (1980) present additional results related to bottom coupling, based mainly on the Lopez Island OBS Intercomparison Experiment.

Observations

Figures E-2 and E-3 show a P arrival and spectra for arrivals from a local earthquake recorded in deep water off the southeast coast of the island of Hawaii on three standard HIG OBS's (HIGS, Sutton et al., 1977a).



Lamer, 1969 ———
 Wolf, 1944 - - - - -
 $f_0 = V_s/2R\sqrt{M/\rho_s R^3}$ ·····

Fig. E-1. Coupling frequency f_0 and resonance amplification, Q , of a mass, M , on the free surface of an elastic half space. R = radius of bearing area; V_s and ρ_s are shear velocity and density in the half space, respectively.

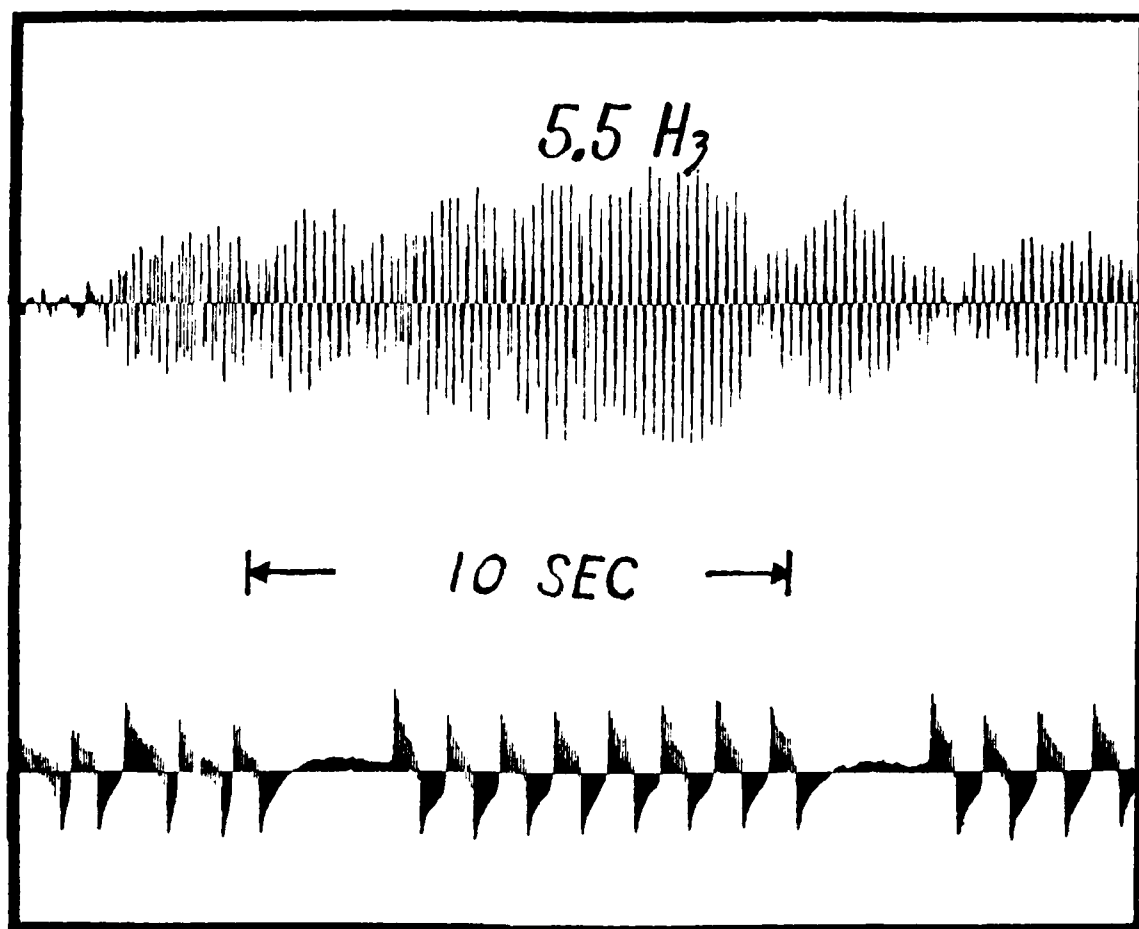


Fig. E-2. P wave from local earthquake recorded on an HIGS OBS in deep water off the island of Hawaii.

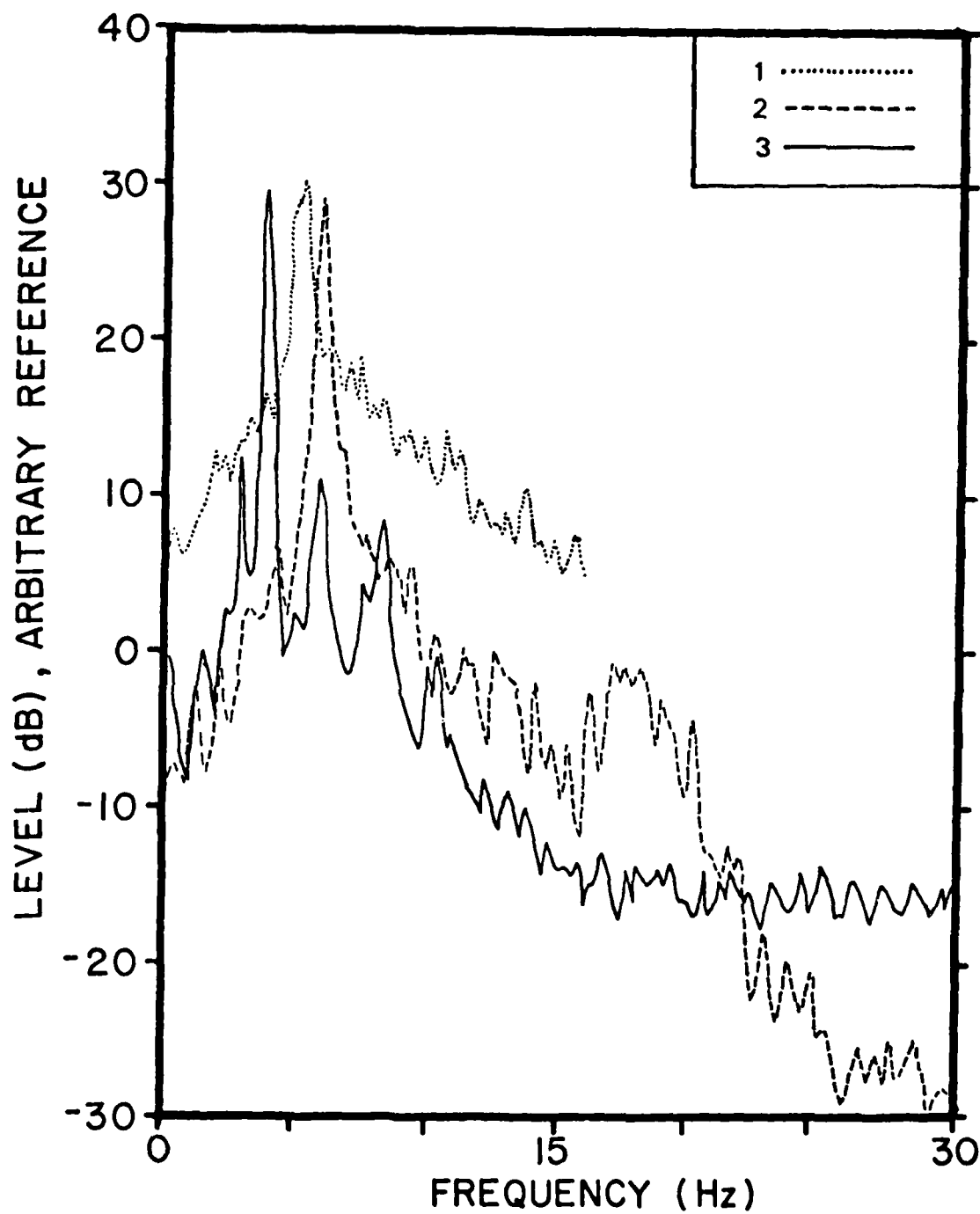


Fig. E-3. Spectra of P wave shown in Figure E-2 (dotted spectrum) and same signal recorded on two additional, nearby HIGS OBS's.

The resonance peaks shown (3.7, 5.3, and 6 Hz) are found on all arrivals on the respective OBS's during the same deployment. Interpreted as a coupling resonance, the Q is about 7 to 20 and the sediment shear velocity, V_s , is between 5 and 10 m/s (see Fig. E-1).

Figure E-4 is a comparison of HIGS and HIGB recordings of the same shot. The HIGB was developed to improve bottom coupling and reduce noise from interaction with bottom currents and from the tape recorder (Byrne et al., 1977). The geophones in the HIGB are placed in a small independent pressure case and separated from the main package by about 1 m (Sutton et al., 1980). The OBS's were located within tens of meters of each other in deep water. The hydrophones are well correlated, showing the similarities in wave forms expected for instruments next to each other. There should be no difference between the hydrophones; however, the modified instrument hydrophone was recorded at 12-dB lower gain because of a cross-talk problem with the time code channel. All channels have been identically filtered to reduce high-frequency noise. The vertical geophones show the effects of deploying the geophones away from the main instrument package. The standard instrument (HIGS) gain was 18 dB lower than the modified (HIGB) for both the vertical and the horizontal; thus, since the gains are set automatically inside each OBS, the noise level is about 8 times lower for the modified instrument than for the standard. Note that the frequency content and wave forms received by the modified instrument vertical component are similar to those of the hydrophone, whereas the wave form of the standard vertical shows a strong resonance at low frequency and little coherence with the wave form on the hydrophone.

A teleseismic event that was clearly recorded on HIGS and HIGB instruments during the Lopez experiment (Sutton et al., 1980) is shown in Figures E-5 and E-6. The instruments were 3-1/3 m apart. At 270-km range, primary arrivals should arrive within about 20° of vertical and be of compressional type for the time-interval shown. In the early part of the record, the hydrophone and HIGB (BOOBS) vertical show excellent correlation as expected for near-vertical incidence. In the latter part, correlation is not as good, with the vertical showing some excess low-frequency energy and similarity with the horizontal component. This may result from converted "granddaddy" type waves that have a relatively weak pressure component (Tuthill et al., 1980). These converted waves produce spectral peaks near 3 Hz on all the components. The HIGS (POBS) vertical shows an emergent character: an excess of low frequency resulting from some combination of coupling resonances, high-frequency attenuation, and sensitivity to cross-coupling from horizontal input. Because of the stiffness of the Lopez sediments the HIGS (and all the other OBS's) probably rested higher in the water than for normal deep ocean sediment. The spectrum from the HIGS horizontal shows a resonance near 8 Hz and resulting drop at higher frequencies in comparison with the HIGB horizontal, as expected from the coupling theory discussed in the following section.

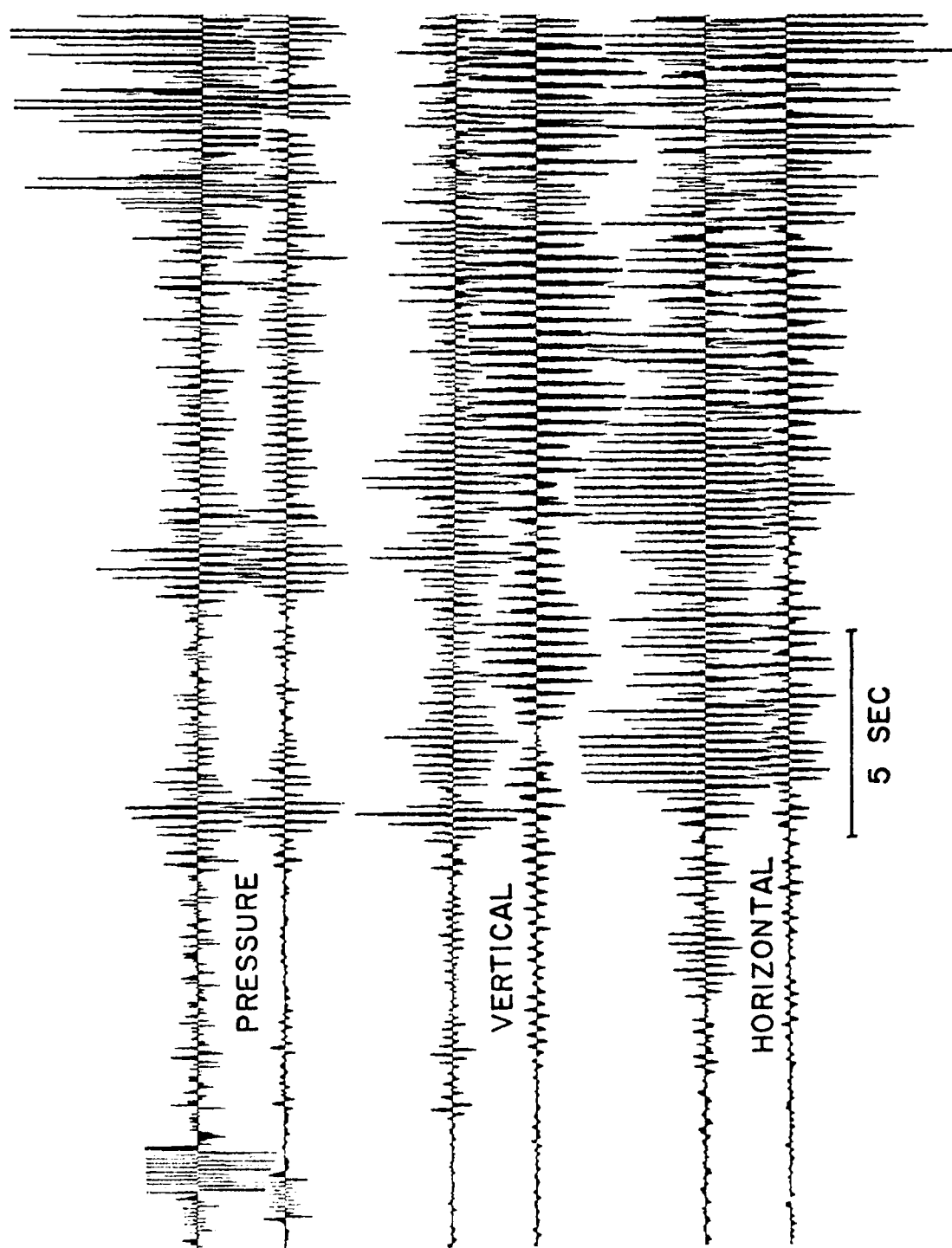


Fig. E-4. Comparison of refraction shot recorded on HIGS (upper for each component) and HIGS ocean bottom seismometers located only meters apart in deep water.

LOPEZ I. E. Q.

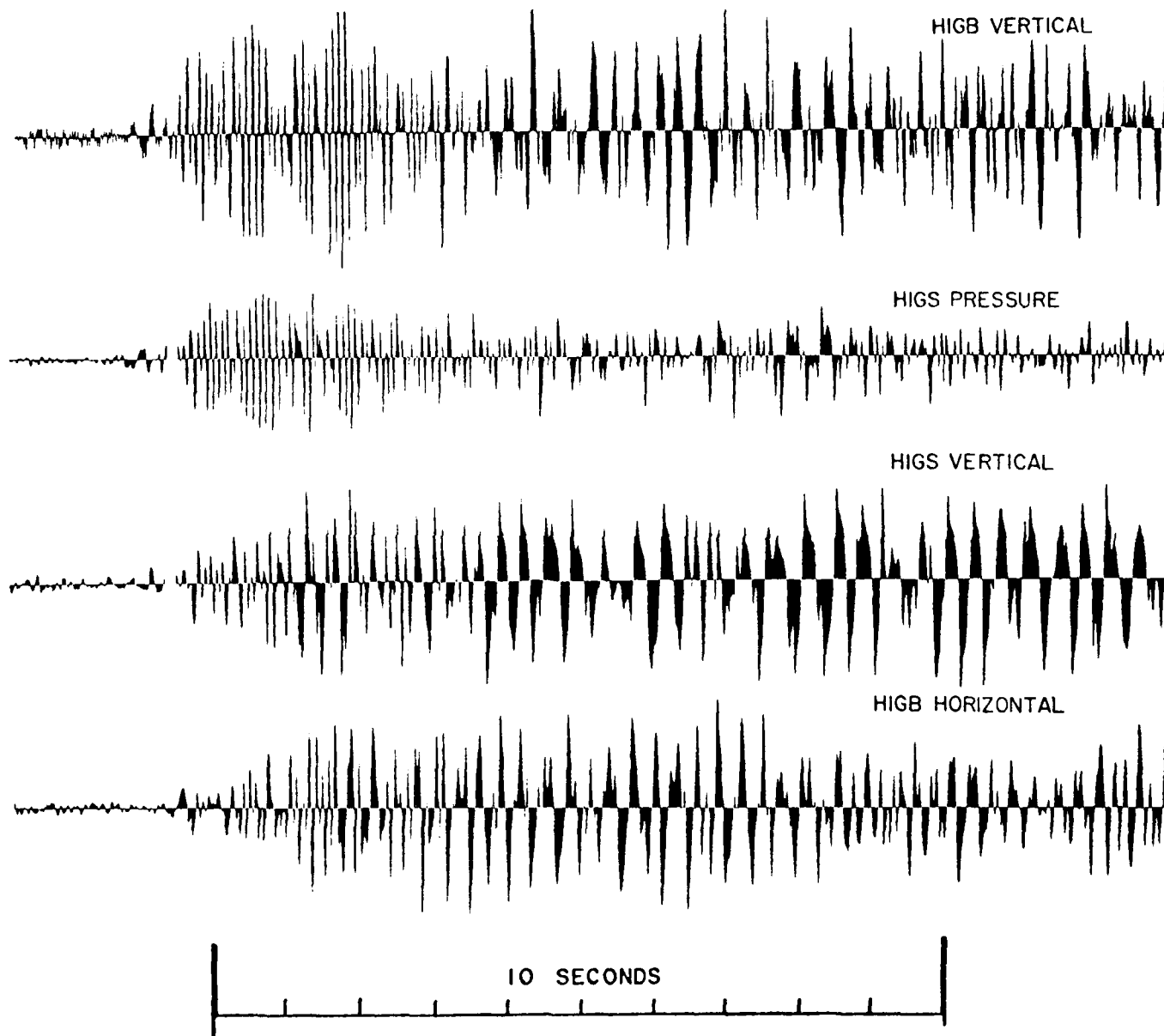


Fig. E-5. Earthquake (or large quarry blast, $M = 3.4$, $H = 3.1$ km, $\Delta = 270$ km) recorded during Lopez experiment on HIGS AND HIGB in water depth of about 8 m.

E.Q.

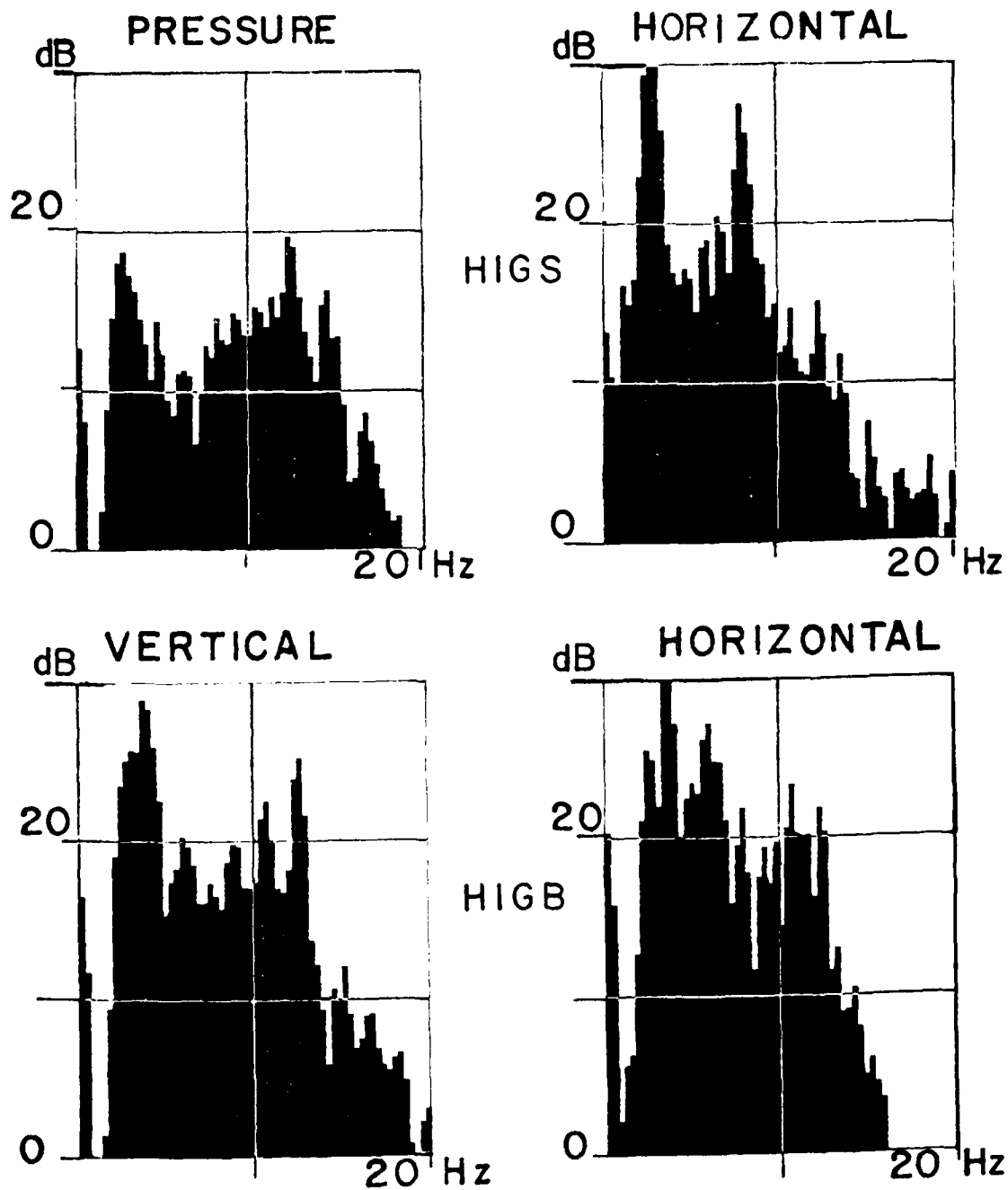


Fig. E-6. Spectra of signal shown in Figure E-5.

Theory

We derive here the theory of coupling of vertical motion of the ocean bottom to vertical motion of an OBS. The OBS shape is simplified to that of a vertical cylinder to enable us to ignore complications from shape and change in bearing area with buoyancy and rigidity of the bottom.

Referring to Figure 1c, we define the following parameters:

- z_s = position of undisturbed surface
- z_1 = position of deformed surface under OBS
- K = effective spring constant of the sediment-OBS contact area
- D = effective damping constant of bottom
- $x = z_s - z_1$ = differential position of OBS
- $M_1 = \rho_1 Ah$ = mass of OBS
- $M_w = \rho_w A(h-x)$ = mass of displaced water
- $M_s = \rho_s Ax$ = mass of displaced sediment
- g = acceleration of gravity

Assuming all coefficients are constant, the equation of motion is

$$-M_1 \ddot{z}_1 + D\dot{x} + Kx = M_1 \ddot{z}_s - (M_w + M_s + M_1 \ddot{z}_s) \quad (1)$$

where $M_1^* = M_1 + M_w + M_s$ is the mass of the OBS and the sediment and water that move with it increasing its inertia. We do not know how to evaluate M_1^* at this time (see Zelikevitch and Prothro, 1980) and will carry it through the derivation.

Since $\ddot{z}_1 = \ddot{z}_s - \ddot{x}$, we can rewrite (1):

$$M_1^* \ddot{x} + D\dot{x} + Kx = (M_1 - M_w - M_s) \ddot{z}_s \quad (2)$$

Using the definitions of M_w and M_s ,

$$\begin{aligned} M_1^* \ddot{x} + D\dot{x} + [K + A g (\rho_s - \rho_w)] x \\ = (M_1 - \rho_w Ah) g + [M_1 - \rho_w Ah - (\rho_s - \rho_w) Ax] \ddot{z}_s \end{aligned} \quad (3)$$

in equilibrium, $\ddot{x} = \dot{x} = \ddot{z}_s = 0$, and

$$x_e = (M_1 - \rho_w Ah) g / [K + (\rho_s - \rho_w) A g] \quad (4)$$

Let $y = x - x_e$, the deflection of the OBS from equilibrium with respect to the ocean bottom. The variable y is thus the error signal between true motion of the ocean bottom and motion of the OBS.

Substituting y for x in Eq. (3),

$$M_1^* \ddot{y} + D\dot{y} + [K + (\rho_s - \rho_w) A g] y = [M_1 - \rho_w Ah - (\rho_s - \rho_w) A (y + x_e)] \ddot{z}_s \quad (5)$$

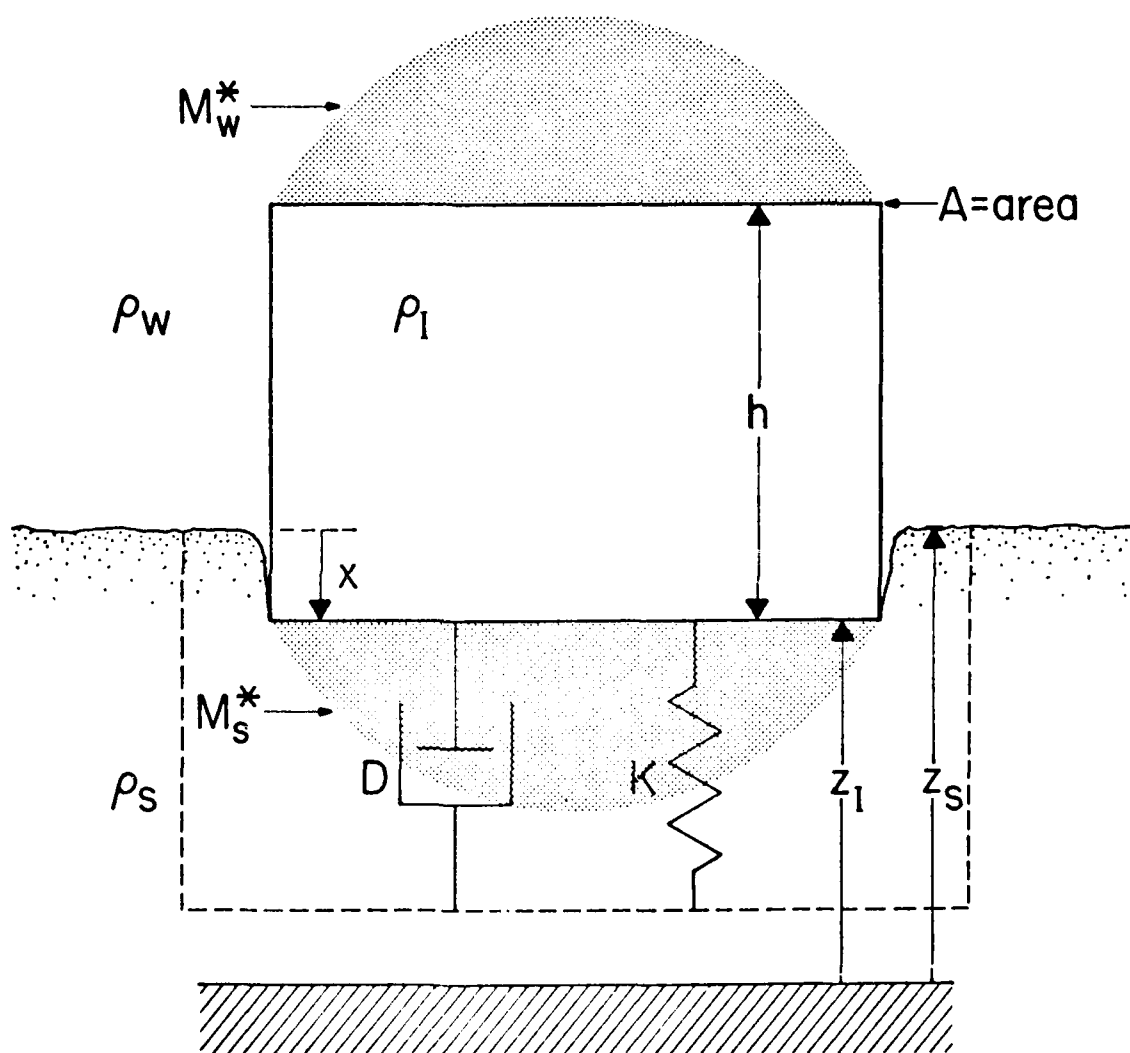


Fig. F-7. Schematic of OBS coupling to ocean bottom.

The term on the right containing y will certainly be insignificant compared to the others; thus,

$$\ddot{y} + \frac{D}{M_I^*} \dot{y} + \frac{K + (\rho_s - \rho_w) Ag}{M_I^*} y = [(M_I - \bar{M}_w - \bar{M}_s) / M_I^*] \ddot{z}_s, \quad (6)$$

where \bar{M}_w and \bar{M}_s are the average displaced water and sediment masses.

Eq. (6) can be rewritten:

$$\ddot{y} + 2h_c \omega_c \dot{y} + \omega_c^2 y = C \ddot{z}_s \quad (7)$$

where $h_c = 1/2Q_c$, the damping coefficient of the bottom coupling,

$$\omega_c^2 = \frac{K + (\rho_s - \rho_w) Ag}{M_I^*}, \quad (\omega_c \text{ is the natural angular} \quad (8)$$

frequency of the bottom coupling) and

$$C = \frac{M_I - \bar{M}_w - \bar{M}_s}{M_I^*}, \quad \text{the coupling coefficient.} \quad (9)$$

Taking the transform of (7)

$$\frac{Y}{Z_s} = \frac{CS^2}{(S^2 + 2h_c \omega_c S + \omega_c^2)} = \frac{CS^2}{\Delta} \quad (10)$$

The position of the bottom of the OBS,

$$z_l = z_s - x = z_s - y - x_c.$$

Therefore the input signal to the OBS (motion of the case) is

$$i = z_l + x_c = z_s - y$$

whose transform is

$$I = Z_s - Y,$$

and the transfer functions of the OBS package is

$$\frac{I}{Z_s} = (1-C) \left[s^2 + \frac{2h_c \omega_c}{(1-C)} s + \frac{\omega_c^2}{(1-C)} \right] / (s^2 + 2h_c \omega_c s + \omega_c^2) \quad (11)$$

From Eq. (11) it is evident that, given the constants C , h_c , and ω_c , the response is completely described. The amplitude response curves for six cases of Eq. (11), shown in Figures E-8 and E-9, demonstrate good response when $\omega < \omega_c$; $h_c < 1$; and/or $C = 0$. The coupling coefficient, C , can be determined with the aid of Eq. (9) provided a reliable value for M_I^* can be obtained (see Zelikovitz and Prothero, 1980). The coupling frequency, ω_c , can be estimated by using Eq. (8). Experimental values for C and h_c can be obtained from mechanical transient tests to be described in the following section.

When conditions are such that $C=0$, coupling is perfect, and the OBS moves exactly with the ocean bottom, although the package may still have a resonance at ω_c for other types of input (such as the transient tests). $C=0$ is the neutral buoyancy case where the mass of the displaced water and sediment equal the mass of the OBS. Earlier workers studying coupling in swamps ignored the effects of buoyancy and the sediments that move with the instrument, thus arriving at the case where $C=1$. We see from Eq. (9) that, since M_I^* will always be greater than M_I and since M_w and M_s will probably never be negligible, C will never reach a value of 1. Note that Eqs. (8) and (9) do not require that the OBS be cylindrical in shape to be valid. As long as the area in contact with the bottom does not change with motion of the OBS, both equations will hold.

The buoyancy effect, in addition to modifying the shape of the response, modifies the resonant frequency and damping from that obtained for the "swamp" case by previous authors. From Eq. (8) we see that the resonant frequency is the RMS of that produced by the effective spring constant of the bottom alone, and by the buoyancy effect alone. As a numerical example, for the HIGB geophone package (Sutton et al., 1980) in average sediments the increase in ω_c would appear to be less than 1%. However, the effect could be important for systems with large surface areas in contact with the bottom.

We can investigate, further, the effects of bearing area on the coupling frequency by rewriting Eq. (8).

$$\omega_c^2 = (a_s r + b_s r^2) / (M_I + c_I r^3) \quad (8')$$

where

- r^2 represents bearing area
- r^3 represents the volume of sediment and water entrained with the OBS
- c_I depends upon the configuration of the OBS
- M_I is OBS mass
- a_s is proportional to sediment rigidity modulus
- b_s depends upon sediment density.

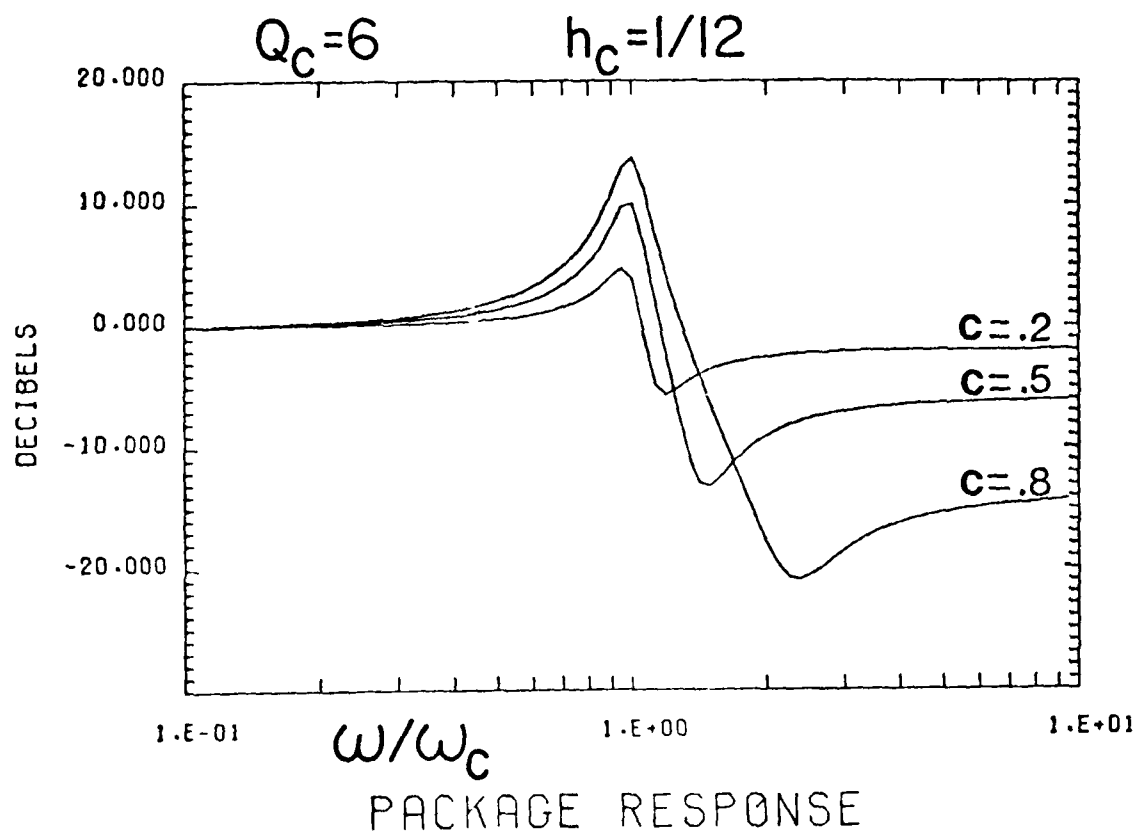


Fig. E-8. OBS package seismic response from Eq. (11) for underdamped coupling.

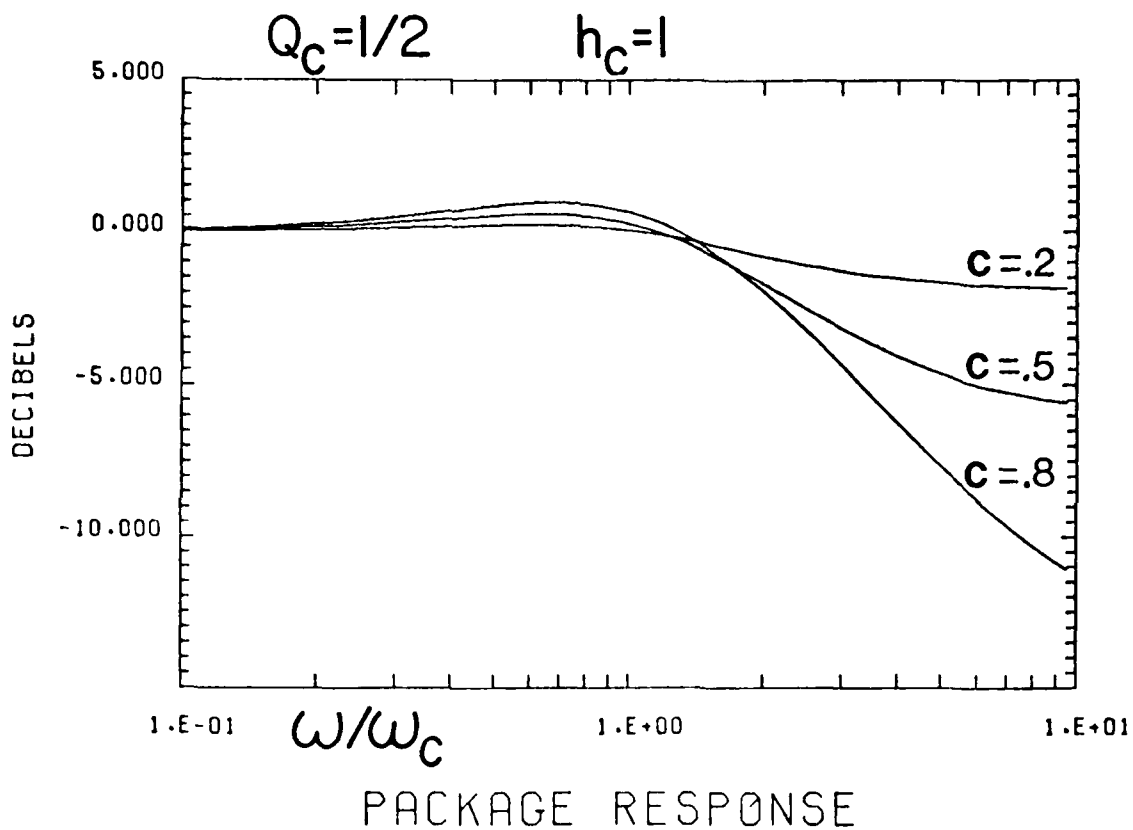


Fig. E-9. OBS package seismic response from Eq. (11) for critically damped coupling.

The r^2 term results from buoyancy and the r'^3 term from the entrained sediment and water. Assuming r' is proportional to r , for a given set of constants (including instrument mass), ω_c varies as $r^{1/2}$ and $r^{-1/2}$ for small and large r , respectively, and varies at most by either r or r^{-1} , depending upon the values of the constants, for intermediate values of r .

The case $C=1$ mentioned earlier is appropriate for the horizontal response of the OBS package to horizontal input signals (provided by the rigidity of the bottom, only). For horizontal input, Eq. (11) reduces to

$$\frac{1}{H_s} = 2h'_c \omega'_c (S + \omega'_c / 2h'_c) / (S^2 + 2h'_c \omega'_c S + \omega'^2_c) \quad (12)$$

In this case the response decreases continuously at frequencies higher than the coupling frequency; as $1/\omega$ for frequencies above $\omega'_c / 2h'_c$.

Mechanical Transient Tests

A schematic diagram for a simple mechanical transient test to determine the frequency and damping of OBS-bottom coupling (ω_c and h_c) is shown in Figure E-10. This test is analogous to the classical weight lift calibration for earthquake seismographs. The float, which provides a constant upward or sideward force on the OBS package, is released at $t=0$ when the current through an electromagnet is interrupted. With use of a small magnet armature and light string or thread the step in force can be made quite pure. However, the pulley rod used for the horizontal test can generate a second signal when the armature hits the pulley. In soft sediment a separation of the pulley from the OBS of 1 or (preferably) 2 m is generally adequate to separate the primary and secondary signals. The size of the float can be adjusted to provide a signal in the normal operating range of the OBS and to test for possible system non-linearities.

An upward or sideward step of force on an OBS at $t=0$ produces initial conditions of $z_I(0) = z_{I0}$, $\dot{z}_I(0) = 0$ and $\ddot{z}_I(0+) = Kz_{I0}/M$ for the position of OBS base relative to its equilibrium position at rest on the sediment. We assume that the OBS moves as a rigid mass, that the motion is rectilinear, and that the motion of the inertial masses in the geophones does not affect the motion of the OBS (i.e., no back coupling).

The equation of motion for the OBS is:

$$M_I^* \ddot{z}_I + D \dot{z}_I + K_s z_I = 0 \quad (\text{assuming no seismic input}) \quad (13)$$

where

$$M_I^* = \text{OBS mass plus mass of sediment and water included in the motion of the OBS}$$

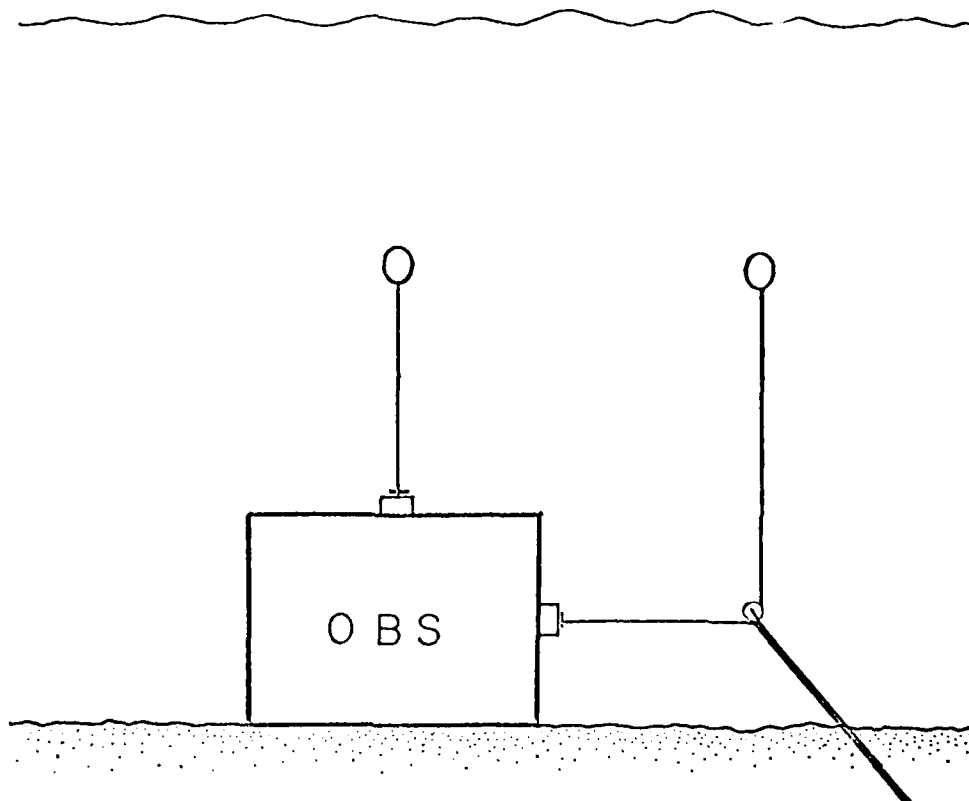


Fig. E-10. Schematic for mechanical step of force test to determine ω_c and h_c .

D = damping constant

K_S = effective spring constant of the OBS-bottom coupling,
including any buoyancy effects.

Rewriting (13) we have

$$\ddot{z}_I + 2h_c \omega_c \dot{z}_I + \omega_c^2 z_I = 0 \quad (14)$$

where $\omega_c^2 = K_S/M_I^*$ and $h_c = 1/2Q_c$ = damping coefficient, ω_c is the free angular frequency of the bottom coupling, and $Q_c = 1/2h_c$ gives the amplification (and bandwidth) of any coupling resonance.

Solutions for our initial conditions are:

$$z_I = z_{I0} e^{-at} \left(\frac{a}{b} \sin bt + \cos bt \right) \quad (15)$$

$$\dot{z}_I = \dot{z}_I = - \left[\frac{a^2 + b^2}{b} \right] z_{I0} e^{-at} \sin bt \quad \left. \vphantom{\frac{a^2 + b^2}{b}} \right\} h_c < 1 \quad (16)$$

where $a = h_c \omega_c$, $b = \omega_c \sqrt{1 - h_c^2}$

$$z_I = z_{I0} (1 + a t) e^{-a t} \quad (17)$$

$$\dot{z}_I = \dot{z}_I = -a^2 t z_{I0} e^{-a t} \quad (h_c = 1) \quad (18)$$

The equation of motion for the seismometer mass is:

$$\ddot{z}_M + 2h_M \omega_M \dot{z}_M + \omega_M^2 z_M = \ddot{z}_I = \dot{\dot{z}}_I \quad (19)$$

where z_M is the relative displacement between inertial mass and OBS frame. Taking the Laplace transform of (19) and (for example) assuming critical damping $h_M = 1$, the seismometer transfer function is:

$$\frac{z_M}{\dot{z}_I} = \frac{S}{(S + \omega_M)^2} \quad (h_M = 1) \quad (20)$$

The emf generated in the seismometer coil is

$$E = GS z_M \quad (21)$$

and the signal transfer function is

$$\frac{E}{\dot{z}_I} = \frac{GS^2}{(S + \omega_M)^2} \quad (22)$$

From Eqs. (18) and (16) the transforms of the transient input signal are

$$V_{1c} = \omega_c^2 z_{I0} / (S + i\omega_c)^2 \quad (h_c = 1) \quad (23)$$

and

$$V_{1u} = -(a^2 + b^2) z_{I0} / [(S + a)^2 + b^2] \quad (h_c < 1) \quad (24)$$

Combining (23) or (24) with (22) we obtain

$$E_c = -\frac{2}{c} z_{I0} G S^2 / (S + i\omega_M)^2 (S + i\omega_c)^2 \quad (h_c = 1) \quad (25)$$

and

$$E_u = -(a^2 + b^2) z_{I0} G S^2 / (S + i\omega_M)^2 [(S + a)^2 + b^2] \quad (h_c < 1) \quad (26)$$

We obtain the geophone output signals for the mechanical transients by taking the inverse transform of (25) and (26):

$$e_c = -\frac{2}{c} z_{I0} G \left\{ \left[\frac{\omega_M^2}{(\omega_c - i\omega_M)^2} t - \frac{2\omega_M}{(\omega_c - i\omega_M)^3} \right] e^{-i\omega_M t} + \left[\frac{\omega_c^2}{(\omega_M - i\omega_c)^2} t - \frac{2\omega_c}{(\omega_M - i\omega_c)^3} \right] e^{-i\omega_c t} \right\} \quad (h_c = 1) \quad (27)$$

$$e_u = -(a^2 + b^2) z_{I0} G \left\{ \left[\frac{\omega_M^2}{(a - i\omega_M)^2 + b^2} t - \frac{2\omega_M(a^2 - a\omega_M + b^2)}{[(a - i\omega_M)^2 + b^2]^2} \right] e^{-i\omega_M t} + \frac{a^2 + b^2}{b[(a - i\omega_M)^2 + b^2]} e^{-at} \sin(bt + \psi) \right\} \quad (h_c < 1) \quad (28)$$

$$\text{where } \psi = \tan^{-1} \left[\frac{-2ab}{(a^2 - b^2)} \right] - 2 \tan^{-1} \left[\frac{b}{(\omega_M - a)} \right]$$

Figure E-11 shows theoretical signals from mechanical transients for five different cases listed in Table E-1, and Figure E-12 shows amplitude spectra for three of the cases. These results are appropriate for horizontal and vertical inputs recorded on horizontal and vertical geophones, respectively. In addition, by observing the vertical geophone output from horizontal transients and vice versa the susceptibility of an OBS to cross-coupling distortion can be evaluated. Some results from mechanical transient tests conducted in shallow water off Oahu were presented by Sutton et al., (1977b and 1978). Sample results from the Lopez Island experiment follow.

Table E-1. OBS coupling parameters for curves shown in Figures E-11 and E-12. ω_M and h_M are both equal to 1.0.

Case	ω_c	H_c	Q_c
1	1	1/12	6
2	2	1/12	6
3	4	1/12	6
4	8	1/12	6
5	4	0	"
6	3	1	1/2
7	1	1	1/2

Lopez Experiment Results

A great deal of information on coupling is contained in the digital records from the mechanical transients and from the blasting cap and airgun shots obtained during the Lopez experiment. These results are summarized in Sutton et al., (1980) and discussed further in Zelikovitz and Prothero (1980), Tuthill et al. (1980), Lewis and Tuthill (1980), and Johnson and McAlister (1980).

In general, the responses to the transient tests of the instruments specially designed for use as standards at Lopez Island exhibit broad, rather featureless spectra, whereas most of the spectra from tests on the operational OBS's show one or more spectral peaks with various bandwidths and amplification (Fig. E-13). Most of the OBS's show a peak between about

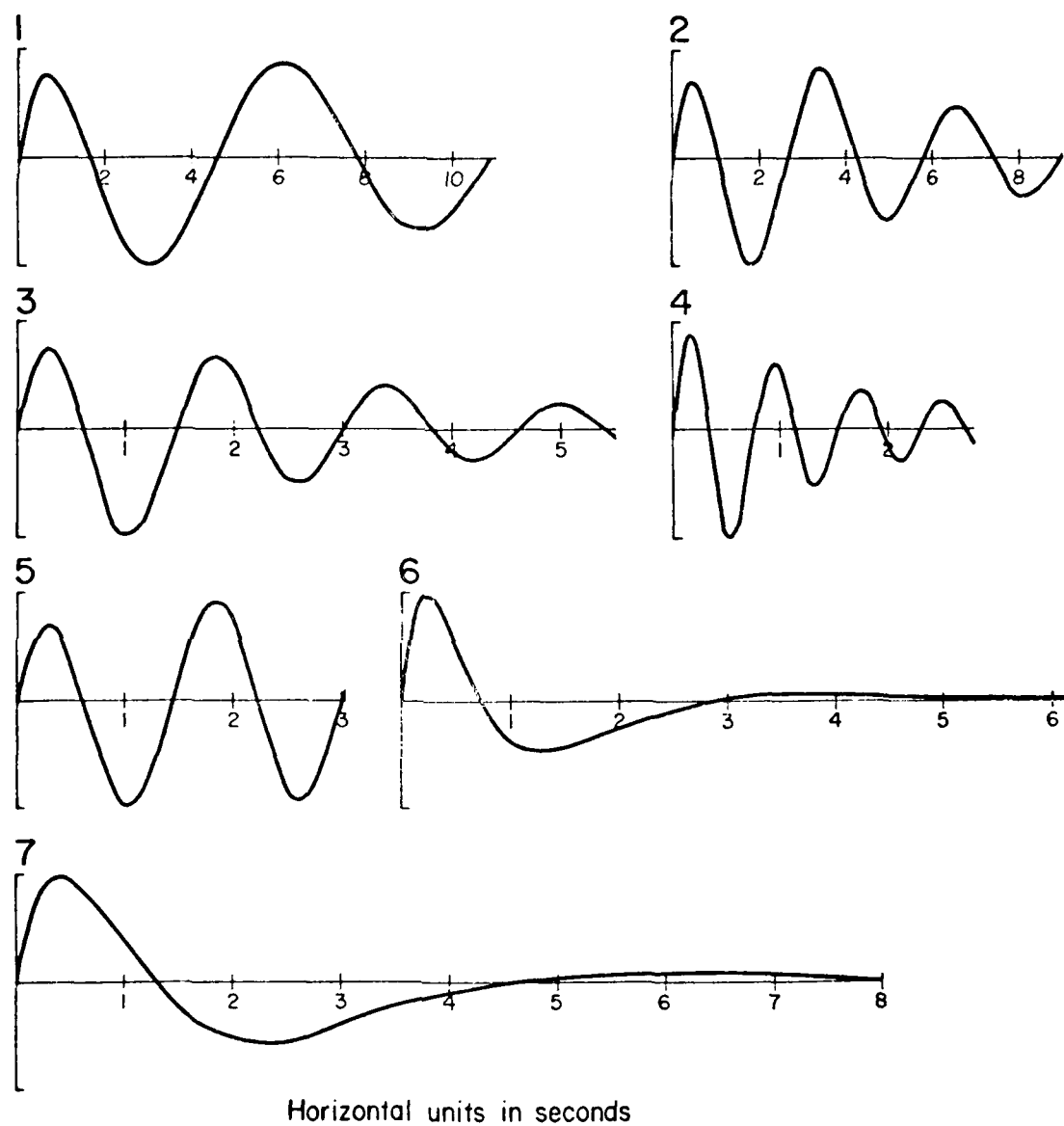


Fig. E-11. Theoretical geophone outputs for mechanical transient test cases one through seven listed in Table E-1.

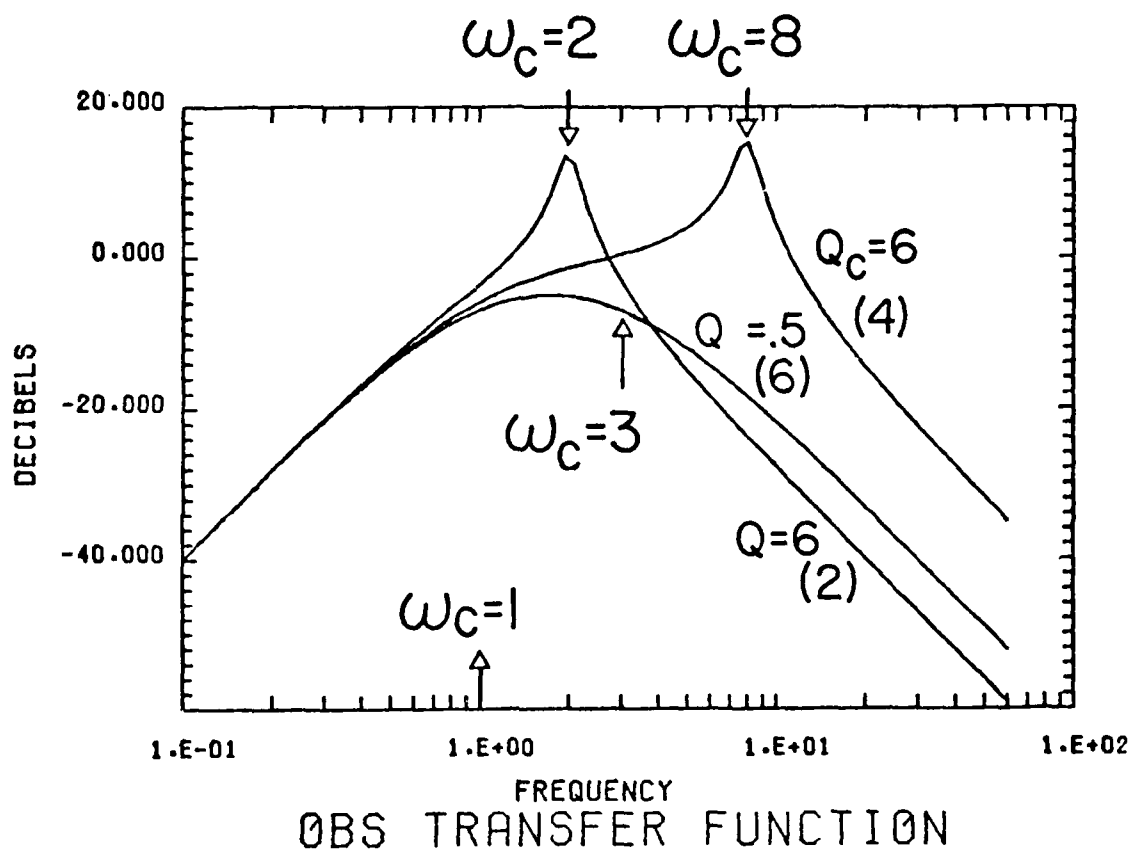


Fig. E-12. Spectra for three of the test outputs (2, 4, and 6) shown in Figure E-11.

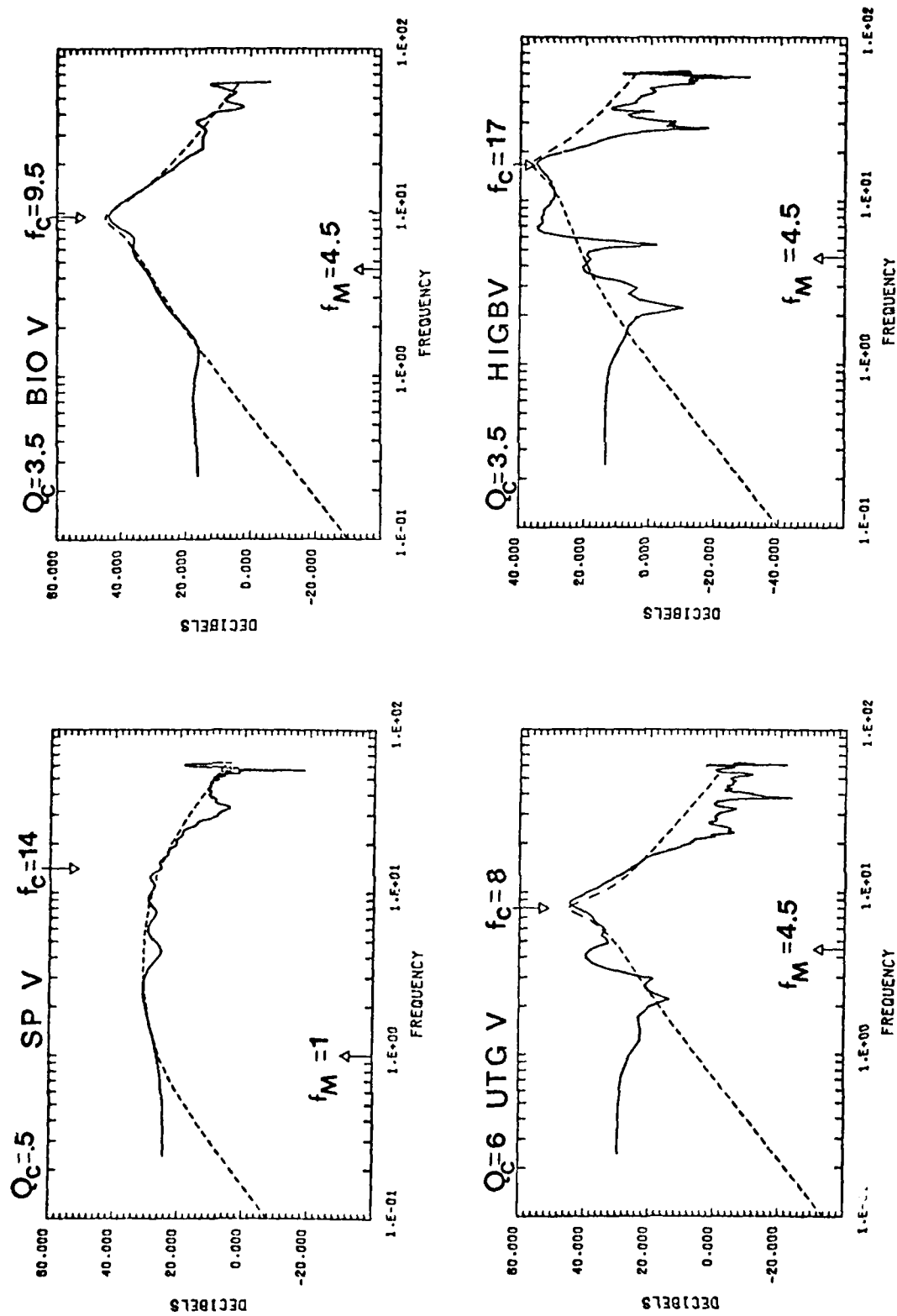


Fig. E-13. Comparison of vertical mechanical transient test data (solid) with theory (dashed) using Eq. (13) and (14). SPV is one of the special instruments developed for the Lopez experiment; the other three are operational OBS's.

8 and 12 Hz for both the vertical and horizontal inputs, suggesting some kind of geological wave-guide resonance; however, its absence on the special standard instruments and general agreement with the coupling theory argue that it is a coupling resonance and that the OBS's have roughly equivalent, bottom-coupling design parameters. In this respect the MITEV and HIGBV (both having geophones separated from the main package) appear to be closest in response to the standard instruments.

Comparison of the spectra from the mechanical transient tests with those from cap and airgun shots and from the background noise often show similar peaks and attenuation of higher frequencies, in agreement with the coupling theory (Figs. E-8 and E-9). The Q of the coupling-resonances are generally greater than predicted from the published theories (Fig. F-1) that do not consider buoyancy forces. The coupling-resonance frequencies may be more reliably predictable.

Figure E-14 shows the signals recorded digitally from an airgun shot, approximately 130 m southwest of the center of the OBS array. Considering differences in sensitivity and frequency response of the various OBS's the first few cycles of the signal recorded on the vertical components agree well, although some arrivals seem somewhat more emergent than others. Between the first arrivals and the large "granddaddy" waves on the right, a wave-train with predominantly horizontal (mainly north-south) motion is observed on the plate (PL) and neutral density (ND) standards and on HIGBH. Although the signal is hardly observable on the vertical standards, it is clearly recorded on most of the OBS verticals. This signal appears to be an example of cross coupling between a horizontal input and vertical output. The observed signals for a given instrument are quite dependent upon the stiffness of the Shoal Bay sediments and upon the frequency of the input signal (narrow band near 6 Hz). For example, BIOV exhibited a strong response near 5 Hz, to a horizontal transient input (Fig. E-15), close to the principal frequency of the airgun signal. Other instruments that show less relative cross coupling from the airgun, e.g., UCSBV, also shown in Figure E-15, exhibited equally strong responses on the vertical sensors to horizontal transients, but at different frequencies. Lewis and Tuthill (1980) present a more complete discussion of the cross-coupling phenomenon.

Conclusion

The theory and mechanical transient tests outlined here and the results of the Lopen Island intercomparison experiment provide reliable guidelines for predicting the response of an OBS under various bottom conditions. This knowledge makes it possible to establish parameters for ocean bottom seismometer design. Generally, a low smooth profile in the water, a large bearing area, and a low package density should provide optimum coupling to the bottom in soft sediment. Careful design should result in a package that will couple well to any type of ocean bottom.

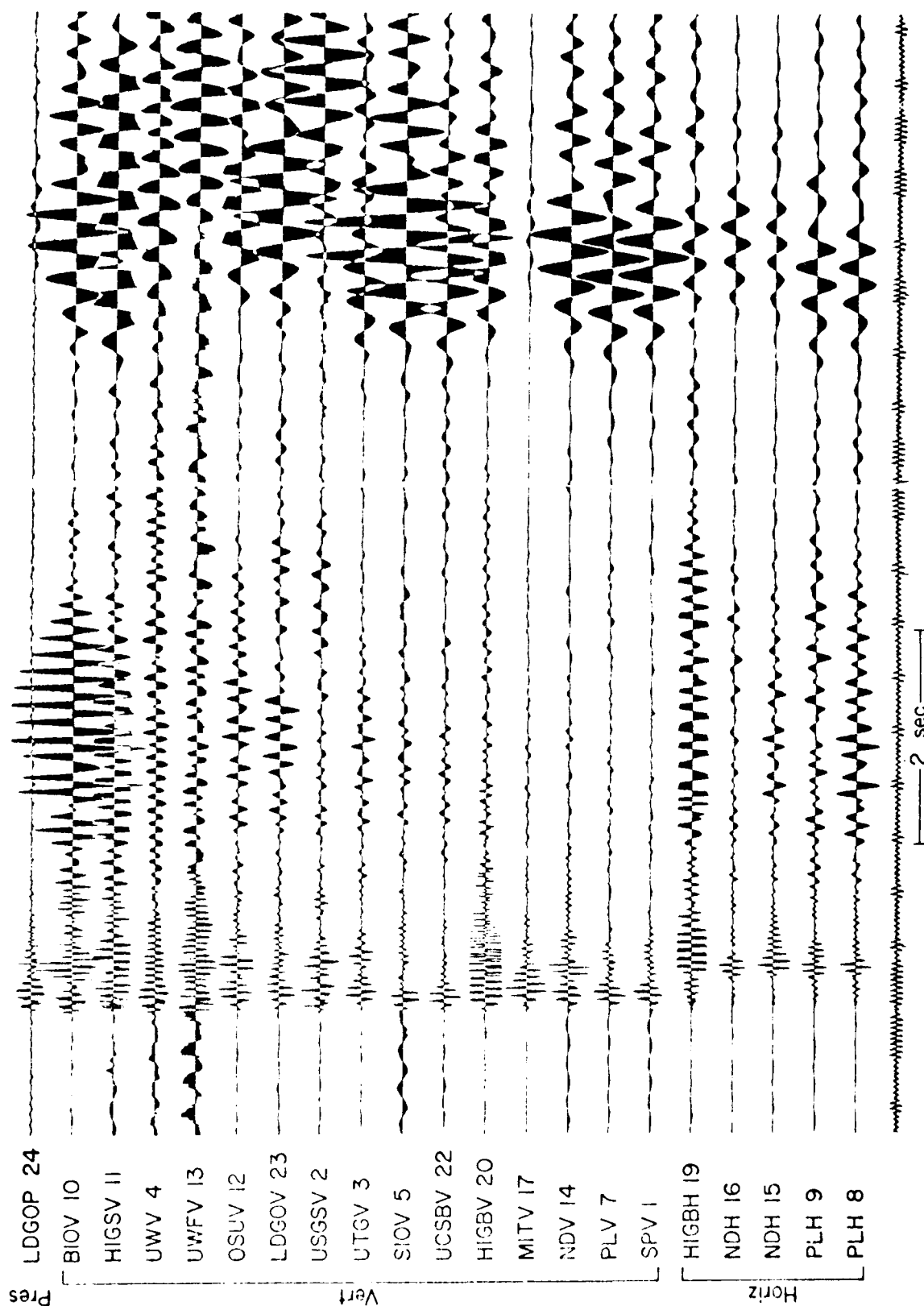
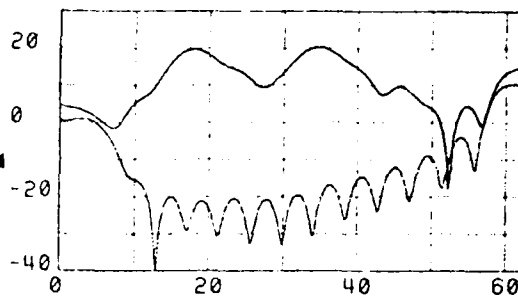
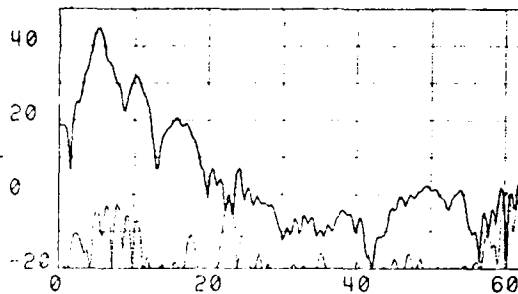
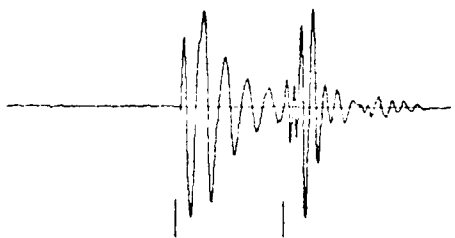


Fig. E-14. Airgun shot (182, digitized event #220) recorded by the Lopez Island experiment array. ND, PL, and SP are special standard instruments; others are operational OBS's. Records of measuring horizontal motion are at the bottom of the figure; records of those measuring vertical motion are in the middle; and a hydrophone (pressure) record is shown at the top.

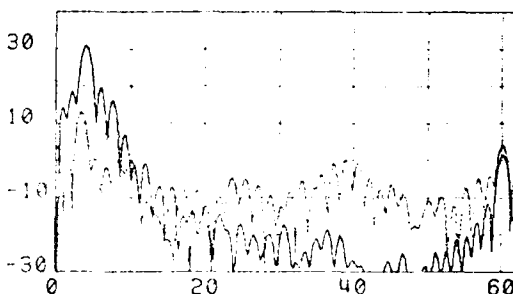
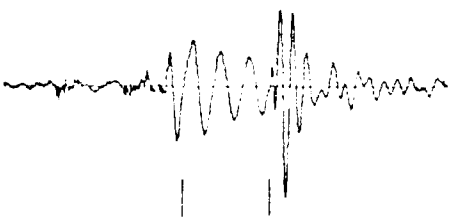
E-26



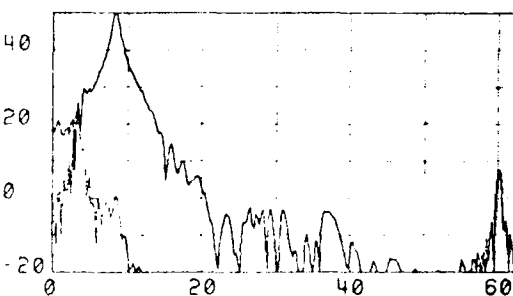
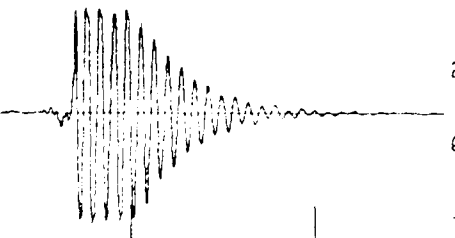
PL V E XIENT 12 -6



BIO V S XIENT 64 -18



UCSBV S XIENT 124-24



UCSBV S XIENT 125-24

Fig. E-15. Horizontal mechanical transient tests recorded on vertical geophones. Horizontal line under time signals represents two seconds; vertical lines bracket portion analyzed. Spectra are in dB and Hz; dotted spectra are for a noise sample of the same length as signal analyzed immediately preceding transient.

References

- Bycroft, G. N., 1956. Forced vibrations of a rigid circular plate on a semi-infinite elastic space and on an elastic stratum. *Phil. Trans. Roy. Soc. Lond.*, V248 A928, p. 327-367.
- Byrne, D., F. K. Duennebier, D. H. Hussong, and G. H. Sutton, 1977. Burp-out ocean bottom seismometer. *EOS, Trans. Am. Geophys. Union*, v. 58, p. 1190 (abstr.).
- Johnson, S. H., and R. E. McAlister, 1980. Bottom seismometer observation of airgun signals at Lopez Island. This report, Appendix I.
- Lamer, A., 1969. Couplage Sol-Geophone. *Geophys. Prosp.*, v. 18, p. 300-319.
- Lewis, B. T. R., and J. D. Tuthill, 1980. Instrumental waveform distortion on ocean bottom seismometers. This report, Appendix H.
- Sutton, G. H., F. K. Duennebier, and E. J. Saade, 1978. Coupling of ocean bottom seismometers to soft bottoms. *EOS, Trans. Am. Geophys. Union*, v. 59, p. 1132 (abstr.).
- Sutton, G. H., F. K. Duennebier, A. R. Lazarewicz, and P. A. Cooper, 1977a. Strong resonances on OBS's. *EOS, Trans. Am. Geophys. Union*, v. 58, p. 1190 (abstr.).
- Sutton, G. H., J. Kasahara, W. N. Ichinose, and D. A. Byrne, 1977b. Ocean bottom seismograph development at Hawaii Institute of Geophysics. *Mar. Geophys. Res.*, v. 3, p. 153-177.
- Sutton, G. H., B. T. R. Lewis, J. Ewing, F. K. Duennebier, B. Iwatake, J. D. Tuthill, and others, 1980. Lopez Island Ocean Bottom Seismometer Intercomparison Experiment, Final Report. HIG-80-4, Hawaii Inst. Geophys., Honolulu. (This report.)
- Tuthill, J. D., B. T. R. Lewis, and J. D. Garmanv, 1980. Stoneley waves, Lopez Island noise, and deep sea noise from 1 to 5 Hz. This report, Appendix G.
- Washburn, H., and H. Wiley, 1941. The effect of the placement of a seismometer on its response characteristics. *Geophysics*, v. 6, p. 116-131.
- Wohi, A., 1944. The equation of motion of a geophone on the surface of an elastic earth. *Geophysics*, v. 9, p. 29-35.
- Zelikovitz, S. J., and W. A. Prothero, Jr., 1980. The vertical response of an ocean bottom seismometer: Analysis of the Lopez Island vertical transient tests. This report, Appendix F.

Appendix F

THE VERTICAL RESPONSE OF AN OCEAN BOTTOM SEISMOMETER:
ANALYSIS OF THE LOPEZ ISLAND VERTICAL TRANSIENT TESTS

THE VERTICAL RESPONSE OF AN OCEAN BOTTOM SEISMOMETER:
ANALYSIS OF THE LOPEZ ISLAND VERTICAL TRANSIENT TESTS

Steven J. Zelikovitz and William A. Prothero Jr.

Department of Geological Sciences
Marine Science Institute
University of California
Santa Barbara, California 93106

Introduction

In seismology, it is desired to record ground motion accurately. However, Ocean Bottom Seismometers (OBS), which are usually rather massive instruments, can significantly distort the measured ground motion, particularly when they rest on sediments of relatively weak stiffnesses. This response problem, which has been recognized in the case of land seismometers for over 30 years, is known to depend on the physical properties of the instrument and of the soil on which the instrument rests. It can be more acute for an OBS due to the possibility of deployment on softer underlying sediments, and more complex due to water-instrument interactions.

The original theoretical development in soil-structure interaction (Richart et al., 1970) provides a framework within which we can study OBS response. Work by E. L. Hamilton (1970, 1971a, 1971b) suggests treatment of marine sediments as an elastic solid that can be represented by a spring-mass-damper system. (Normally, soil-structure interaction studies require the use of finite element techniques because they most often involve structures with many degrees of freedom, resting on complex foundations.) The stiffness and damping coefficients, or foundation impedances, are functions of the bearing radius of the instrument and the elastic properties of the soil. The presence of water can be accounted for by using an "effective mass" for the OBS, which includes the inertial effects of the surrounding fluid. The theory and data analysis deal strictly with the vertical motion. Horizontal motions will also produce important effects but are not treated in this paper.

Since the ultimate goal of this study is finding a calibration technique for any OBS at any site, we explore the response problem both through modeling experiments and by analysis of the Lopez Island vertical transient tests. The Lopez results allow us to compare the output of many instruments and standards subjected to identical step-function inputs.

The modeling experiments similarly consider the response of an ideal model to a variable frequency sinusoidal input. Foam rubber of known elastic properties serves as a homogeneous "ideal" soil in the modeling experiments. We investigate soil-instrument interaction by applying vertically oscillating forces to masses of varying bearing radius placed on the foam soil model. This enables us to verify the continuum mechanical theory for the simple cases and model more complex configurations, which do not easily lend themselves to a theoretical treatment. The experiments with foam rubber also help us to identify some of the important considerations in the analysis of the Lopez data. In addition, they suggest that a possible in-situ technique for calibrating an OBS might make use of an attached shaking unit.

A harmonic oscillator subjected to a step-function input force will exhibit a decaying sinusoidal output. Clearly, the Lopez transient test data shows this decaying oscillatory behavior with a measurable frequency for every instrument. The decay rate can also be measured and is a function of the damping in the system. By relating these "ringdown"

frequencies to the effective masses and bearing radii of the OBS's, a shear modulus value for Shoal Bay mud can be obtained. Since the OBS's and standards were placed on the bottom in a circle of small diameter, the shear modulus value felt by each instrument should be comparable. We attempt to explain four notable discrepancies by examining the assumptions inherent in the simple model. Embedment due to bearing pressure of the instrument in a nonuniform vertical soil profile provides a convincing explanation of why certain instruments feel a higher shear modulus.

Damping factors can also be obtained from the Lopez data. Although the logarithmic decrement of the ringdown cannot be measured with high accuracy, a range in value for each damping factor is reported. These values are compared to a theoretical damping curve for Lysmer's and Richart's (1966) elastic half space analog.

Background and Theory

E. L. Hamilton in several papers (1970, 1971a, 1971b) concludes that equations of Hookean elasticity can be used to calculate the elastic constants for water-saturated sediments. Therefore, we begin by modeling an OBS as a rigid circular mass resting on an elastic half space with properties, G -shear modulus, ν -Poisson's ratio, and ρ -density (see Fig. F-1). Hsieh (1962) developed the lumped parameter system shown in Figure F-1 as follows:

$$M\ddot{Z} = Q - P \quad (1)$$

$$P = C_z \dot{Z} + K_z Z \quad (2)$$

$$M\ddot{Z} + C_z \dot{Z} + K_z Z = Q = Q_0 e^{i\omega t} \quad (3)$$

Lysmer and Richart (1966) found frequency independent vertical stiffness and damping constants as functions of the mass radius (R) and soil properties G , ν , and ρ . The constants K_z and C_z are given by:

$$K_z = \frac{4GR}{1-\nu}, \quad C_z = \frac{3.4R^2}{1-\nu} \sqrt{\rho G} \quad (4)$$

Substituting these constants into Eq. (3) yields a linear differential equation with constant coefficients, sometimes called Lysmer's analog. Using Eq. (4), the natural frequency of this damped harmonic oscillator will be:

$$f_n \approx \frac{1}{2\pi} \sqrt{\frac{4 GR}{(1-\nu) M} (1 - 2D^2)} \quad (5)$$

where D is a damping constant which is the actual damping constant divided by the critical damping constant C_E/C_c . Lysmer's analog breaks down

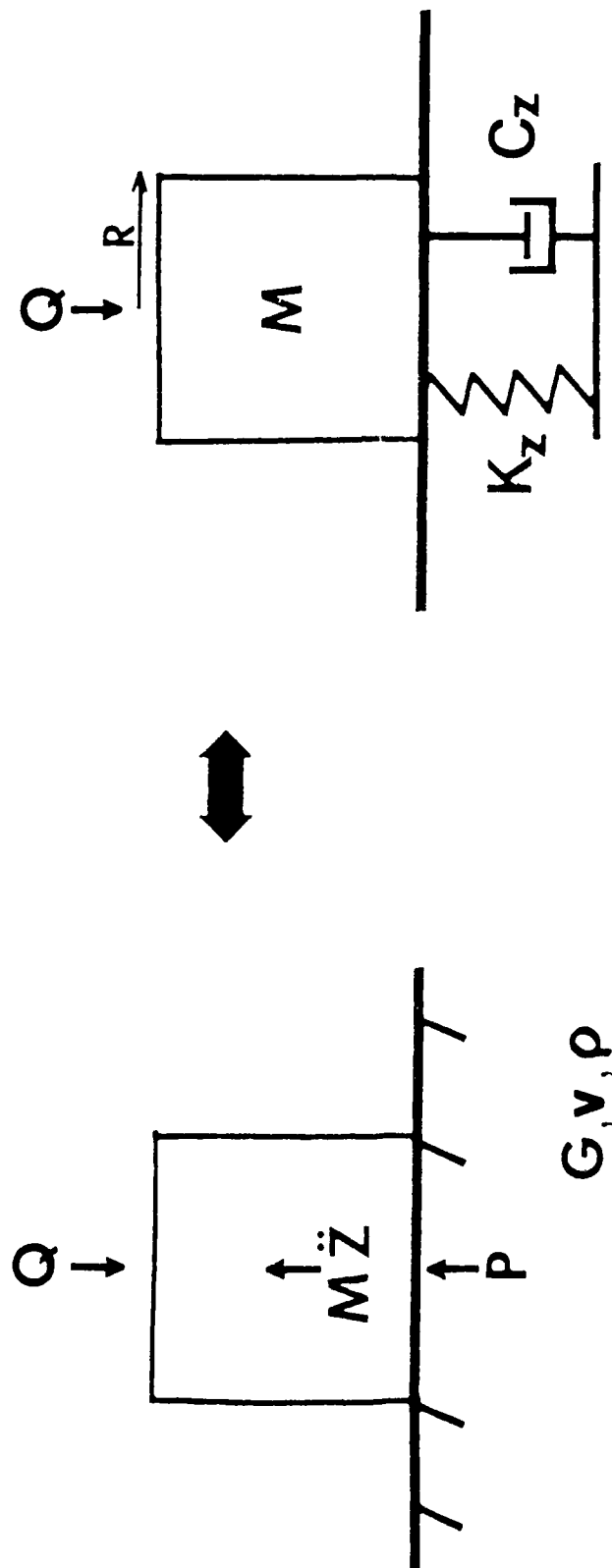


Fig. F-1. The elastic half space analog, using spring constant (K_z) and a damper (C_z) to represent the vertical foundation impedances, which are functions of the soil properties.

for $D \geq .425$. An excellent discussion of this subject is found in Richart et al. (1970).

To this point, the instrument water interaction has been neglected. There are three terms that enter the equation of motion: hydrodynamic drag, wavemaking, and virtual mass. The size and depth location of the instrument make the relative magnitude of drag and wavemaking forces insignificant with respect to the inertial effect of the fluid (Byrd, 1978).

Figure F-2 shows the inertial and mechanical forces acting on a submerged mass resting on an elastic solid, which is represented by a spring and dashpot. The position of the mass relative to an inertial frame of reference is $x + R_0 + \Delta R$, where R_0 is the steady state radius of the earth, ΔR is the free field displacement, and x is the displacement of the mass relative to the free field position of the seafloor. The acceleration of M relative to the seafloor is then \ddot{x} . There is also a virtual mass term or added mass effect from the movement of the mass through water. This effect is caused by hydrodynamic forces exerted on an accelerating mass because of the necessary acceleration of the surrounding water through which the mass moves (Batchelor, 1967). Since the wavelength of sound at 100 Hz is about 15 m, we can assume, for OBS-sized instruments, that the water surrounding the instrument moves with the bottom. So, the virtual mass force due to the relative motion of the instrument and water will be $M_v \ddot{x}$. Now the buoyancy force is due to the difference in the weight of the OBS and the weight of the displaced water, which is its mass multiplied by the acceleration of its local frame of reference. We must include the acceleration of gravity (g) and the acceleration because of ground motion $\ddot{\Delta R}$, so the total buoyant force is given by $(M - M_w)(g + \ddot{\Delta R})$.

The use of this buoyancy term is the simplest way to include inertial effects of the acceleration of the water-OBS system. The equation of motion obtained by balancing these forces and the stiffness and damping forces is:

$$M\ddot{x} + M_v\ddot{x} + C_z\dot{x} - K_z(x_0 - x) + (M - M_w)(g + \ddot{\Delta R}) = 0 \quad (6)$$

where M is the mass of the instrument, M_v is the virtual mass effect due to the acceleration of surrounding water, M_w is the mass of the displaced water, x_0 is the equilibrium position of the spring, and $\ddot{\Delta R}$ is the free field ground motion acceleration. The weight of the instrument in water is balanced by the equilibrium spring force. Therefore the equation reduces to:

$$(M + M_v)\ddot{x} + C_z\dot{x} + K_zx = -\ddot{\Delta R}(M - M_w) \quad (7)$$

We see that if the instrument is neutrally buoyant ($M - M_w = 0$), \ddot{x} and \dot{x} will be zero as there is no input force to the mass spring system. Thus, the OBS moves exactly with the bottom as expected intuitively.

A similar equation of motion has been derived by Sutton et al. (1980, Eq. (5)). Our equations differ in that we include virtual mass effects from hydrodynamic theory and ignore their term M_s , which is the mass of

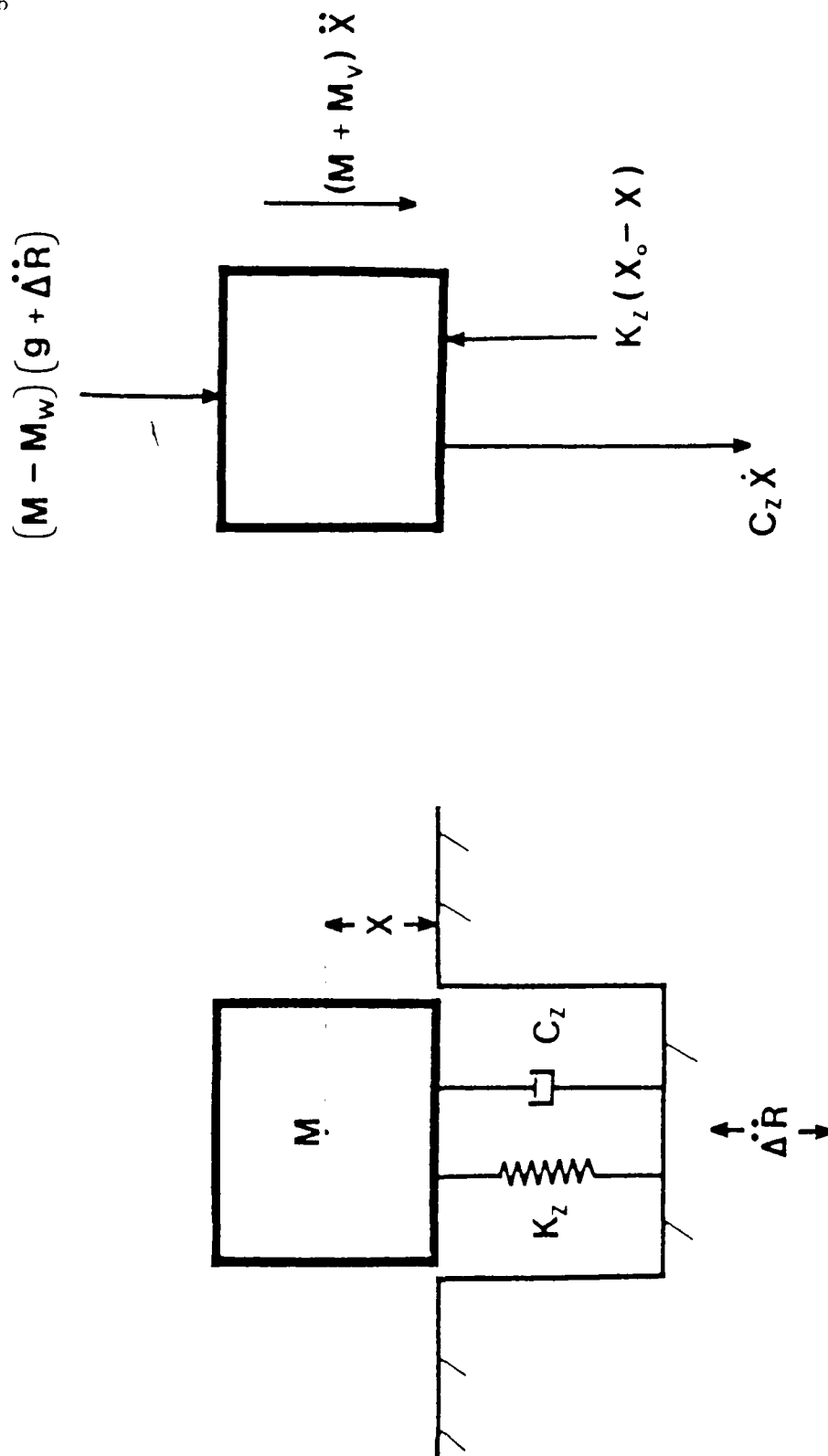


Fig. F-2. A submerged mass-spring damper system, subjected to vertical ground motion with acceleration R . The inertial and mechanical forces acting on this mass are shown in a freebody diagram. M_w is the virtual mass term and M_w is the mass of the displaced water.

the displaced sediment, which gives rise to an additional buoyancy force. This force may be neglected for the Lopez experiment. These equations of motion lead to a coupling constant, $C = (M - M_w) / (M + M_w)$, which represents the ratio of the buoyant mass to the dynamic mass of the OBS-water system (Sutton et al. 1980a). $C = 0$ represents perfect coupling, and $C = 1$ is the worst case. Stated another way, the OBS response can be compared to that of a harmonic oscillator with input force proportional to the unbalanced buoyancy of the OBS in the water and a mass equal to the OBS-water dynamic mass. The spring constant and damping are caused by the soil stiffness and energy radiated to infinity.

Since the free field ground motion (\ddot{x}) is zero for the vertical transient tests at Lopez, the equation is modified by replacing the right-hand side by the force induced by a step function transient input:

$$(M + M_w)\ddot{x} + C_Z\dot{x} + K_Zx = F(t). \quad (8)$$

For sinusoidal oscillation of the instrument with an attached shaking unit:

$$(M_t + M_w)\ddot{x} + C_Z\dot{x} + K_Zx = -M_s\ddot{y} \quad (9)$$

where M_s = mass of shaking unit

$M_t = M + M_w$

y is the acceleration of the shaking mass.

Eq. (5) gives the natural frequency for any of the above three cases if M is replaced by the effective mass M_E where

$$M_E = M + M_w \quad (10)$$

Those familiar with various OBS's realize that they are generally complex in form; however, most can be approximated by combinations of simple geometric shapes. The added mass terms for a sphere ($1/2 M_w$), a disc ($4/3 \rho_w R^3$), and a cylinder ($.6M_w$) are used to calculate the effective mass of each instrument and standard (Batchelor, 1967; Byrd, 1978). M_w is the mass of the displaced water, ρ_w is the water density, and R is the radius of the disc.

Eqs. (7), (8), and (9) assume a mass with a circular bearing radius. For vertical motion, the theory is valid for all tripod-based instruments with circular contacts. As well, OBS's where one dimension does not exceed twice the other may be similarly treated (Richart et al., 1970). (The bearing radius is computed by assuming the rectangular area to be circular.)

Damping in Lysmer's analog is due to radiation losses by the propagation of seismic energy to infinity and can be calculated:

$$D = \frac{C_z}{C_c} \quad (11)$$

$$C_c = 2K_z M_E = 2 \sqrt{\frac{4GRM_E}{1-\nu}} \quad (12)$$

$$D = .425/\sqrt{B} \quad (13)$$

where C_c is critical damping and B is a dimensionless mass factor

$$B = \frac{1-\nu}{4} \frac{M_E}{MR} \quad (14)$$

B is a comparison of the mass of the instrument to the mass of the soil influencing the instrument. In terms of a harmonic oscillator model, it is a ratio of the moving mass to the mass of the spring. A high B value signifies a comparatively massless spring and therefore correspondingly low radiation damping. However, low B values signify a spring with mass approaching that of the instrument, and thus high radiation damping would result. The analogy to a mass spring system differs, however, since the energy is radiated away to infinity in the half-space but it is contained in modes of oscillation of the spring in the mass-spring system. The effect of the mass of the half-space that moves with the OBS is included in Eq. (5) in the damping coefficient, D . It should be noted that under the conditions that Lysmer's analog holds ($B \geq 1$), the mass of the OBS must be relatively large compared to the mass of the sediment that would move under its influence.

The above theory includes several idealizations. OBS's do not rest on the bottom sediments but embed themselves to a depth depending most importantly on their bearing pressure. Also, the soil beneath the instrument is neither homogeneous, isotropic, nor semi-infinite. These assumptions and others of a more subtle nature will be discussed further in the analysis and discussion section.

Model Investigation

For Lysmer's and Richart's (1966) mass-spring-damper model, a reciprocity exists between response due to ground motion (from Eq. 7):

$$\frac{\bar{x}}{\bar{r}} = \frac{M-M_w}{M+M_v} \left(\frac{1}{\frac{\omega_0^2}{\omega^2} - 1 + i \frac{C_z}{(M+M_v)\omega}} \right) \quad (15)$$

and the response computed by shaking the instrument with a displacement $y = \bar{y} \exp(i\omega t)$:

$$\frac{\bar{x}}{\bar{y}} = \frac{M_s}{M_t + M_v} \left(\frac{1}{\frac{\omega_0^2}{\omega^2} - 1 + i \frac{C_z}{(M_t + M_v)\omega}} \right) \quad (16)$$

The only difference is an amplitude factor reflecting the inertia transfer between the shaker and the larger instrument mass.

In order to verify the theory and develop a procedure for studying more complex cases, experiments were performed with foam rubber. The experiments were conducted in air ($M_v, M_w = 0$) and were intended to study soil-structure interaction. Different masses of varying bearing radius were placed on foam rubber and oscillated with a sinusoidal input force. The resonant frequency depends on the stiffness and damping constants and therefore on the elastic properties of the foam (Eq. 4). Young's Modulus, the modulus of rigidity and the density of several types of foam were also measured in static experiments. A high-density loaded foam ($G = 3.5 \times 10^7 \text{ N/M}^2$, $E = 1.1 \times 10^8 \text{ N/M}^2$, and $\rho = 31 \text{ kg/M}^3$) was chosen for use in all experiments because of its linear stress-strain relationship over a wide range of stresses. We then compared values of the elastic parameters determined from the static tests to those determined by shaking a model OBS resting on foam.

Figure F-3 shows the experimental configuration used in finding the resonant frequency of the mass-spring-damper analog. A sinusoidal voltage is applied to geophone A, causing the moving mass to oscillate and thus applying a sinusoidal force to the system. Geophone B acts as the seismometer, which senses the motion induced by Geophone A. Both geophones are mounted rigidly in a PVC holder that is fastened to discs of various radii. The mass of the model includes the mass of the geophones, holder, disc, and any added weights. The area of the foam, on which the model rests, is large enough to approximate the elastic half space in two dimensions. The thickness of the foam can be varied to allow us to model the transition between an elastic half space and an elastic layer on a rigid stratum. By slowly varying the input frequency, the resonant frequency is determined for each disc-mass system. Plotting the natural frequency against $(R/M)^{1/2}$ should return a line proportional to the dynamic shear modulus of the foam according to Eq. (5), assuming small damping. The results are shown in Figure F-4 along with a hashed line corresponding to the shear modulus obtained in static tests. One source of variation in the points from the static shear modulus value is the neglecting damping. The radiation or geometric damping computed using Eqs. (9) and (10) is negligible because of the low density of the foam; however, the viscous and material damping, although unaccounted for in an elastic model, will cause deviations of the points from the line.

The ratio of the thickness of the foam (H) to the bearing radius of the disc (R) is also tabulated for each point on Figure F-4. For H/R large, the foam can be treated as a semi-infinite elastic half space, but

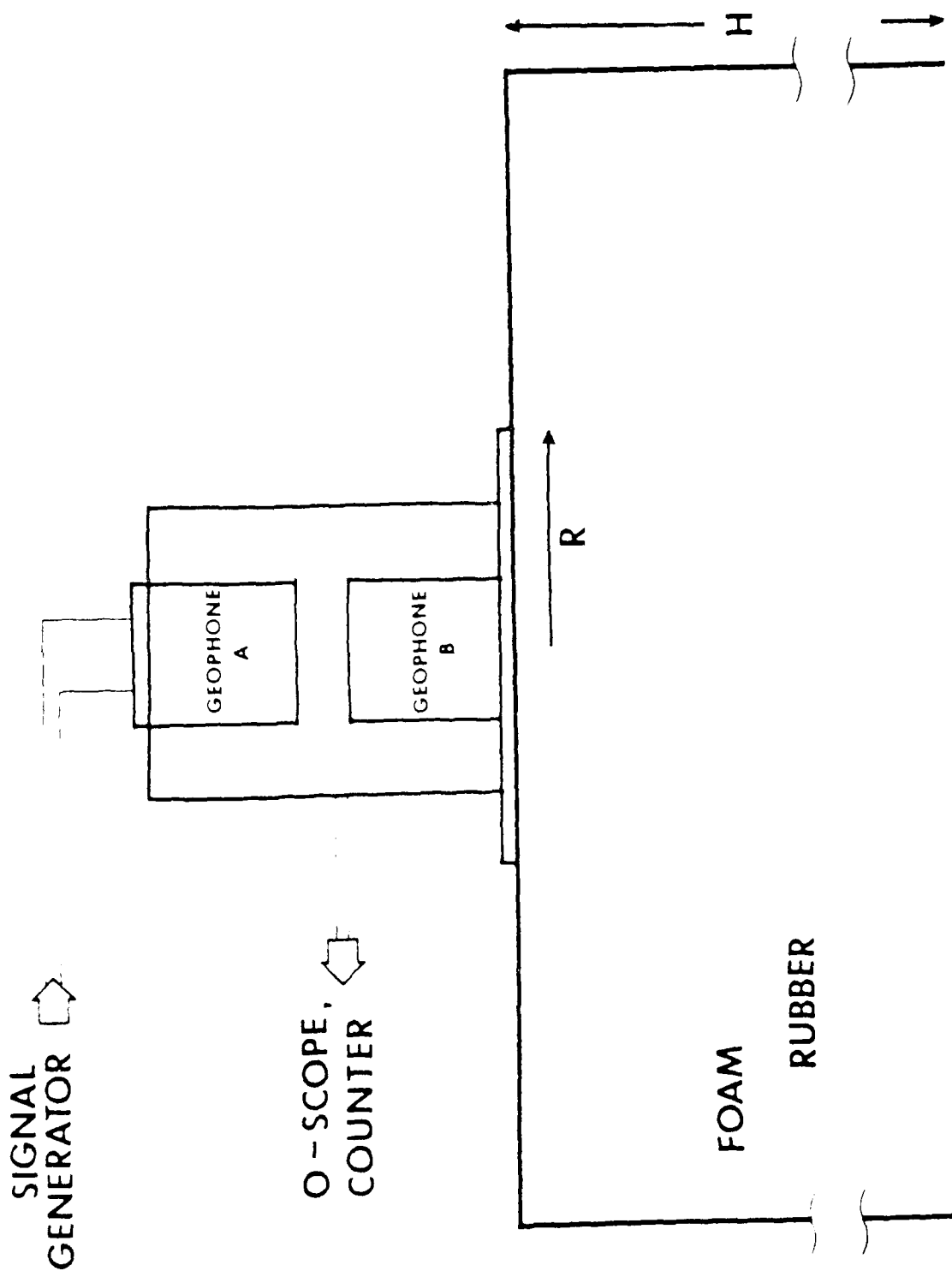
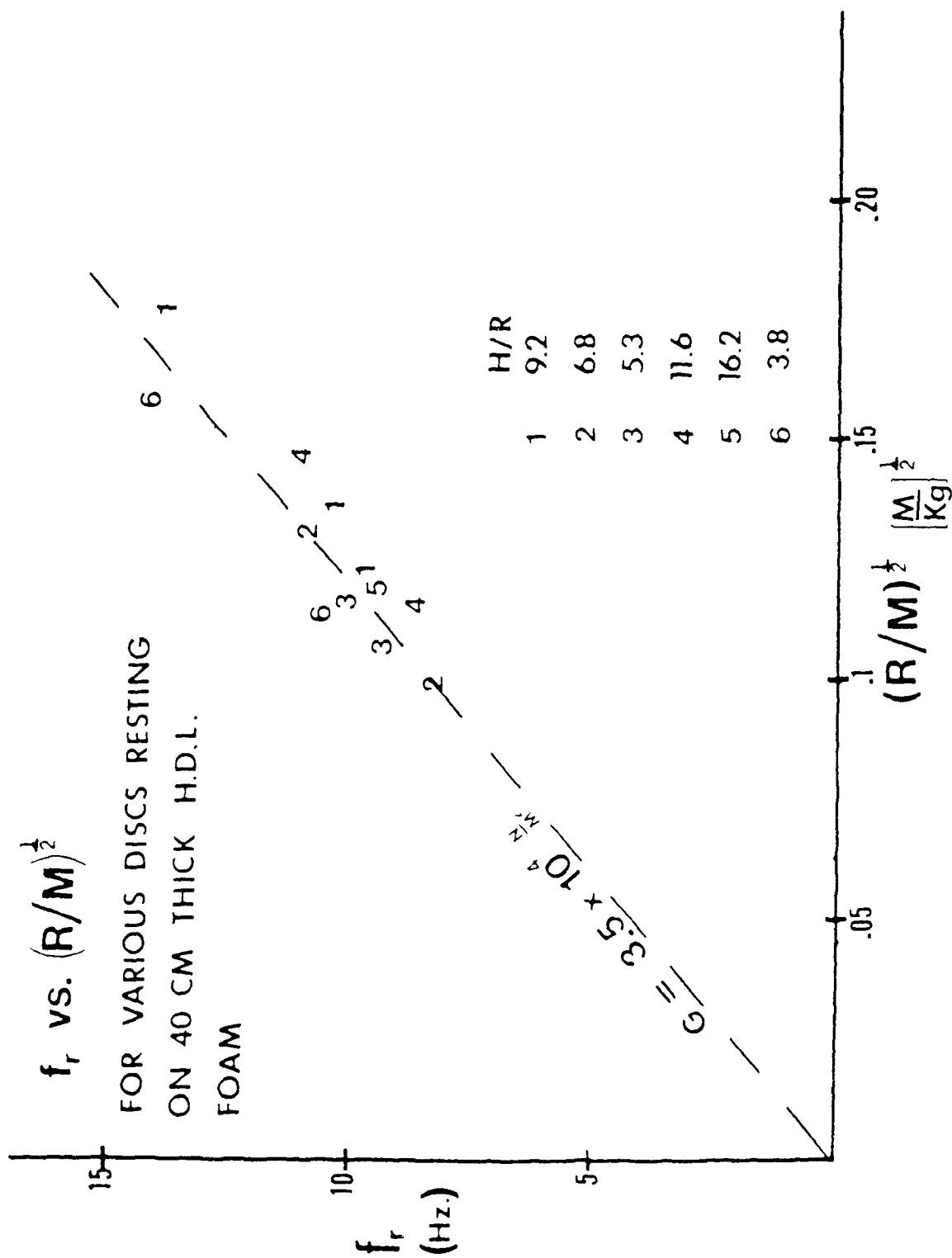


Fig. F-3. Schematic of a foam rubber modeling experiment, designed to investigate instrument-soil interactions. Geophone A is driven by an external sine wave current source and Geophone B measures the resulting displacement.



F-11

Compare the shear modulus value of a high-density loaded foam obtained statically with
that in the dynamic experiment shown in Figure F-3.

UNCLASSIFIED

LOPEZ ISLAND OCEAN BOTTOM SEISMOMETER
OCT 80 G H SUTTON, B T LEWIS, J EWING
HIG-80-4

ARLSON EXPERIMEN-
N00014-75-C-0209
NL

శ్రీ సత్యం

END
DATE
FILMED
2-81
DTIC

for large bearing radius discs, the rigid stratum beneath the foam must be taken into account. Note points 2, 3, and 6 which show progressively larger shear modulus values with respectively decreasing H/R values.

Lopez Data Interpretation

The elastic soil model was also applied to the Lopez vertical transient test data. The bearing radius and mass of each instrument was calculated from the physical properties supplied by its institute of origin (Table F-1). The error estimate associated with each OBS effective mass is based on the degree to which it could be thought of in terms of simple geometric shapes.

The natural frequency of each instrument-soil-water system was measured directly from the vertical transient test data acquired at Lopez. (For data payouts, see Loncarevic, 1979; Sutton et al., 1980b.) Measured ringdown frequencies, as recorded in Table F-2, have an estimated error of .5 Hz for $f_N \leq 10$ Hz and ± 1 Hz for $f_N \geq 10$ Hz. f_N is plotted against $[R(1 - 2D^2)/ME]^{1/2}$ in Figure F-5. Two lines are superimposed to illustrate the trends in the data, including approximate shear modulus and velocity values.

Damping factors can also be retrieved from the original transient test data by modeling the decay of a damped harmonic oscillator (see also Sutton et al., 1980a). The decay time is quite sensitive to the damping for most of the transients. In Figure F-6 the damping factors are plotted against B values, calculated using Eq. (10) and the data in Table F-1. For comparison the D versus B curve for a true elastic half space is also plotted. A value for ν of the .48 is used throughout.

Analysis and Discussion

If all the assumptions implicit in the proposed model were valid, all the plotted points in Figure F-5 would fall on a single straight line corresponding to the shear modulus of Shoal Bay mud. Also, some variation in the soil beneath each instrument is expected and will cause scatter in the computed shear modulus values.

Up to now, we have treated the Shoal Bay mud as a semi-infinite elastic half space. We do, however, have reflection data (Sutton et al., 1980b) from this site indicating that the top silt layer under the instruments is only $2\frac{1}{2}$ to 3 m deep. The properties of the "basement rock" are not known. Intuitively, it might be either a glacial deposit or a hard siltstone or sandstone, but it is definitely of higher rigidity than the overlying silt.

Arnold et al. (1955) and Bycroft (1956) studied the effects of a rigid boundary under an elastic layer and Luco (1974) investigated

Table F-1

Relevant Physical Properties of OBS's and Standards

OBS	Mass in Air (kg)	Effective Mass (kg)	Error ΔM_e (kg)	Bearing* Area (m ²) per foot pad	Bearing Radius (m)	Bearing Pressure (kg/m ²)
BIO	135	200	5	.36	.34	94
HIGB	8	10.4	1	.022	.084	150
MIT	310	610	25	1.27	.64	41
MITEX	17	28	2	.13	.20	70
PLS	60	260	10	.98	.56	34
SIO	190	250	5	.08 (3)	.16 (3)	173
UCSB	170	220	10	.073 (3)	.152 (3)	123
USGS	118	163	5	.14	.21	150
UTG	60	83	3	.008 (3)	.05 (3)	470
UW	144	180	4	.003 (3)	.03 (3)	2000
UWF	530	680	10	.13	.20	1800

*The quantity in parentheses represents the number of footpads.

Table F-2

OBS Coupling Properties

OBS	Freq. (Hz) Measured	Freq. (Hz) Corrected	Inferred Shear Modulus $G - (N/m^2)$	Damping Factor	Effective Mass Ratio (B e), $V = .48$	H/R
BIO	9.6	9.7	2.9×10^5	.15 - .18	.43	8
HIGB	17	17	1.9×10^5	.14 - .15	1.5	34
MITEX	22	23	5×10^5	.3 - .32	.27	14
PLS	10.2	10.3	2.6×10^5	.13 - .15	.12	4.9
SIO	11	11	3.3×10^5	.09 - .1	1.7	13
UCSB	8.2	8.2	1.7×10^5	.06 - .07	1.7	18
USGS	3.9	8.9	3.1×10^5	.04 - .05	1.4	13
UTG	7.3	7.3	1.7×10^5	.04 - .06	17.8	55
UW	7.5	7.5	5.6×10^5	.05 - .08	168	98
UWF	8.5	8.6	1.3×10^6	.09 - .24	6.7	13

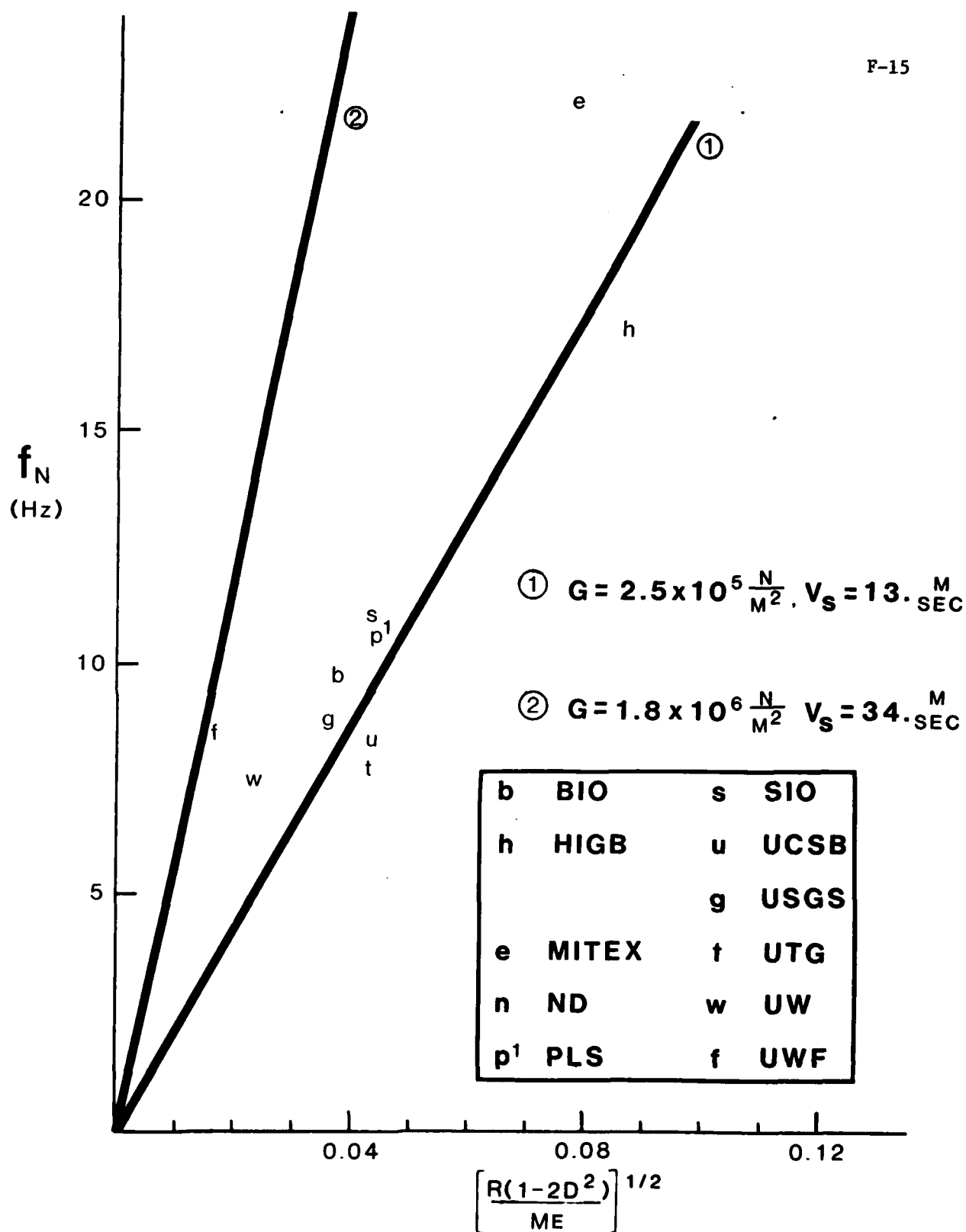


Fig. F-5. This plot of ringdown frequency versus $[R(1 - 2D^2)/M_E]^{1/2}$ should return the shear modulus of Shoal Bay mud. The two lines represent the shear velocities of 13 and 34 m/sec, respectively.

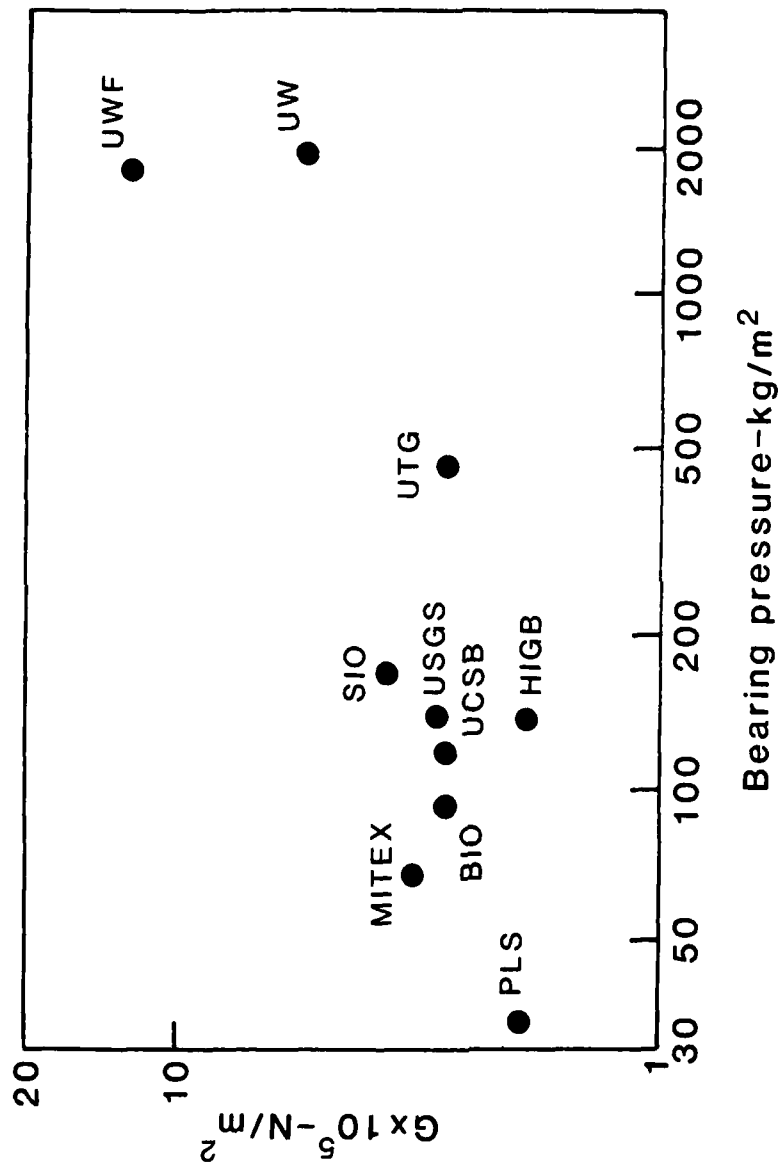


Fig. F-6. Shear modulus inferred from the ringdown frequencies versus static bearing pressure. The general trend of increasing shear modulus with increasing bearing pressure indicated that heavier instruments sink deeper in the soft sediments, to stiffer material.

foundation impedances for layered elastic media. One important conclusion of these studies is that the underlying layer begins to have a significant effect on the stiffness when H/R is less than 6; H is the thickness of the top elastic layer and R is the bearing radius of the instrument. This effect is also observed in the foam rubber experiment.

Another important effect is the varying embedment of the instruments resulting from variations in their bearing pressure. The bearing pressure in Table F-1 is a static value equal to the weight of the OBS in water divided by the total footpad area. If the instrument were deployed in free fall, the pressure would be considerably greater when it hits bottom. Considerable variation in embedment might be expected due to this effect. Figure F-6 shows a plot of bearing pressure versus shear modulus, G , inferred from the ringdown frequencies. A clear trend toward increasing shear modulus for more massive instruments is indicated.

The damping factors are plotted versus B in Figure F-7. The deviation from the elastic half space model increases at low B values, where Lysmer's analog begins to break down. Sources of damping such as hydrodynamic losses and losses due to soil-water exchange should be considered. It is surprising that the plate standard has such low damping. Its very low bearing pressure may be a factor, allowing it to rest on the very weakest sediments, yet its large diameter causes it to feel deeper, more competent material for the transient test. Since the damping is due to radiated seismic energy, reflected energy from underlying layered structures is sure to cause significant effects. Damping factors would intuitively seem to be more sensitive than ringdown frequency to reflected energy from layered structures.

With geometric damping included, the average shear velocity recorded by the instruments, which fall along line "1" in Figure F-5, is 15 m/sec; and for those along line "2", 33 m/sec. It is both interesting and encouraging to note that Lewis and Tuthill (1980) indicate that "granddaddy" waves measured at Lopez had group velocities ranging between 10 and 30 m/sec. Also, the time difference between P-S conversions and initial P arrivals from airgun records suggest a shear wave velocity of 15 m/sec in the 3-m silt layer.

In Situ Calibration

The reciprocity between shaking the instrument and ground motion demonstrated by Eqs. (15) and (16) suggests the viability of an in situ calibration technique. A first step might be to verify Eq. (7) by conducting foam rubber modeling experiments in water. (These experiments would concentrate on the instrument-water interactions.)

An in situ calibration method might rely on an attached shaking unit to determine the stiffness and damping constants of the soil, following the analysis of the Lopez data and foam rubber experiments. An estimate of the vertical motion response function would be computed from these

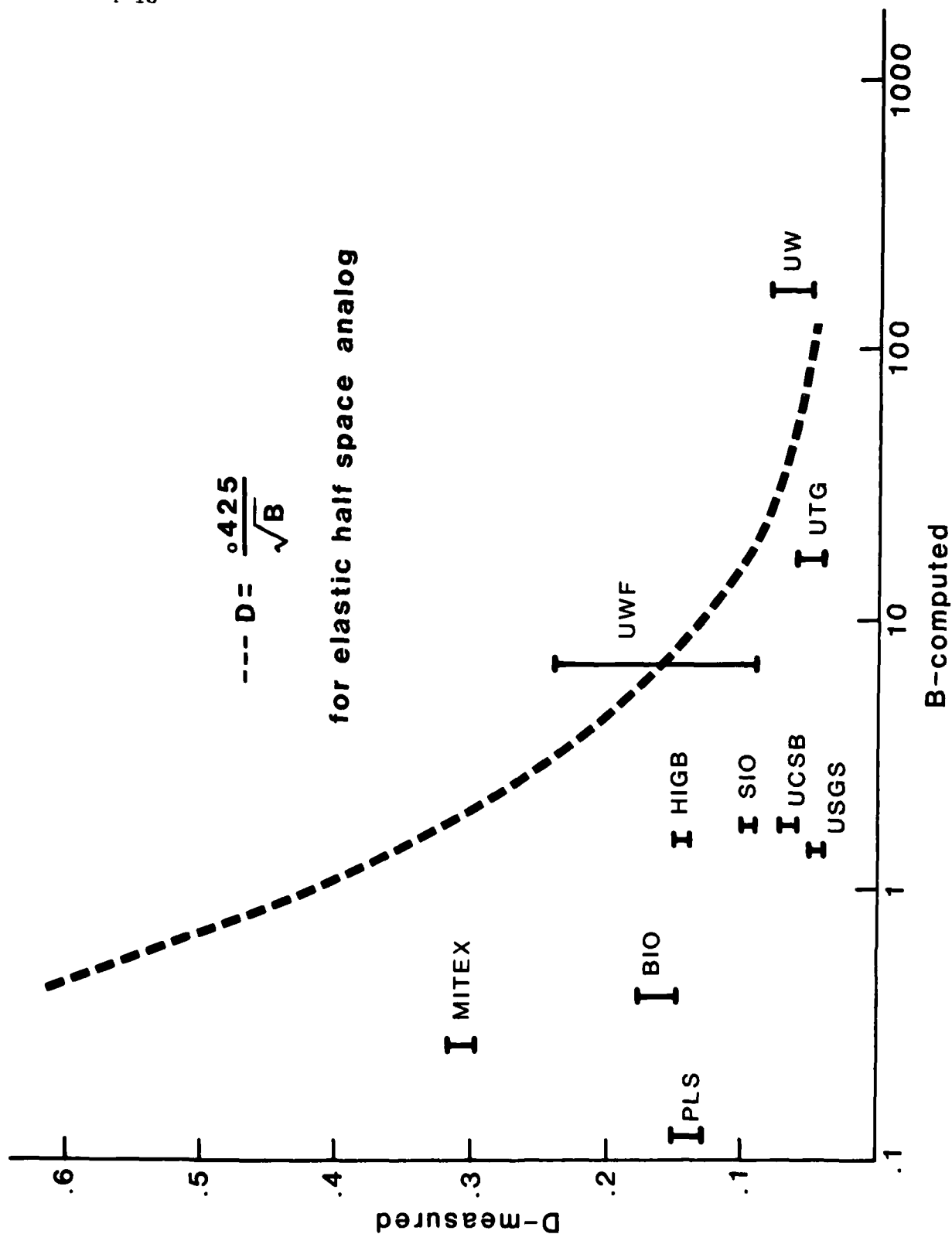


Fig. F-7. The damping factors measured from the transient test data are plotted against the effective mass ratio's of the OBS's. The theoretical curve for a simple elastic model is illustrated for comparison.

soil constants, the virtual mass term and the physical properties of the instrument and Eq. (15). The response function for that particular site would then be used to deconvolve the recorded output. More work is necessary to understand the instrument response to horizontal ground motion inputs. Instrument rocking and shear in the water column are expected to cause significant effects.

Implications for OBS Design

Eq. (7) suggests that a high damping factor will result in the most smoothly varying and uncomplicated coupling response. Further, if K_2 is increased, the coupling resonance may be above the seismic band of greatest interest, so it can be ignored. This would imply that the bearing area should be large to decrease the B value. However, the plate "feels" the same shear modulus as do the other instruments yet has an anomalously low damping factor. Another way of improving the coupling is to make the instrument more nearly neutrally buoyant. This will affect the horizontal coupling, although probably adversely. Given the complications in variable soil conditions, impact geometry upon deployment, and variable damping factors, an in situ method of calibration becomes highly attractive and may be the only way of calibrating an OBS to ground motion.

Conclusions

We have a reasonable understanding of the Lopez Island vertical ringdown frequencies. Although a simple uniform elastic model does not explain all the results, it can be refined to give qualitative explanations of certain discrepancies. The damping factors do not fit the half space model and it seems that reflected radiation or other factors must also be important.

The model fit establishes that the resonant frequencies excited by the Lopez vertical transient tests are due to soil-instrument-water interactions. These resonances occur within the bandwidth of seismic interest and therefore will distort the recorded signal.

The eventual aim in studying this problem is to develop an in situ calibration technique for any OBS at any site, since the response will surely be extremely site dependent. The transient tests performed at Lopez Island and the foam rubber experiments yield the response of an instrument to ground motion. All of the dynamic and elastic soil parameters relevant to vertical motion are contained in the transient test data. In situ calibration is, therefore, not only desirable but feasible and should be considered by every institute deploying OBS's.

A complete understanding of OBS response also requires studies of the horizontal motions of the instruments. This is a more complex problem, yet one that is tractable. Foam rubber modeling would be

particularly useful for horizontal motion, to demonstrate the behavior of differing instrument bearing configurations. This would avoid a lengthy theoretical development that is not critical to either an understanding of the problem or the determination of the appropriate response deconvolution parameters, since in situ calibration will probably be necessary for accurate waveform studies.

Acknowledgments

We acknowledge several helpful discussions with George Sutton. This work was supported by ONR contract No. N00014-78-C-0522. Reproduction in whole or in part is permitted for any purpose of the United States Government.

References

- Arnold, R. M., G. N. Boycroft, and G. B. Warburton, 1955. Forced vibrations of a body on an infinite elastic body. J. Appl. Mech., Trans. ASME, v. 77, p. 391-401.
- Batchelor, G. K., 1967. An Introduction to Fluid Dynamics. Cambridge University Press, Cambridge, England.
- Bycroft, G. N., 1956. Forced vibrations of a rigid circular plate on a semi-infinite elastic space and on an elastic stratum. Philos. Trans. R. Soc. London, Ser. A, v. 248, p. 327-368.
- Byrd, R. C., 1978. A laboratory study of the fluid-structure interaction of submerged tanks and caissons in earthquakes. NOAA, Office of Sea Grant Report No. UCB/EERC-78/08, May, 150 pp.
- Hamilton, E. L., et al., 1970. Velocities of compressional and shear waves in marine sediments determined in situ from a research submersible. J. Geophys. Res., v. 75, no. 20, p. 4039-4049.
- Hamilton, E. L., 1971a. Elastic properties of marine sediments. J. Geophys. Res., v. 76, no. 2, p. 579-602.
- Hamilton, E. L., 1971b. Prediction of in situ acoustic and elastic properties of marine sediments. Geophysics, v. 36, no. 2, p. 266-284.
- Hsieh, T. K., 1962. Foundation Vibrations. Proc. Inst. Civ. Eng., v. 22, p. 211-226.
- Lewis, B. T. R., and J. D. Tuthill, 1980. Instrumental waveform distortion on ocean bottom seismometers. This report, Appendix H.
- Loncarevic, B. D., 1979. Draft Catalog OBS Calibration Events, Lopez Island, 1978, Bedford Institute of Oceanography.
- Luco, J. E., 1974. Impedance functions for a rigid foundation on a layered medium. Nuc. Eng. Des., v. 31, p. 204-217.
- Lysmer, J. and F. E. Richart, Jr., 1966. Dynamic response of footings to vertical loading. J. Soil Mech. Found. Div., Proc. ASCE, v. 92, no. SM1, p. 65-91.
- Richart, F. E., Jr., J. R. Hall, Jr., and R. P. Woods, 1970. Vibrations of Soils and Foundations. Prentice-Hall, Inc., Englewood Cliff, N.J., 414 pp.
- Sutton, G. H., F. K. Duennebier, and B. Iwatake, 1980a, Coupling of ocean bottom seismometers to soft bottoms. This report, Appendix E.
- Sutton, G. H., B. T. R. Lewis, J. Ewing, F. K. Duennebier, B. Iwatake, and J. D. Tuthill, 1980b. Lopez Island Ocean Bottom Seismometer Inter-comparison Experiment, Final Report. HIG-80-4, Hawaii Inst. Geophys., Honolulu. (This report.)

Appendix G

STONELEY WAVES, LOPEZ ISLAND NOISE,
AND DEEP SEA NOISE FROM 1 TO 5 HZ

STONELEY WAVES, LOPEZ ISLAND NOISE,
AND DEEP SEA NOISE FROM 1 TO 5 HZ

Jonathan D. Tuthill
Brian T. R. Lewis
Jan D. Garmany

Geophysics Program and Dept. of Oceanography
University of Washington
Seattle, Washington 98195

Abstract

The Lopez Island OBS Intercomparison Experiment provided a data set of sufficient spatial density to allow study of the propagation of shot-generated Stoneley waves as well as ambient background noise. The Stoneley waves were observed propagating at velocities of 20 to 50 m/sec. Phase velocities were determined by fitting peaks in the frequency wave number spectrum. Group velocities were calculated by narrowly filtering the data and determining the arrival time of the peak in the frequency packet. Particle displacement plots illustrate the surface wave character of these waves. The analysis of the ambient background noise failed to produce a clearly defined dispersion curve yet it did allow bounds to be placed on the velocities (20 to 50 m/sec). The data were modeled using eleven layers overlying a half-space. The results indicated that the top 7 m of the sediment column at Lopez Island is best approximated by two zones. In the upper zone there is a fairly rapid range of shear velocity with depth. This zone overlays a region in which the shear velocity gradient is much lower. Deep ocean background noise from University of Washington ocean bottom seismometers was also examined. Although insufficient data precluded any velocity analysis, definite similarities exist between these data and noise data observed at Lopez Island.

Introduction

The Lopez Island OBS Intercomparison Experiment provided a unique set of data for evaluating the particle motion, frequency spectra, and wave number spectra of background seismic noise and shot-generated, low-velocity dispersive surface waves. These waves have been named granddaddy waves (Heron et al., 1968) because of their extremely large amplitude relative to other shot-generated phases. It is the purpose of this paper to show that these granddaddy waves and the Lopez noise at least in the 1- to 5-Hz band propagate as Stoneley waves and to suggest that deep water noise in this frequency band may also propagate in this mode.

Understanding the causes and modes of propagation of ambient deep ocean bottom noise in the 1 to 100 Hz band is an important problem to ocean bottom seismology for a number of reasons. First, as most marine seismic refraction experiments are conducted in this frequency band, the existence of any significant amount of noise can severely degrade the data. Unpublished OBS data suggest that noise level in this band varies widely with geographic location. Second, knowledge of noise characteristics should furnish information constraining OBS design parameters, allowing the effects of noise to be minimized.

Prior to the Lopez Island Experiment there were some (unpublished) indications that deep sea noise might be of short wavelength. This being the case, an array of closely spaced sensors would be required to determine phase velocity. As it turned out, the Lopez Island array, which had a maximum dimension of about 40 m, was reasonably well-suited for noise analysis (see Sutton et al., 1980, for locations). As comparable data from a deep water array do not now exist, only the similarities between Lopez Island and deep water data can be noted and the probable characteristics of deep water noise inferred.

In the following four sections the nature of the granddaddy waves as well as an ambient background noise, observed both at Lopez Island and at deep ocean sites, will be addressed. It will be shown that the granddaddy waves observed in both environments have similar spectra and velocity dispersion curves, and represent Stoneley waves propagating along the sediment-water interface. Also, it will be shown that noise from 1 to 5 Hz at Lopez Island propagates in a Stoneley mode, which will lead to the inference of similar properties for deep sea noise; also theoretical models will be compared to observed data.

Characteristics of Granddaddy Waves Produced by Explosions

Lopez Island. For a description of the Lopez Island experiment the reader is referred to Sutton et al. (1980). During this experiment a number of cap shots and airgun shots were fired that produced low-velocity dispersed wave trains. An example of these waves is shown in

Figure G-1 on a time-distance graph. Because of their extremely low velocity relative to the P wave velocity of water and the proximity of the shots, the P arrival time has been used as the origin time. Ranges or shot locations relative to the array were determined with a non-linear least squares algorithm, which solved for shot location and velocity. The inputs for this technique were instrument location and arrival times for a given frequency packet. For a more complete discussion of this technique, see Tuthill (1980).

The dispersed wave trains, as illustrated in Figure G-1, have a group velocity of approximately 20 m/sec. The energy in these waves is concentrated in a 1- to 5-Hz band as shown by the sample spectrum in Figure G-2 from airgun shot 120. The calculated Fourier spectra from instruments with 1-Hz and 4.5-Hz seismometers show little difference, suggesting that the low-frequency cutoff at about 1 Hz may be real and not entirely caused by instrument response. It was also observed that these waves were highly attenuated on a hydrophone placed about 1 m above the bottom.

Because the particle motion is a discriminant of the wave type, a method of graphically displaying this motion was devised. Any two components are combined into an instantaneous displacement vector and these are plotted as a function of time. Figures G-3a and G-3b illustrate the synthesized particle motions for four different phase angles and three different amplitude ratios, between two components. Rectilinear motion corresponds to a phase difference of 0° and elliptical motion corresponds to a phase difference of 90° . With the actual data, ground velocity has been changed to ground displacement by the usual frequency domain method. An example of these methods applied to the dispersed wave train generated by airgun shot 182 is shown in Figures G-4 and G-5. This plot demonstrates that the particle motion is elliptical and thus is consistent with the motion of a surface wave.

In determining the group velocity dispersion curve for these waves the data were first narrow-band filtered (.5-Hz band width) at various center frequencies with a 4-pole Butterworth filter. The envelope of this filtered wave train was determined by taking the modulus of the analytic signal defined by $f(t) - i F_H(t)$, where $F_H(t)$ is the Hilbert transform of $f(t)$ (Bracewell, 1965). The travel time for this frequency band is given by arrival of the peak of the envelope. An example of this method applied to the spike vertical standard for the capshot, Georec 239, is shown in Figure G-6. These times furnished the travel time input for the non-linear least squares method described above.

The determination of phase velocity proved to be more difficult. The approach was to take the frequency wave number spectrum of the two-dimensional array and use the peaks in the wave number spectrum for a particular frequency to establish ω/k (the phase velocity). In this method accurate inter-element spacings are critical and one assumes

G-4

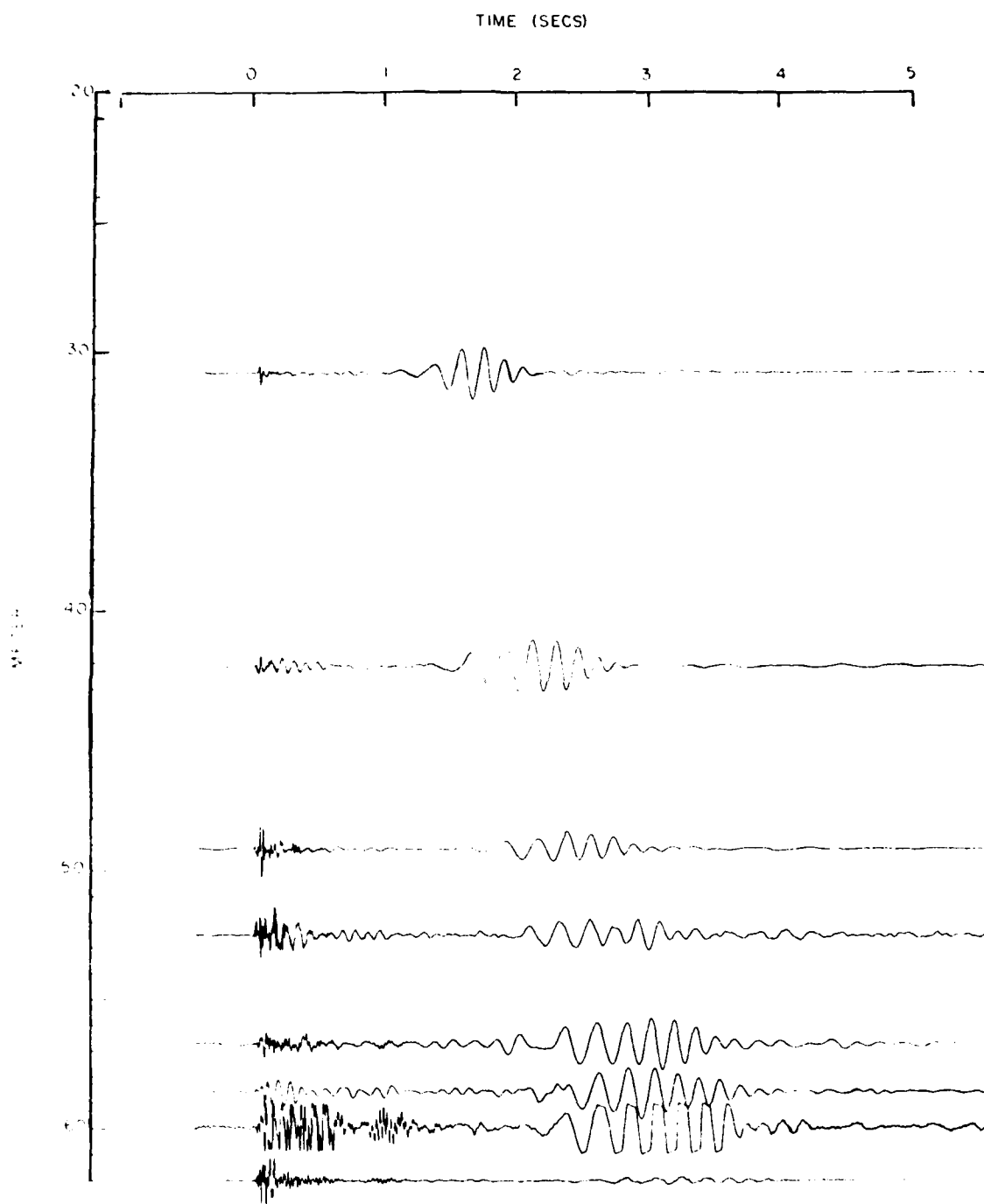
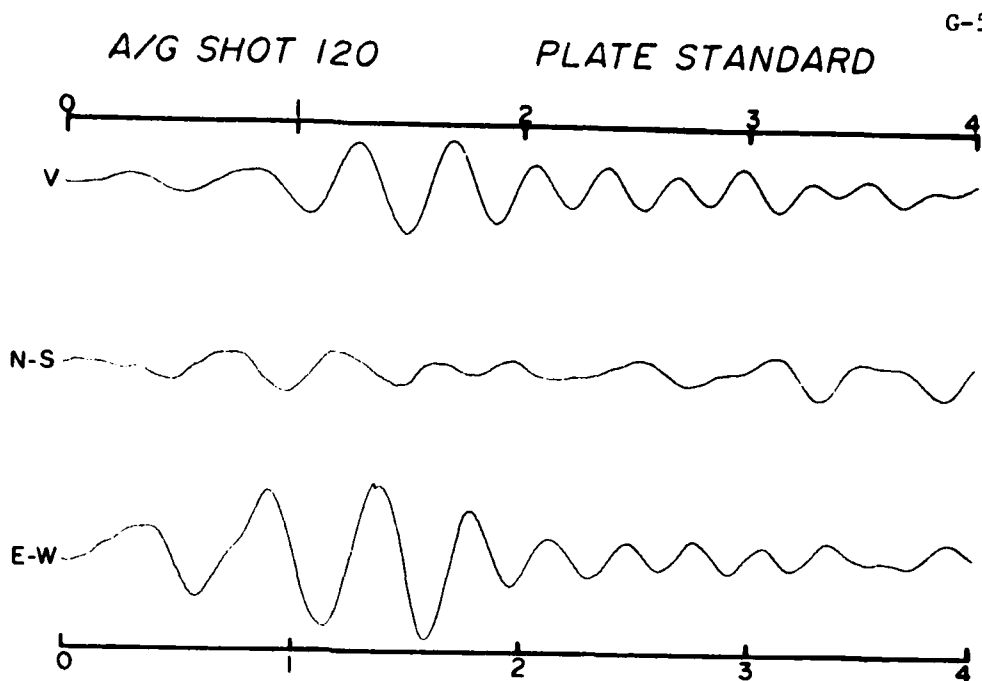


Fig. G-1. Record section for capshot at south current meter.

a



b

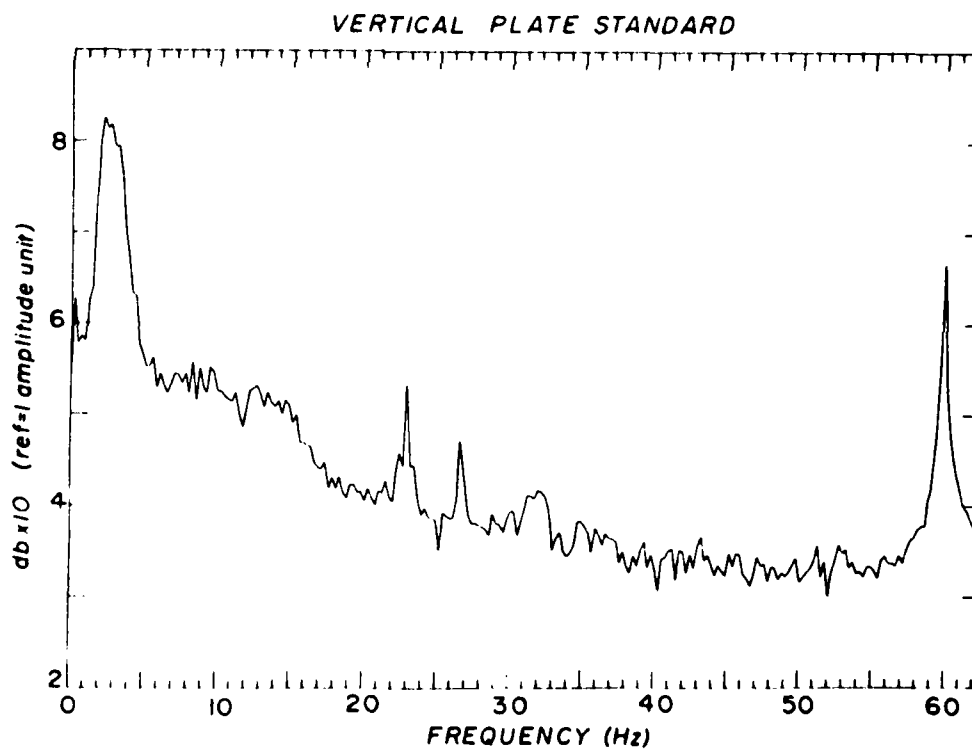


Fig. G-2(a). Particle displacement 3-components for plate standard airgun shot 120. (b). Spectrum for vertical component of plate.

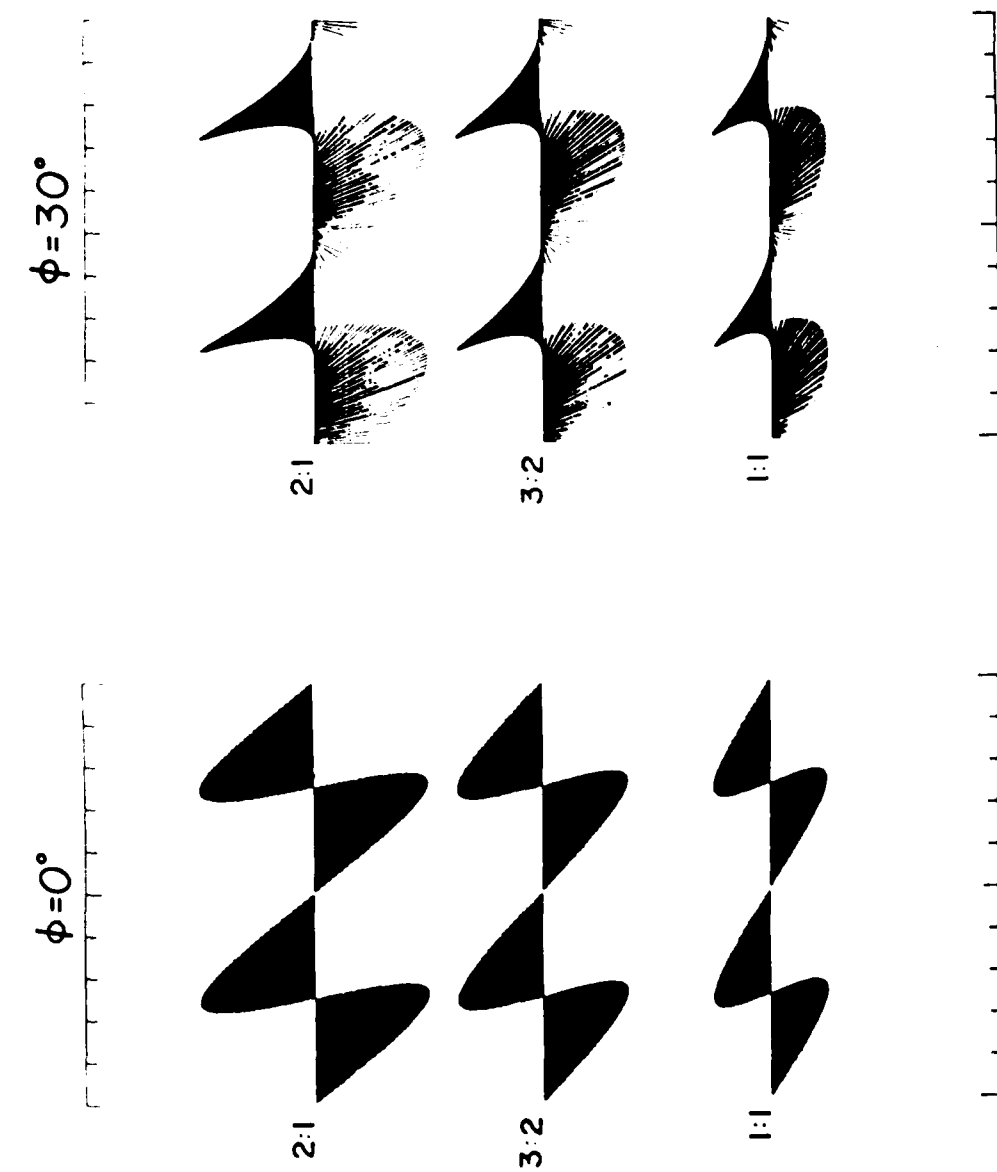
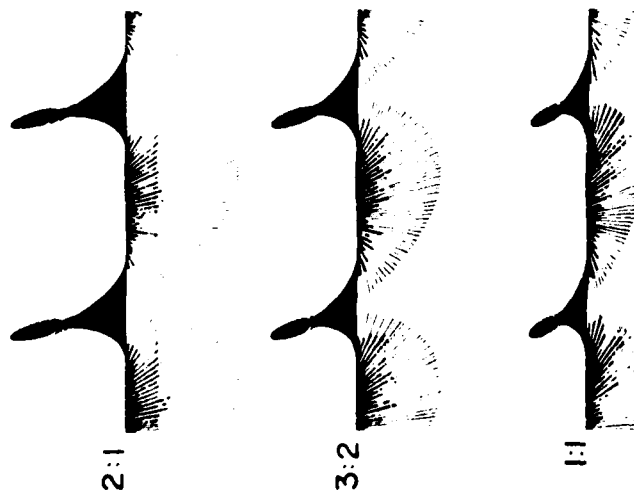


Fig. G-3a. Synthesized particle motion for phase angles of 0° and 30° .

b

$\phi = 60^\circ$



$\phi = 90^\circ$

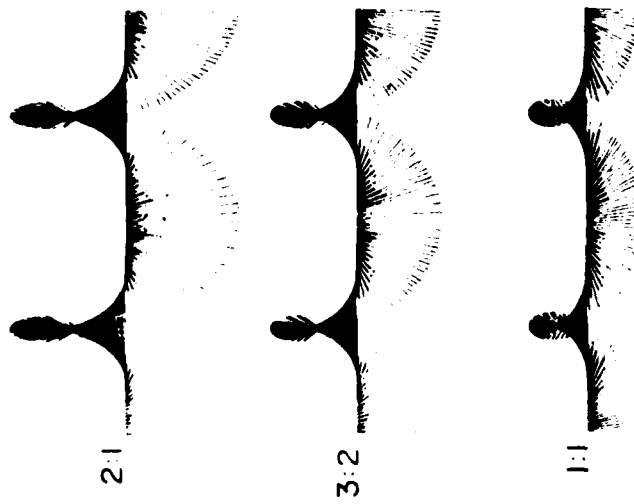


Fig. G-3b. Synthesized particle motion for phase angles of 60° and 90° .

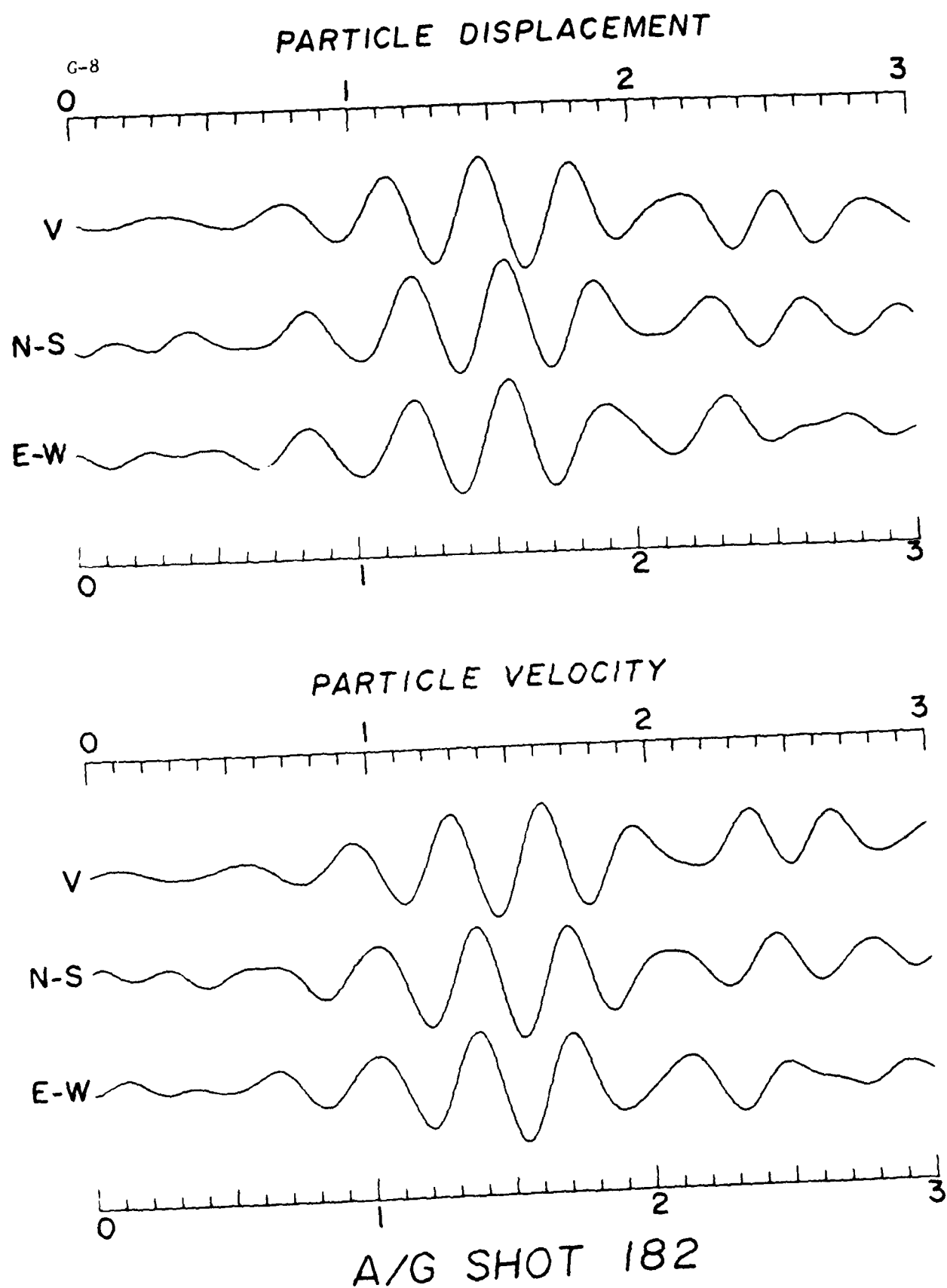
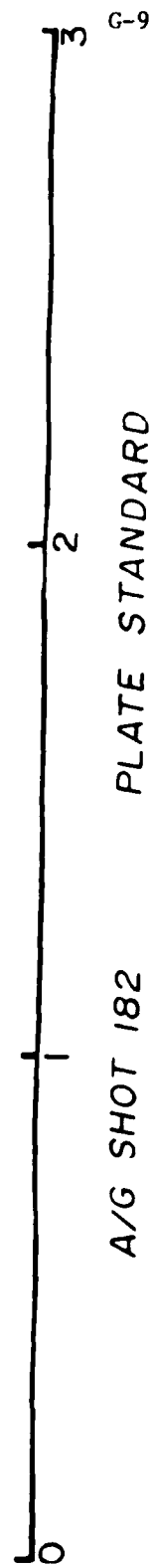


Fig. G-4. Particle velocity and particle displacement of airgun shot 182.

PARTICLE DISPLACEMENT



A/G SHOT 182

PLATE STANDARD

Fig. G-5. Particle motion plot of airgun shot 182.

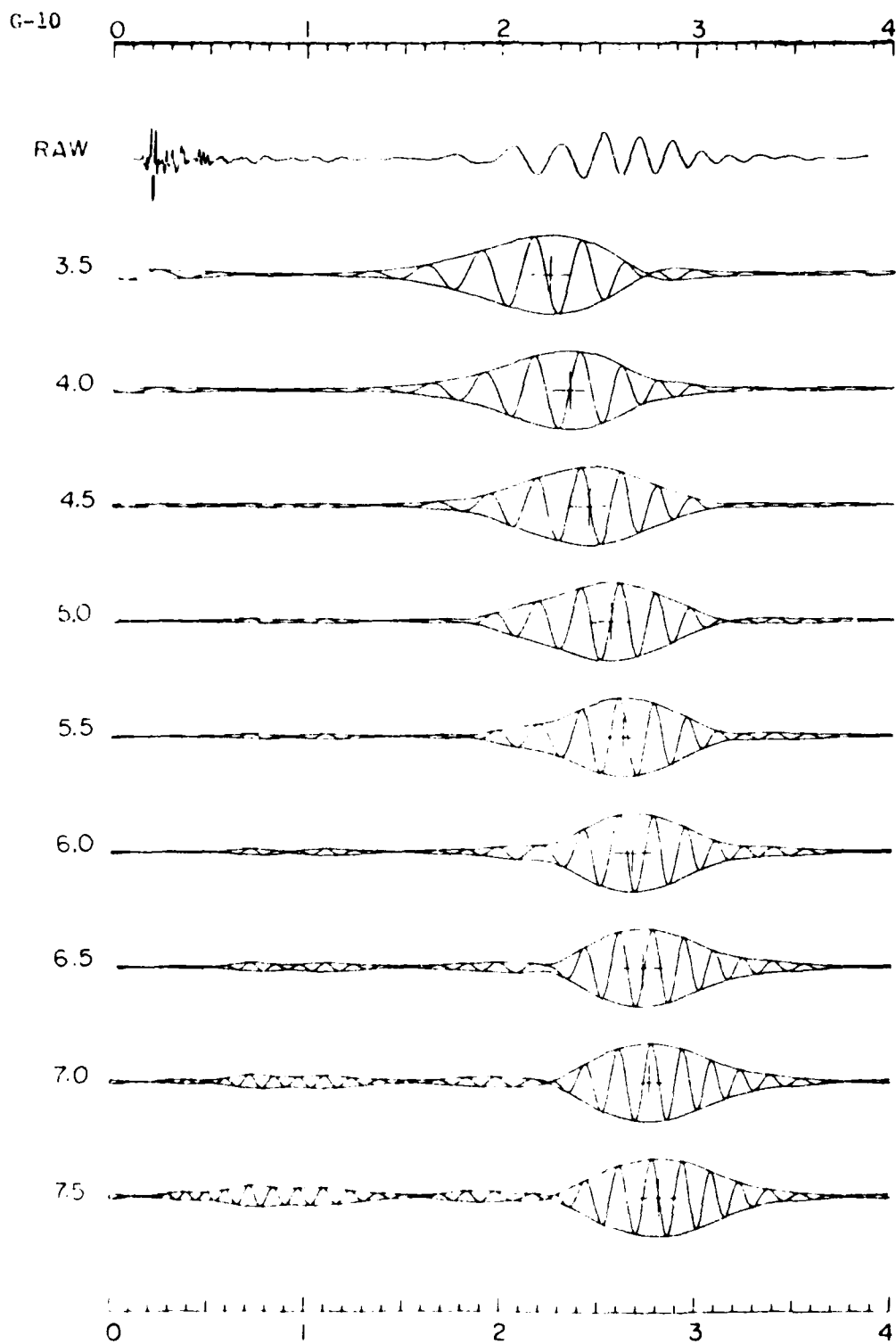


Fig. G-6. Narrow bandpass filter seismograms and their Hilbert transform envelope of dispersed waves.

plane waves propagating across the array. In actuality the shots were close enough to the array that this assumption was violated significantly and the method did not yield stable results. To improve the stability the array element positions were projected onto a plane including the shot, and the two-dimensional frequency-wave number spectrum was calculated. The resulting ω - k values were contoured and an example is shown in Figure G-7. The dashed line shows the peak that was fit to give an expression for $\omega(k)$. The final observed group and phase velocity dispersion curves are shown in Figure G-8.

Deep Sea. Observations of dispersive Stoneley waves on the sea floor have been made several times. Hamilton et al. (1969) used submersibles to deploy small charges at short distances from geophones to measure Stoneley wave velocities and hence to infer sediment shear velocities. However, the experiment described by Davies (1965) is more comparable to the results discussed here. In that experiment an array of hydrophones was deployed on the sea floor to record shots detonated on the sea floor at ranges up to a few kilometers. Large-amplitude dispersed waves were recorded that Davis interpreted to be Stoneley waves. In this case the use of hydrophones to record these waves was successful because they were placed on the sea floor. If they had been positioned a few meters above the bottom they would probably have only weakly observed these waves. An example of time series recorded by Davies at a range of 0.6 km is shown in Figure G-9. The spectrum of this signal is displayed in Figure G-10 and shows a strong peak from 1 to 5 Hz. (Note: The time series was obtained from photographically enlarging a journal figure and hence the spectrum obtained from this time series is only approximate).

The resulting group velocity dispersion curve, inferred phase velocities, and model that fit these data are shown in Figure G-11. Note that the dispersion is critically dependent on the shear velocity gradient in the upper 20 of sediment.

Characteristics of Ocean Bottom Noise

Lopez Island. Numerous samples of background noise were taken during the Lopez Island experiment (see Sutton et al., 1980). Almost without exception the noise as recorded on the standard instruments was peaked from 1 to 5 Hz. An example from the plate standard is shown in Figure G-12, which included the particle velocity, the spectrum of the particle velocity, and the particle displacement. The noise peaks from 20 to 30 Hz can be related to mechanical sources such as motor boats and are not included in this analysis.

To establish that the noise is propagating in the Stoneley wave mode it needs to be verified that (1) the particle motion is elliptical, (2) the amplitude is attenuated in the water, and (3) the phase velocity

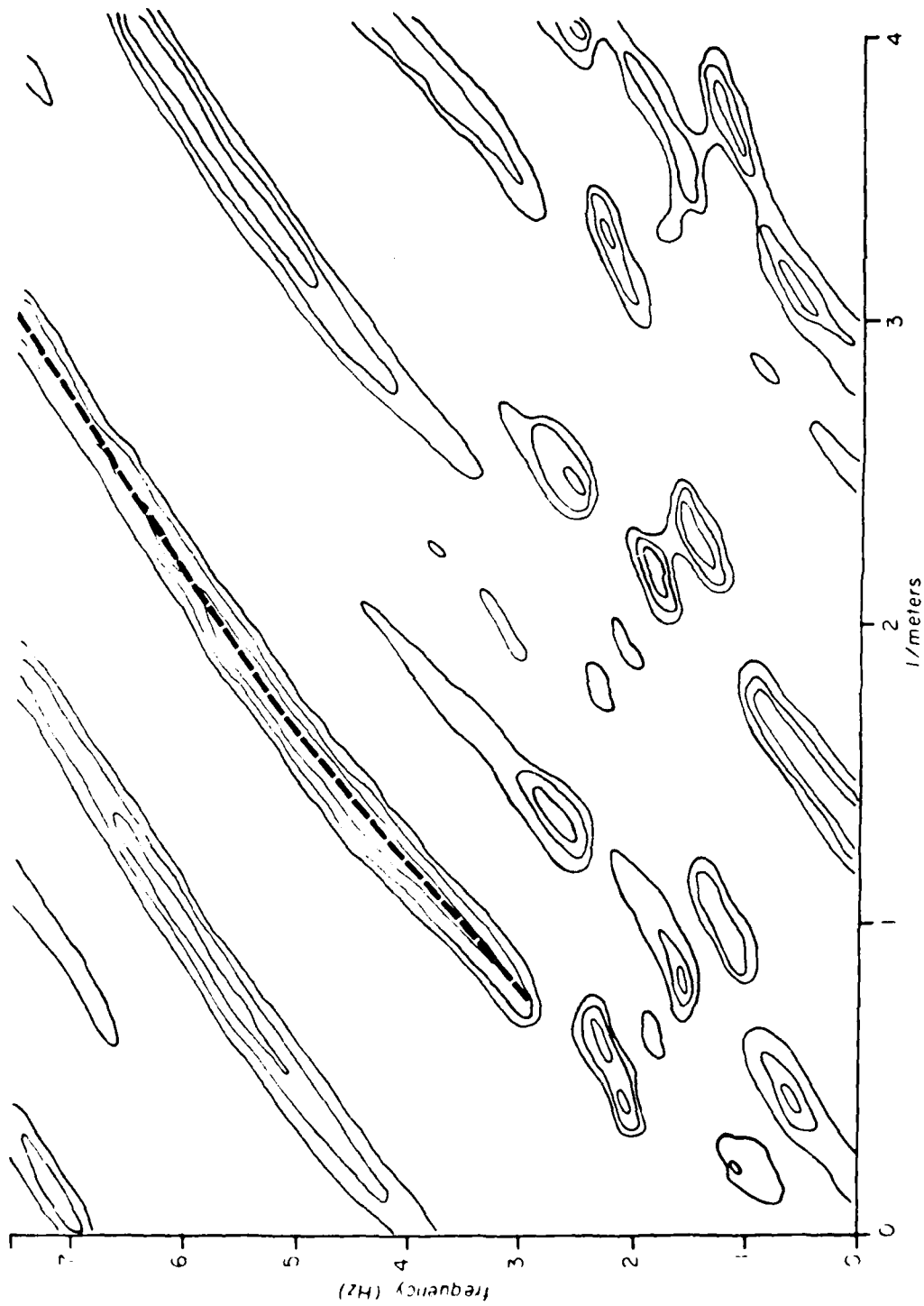


Fig. G-7. Contour plot of frequency-wave number spectrum; capshot at south current meter.

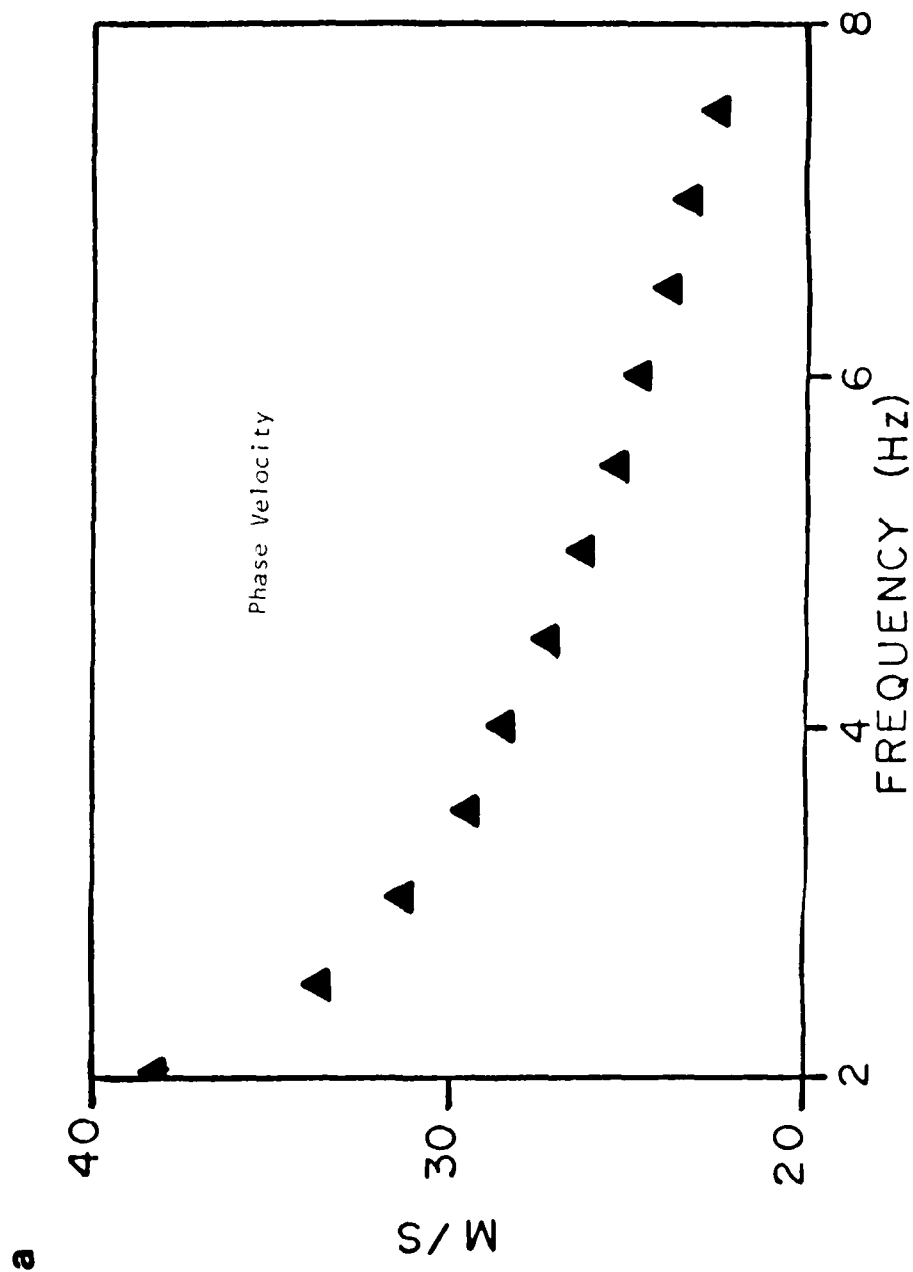


Fig. G-8a. Observed phase velocities.

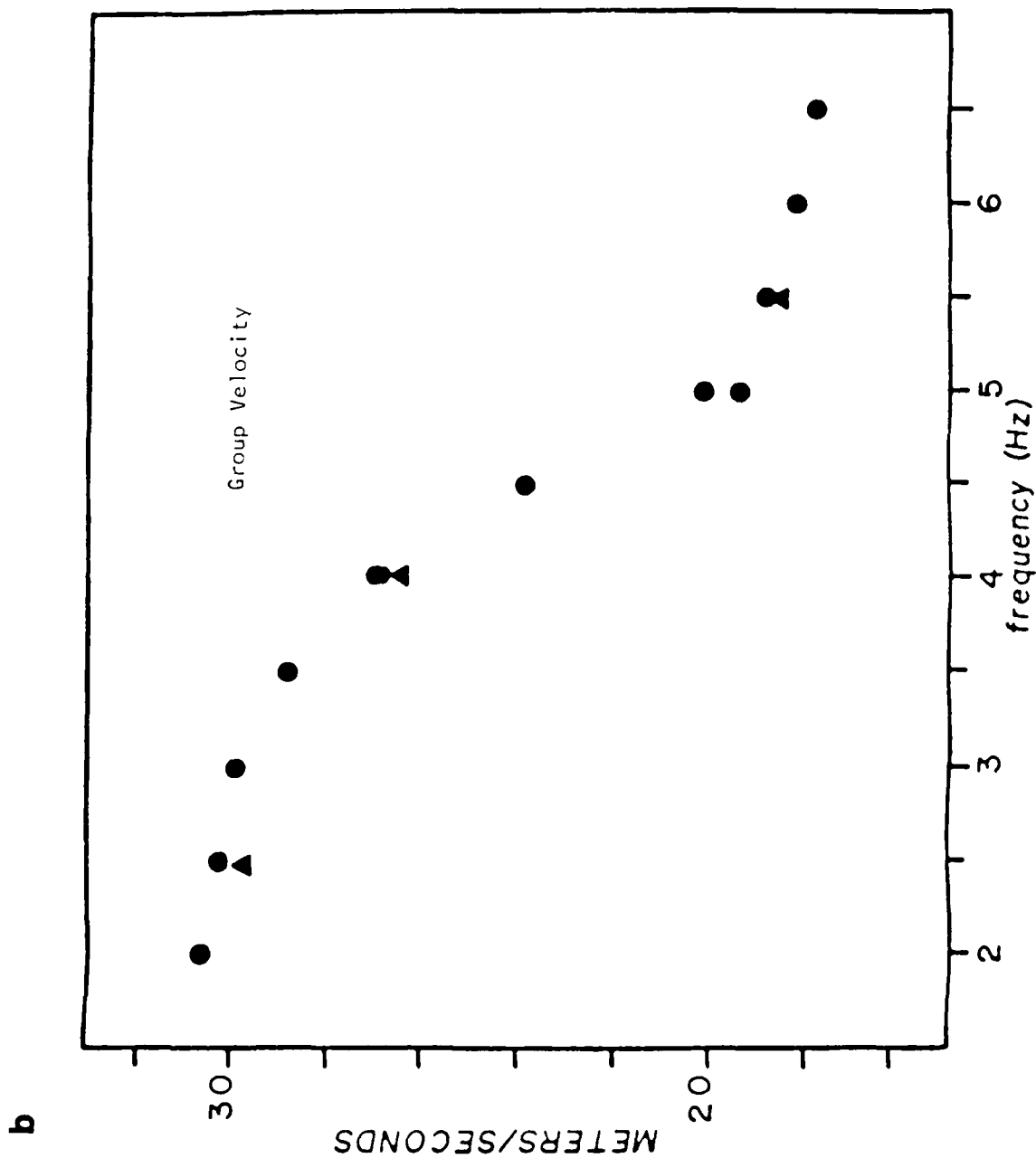


Fig. G-8b. Observed group velocities. (Triangles represent points for which location and velocity were determined from the data; dots represent points for which only velocities were determined by using locations derived from previous inversion.)

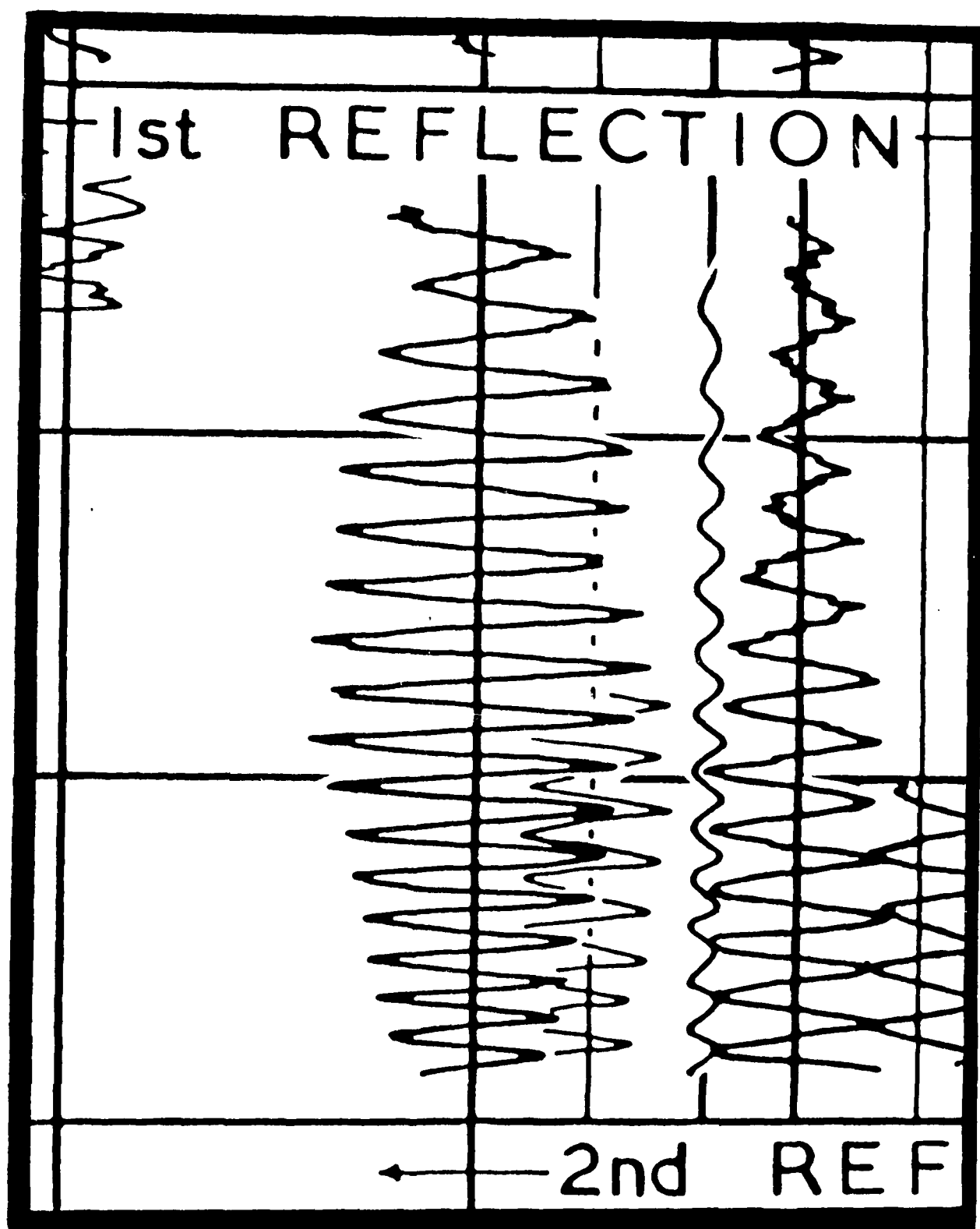


Fig. G-9. Davies (1965) data.

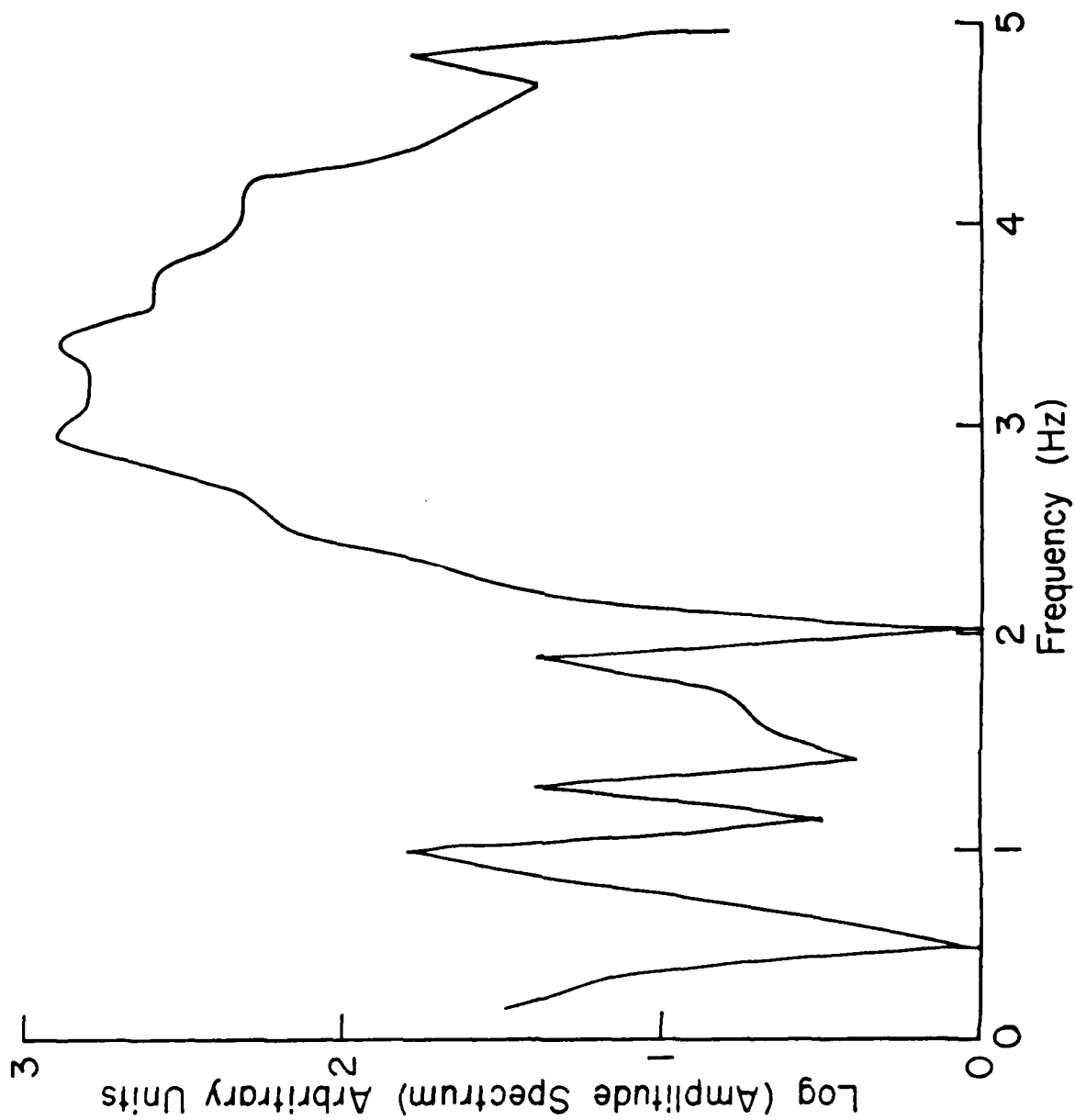


Fig. G-10. Spectrum of Davies (1965) data.

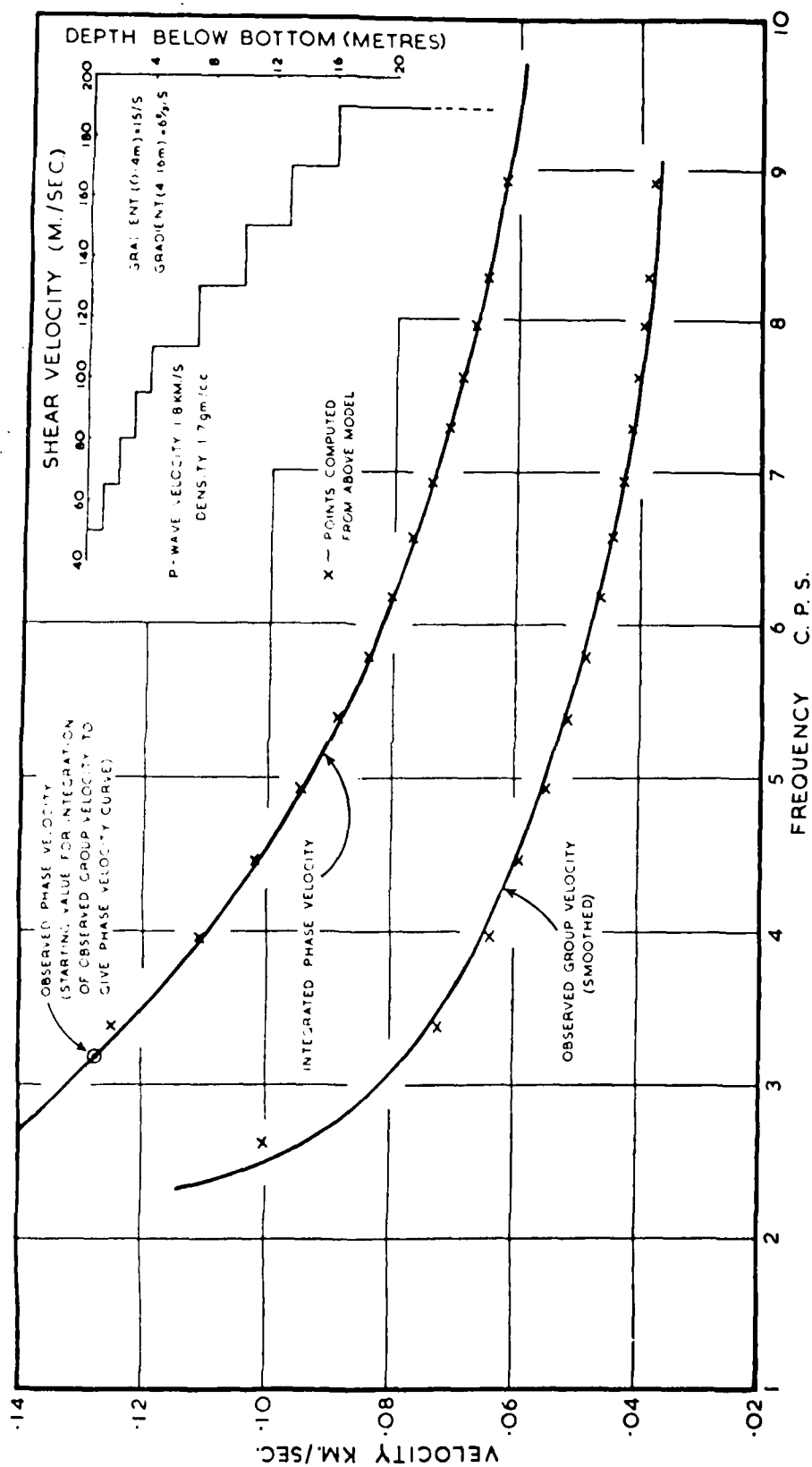


Fig. G-11. Davies (1965) dispersion curve and model.

G-18

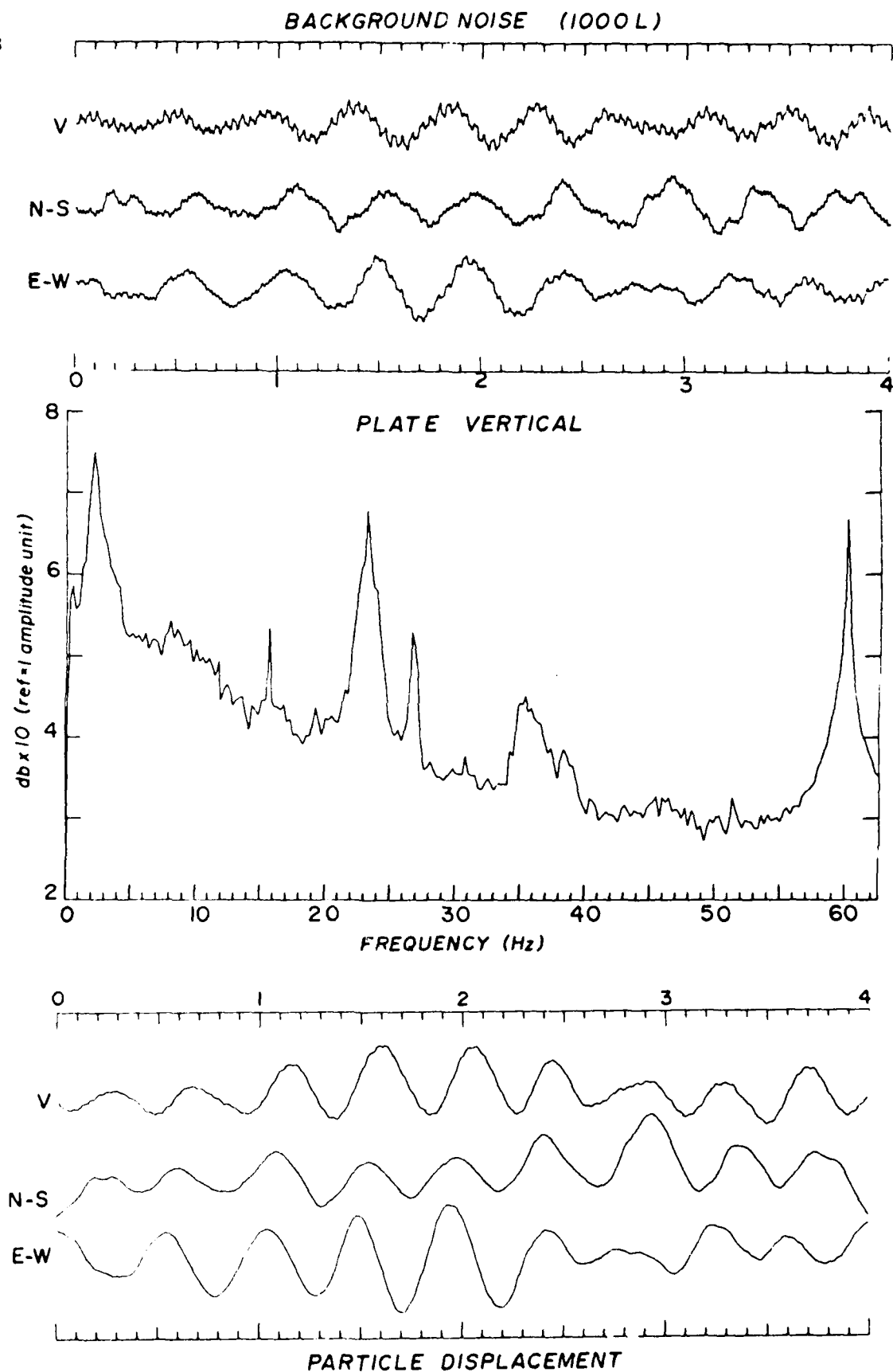


Fig. G-12. Seismogram, spectrum, and particle displacement; noise sample from plate standard.

has the correct value relative to the sediment shear velocity. The shear velocity of the sediment can be established from the shot-generated dispersive waves.

Particle motion diagrams from the noise displacement as recorded on the plate are shown in Figure G-13. This figure shows clearly that the motion is predominantly elliptical for the 2-Hz frequencies in this record. Pressure recordings of the noise by the hydrophone show the 1- to 5-Hz energy to be highly attenuated relative to other frequencies (see Sutton et al., 1980).

The phase velocity of the noise as a function of frequency was attempted by taking the three-dimensional frequency wave number spectrum. This allows one to determine both the azimuthal variation of the noise and its velocity at a particular frequency. Numerically the wave number spectrum is very sensitive to sensor location and to the assumption of plane wave propagation. The latter assumption would be violated if the noise sources are close to or within the array. Further, the wave number resolution and the response of the array will not be ideal (i.e., like a delta function, Fig. G-14a). Some or all of these factors are responsible for the degradation of the actual wave number spectra obtained. An example of the spectrum taken at 2 Hz is shown in Figure G-14b. However, in spite of the poor resolution, we can definitely bound the phase velocity at 2 Hz between 20 and 50 m/sec.

Deep Sea Noise

Unfortunately, data adequate to define the velocities of deep sea noise, that is, data having closely spaced sensors, do not now exist. The best that can be done at present is to document the spectra and particle motion. To do this we have chosen a worst case sample of noise taken at Lat. 16°N, Long. 145°W. This was the site of a joint experiment in which both Scripps and the University of Washington deployed several instruments. All the OBS's at this general location were placed on sediment and had very high levels of noise at 1 to 3 Hz. In fact the noise was so large that in order to extract refraction arrivals the data had to be severely filtered to remove this noise component. This filtering, of course, severely degraded the information of interest. An example of the ground noise velocity, its spectrum, and corresponding ground displacement are shown in Figure G-15. These data show a very high noise peak at about 2Hz. The corresponding particle motion in Figure G-16 shows the noise to be predominantly elliptical in motion and non-uniform in azimuth. Although not proof that this noise is propagating as Stoneley waves, this is suggested as a possibility based on the similarities with the Lopez noise and the shot-generated dispersed waves.

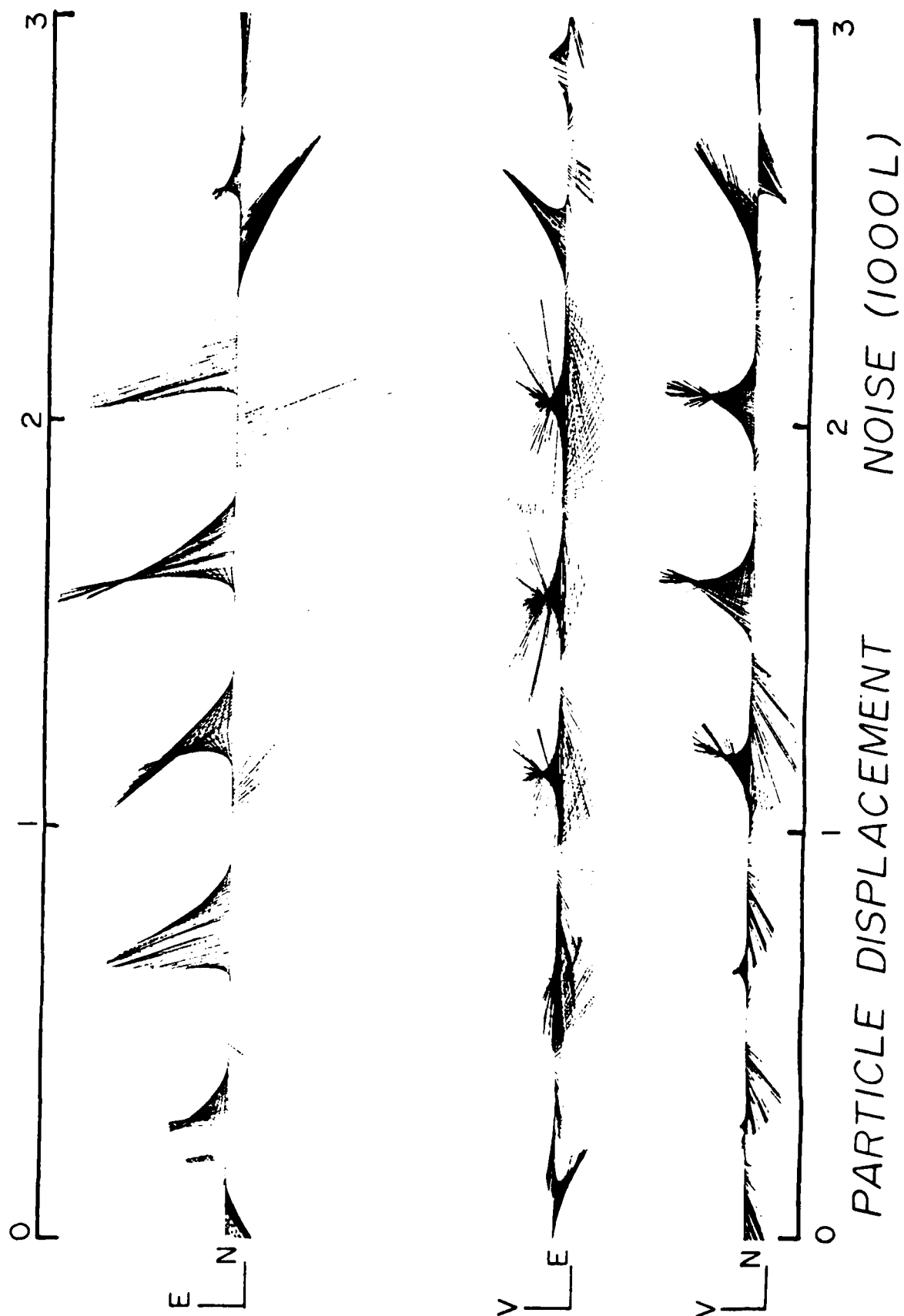


Fig. G-13. Particle motion noise sample from plate standard.

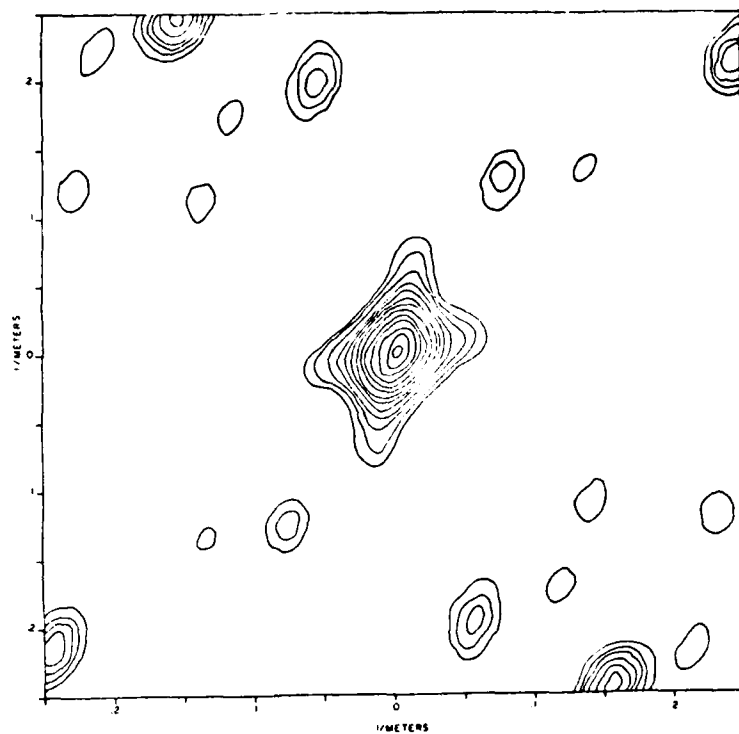


Fig. G-14a. Array wave number spectrum at 2 Hz.

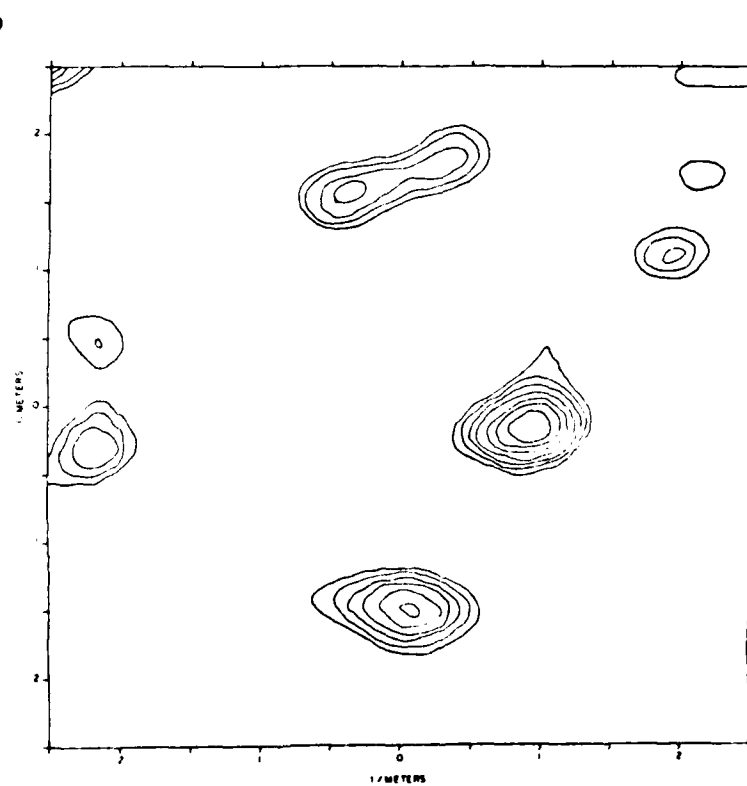
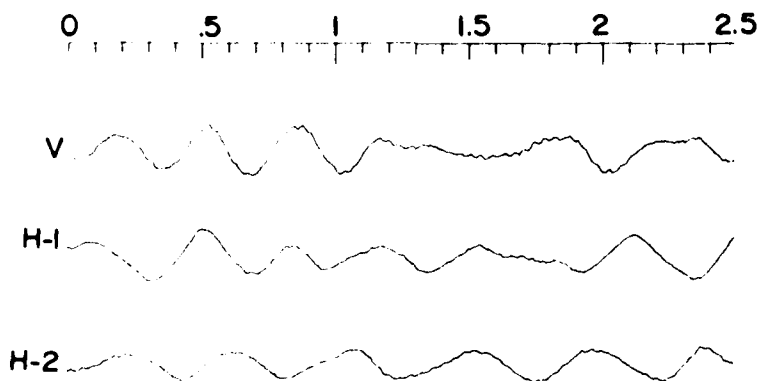
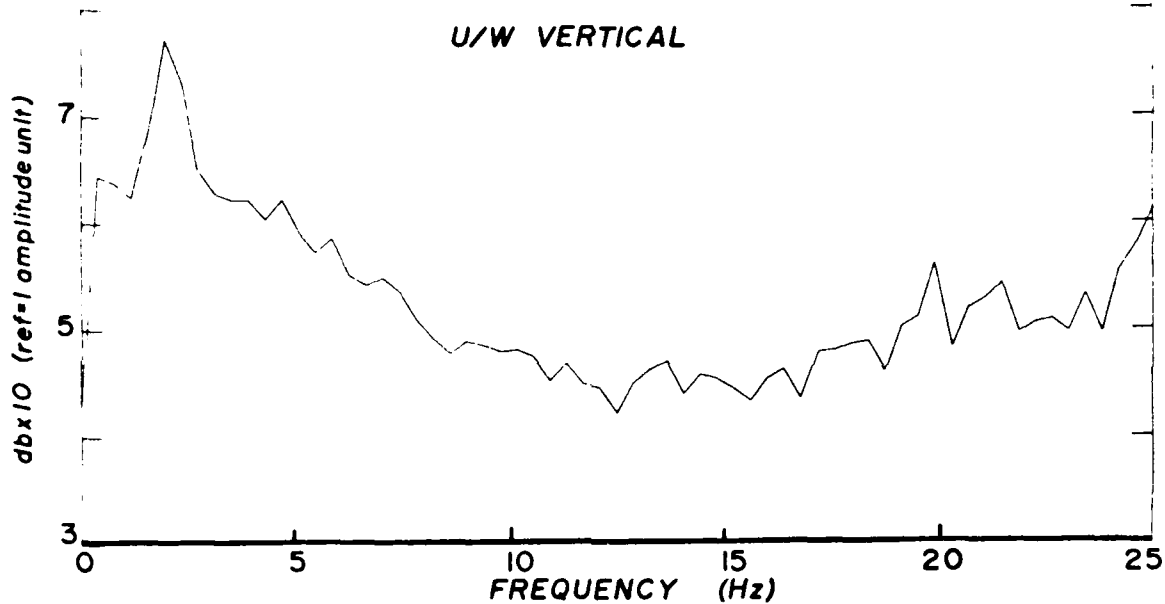
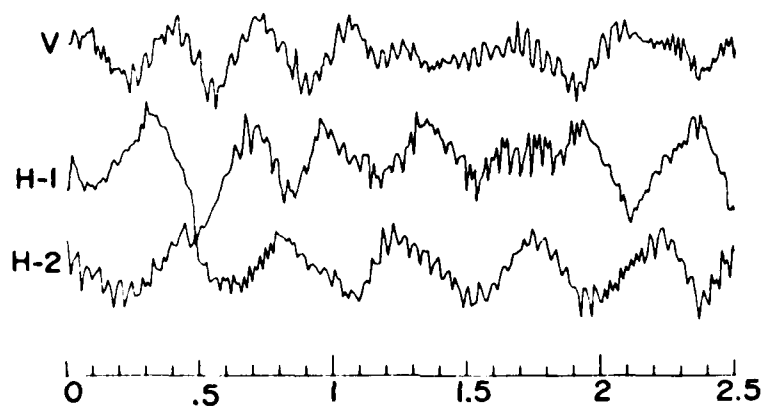


Fig. G-14b. Noise-wave number spectrum at 2 Hz (11 instruments).

DEEP OCEAN NOISE U/W OBS

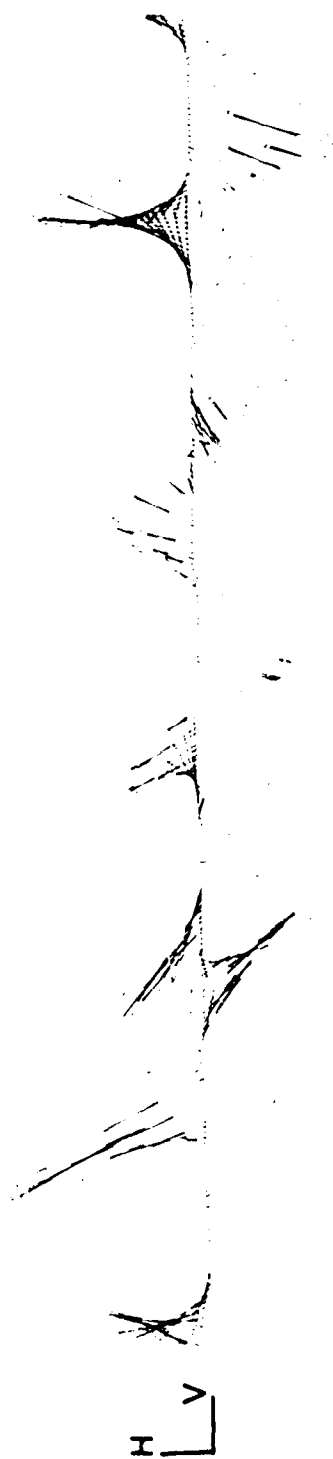
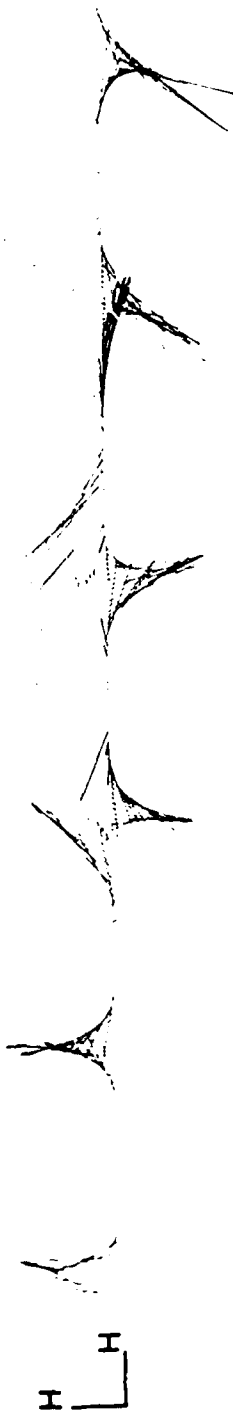
G-22



PARTICLE DISPLACEMENT

Fig. G-15. Seismogram, spectrum, and particle displacement from deep ocean noise, University of Washington OBS.

0 .5 1 1.5 2 2.5



0 .5 1 1.5 2 2.5

DEEP OCEAN NOISE

U/W OBS

Fig. G-16. Particle motion from deep sea noise, University of Washington OBS.

For purposes of comparison, the deep sea noise spectrum is compared with the other spectra in Figure G-17. The similarities are quite obvious.

Comparison with Theory

In this section it is shown that the data presented in this paper are consistent with the propagation of a dispersed surface wave at the interface between the water and the sea floor. Further, it is shown that the dispersion characteristics are related to the gradient in sediment shear velocity just below the sea floor.

A liquid layer over an elastic, homogeneous half-space. A convenient starting point is with the simple model in order to evaluate the effect of the liquid layer on the velocity and dispersion. Biot (1952) investigated this problem and showed that Stoneley waves were simply the high-frequency limit of Rayleigh waves, or equivalently, for wavelengths short compared to the water thickness the fundamental mode surface waves are confined to the water-solid interface. The equations relating the phase velocity V_p to the water thickness H and the wavelength λ are

$$4(1 - (V_p/\beta_2)^2)^{\frac{1}{2}} - (2 - (V_p/\beta_2)^2)^2 / (1 - (V_p/\alpha_2)^2)^{\frac{1}{2}} =$$

$$\frac{\rho_1}{\rho_2} \frac{(V_p/\beta_2)^4}{((V_p/\alpha_1)^2 - 1)^{\frac{1}{2}}} \tan[2\pi h \frac{((V_p/\alpha_1)^2 - 1)^{\frac{1}{2}}}{\lambda}]$$

$$\text{for } V_p > \alpha_1$$

and

$$4(1 - (V_p/\beta_2)^2)^{\frac{1}{2}} - ((2 - V_p/\beta_2)^2) / ((1 - V_p/\alpha_2)^2)^{\frac{1}{2}} =$$

$$\frac{\rho_1}{\rho_2} \frac{(V_p/\beta_2)^4}{((V_p/\alpha_1)^2 - 1)^{\frac{1}{2}}} \tanh[2\pi h \frac{((V_p/\alpha_1)^2 - 1)^{\frac{1}{2}}}{\lambda}]$$

$$\text{for } V_p < \alpha_1$$

where α_1 , α_2 are compressional wave velocities of the water and solid, β_2 is the shear velocity of the solid, ρ_1 and ρ_2 are the densities, and λ is the wavelength.

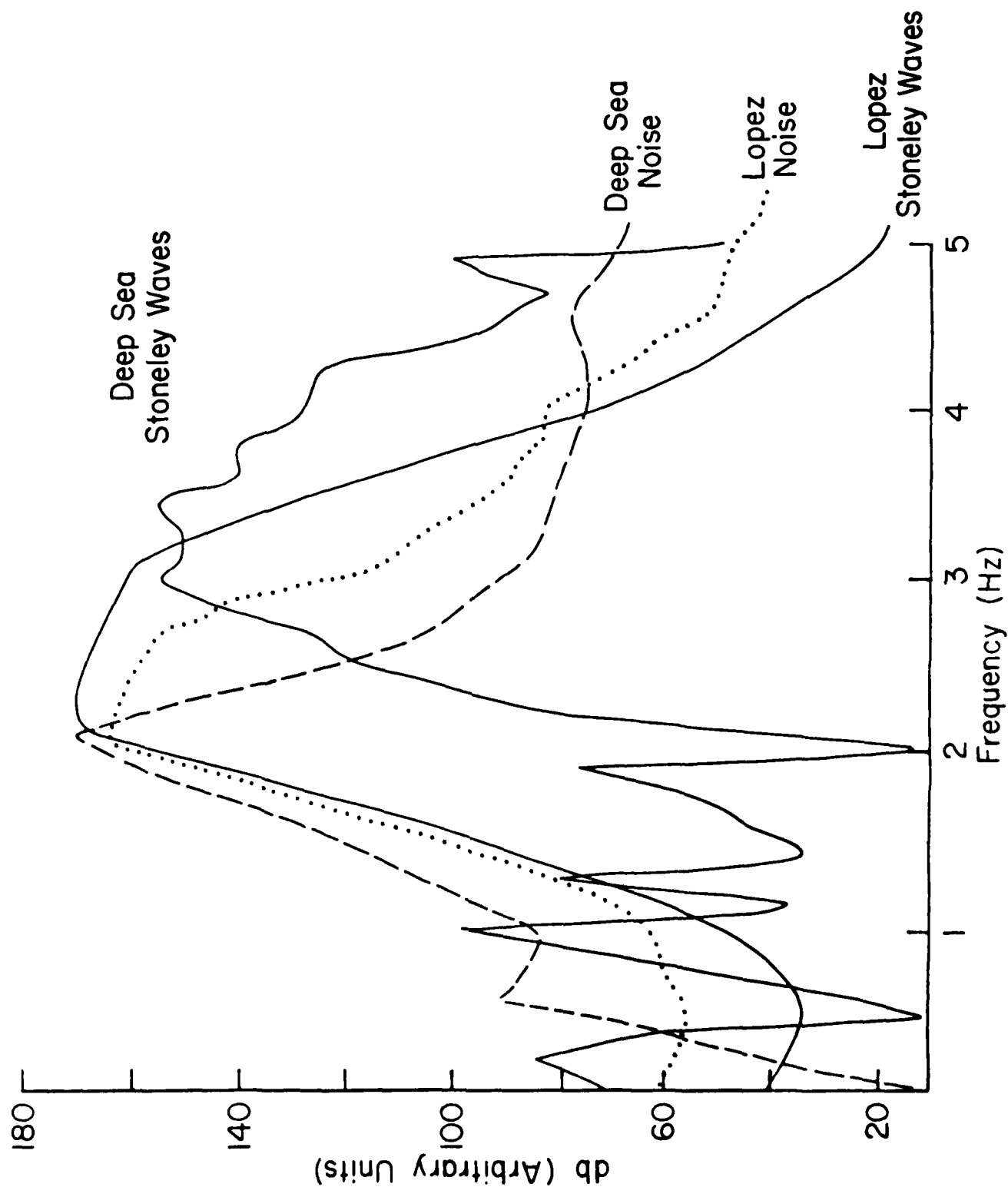


Fig. G-17. Comparison of spectra from Lopez shot, Davies shot, Lopez noise, and deep sea noise.

These equations have been solved for the fundamental mode for various values of β_2 , h and λ , and the results are listed in Table G-1. It is clear from the table that as β_2 approaches α_1 the waves are highly dispersed whereas for $\beta_2 \ll \alpha_1$ the waves are essentially non-dispersive. It is also apparent that the phase velocities are insensitive to water depth for $\beta_2 \ll \alpha_1$. Physically this is due to the wavelengths in the solid being so small relative to the water thickness that the wave is effectively confined to the interface. It should be noted that for the frequencies of interest (1 to 10 Hz) and for $\beta_2 = 50$ m/sec even a 1-m water layer is unimportant, and these waves are non-dispersive. The non-dispersive nature is due to the homogeneous half-space assumption and implies that the observed dispersion must be caused by velocity changes below the sediment-water interface. This is the same conclusion reached by Davies (1965). The effect of the water in the high-frequency limit is to depress the phase velocities to about $0.86 \beta_2$ compared to $0.95 \beta_2$ for Rayleigh waves on the free surface of an incompressible half-space.

A layered half-space. For the case of a single water layer overlying a homogeneous half-space we have shown that for $\beta_2 \ll \alpha_1$ the water layer can be effectively disregarded, as far as dispersion is concerned. This implies that the observed dispersion at Lopez Island and in the deep ocean must be caused by velocity changes in the top few meters of the sediment. This is how Davies (1965) modeled his data and we have undertaken a similar approach for the Lopez Island data. A program to calculate Rayleigh wave group velocity for a layered half-space was used to generate a model that fit the observed group velocities reasonably well. The final layered model (Fig. G-18) can be divided into two zones of nearly equal thickness (~ 3 m). The upper zone has a high shear velocity gradient and the lower zone has a very low shear velocity gradient.

We note that this general model is the same type used by Davies (1965) although the sediment shear velocities inferred from Lopez Island are appreciably lower. At Lopez Island the shear velocity in the upper few meters are about 15 to 20 m/sec. There was, however, no Airy phase seen in the data, so further modeling is warranted.

Conclusions

We have shown that large-amplitude, low-velocity dispersed waves generated by shots at Lopez Island correspond to Stoneley wave propagation at the water-sediment interface and that the dispersion is caused by the shear velocity structure in the upper few meters of the sediment. We find that the sediment shear velocities at Lopez Island are about a factor of two less than those found by Davies in a deep water sample. Clearly the shear velocity will be determined by the

Table G-1

Phase velocity versus frequency for a water layer of thickness H, velocity 1500 m/sec and density 1 gm/cm³, overlying a homogeneous half space of compressional velocity α_2 , shear velocity β_2 and density ρ_2 .

H (m)	α_2 (m/sec)	β_2 (m/sec)	ρ_2 (gm/cm ³)	1 Hz	3 Hz	6 Hz	9 Hz
100	3000	2000	2.0	1727	1569	1411	1379
100	2000	1000	1.5	879	816	816	816
100	1600	50	1.5	43.9	43.9	43.9	43.9
10	1600	50	1.5	44.7	43.9	43.9	43.9
1	1600	50	1.5	47.1	46.3	44.7	43.9

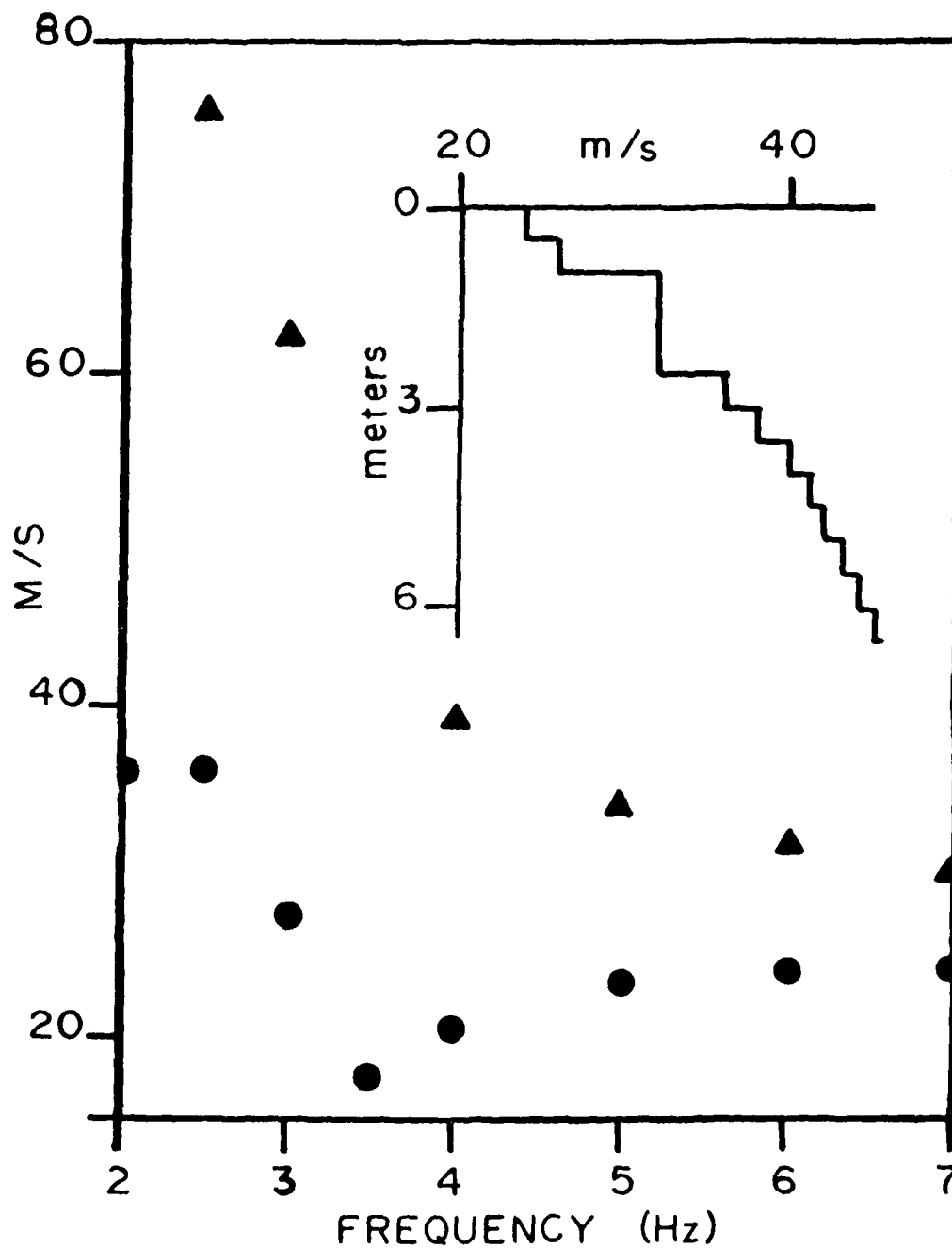


Fig. G-18. Phase and group velocity dispersion curves for the model shown. Triangles represent phase velocities; circles represent group velocities.

sediment type, porosity, and degree of lithification, which in general will depend on the geographic location.

We have also shown that the background noise at Lopez Island has spectra, particle motion, and phase velocities similar to the shot-generated dispersed waves, which implies that the predominant noise is also propagating as Stoneley waves. In deep water the documentation of noise is insufficiently precise to prove that Stoneley waves are the predominant mode of propagation, but the available data are not inconsistent with this hypothesis.

There are several implications of these findings that are of importance to ocean bottom seismology.

(1) The very low velocity of the noise implies wavelengths of a few meters to tens of meters depending on the actual shear velocity of the sediments. Consequently, the noise will be incoherent between sensors spaced more than a few tens of meters apart.

(2) The fact that the noise is most likely propagating in the Stoneley mode implies that the amplitude of the noise will decrease as $e^{-2\pi Z/\lambda}$ away from the interface (Z = distance from the interface, λ = wavelength). For frequencies of 2 Hz and velocities of 20 m/sec $e^{-2\pi Z f/v} = e^{-1}$ for $Z \approx 1.6$ m. This implies that the noise can be greatly reduced either by placing a hydrophone a few meters above the bottom or burying a seismometer a few meters below the bottom.

Another aspect of these data that we have not yet discussed is the narrow spectrum of the dispersed waves, the energy falling between 2 and about 5 Hz. We suspect that the high-frequency cutoff may be controlled by non-elastic attenuation in the sediments and the low-frequency cutoff controlled by the shear velocity profile in the sediments. For low frequencies, or long wavelengths, the waves may be sampling a higher shear velocity which will cause them to be decoupled from the main dispersed wave train. These combined effects may concentrate the noise power from 2 to 5 Hz. Since most OBS's are placed in sediment ponds and most long-range refraction profiles use this frequency band for propagation of the "signal", it is clear that improvement in the design of OBS's could result in a significant increase of signal-to-noise ratio.

References

- Biot, M. A., 1952. The interaction of Rayleigh and Stoneley waves in the ocean bottom. Bull. Seismol. Soc. Am., v. 42, p. 81.
- Bracewell, Ron, 1965. The Fourier Transform and Its Application. McGraw-Hill, New York.
- Davies, D., 1965. Dispersed Stoneley waves on the ocean bottom. Bull. Seismol. Soc. Am., v. 55, p. 903.
- Heron, E. M., J. Dorman, and C. L. Drake, 1968. Seismic study of the sediments in the Hudson River. J. Geophys. Res., v. 73, p. 4701.
- Hamilton, E. L., et al., 1969. In situ determination of the velocities of impressional and shear waves in marine sediments from a research submersible. NUC TP 163, Naval Undersea Center, San Diego, California.
- Sutton, G. H., B. T. R. Lewis, J. Ewing, F. K. Duennebler, B. Iwatake, and J. D. Tuthill, and others, 1980. Lopez Island Ocean Bottom Seismometer Intercomparison Experiment, Final Report. HIG-80-4, Hawaii Inst. Geophys., Honolulu. (This report).
- Tuthill, J. D., 1980. The propagation of Stoneley waves in unconsolidated marine sediments. M.S. Thesis Univ. of Washington, Seattle, Washington, in preparation.

Appendix H

INSTRUMENTAL WAVEFORM DISTORTION
ON OCEAN BOTTOM SEISMOMETERS

INSTRUMENTAL WAVEFORM DISTORTION
ON OCEAN BOTTOM SEISMOMETERS

Brian T. R. Lewis and Jonathan D. Tuthill

Geophysics Program
Department of Oceanography
University of Washington
Seattle, Washington 98195

Abstract

Data from the 1978 Lopez Island OBS Intercomparison Experiment and deep sea data from University of Washington OBS's show that there is a considerable amount of waveform distortion resulting from the conversion of horizontal motion into vertical motion, here called cross-coupling distortion. This distortion, which substantially reduces the significance of waveform matching with synthetic seismograms, appears to result from rotation imparted to the OBS package by near-vertically traveling shear energy. The degree of this rotation seems to depend on the instrument surface area above the seafloor and the geometry and surface area of the "feet" connecting the package to the seafloor. The sensitivity and response of the seismometers within the package to this rotation depends on the precise location of the seismometers with respect to the axis of rotation. The results suggest how to modify OBS designs to minimize these effects.

Introduction

One of the principal objectives of the Lopez Island OBS Intercomparison Experiment was an evaluation of the coupling of the various OBS designs to the ocean bottom. As a result of this experiment it was found that most instruments (except the standards) had a cross-coupling problem in which near-vertically traveling shear motion was coupled into vertical motion. This effect was also observed during the transient tests, in which horizontal transients of force produced substantial outputs on the vertical seismometers, and it is documented by Sutton et al. (1980). In this paper we further document this effect by using controlled sources at the Lopez site and in deep water sites, and in addition we offer possible explanations and remedies for its cause.

Cross-Coupling Data from Lopez Island Shots

One of the best demonstrations of the cross-coupling problem is the data from airgun shot 182 (Fig. H-1). There are three distinct energy packets on these shot records. Before 1 sec on Figure H-1 there is a P arrival distinguished by its predominant vertical motion. Between 1 sec and 5 sec the motion is predominantly horizontal, due to near-vertically traveling S waves. The beginning of this wave train is probably leaky S waves. Beyond a travel time of 6 sec the motion is due to a dispersive surface wave whose characteristics are described by Tuthill et al. (1980). It is the S part of the record in which we are interested here, as recorded on the vertical components. OBS recordings of this shot are shown in Figure H-2. We note that whereas the standard instrument's component showed very little motion for the S phase, the OBS's show a wide range of vertical response to this wave train. This response is clearly an artifact of the instrumentation and is a distortion of the true particle motion. A relative ranking of the instruments according to the degree of distortion is shown in Figure H-3 by plotting the ratio of the maximum vertical amplitude of the leaky mode to the amplitude of the first two cycles of the P wave.

Cross-Coupling Data from Deep Ocean Results

In this section we document a case of deep water cross-coupling distortion similar to that seen in the Lopez Island data. The deep water data come from a deployment of four University of Washington OBS's on the Cascadia Basin off the coast of Washington in September 1978. The water depth at that site was about 3 km, the sediment thickness is about 2 km, and the sediments are regular and flat-lying. The OBS's were deployed in a linear array about 4 km long; three of the OBS's had concrete anchors and one had a tripod anchor. Schematic diagrams of these instruments are shown in Figures H-4 and H-5. Vertical component records for one shot across the array are shown in Figure H-6 and horizontal component records for the same shot are shown in Figure H-7. Figure H-8 shows a comparison

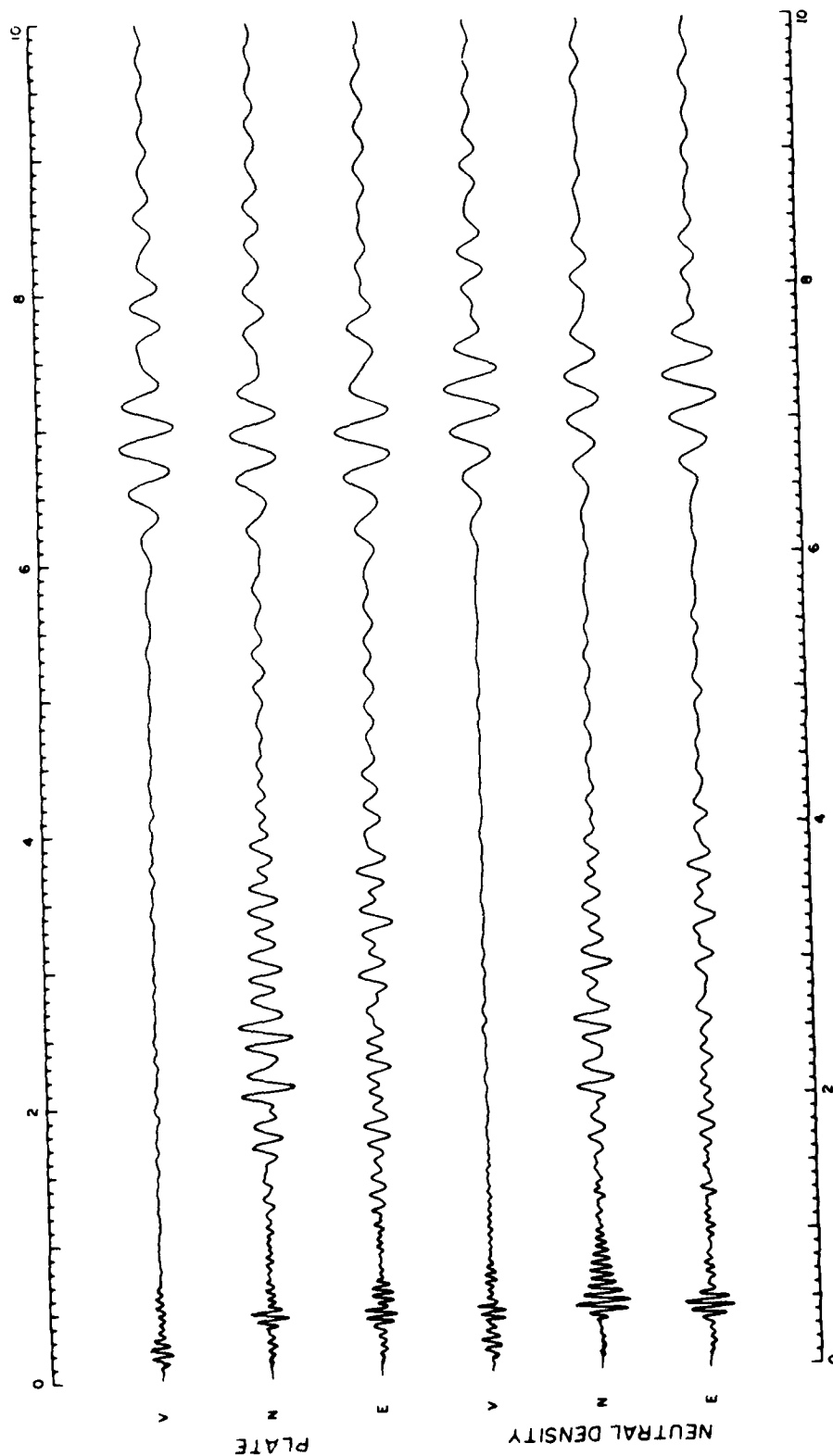


Fig. H-1. Recordings of airgun shot 182 by the standard instruments. Note the large amplitude "granddaddy wave" at the end of the wave train and the predominantly horizontal motion between 2 and 3 seconds.

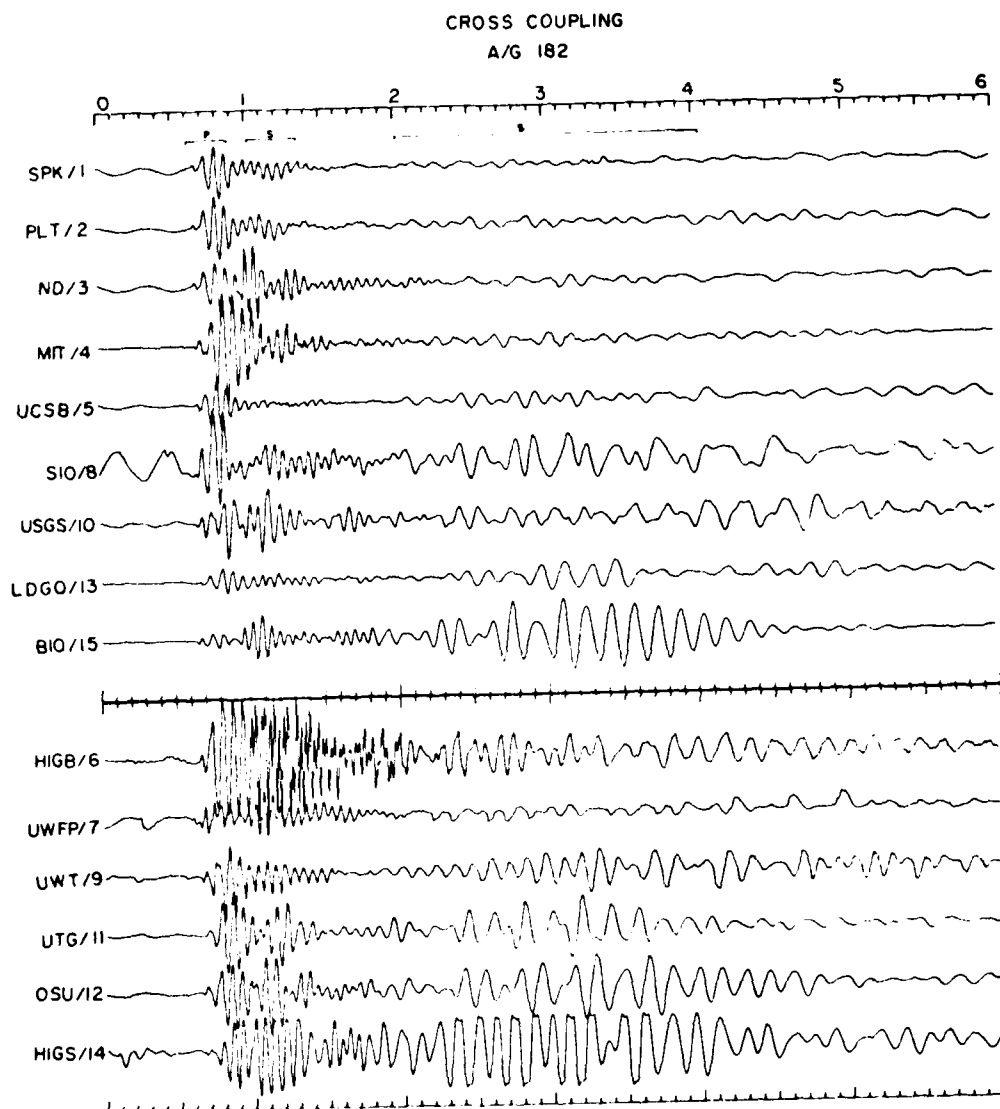


Fig. H-2. Recordings of airgun shot 182 by the OBS's and the standard verticals. The large amplitude energy between 2 and 3 sec seen on most of the OBS's is horizontal motion cross coupled in the vertical seismometers.

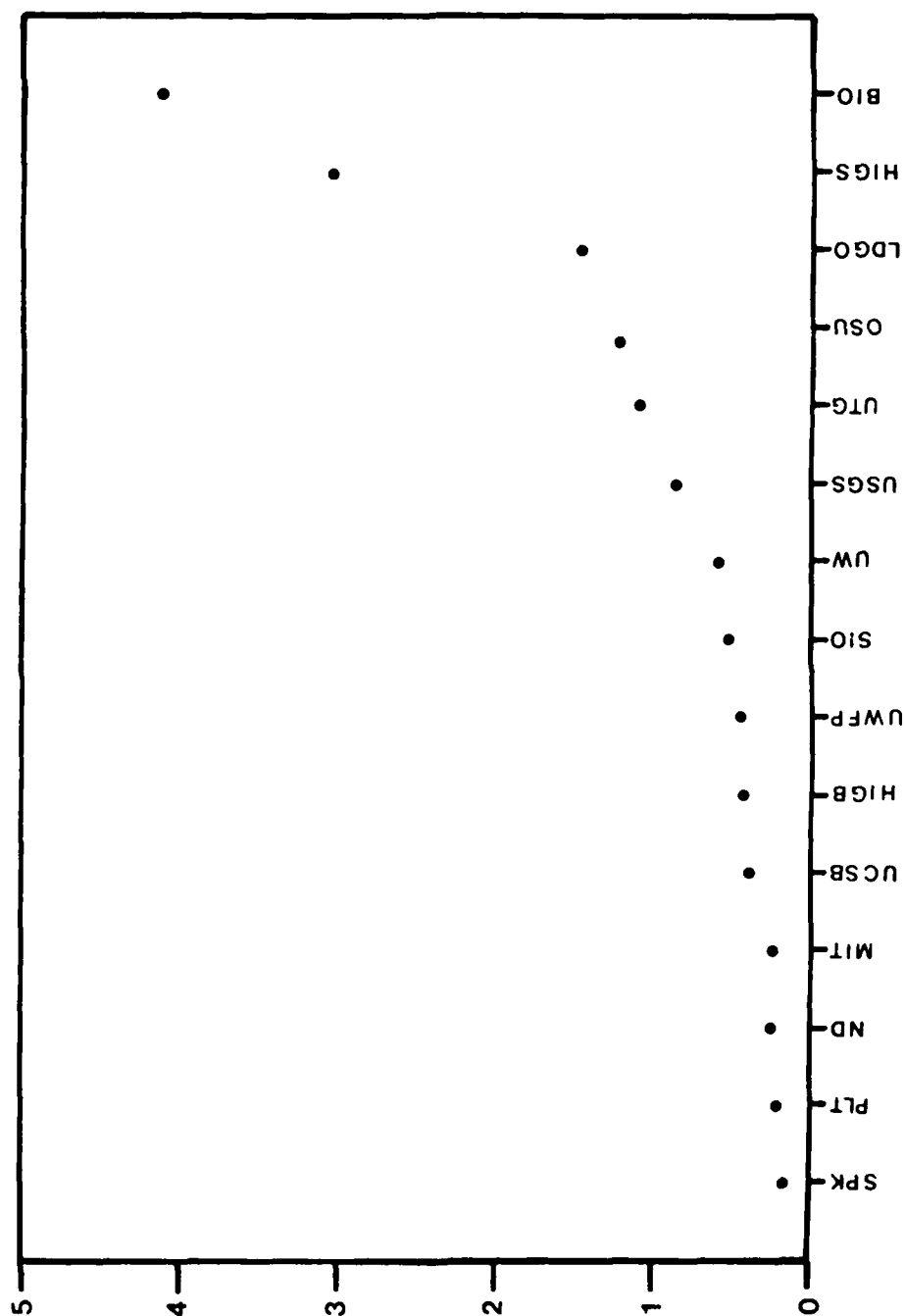


Fig. H-3. Ranking of the instruments according to the degree of cross coupling. The ordinate represents the ratio of the maximum amplitude of the cross-coupled shear motion to the first two cycles of P motion.

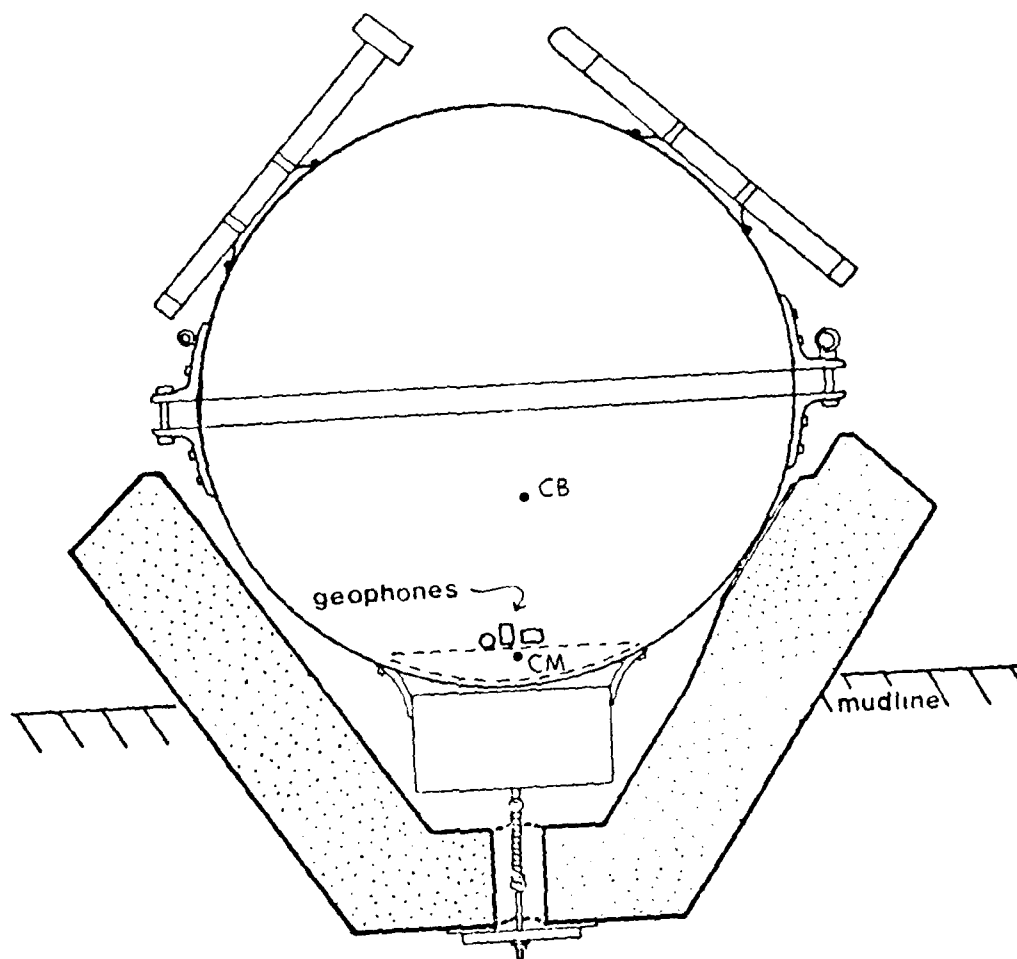


Fig. H-4. A schematic drawing of the University of Washington OBS with the "flower pot" anchor. C. is the center of buoyancy; CM is the center of mass.

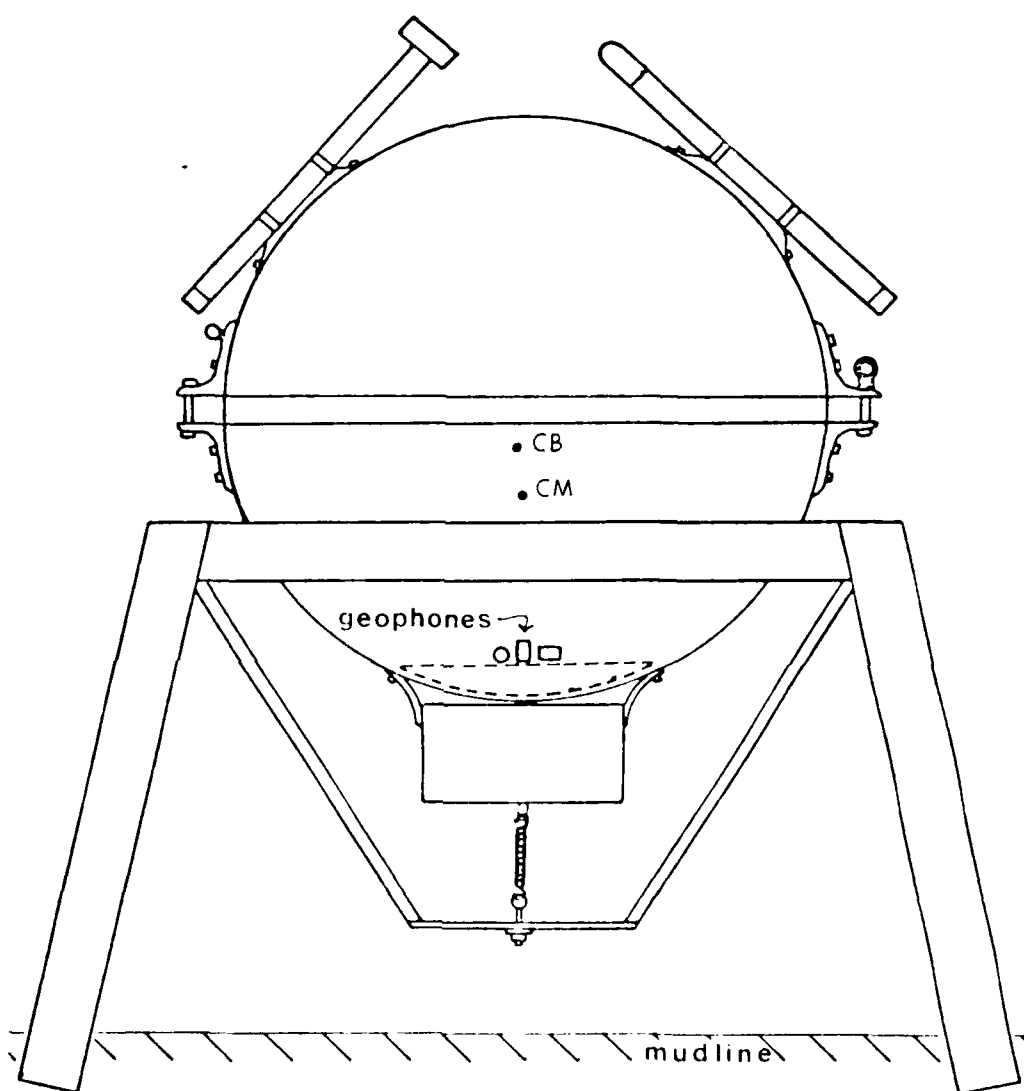


Fig. H-5. A schematic drawing of the University of Washington OBS with the "tripod" anchor. CB is the center of buoyancy; CM is the center of mass.

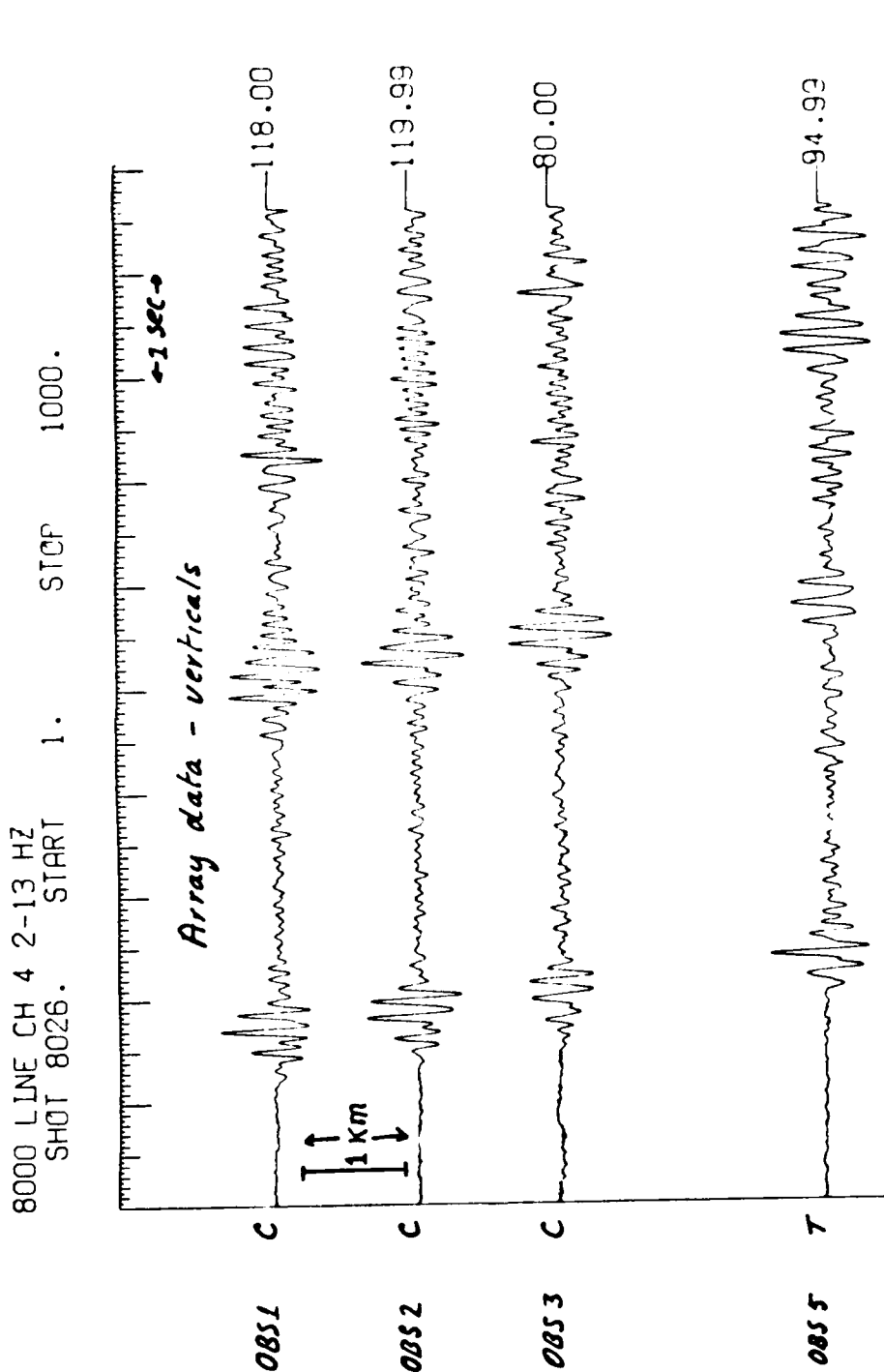


Fig. H-6. A comparison of vertical component recordings of a shot at about 20-km range by the concrete flower pot instruments and the tripod instruments. Note the similarities in waveform for the first P arrival and the differences in waveform toward the end of the record. The differences are caused by cross-coupled shear energy.

8000 LINE CH 2 2-13 HZ
SHOT 8026. START 1. STOP 1000.

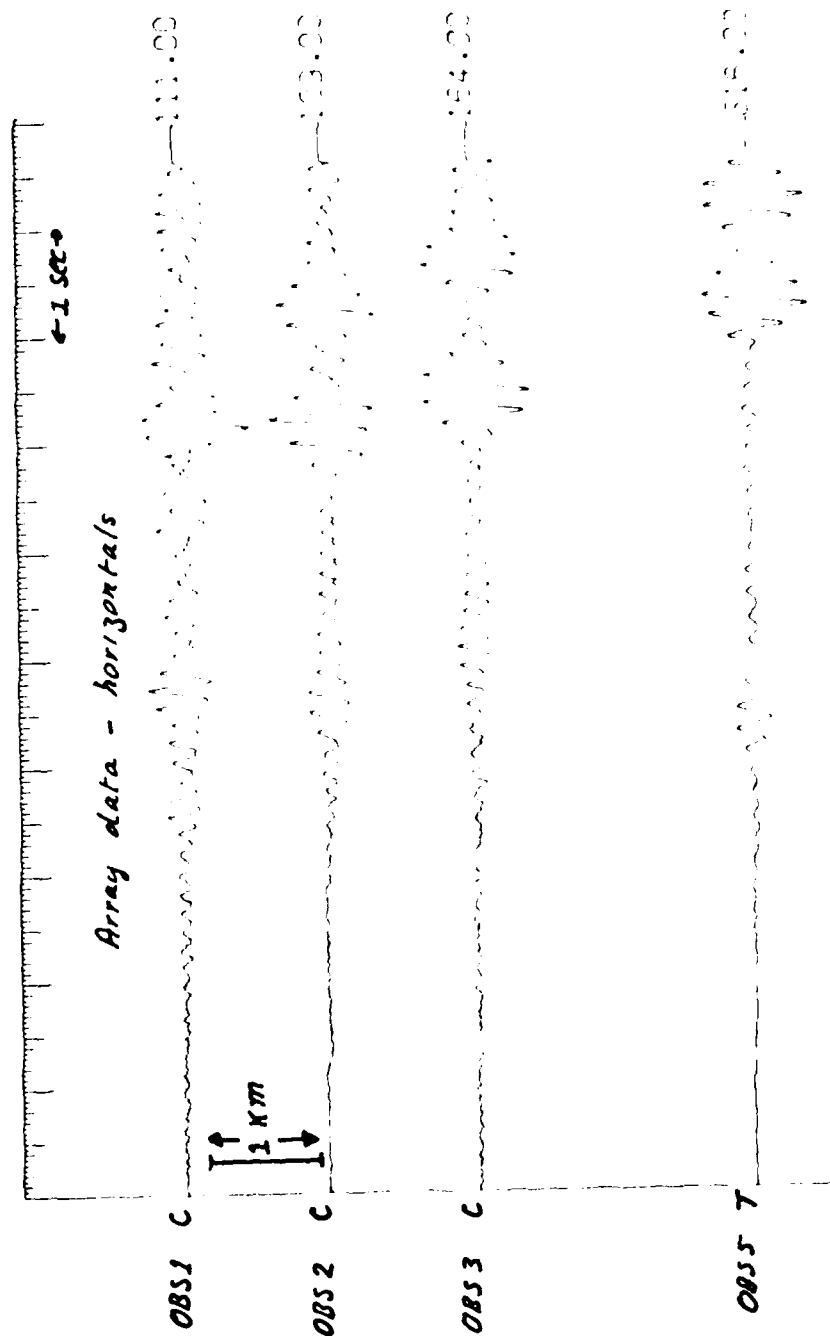
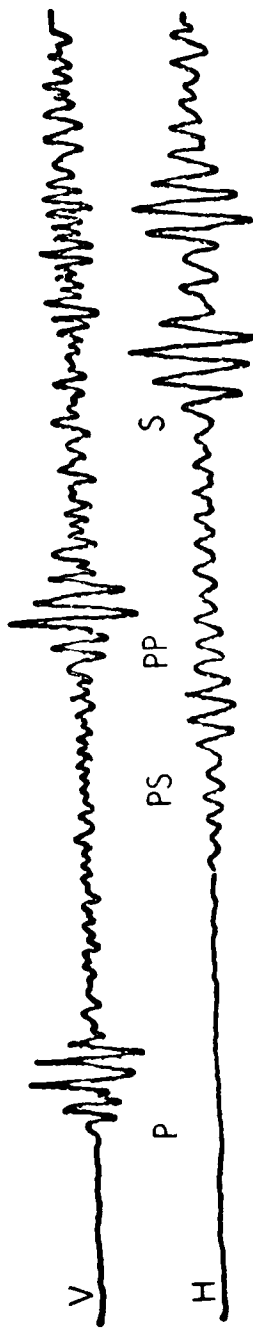


Fig. H-7. A comparison of horizontal component recordings of the same shot shown in Figure H-6. The largest amplitude events correspond to refracted shear arrivals.

CONCRETE ANCHOR



TRIPOD ANCHOR

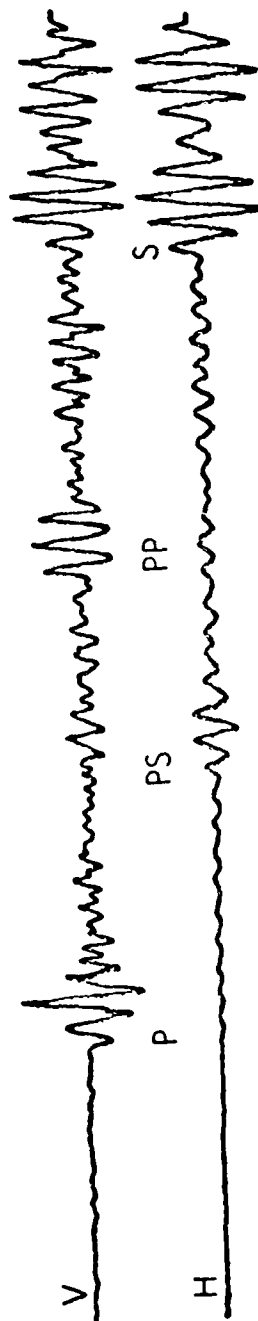


Fig. H-8. A comparison of horizontal and vertical motion recorded by the concrete and tripod systems for the shot shown in Figure H-6. This figure shows that the differences between the vertical components are due mostly to cross-coupled shear energy.

of vertical and horizontal data for a concrete anchor and the tripod anchor for this shot. From an inspection of Figures H-6, H-7, and H-8, it is clear that the P arrival has a high coherence across the array and is essentially independent of the anchor type. However, when we inspect the refracted S part of the wave train we note that although the horizontals are reasonably coherent the vertical motion shows little correlation from OBS to OBS. This is especially seen when comparing the concrete and tripod anchors. We interpret this to be waveform distortion due to cross coupling of horizontal motion into vertical motion, in a manner exactly analogous to the Lopez Island results.

We point out that we have chosen this data set to demonstrate this result because the S and P-S arrivals are well separated from the P arrival because of the large sediment thickness. In cases of much thinner sediments (a few meters to tens of meters), the P-S arrivals will occur during the P arrivals and the cross coupling will considerably distort the P waveform, making it uninterpretable.

Possible Causes of Cross-Coupling Distortion

In Figure H-3 we ranked the OBS's according to degree of cross coupling and we note that those instruments with a large cross section in the water and a low spread of support on the ocean bottom (inverted pendulums) have the worst degree of cross-coupling. Tripod-type instruments with large foot pads spread far apart do a lot better, whereas the spike, plate and instruments with remote sensor packages do the best. This in itself suggests that the cause of the cross coupling is rocking induced by lateral translation caused by shear motion.

There are several mechanisms by which rocking motion can be translated into vertical motion. Three mechanisms are described below and in each of these we assume that the hydrodynamic resistance caused by the cross section in the water is greater than the spring constant associated with the coupling to the soft sediments. That is, we assume that the cross section in the water remains fixed with respect to the water and the lateral translation is taken up by depressing the feet into the sediment. The three mechanisms are:

(a) Uniform sediment properties under each foot. In this case the rocking will occur about an axis close to the center of area above water and the effect on the vertical and horizontal seismometers will depend on the precise location of the sensors with respect to the axis. This is denoted in Figure H-9 as motion R_1 and has been experimentally verified by rocking the University of Washington tripod OBS about axes at different heights from the vertical seismometer. Depending on the location of the vertical seismometer, frequencies at twice the driving frequency can be induced; this mode is especially important when the sensor is at the axis of rotation.

POSTULATED CROSS COUPLING MECHANISMS

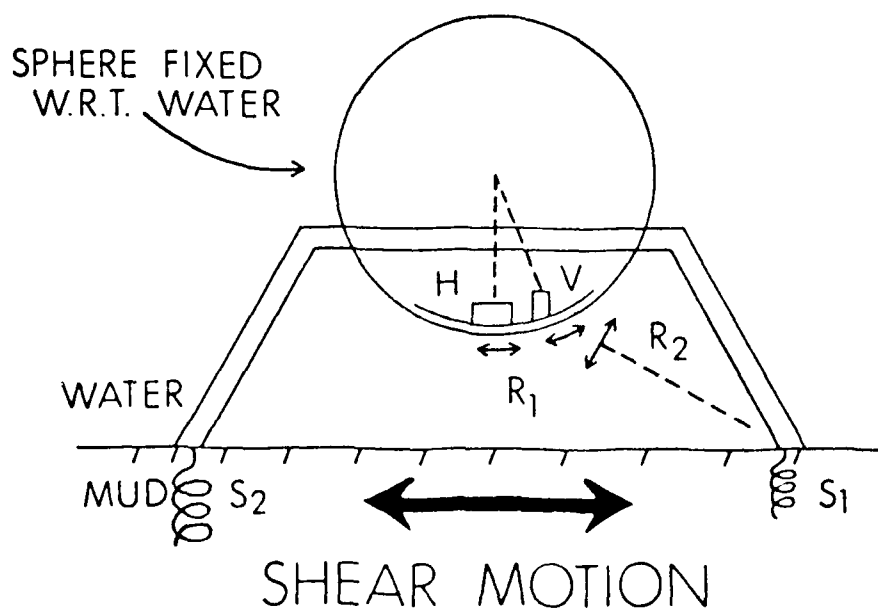


Fig. H-9. A schematic diagram of possible cross-coupling mechanisms.

R_1 represents rotation caused by rocking on a uniform bottom.

R_2 represents rocking caused by a non-uniform bottom, represented by different spring constants S_1 and S_2 . The sensitivity of the vertical seismometer to R_1 depends on its precise location with respect to the axis of rotation.

(b) Non-uniform sediment properties under each foot. This case is equivalent to having different spring constants under each foot and can be caused by the instrument landing unevenly on a bottom with a high shear strength gradient in the upper few centimeters. In this case, rocking will be effectively about the foot with the highest spring constant and is denoted by motion R₂ in Figure H-9. Again the effect will depend on the precise location of the sensor but in general it will produce dominantly vertical motion.

(c) Inverted pendulum case. These instruments usually have the sensors close to the mud line and the center of buoyancy and area a meter or so above the mud line. Mechanisms (a) and (b) are not applicable to this case since it is impossible with small rotations about a center of rotation near the flotation to produce vertical to horizontal cross-coupling ratios of one or greater, as has been observed. The most likely cross-coupling mechanism in this case is a dynamic interaction of buoyancy forces with the spring constant associated with bottom coupling. More specifically, small rotations caused by lateral translation of the foot will induce buoyant restoring force acting against the bottom coupling spring constant. Resonances at the exciting frequency could produce large amplification of the vertical motion. We have not attempted a mathematical or physical modeling of this situation. To be complete such a model should incorporate hydrodynamic effects.

Conclusions

We have demonstrated that instrumental waveform distortion of near-vertically traveling shear energy occurs on all OBS's to some degree. The distortion results from the cross-coupling of horizontal into vertical motion and is dependent on the geometry of the instrument, the location of the sensors within the instrument, and the homogeneity of the ocean bottom.

The cross coupling can be reduced by having small sensor packages remote from the main instrument or by having low-profile instruments with widely spaced feet and large footpads. These factors should be considered along with the other OBS design parameters described by Sutton et al. (1980) for coupling frequencies and Tuthill et al. (1980) for noise reduction.

References

- Sutton, G. H., F. K. Duennebier, and B. Iwatake, 1980. Coupling of ocean bottom seismometers to soft bottoms. This report, Appendix E.
- Tuthill, J. D., B. T. R. Lewis, and J. D. Garmany, 1980. Stoneley waves, Lopez Island noise, and deep sea noise from 1 to 5 Hz. This report, Appendix G.

Appendix I

BOTTOM SEISMOMETER OBSERVATION
OF AIRGUN SIGNALS AT LOPEZ ISLAND

BOTTOM SEISMOMETER OBSERVATION
OF AIRGUN SIGNALS AT LOPEZ ISLAND

S. H. Johnson¹ and R. E. McAlister²

School of Oceanography
Oregon State University
Corvallis, Oregon 97331

Abstract

First arrival compressional wave signals from an airgun source, as detected by a variety of seismometers in a shallow bay, are remarkably uniform; however, minor variations in wavelet appearance imply some combination of instrument response and coupling to the bottom. Signal spectra show typically a spectral peak at 12 Hz and an envelope very similar to that expected from an airgun source. Those instruments with a decoupled geophone package have spectra most like the theoretical spectrum but spectra for the other instruments are not significantly different. Little variation exists in spectra between tripod-mounted and inverted-pendulum OBS configurations for the low-amplitude P-waves observed here. The signal source is the principal influence on the resulting spectra rather than OBS configuration or bottom coupling.

¹Now at Amoco Production Research, P.O. Box 591, Tulsa, Oklahoma 74102.

²Now at Intel, Inc., Hillsboro, Oregon.

Introduction

The Lopez Island intercomparison experiment provides a unique set of data to study bottom coupling and response of ocean bottom seismographs (OBS) to seismic waves in shallow water. The data are particularly useful because signals from each instrument were brought ashore in real time by cable and recorded on a 24-channel digital recorder to provide wide-dynamic-range records of multiple instruments for direct comparison during extended computer analysis in the laboratory. One of the seismic sources recorded during the experiment was a 40-inch³ bolt airgun fired to the OBS array from various azimuths and ranges. Because an OBS is commonly used as a receiver for an airgun source during marine experiments it is useful to examine, under controlled conditions, the effectiveness of such an instrument for the detection of airgun-generated ground motion at a water-solid interface. The interaction of seismic waves in shallow water and an instrument's response on the bottom is complex (Lewis and Tuthill, 1980; Tuthill et al., 1980) and in this report we will restrict our attention to compressional waves generated at ranges of 300 to 700 m.

Data

Figure I-1 shows a set of airgun shots from a seismic profile in a NW direction across Shoal Bay on Lopez Island as detected by the well-coupled spike vertical standard geophone and by the Oregon State University OBS vertical component. Two wave groups occur within the first two seconds of record and have phase velocities of 550 and 2,850 m/s. The shots in Figure I-1 are about 80 m apart at ranges between 300 to 700 m from the OBS array. The two record sections are nearly identical except for phase and amplitude differences (instrument responses have not been equalized). In order to quantize characteristics of the seismic signals from the various instruments, we have analyzed the first arrivals from two shots at 700- and 600-m distance. It was necessary to use two shots because not all instruments were wired to the digitizer at the same time. We assert that the proximity of the shot points to each other and the uniformity of the bottom (Sutton et al., 1980b) result in comparable seismic signals. We restrict our attention to the high-velocity arrivals since the lower-velocity arrivals may represent a shear phase. At the greatest distance commensurate with adequate signal level, we study the first 1.024 s (256 samples) of signal from each of the instruments as shown in Figure I-2. Spike, neutral density, and plate-mounted vertical geophone standards (SPV, NDV, PLV) represent the range of strong to weak bottom coupling. The three or four letter code in the signal label identifies the originating institution for each instrument.

Theoretical Airgun Signal

The analysis that follows requires a source signal from the airgun used during the experiment. Because such a signal was not recorded during the experiment, we generated a theoretical signal by using the method of

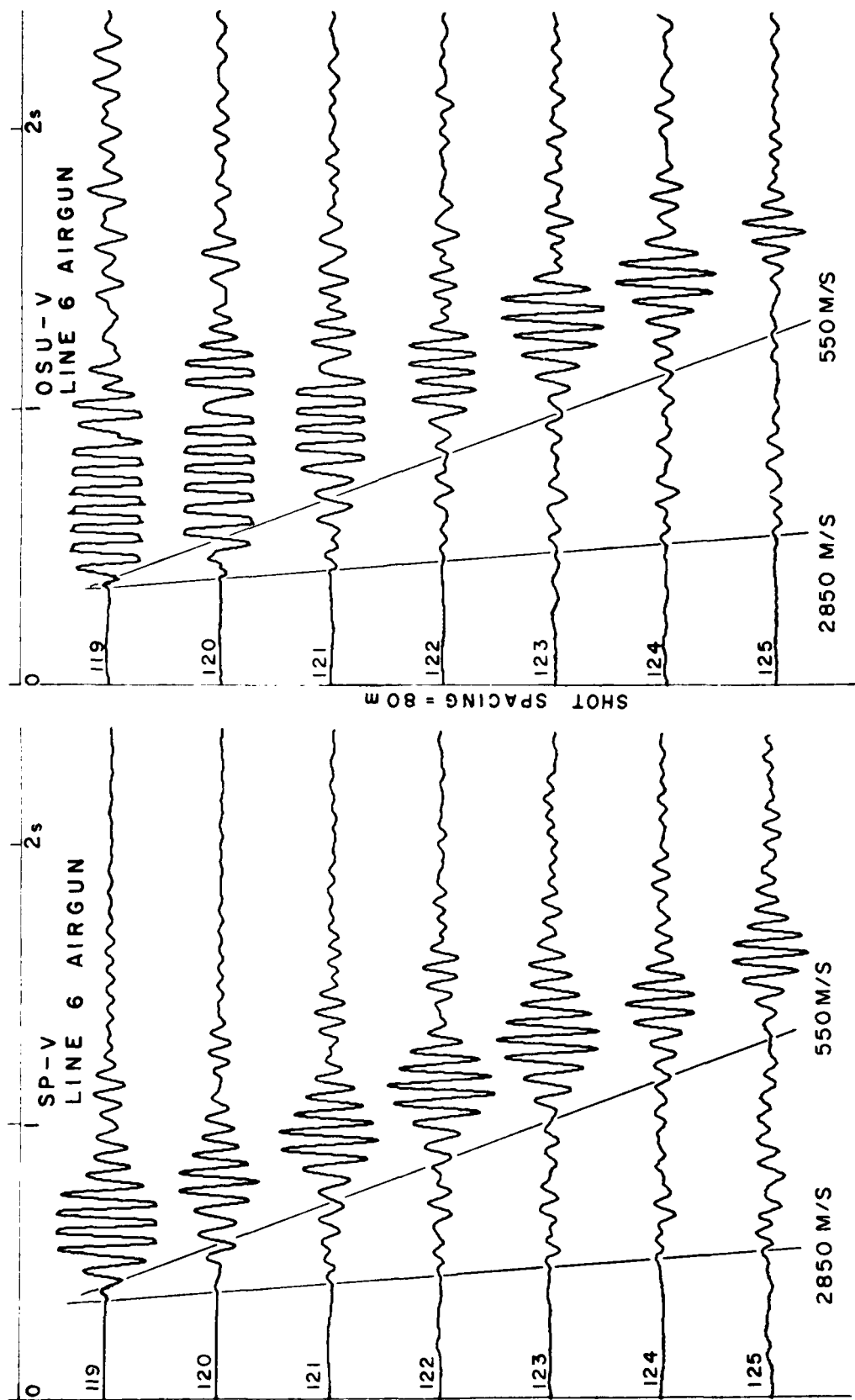


Fig. I-1. Record sections of arrivals to the spike vertical standard and to the vertical component of the Oregon State OBS along line 6, which was shot northwest from the array. Shot 125 is approximately 700 m from the array.

I-4

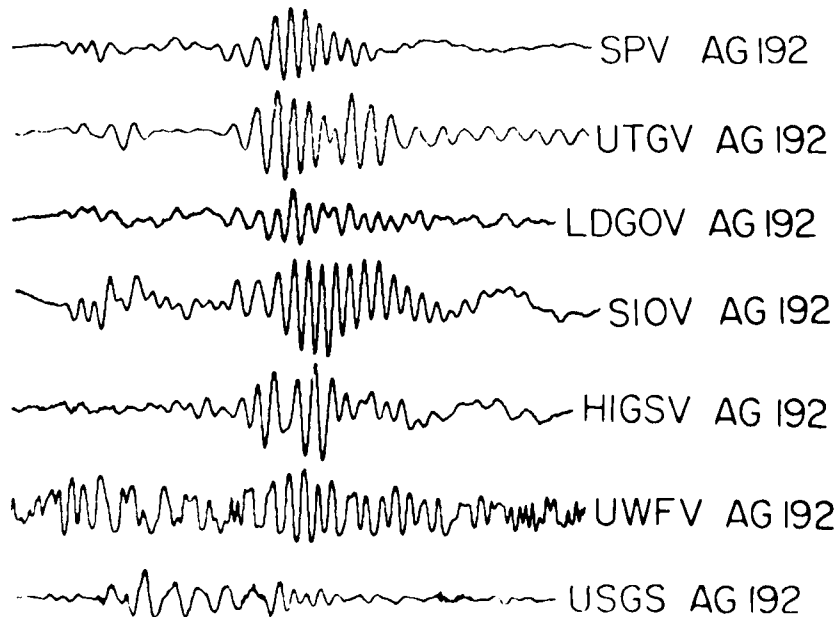
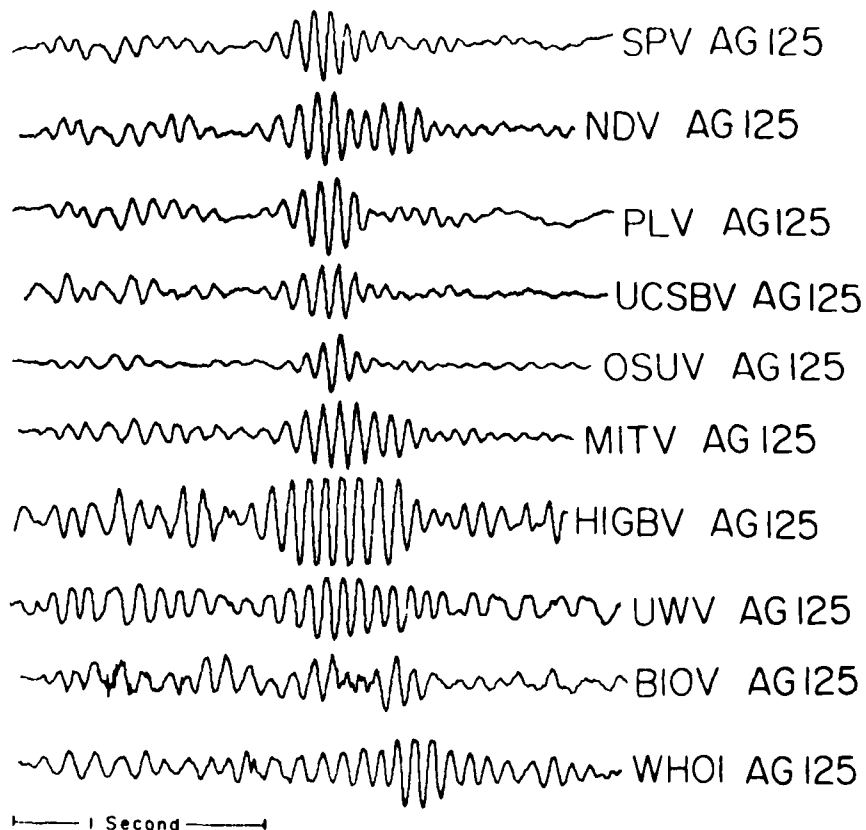


Fig. I-2. Comparison of seismograms analyzed in this study. The vertical component of each instrument is represented at least once. FKV and UWFV are identical capsules but in tripod and concrete stands respectively; HIGSV and HIGBV are, respectively, standard cylindrical pressure case and full-scale microphone configurations. WHOI is a hydrophone.

Ziolkowski (1970). The theory is based on dynamic and thermodynamic relations derived by Gilmore (1952) for an oscillating spherical bubble. The theoretical damped pressure wave generated under conditions at Lopez Island is given in Figure I-3a. Reflections of the signal from the air-water and water-bottom interfaces were delayed, attenuated and summed until their amplitude became less than 1% of the initial value (assuming $1/r$ spreading) as shown in Figure I-3b. The signal was filtered at 125 Hz and resampled at 4 ms (250 sps) to duplicate the conditions under which the OBS signals were digitized (Fig. I-3c). A fast-Fourier transform (FFT) algorithm generated the power spectrum of Figure 3d from 1.024 s (256 samples) of the filtered airgun signal. The spectrum has a peak at 14.5 Hz corresponding to the 69-ms bubble pulse period shown in Figure I-3a.

Observed Spectra

The initial portion of the observed wave signals in Figure I-2 were processed by the FFT to generate the spectra shown in Figures I-4, I-5 and I-6. Figure I-4 shows the theoretical spectrum to be in good agreement with the spectra for the standard geophones. In general, the observed spectra have a single maximum at about 13 Hz and, neglecting minima due to interference effects, fall off very much like the theoretical spectra. For comparison, Figure I-4 shows a shot close to the spike vertical, which is nearly identical to the theoretical. A geophone on land recorded shot 188 also, but the high background noise tends to mask any spectral peak.

Spectra for eight instruments are shown in Figure I-5 for airgun shot 125. The narrowest peaks are displayed by MITV and HIGBV, both of which had geophones in a separate pressure case to isolate the sensor from recording vibration. The low profile of the fall-away package appears to have the added advantage of producing more faithful representation of the ground motion in comparison to the spectra of other OBS's. This is probably due to the improved coupling of the sensor case of the bottom (Sutton et al., 1980a). The responses for the remaining five instruments are shown in Figure I-6 for airgun shot 192. These spectra are noisier than those for shot 125 but demonstrate a peak corresponding to the theoretical signal. The USGS instrument shows a lack of energy above 10 Hz. The reason for it is unknown, but the waveform is markedly unlike the others.

Discussion

The waveforms as detected by the OBS instruments for shots 125 and 192 are in general similar to, but in detail somewhat different from, those of the standard instruments. These differences are probably due to instrument responses that have not been incorporated in the presentation of seismograms. Comparison of spectra from distant shots (which should minimize cross coupling between horizontal and vertical motions of the

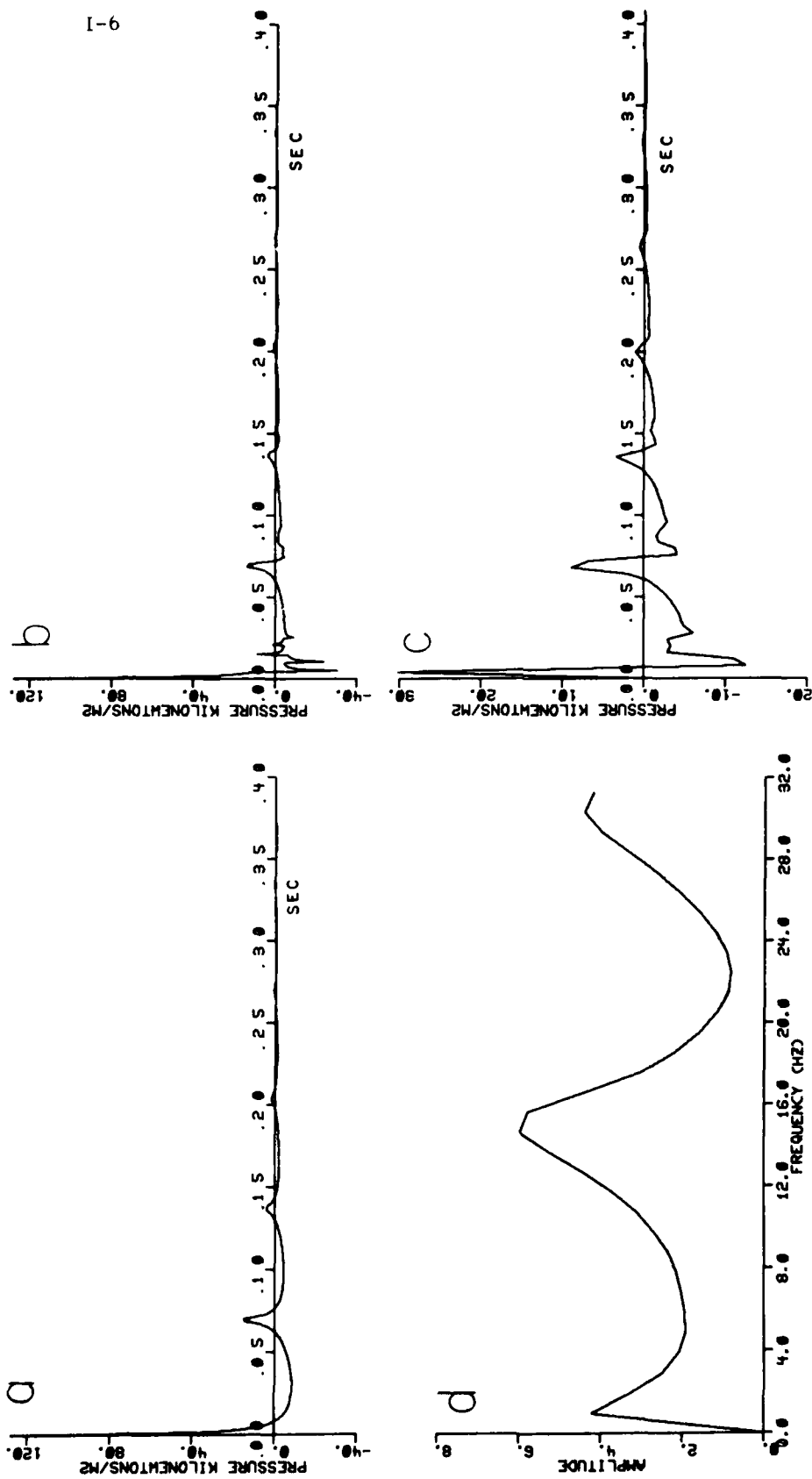


Fig. I-3. Theoretical airgun signal for a 40 cu.in.airgun at a depth of 3.4 m operated at 1883 psi in water 7.7 m deep. (a) Pressure pulse computed at 10- μ s intervals 4.3 m beneath the airgun. Signal was computed to 1.024 s but only the first 0.400 s is shown. (b) Pressure pulse plus three surface and two bottom reflections. A reflection coefficient of -1 was assumed at the water surface and the bottom reflection coefficient was computed assuming normal incidence at the interface between water (1.48 km/s) and the bottom (2.85 km/s). (c) Complete pressure pulse that has been filtered at 125 Hz and resampled at 4 ms (250 sps). (d) FFT of the complete filtered pressure pulse using 256 sample points (1.024 s).

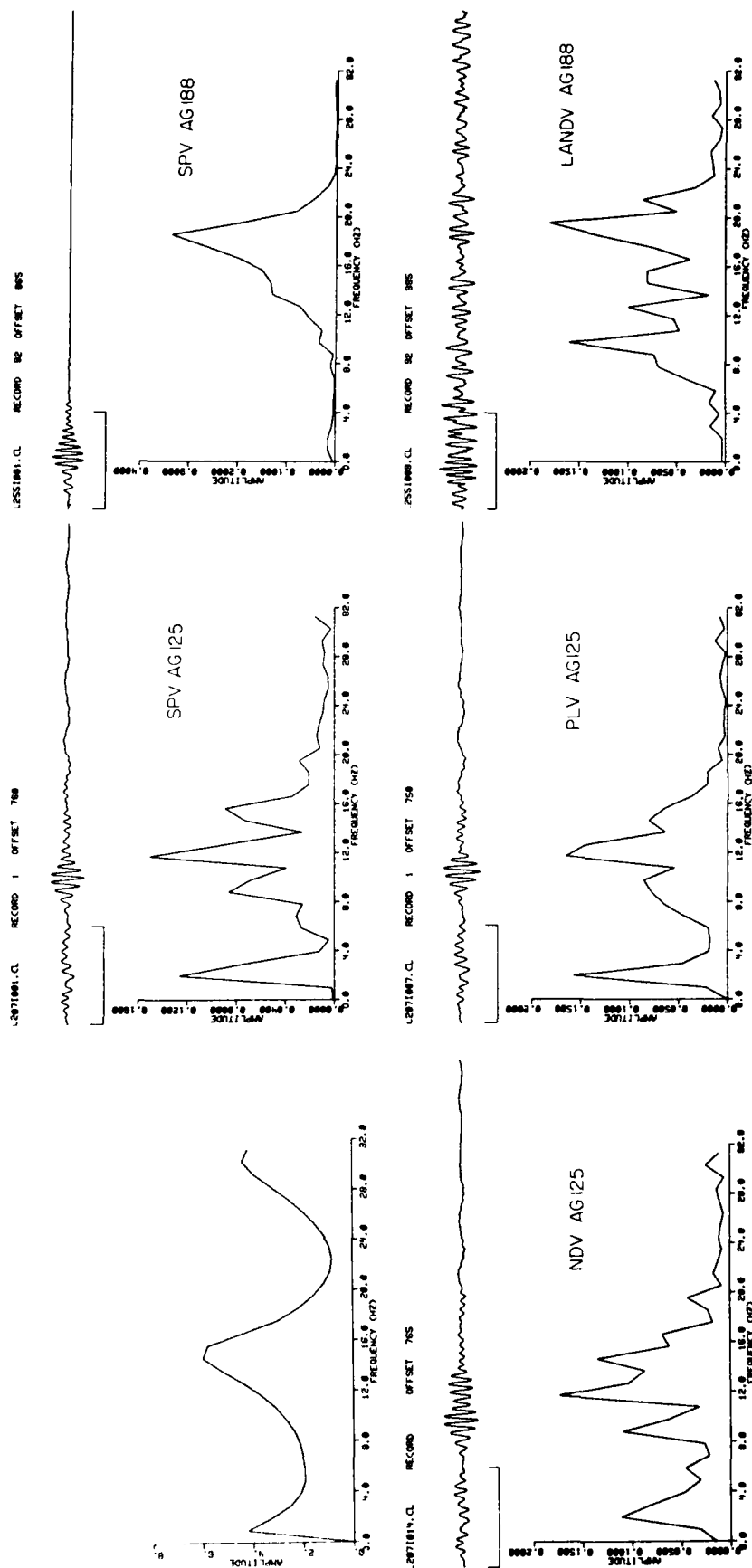
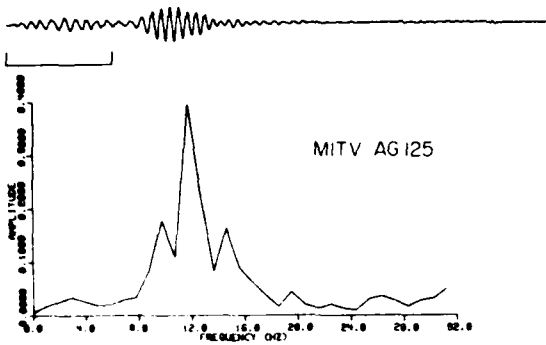


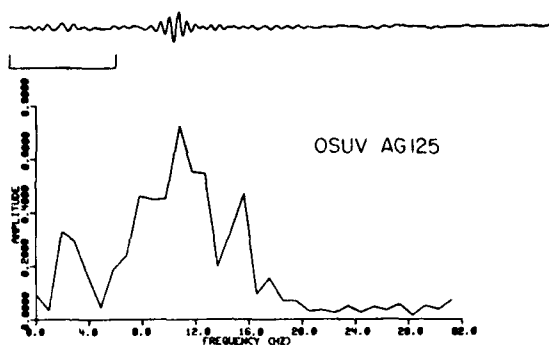
Fig. I-4. Theoretical spectrum and observed spectra for the standard vertical instruments at a distance of 700 m. For comparison, a shot (AG 188) close to the spike vertical at a distance of about 300 m and to a vertical geophone onshore are shown (upper right).

I-8

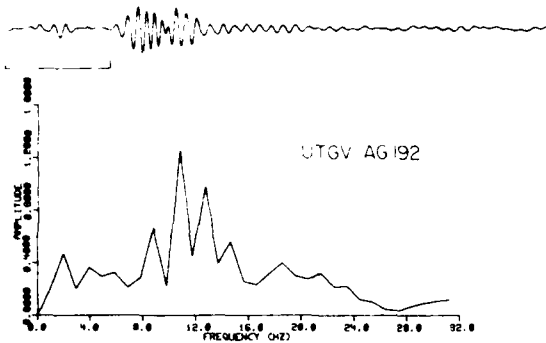
2071017.CL RECORD 1 OFFSET 705



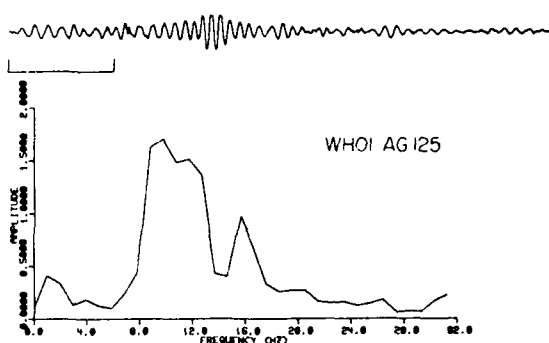
2071012.CL RECORD 1 OFFSET 700



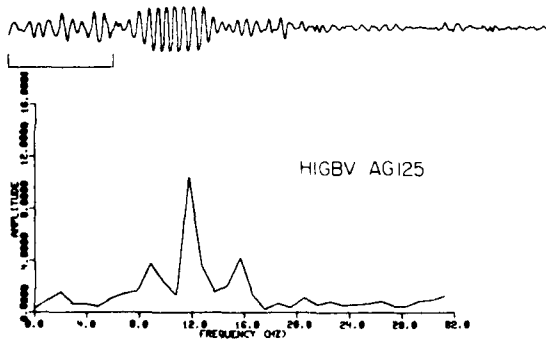
2551000.CL RECORD 2 OFFSET 000



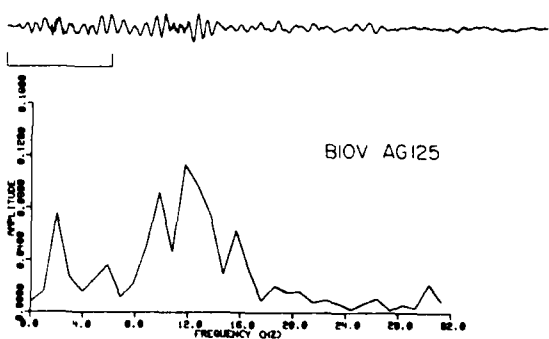
2071006.CL RECORD 1 OFFSET 692



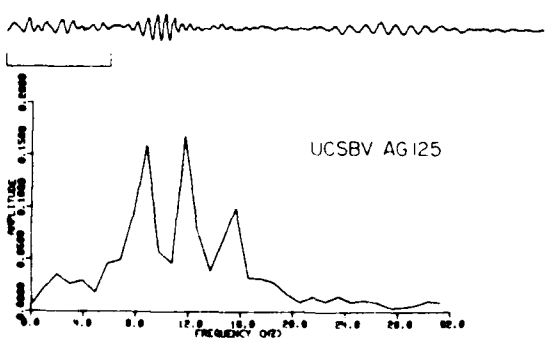
2071009.CL RECORD 1 OFFSET 705



2071010.CL RECORD 1 OFFSET 700



2071002.CL RECORD 1 OFFSET 705



2071004.CL RECORD 1 OFFSET 700

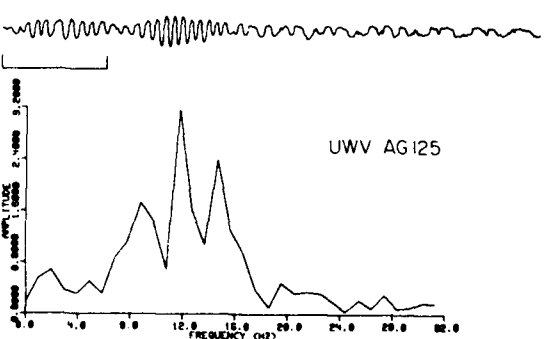
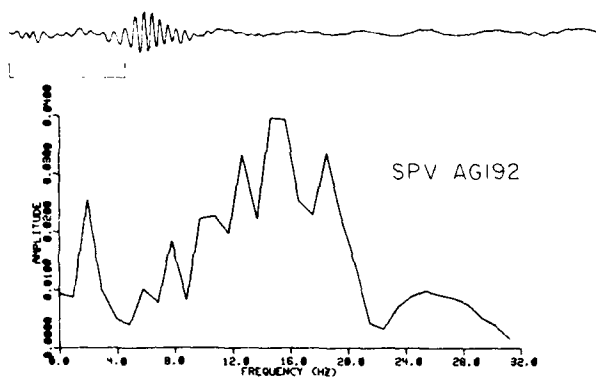
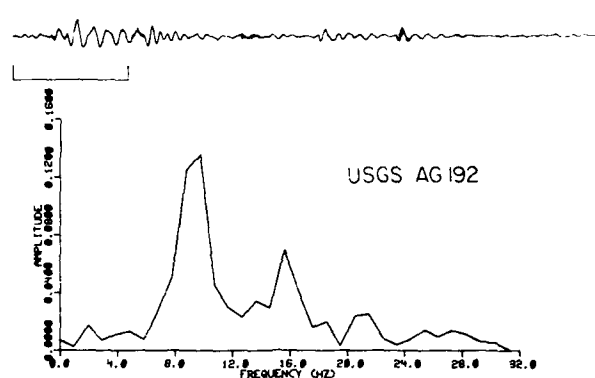


Fig. I-5. Seismograms and spectra for eight instruments from airgun shot 125.

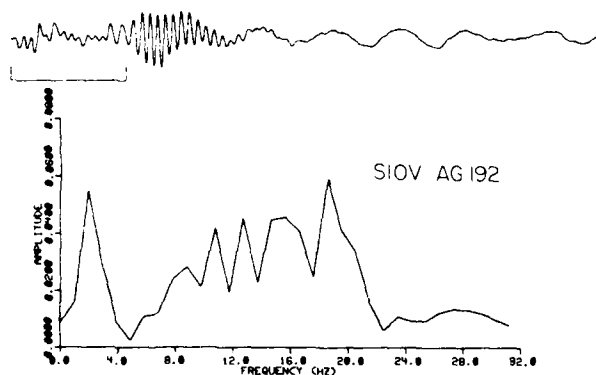
L2551001.CL RECORD 2 OFFSET 989



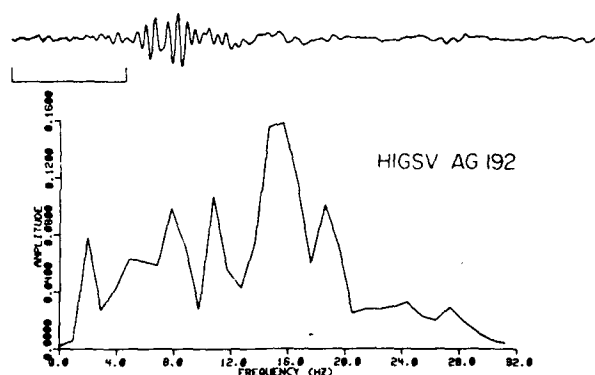
L2551002.CL RECORD 2 OFFSET 989



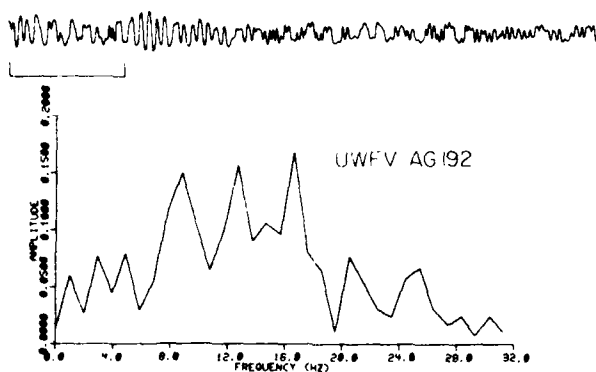
L2551005.CL RECORD 2 OFFSET 989



L2551011.CL RECORD 2 OFFSET 989



L2551013.CL RECORD 2 OFFSET 989



L2551029.CL RECORD 2 OFFSET 989

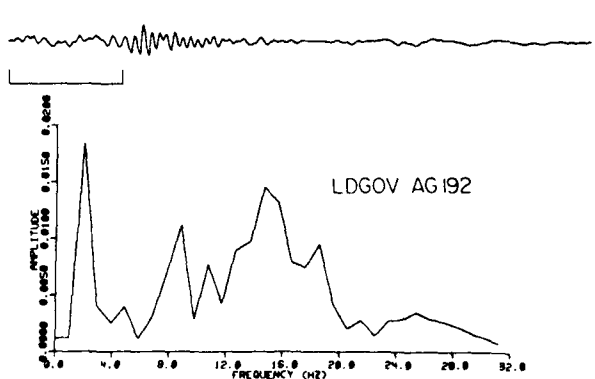


Fig. I-6. Seismograms and spectra for five instruments from airgun shot 192 at a distance of 600 m. The spike vertical standard is shown in upper left for comparison with SPV AG125 in Figure 4.

instrument due to rocking) are similar and resemble the spectrum expected on a theoretical basis. However, subtle differences remain between instrument spectra. The spectra most consistent with the theoretical are those whose geophone packages coupled properly to the bottom, i.e., the external geophone package. Of the remaining OBS types, there is little in the spectra of the compressional waves to distinguish signals of tripod-mounted spheres from those of inverted pendulum designs (where the float is located higher than the sensor). Exceptions to this are the UCSB instrument whose instrument response peaks at 8 Hz and the USGA instrument mentioned earlier.

Particularly noticeable in Figure I-5 is the frequency of the spectral peak at 12 Hz for the observed signals in comparison to 14.5 Hz for the theoretical signal. If we assume that this is due to frequency-dependent attenuation of the signal, we can calculate the Q of the medium. The spectral ratio between the theoretical signal and the spike vertical was formed for airgun shot 125. The values of this ratio versus frequency are shown plotted in Figure I-7 and a best fit straight line is drawn through the points. The slope of the line is related to attenuation and we compute a Q of 8.1 for the 2.85 km/s seismic layer.

The basement rock of Lopez Island is a siltstone-sandstone conglomerate of marine origin (Sutton et al., 1980b). The value of Q agrees favorably with laboratory measurements of Toksoz et al. (1979) on Boise and Navajo sandstone ($Q = 6.9 - 7.3$). We conclude that the frequency shift of the spectral peaks at Lopez Island is due to the low Q of the basement rock.

These observations of airgun signals confirm studies of OBS response from lift tests (Sutton et al., 1980a) and from particle motion studies (Lewis and Tuthill, 1980) but are somewhat less definitive. For low-amplitude P waves having a predominately vertical ray path, seismograms obtained with a wide variety of OBS designs compare favorably with signals from the standards. Large-amplitude waves with considerable horizontal motion adversely affect the OBS signal except for OBS with externally deployed geophones. Broadening and splitting of airgun spectra may be caused by coupling and the physical configuration of the instrument. The spectra observed for low-amplitude P-waves suggest that the spectrum of the source dominates over either OBS configuration or coupling of the instrument to the bottom. Finally, we suggest that the spectra of first arrival P-waves can be determined adequately from the signals of most of the OBS instruments at Lopez Island.

Acknowledgments

We are indebted to John Orcutt, who provided us and other Lopez Island participants with digital tapes from the experiment. This research was supported by the Office of Naval Research under contract N00014-79-C-0004.

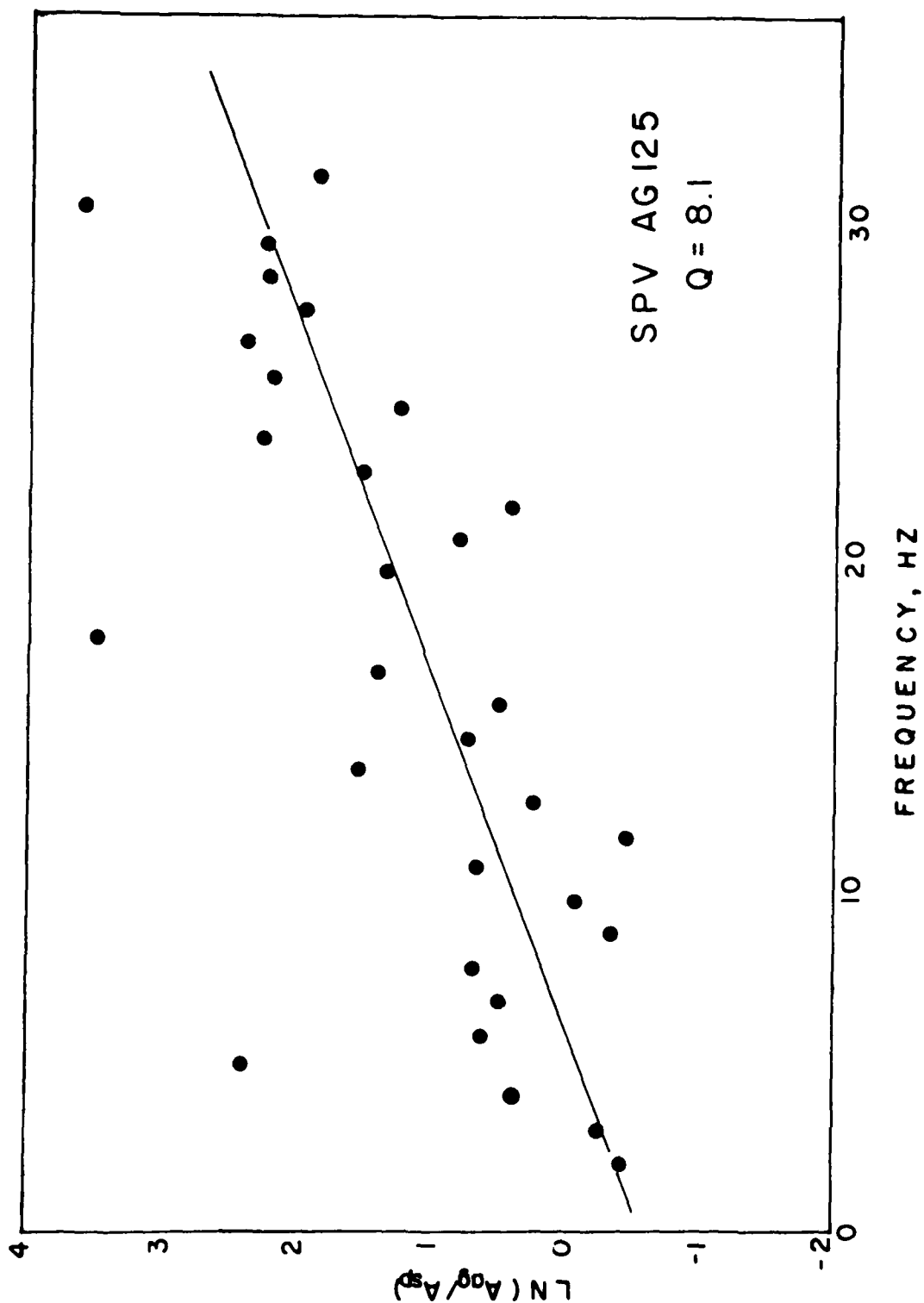


Fig. I-7. Spectral ratio of the theoretical airgun source function to the spike vertical standard for airgun shot 12. Attenuation is computed from the slope of the straight line fit to the points and gives $Q = 8.1$.

References

- Gilmore, F. R., 1952. Collapse of a spherical bubble. Report No. 26-4, Hydrodynamics Laboratory, California Institute of Technology, Pasadena, California.
- Lewis, B. T. R., and J. D. Tuthill, 1980. Instrumental waveform distortion on ocean bottom seismometers. This report, Appendix H.
- Sutton, G. H., F. K. Duennebier and B. Iwatake, 1980a, Coupling of ocean bottom seismometers to soft bottoms. This report, Appendix E.
- Sutton, G. H., B. T. R. Lewis, J. Ewing, F. K. Duennebier, B. Iwatake and J. Tuthill, 1980b. Lopez Island Ocean Bottom Seismometer Inter-comparison Experiment. This report.
- Toksoz, M. N., D. H. Johnson and A. Timur, 1979. Attenuation of seismic waves in dry and saturated rocks. I. Laboratory measurements, Geophysics, v. 44, p. 681-690.
- Tuthill, J. D., B. T. R. Lewis, and J. D. Garmany, 1980. Stoneley waves, Lopez Island noise and deep sea noise from 1 to 5 Hz. This report, Appendix G.
- Ziolkowski, A., 1970. A method for calculating the output pressure waveform from an airgun. Geophys. J. R. Astr. Soc., v. 21, p. 135-161.

Appendix J

CURRENT-GENERATED NOISE
RECORDED ON OCEAN BOTTOM SEISMOMETERS

CURRENT-GENERATED NOISE RECORDED ON OCEAN BOTTOM SEISMOMETERS

Frederick K. Duennebier, Grant Blackinton, and George H. Sutton

Hawaii Institute of Geophysics
University of Hawaii at Manoa
Honolulu, Hawaii 96822

Abstract

High-amplitude, narrow band noise that correlates with periods of high ocean bottom currents and the tidal cycle is occasionally observed on ocean bottom seismometers (OBS). The geophones on OBS's of different configurations are not equally sensitive to this noise and hydrophones are almost unaffected. With a suitable design, it should be possible to eliminate this noise problem.

Introduction

The effects of water currents on OBS's have been discussed in the literature, most recently by Kasahara et al. (in press). They relate the observed vibrations to Karman vortex shedding off various parts of the instrument and find that effects of Karman shedding are observable at water speeds above about 10 cm/sec. This value, however, is probably dependent on configuration of the package. In Karman shedding vortices of water spin away downstream from an obstruction and exert a force on the object. The vortices spin off at well-defined intervals resulting in a harmonic force on the body. The frequency of the force is governed by the equation $f = \frac{Cv}{d}$, where f is the frequency, v is the speed, d is the diameter of the body and C is the strouhal number. The strouhal number depends on the shape of the body and varies between 0.15 and 0.2 in this case. The shedding is non-linear in that the vortices do not begin to spin off until a critical speed is reached. The motions resulting from these forces can be amplified if the shedding frequency is near a natural resonance of the obstruction. Karman shedding in air caused by wind blowing around wires or flag poles generates a moan or whistle. Water density is about 1000 times greater than that of air; thus dynamic pressures against a body in water are about 1000 times greater than for that body in air at the same speed. The pressure exerted by a 3-m/sec (6-kt) wind is approximately equivalent to a current of 10 cm/sec. since pressure increases as the square of the speed.

In this paper we describe the effects of current on HIG OBS's, discuss design parameters that should minimize this noise, and speculate about the effects of currents on long-period seismic observations.

Analysis

The correlation of noise level recorded on an OBS south of the island of Hawaii in 5 km of water with current speed and tide can be seen in Figure J-1. The noise level has been reduced to nm (rms) of equivalent vertical ground motion to show the sensitivity of this OBS to currents. The tide is the theoretical ocean tide (Longman, 1959) computed for a point about halfway between the OBS and the current meter (which were separated by about 50 km). The lack of a perfect correlation between noise level and current speed is probably the result of two factors: (1) the distance separating the two instruments and (2) the sensitivity of the OBS to currents from different directions. The OBS is elongate in one direction (Fig. J-2) and may be more sensitive to current-induced noise in one direction than in the other. Spectra of the noise observed by the horizontal geophone in this OBS are shown in Figure J-3. The lower spectrum was taken when no current noise was visible and the upper when it was strong. The monochromatic character (with overtones) and narrow bandwidth of the current noise is obvious. The frequency of the noise is observed to increase slightly as the noise level increases. These spectra are similar to those observed by Bradner et al. (1965), who suggested that the noise was caused by Karman vortices from a radio antenna.

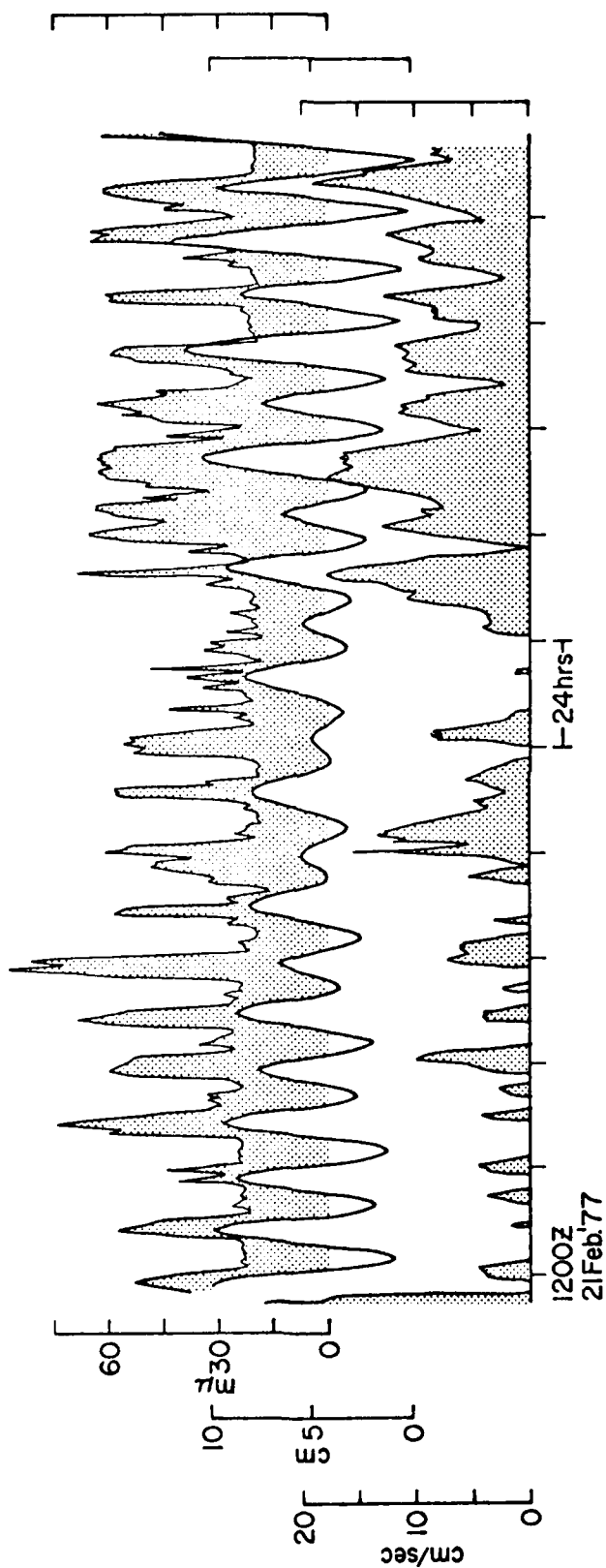


Fig. J-1. Noise amplitude on an OBS vertical geophone (top), theoretical ocean tide (middle), and ocean bottom current (bottom) south of Hawaii. The OBS and current meter were about 50 km apart in about 5 km of water. The traces have been offset slightly (± 3 hr) in time to remove phase differences. The increase in noise level on the OBS is apparently caused by changes in the tidal potential.

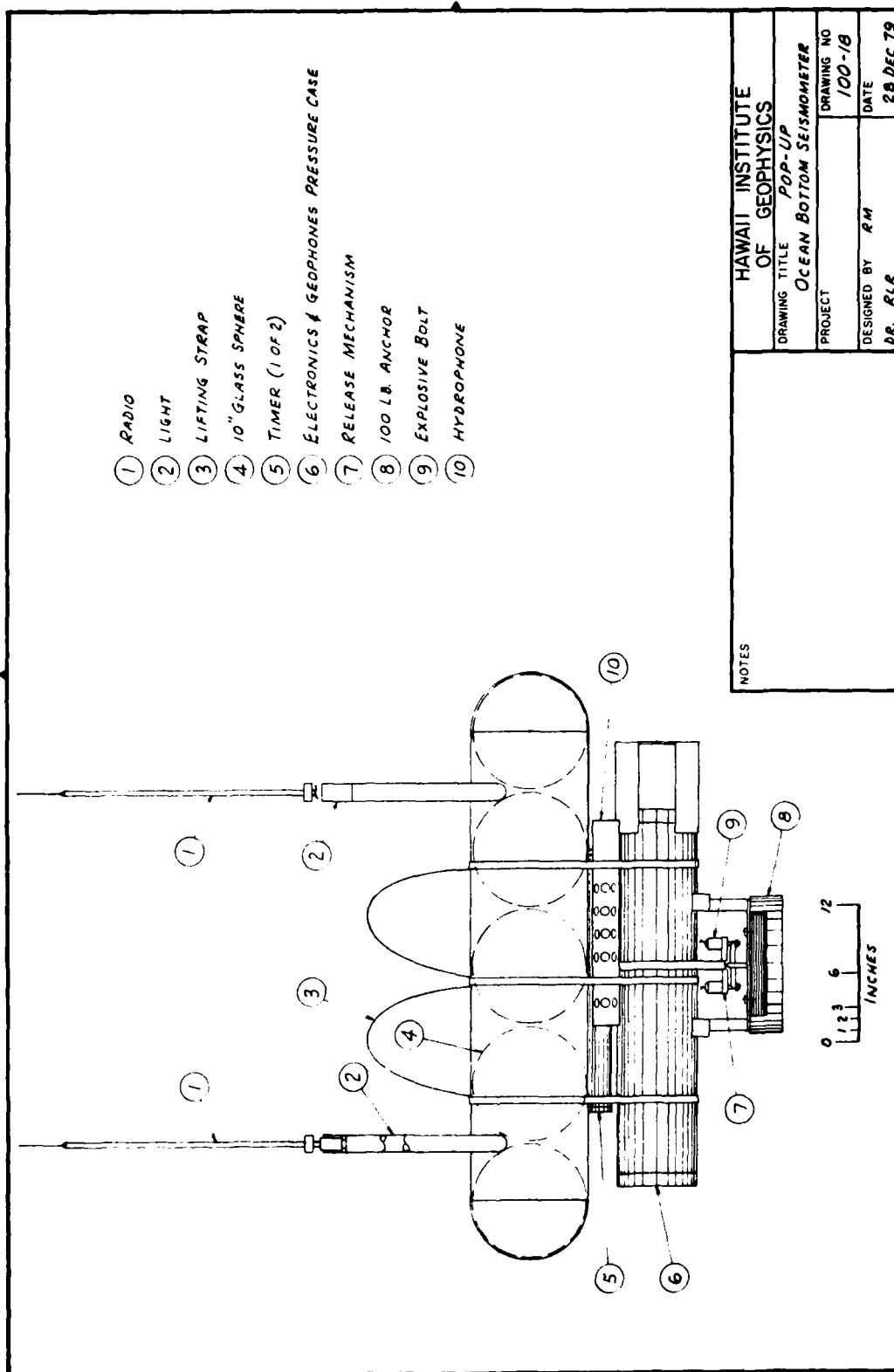


Fig. J-2. HIG "standard" ocean bottom seismometer. A vertical and a horizontal geophone are located inside the pressure case. Much of the observed current noise may be caused by vortex shedding from the radio antennas.

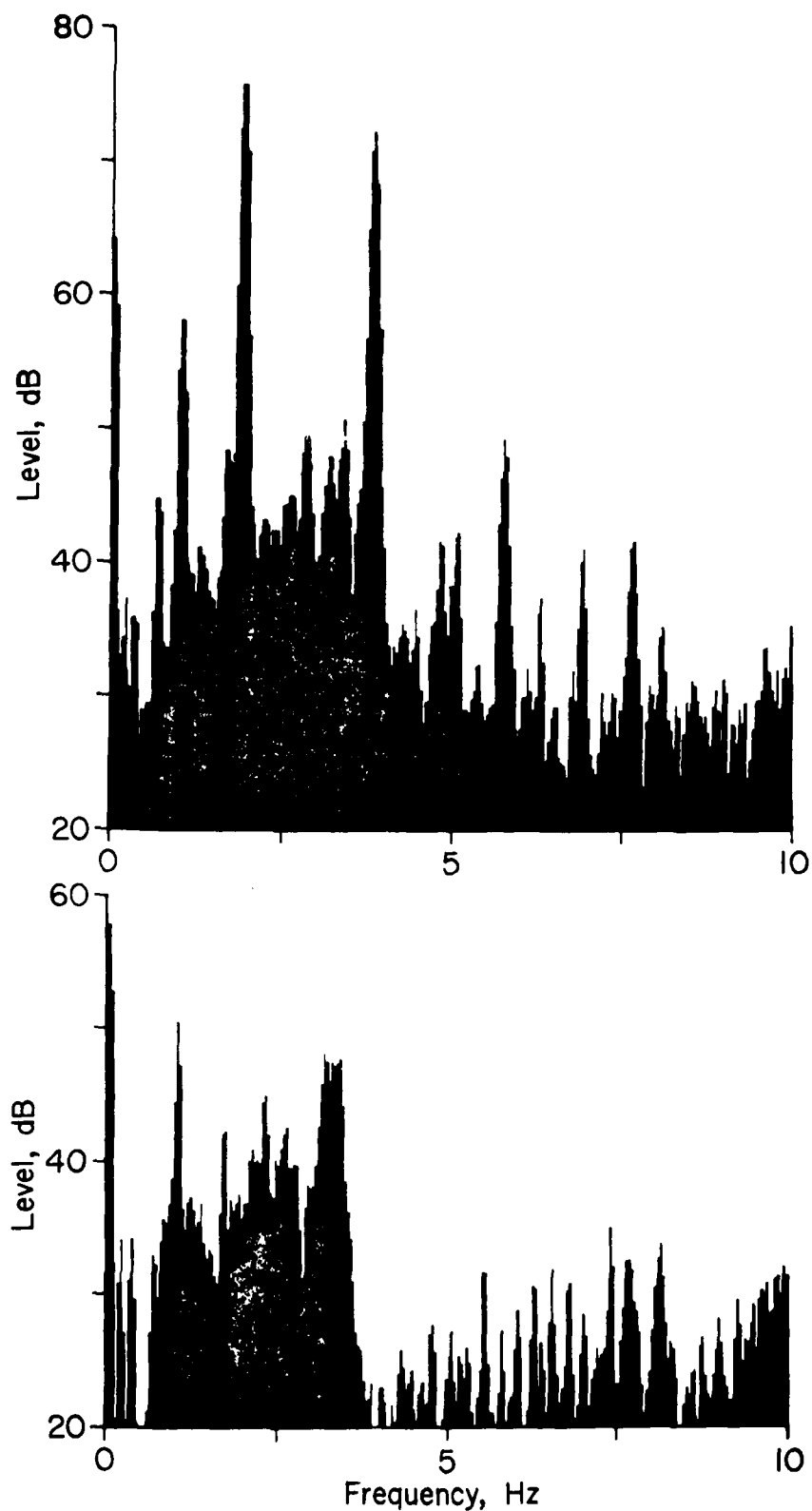


Fig. J-3. Spectra of background noise observed on an OBS of the type shown in Figure J-2. The lower plot shows noise levels during a period when no current noise was present. The upper plot shows the same OBS about an hour later. The current noise is visible as the narrow-band peaks near 2, 4, and 6 Hz. The peak near 1 Hz is probably 60-Hz noise generated during playback.

We first connected the 2-Hz "whistle" heard on HIG OBS's with the tidal cycle in 1976, and also noticed that the resonant frequency of our recovery radio beacon antennas was close to 2 Hz. In 1977, seven OBS's were dropped with various antenna configurations; some with balls attached near their centers or tops, some with flags attached to the top, and some with 2-inch-diameter PVC pipes around them. The recordings obtained from these OBS's showed some changes in resonant frequency but no consistent differences in current noise susceptibility. Although the antennas may be the main source of this noise, other parts of the OBS package may also be sources. In 1978 we designed a new style OBS (Fig. J-4) with isolated geophones in an attempt to overcome the current noise problem, to isolate the geophones from tape recorder noise, and to improve mechanical coupling to the ocean bottom.

The new configuration is much less sensitive to current noise. Figure J-5 compares noise levels observed by the two styles of HIG OBS's located within 100 m of each other in deep water. The spikes on each record are signals from explosives set off for a refraction line. The strong increase in the background level on the right side of traces B and C is current noise identical to that described above. Note that the hydrophone (trace A) and the two lower traces (D and E) are not affected by this noise. The hydrophone is attached to the package containing the geophones that produced traces B and C. The configuration of the OBS that recorded traces D and E (Fig. J-4) differs significantly from the OBS that produced traces B and C (Fig. J-2) in that the geophones are mechanically decoupled from the main package. The geophone package thus has a much lower profile, less complexity, and smaller cross section exposed to the current. We do not know if all (or any) of the above differences account for the reduction in current noise sensitivity, although the analysis of Kasahara et al. (in press) suggests that antennas attached to the sensor package are a major problem. He states that the problem can be reduced by attaching a fin to the antenna.

We estimate that from 5% to 15% of our geophone data from OBS's of the type shown in Figure J-2 is degraded by current noise. While the isolated-geophone package also has other advantages (Sutton et al., 1980a), the improvement in data quality shown in Figure J-5 is worth the added mechanical complexity of the isolated-geophone design.

Although many different OBS configurations are in use, only a few authors have mentioned current noise problems in their data. Whether it does not occur, is not recognized or observed, or is simply ignored is important to OBS design. If OBS's, especially OBS's with internal geophones, now exist that are insensitive to current noise, then one of the motives for building isolated-geophone OBS's becomes unimportant. One of the purposes of the Lopez Island OBS Intercomparison Experiment was to determine the effects of current noise on the various instruments (Sutton et al., 1980b). Unfortunately, the maximum currents observed during the experiment (5 cm/sec) were less than the 10 cm/sec found by Kasahara et al. (in press) as a threshold for the onset of Karman vortex shedding. The noise level at Lopez during the quietest times was about 50 nm at 2 Hz, which is higher than most of the current noise amplitudes from Figure

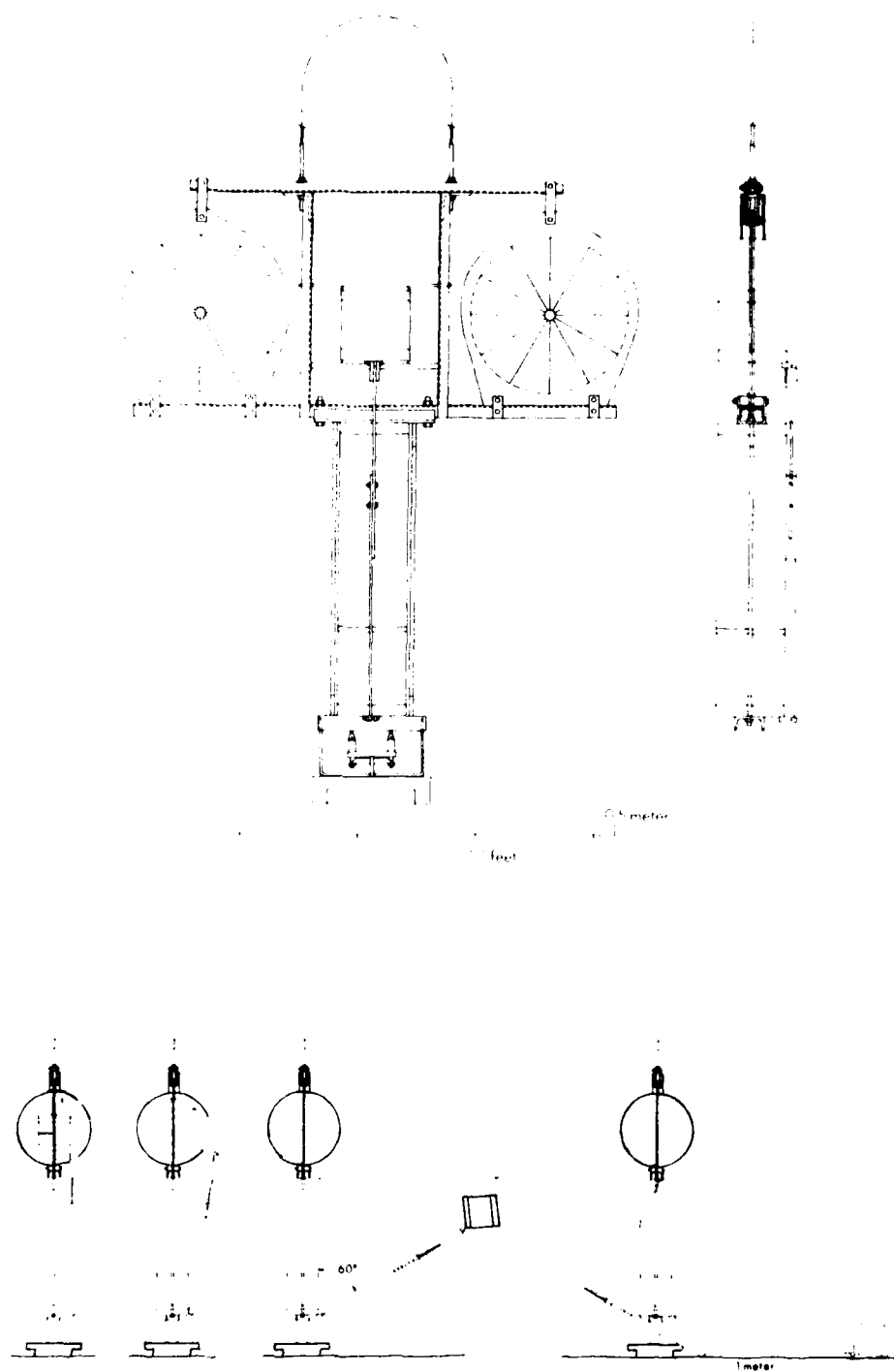


Fig. J-4. HIG external geophone OBS. The geophones are deployed away from the main recording package to decrease current and tape recorder noise and to improve coupling to the bottom.

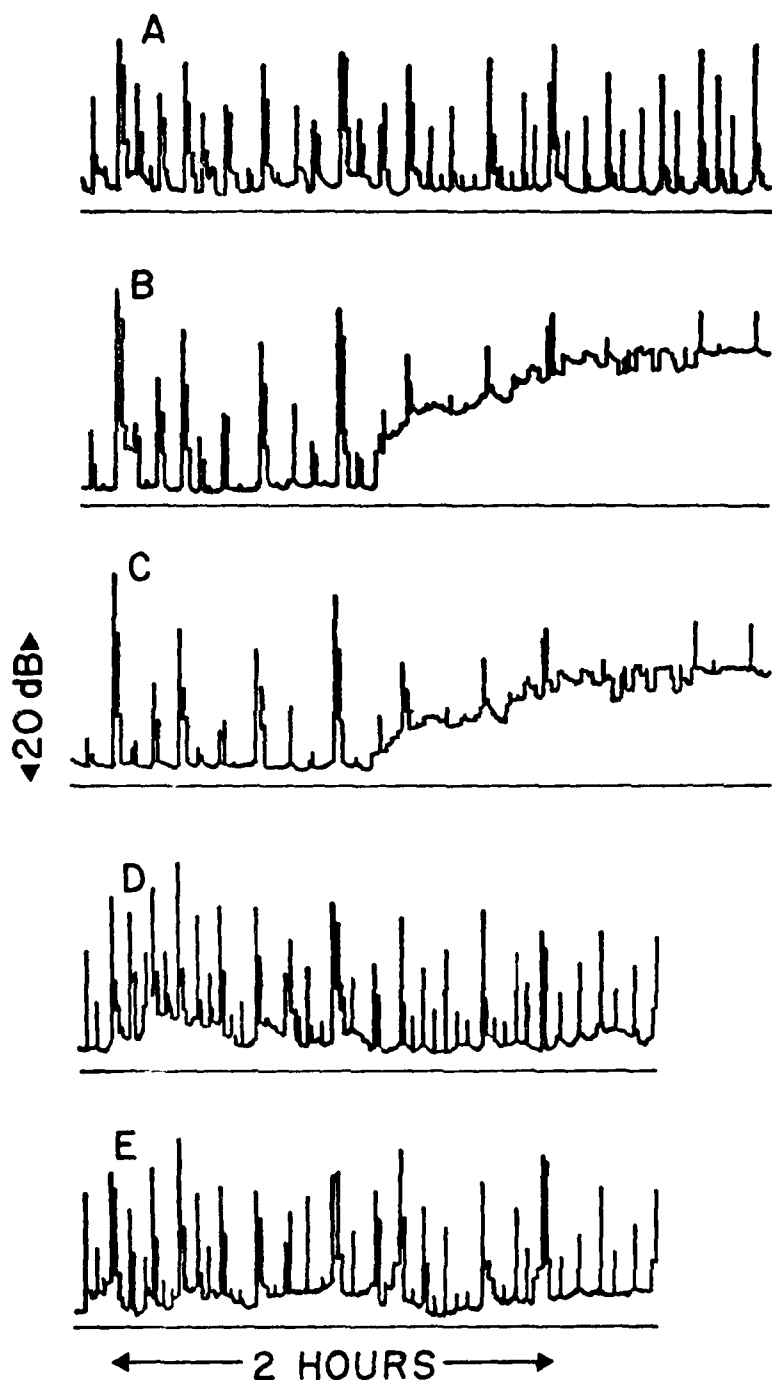


Fig. J-3. One-minute average noise levels versus time for the two different styles of OBS recorded in the same place at the same time during the shooting of a refraction line. Trace A is the record from a hydrophone; B is from a vertical; and C is from a horizontal geophone in an enclosed-geophone OBS (Figure J-2). D and E are records from vertical and horizontal geophones in a deployed-geophone OBS (Figure J-4). The increase in noise level to the right of traces B and C is caused by bottom currents. This noise does not appreciably affect the hydrophone (A) or the deployed geophones (D and E).

J-1. Even if noise was generated, it would be barely detectable. An HIG OBS identical to that shown in Figure J-2, and known to be susceptible to current noise, was present at the Lopez Experiment and recorded none. The Lopez Experiment did not test OBS's for current noise susceptibility nor has any test for this parameter been made for most of the OBS's now in use.

Vortex shedding is not the only possible mode of coupling current noises to OBS's. An instrument resting on soft sediments can be tilted by the current pressure against it. For example, an OBS with a circular cross section about one meter in diameter centered about 0.5 m above the ocean bottom with a tripod base and mass of 200 kg in Lopez-type sediments (Sutton et al., 1980b) would tip about 5×10^{-6} m (10^{-5} radius) in response to a 10 cm/sec current. While a tilt such as this would not be important for short-period seismometers, long-period horizontal seismometers would be driven off scale. A small fluctuation in current speed would produce objectionable noise at shorter periods.

Conclusions

Current noise is a known problem for at least some ocean bottom seismometers. At short periods, the principal mode of noise transmission appears to be the shedding of Karman vortices from antennas and other resonant obstructions. At long periods, tilting of the OBS caused by ocean bottom currents could be a serious problem. Both problems can be improved significantly by isolating the sensors from possible current noise sources (analogous to planting geophones on land away from trees) and by keeping the cross section to the water as small as possible. The isolated-sensor HIG OBS appears to have a relatively low current noise sensitivity. Most OBS's, however, have never been tested for current noise sensitivity.

Acknowledgments

Research into using OBS's as current meters was begun in 1977 by our colleague Robert Harvey but, sadly, was interrupted when he was lost at sea in December, 1978. The data from which Figure J-1 was produced were obtained by Dr. Harvey. We thank Rita Pujalet for her editorial help, Steve Dang for drafting the figures, and Kenji Nemoto for translating Kasahara et al. (in press). This research was supported by ONR and NSF.

References

- Bradner, H. J. Dodds, and R. Foulks, 1965. Coherence measurements with time sampling ocean bottom seismometers. Proc. IEEE, v. 53, p. 1906-1908.
- Kasahara, J., S. Nagumo, S. Koresawa, and T. Daikubara, 1980. Experimental results of vortex generation around ocean-bottom seismograph due to bottom current. Bull. Earthq. Res. Inst. (In press.)
- Longman, I. M., 1959. Formulas for computing the tidal accelerations due to the moon and the sun. J. Geophys. Res., v. 64, no. 12, p. 2351-2355.
- Sutton, G. H., F. K. Duennebie, and B. Iwatake, 1980a. Coupling of ocean bottom seismometers to soft bottoms. This report, Appendix E.
- Sutton, G. H., B. T. R. Lewis, J. Ewing, F. K. Duennebie, B. Iwatake, J. D. Tuthill, and others, 1980b. Lopez Island ocean bottom seismometer intercomparison experiment Final Report. HIG-80-4, Hawaii Inst. Geophys., Honolulu. (This report.)

Unclassified

SECURITY CLASSIFICATION OF THIS PAGE (When Data Entered)

14 REPORT DOCUMENTATION PAGE		READ INSTRUCTIONS BEFORE COMPLETING FORM
1. REPORT NUMBER HIG-80-4	2. GOVT ACCESSION NO. AD-A094355	3. RECIPIENT'S CATALOG NUMBER
4. TITLE (and Subtitle) LOPEZ ISLAND OCEAN BOTTOM SEISMOMETER INTERCOMPARISON EXPERIMENT. Final Report.		5. TYPE OF REPORT & PERIOD COVERED Final report.
7. AUTHOR(s) G.H. Sutton, B.T.R. Lewis, J. Ewing F.K. Duennebier, B. Iwatake, J.D. Tuthill, and others		8. CONTRACT OR GRANT NUMBER(s) N00014-75-C-0209
9. PERFORMING ORGANIZATION NAME AND ADDRESS Hawaii Institute of Geophysics 2525 Correa Road Honolulu, Hawaii 96822		10. PROGRAM ELEMENT PROJECT, TASK AREA & WORK UNIT NUMBERS
11. CONTROLLING OFFICE NAME AND ADDRESS Office of Naval Research Ocean Sciences & Technology Division Bay St. Louis, MS 39520		12. REPORT DATE October 1980
14. MONITORING AGENCY NAME & ADDRESS (if different from Controlling Office) Office of Naval Research Branch Office 1030 East Green Street Pasadena, CA 91106		13. NUMBER OF PAGES 272
		15. SECURITY CLASS. (of this report)
		15a. DECLASSIFICATION/DOWNGRADING SCHEDULE
16. DISTRIBUTION STATEMENT (of this Report) Approved for public release; distribution unlimited.		
17. DISTRIBUTION STATEMENT (of the abstract entered in Block 20, if different from Report)		
18. SUPPLEMENTARY NOTES		
19. KEY WORDS (Continue on reverse side if necessary and identify by block number) Ocean bottom seismometer Seismic noise Sediment properties Ocean currents Lopez Island Seismic coupling Hydrophone Geophone		
20. ABSTRACT (Continue on reverse side if necessary and identify by block number) The purpose of the Lopez Island Ocean Bottom Seismometer Intercomparison Experiment was to determine the effects of coupling and bottom currents on ocean bottom seismometers. Twelve operational OBS's, three specially designed three-component systems, and a hydrophone were compared with each other. Unlike seismometers placed on hard rock at land stations, ocean bottom seismometers can be affected by soft sediments (which act as lossy mechanical springs) and by buoyancy. Coupling through soft sediments can modify the response to		

DD FORM 1 JAN 73 1473

EDITION OF 1 NOV 65 IS OBSOLETE
S N 0102-014-6601

Unclassified

SECURITY CLASSIFICATION OF THIS PAGE (When Data Entered)

164400

CM

Unclassified

SECURITY CLASSIFICATION OF THIS PAGE(When Data Entered)

ground motion much as a low pass filter does, and high buoyancy tends to counteract this effect. These effects are observed in the Lopez data, which consist of signals from mechanical transient tests, cap shots, airgun pulses, and general background noise. The modification of response is pronounced for some instruments and barely noticeable in others. Instruments that stand high in the water relative to their base width tend to be susceptible to rocking motion that shows up as a mechanical cross coupling between horizontal and vertical motion. Correlation of Lopez results with coupling theory suggests that it is possible to design ocean bottom seismometers that will couple well to any sediment. Current levels at the Lopez site (<5 cm/sec) were too small to produce noticeable effects on any of the instruments; however, the same design criteria that will minimize coupling problems will also lessen problems caused by ocean currents.

Unclassified

SECURITY CLASSIFICATION OF THIS PAGE(When Data Entered)

DAT
ILM